ACTIVATION OF CARBON DIOXIDE – CONVERSION TO FUELS AND CHEMICALS

A Thesis submitted to
Madurai Kamaraj University
for the award of the Degree of

DOCTOR OF PHILOSOPHY
IN
CHEMISTRY
By
V. JEYALAKSHMI
(Reg. No. F8645)

Research Supervisor
Dr. R. MAHALAKSHMY, M.Sc., Ph.D.,
Assistant Professor
Post graduate and Research Department of Chemistry
Thiagarajar College (Autonomous)
Madurai - 625 009

MADURAI KAMARAJ UNIVERSITY
(University with Potential for Excellence)
MADURAI - 21

MARCH – 2016

Dedicated to
my Parents

THIAGARAJAR COLLEGE, MADURAI-9

(An Autonomous Institution Affiliated to Madurai Kamaraj University)
Re-Accredited with 'A' Grade by NAAC

Post Box No. 107
139-140, Kamarajar Salai
Madurai – 625 009, Tamilnadu
Mobile No. : +91-9443027784
E-mail: mahabioin@yahoo.com

Dr. R. MAHALAKSHMY, M. Sc, Ph.D
Assistant Professor of Chemistry

Date:

CERTIFICATE

Certified that the thesis entitled, **"ACTIVATION OF CARBON DIOXIDE – CONVERSION TO FUELS AND CHEMICALS"** submitted by **Ms. V. JEYALAKSHMI (Reg. No. F 8645)**, Research Scholar, Post Graduate and Research Department of Chemistry, Thiagarajar College, Madurai is a record of research work carried out by her for the degree of **Doctor of Philosophy in Chemistry** under my guidance.

This thesis is an original work of the candidate and to the best of my knowledge has not been submitted, in part or in full for any other diploma, degree, fellowship or other similar title in this or other similar university. No portion of this thesis is a reproduction from any other source, published or unpublished, without acknowledgement.

Signature of the Guide
(Dr. R. MAHALAKSHMY)

DECLARATION

I declare that the thesis entitled **"ACTIVATION OF CARBON DIOXIDE – CONVERSION TO FUELS AND CHEMICALS"**, is the result of a study originally carried out by me under the guidance of **Dr. R. MAHALAKSHMY**, Assistant Professor, Department of Chemistry, Thiagarajar College, Madurai. This work has not been submitted earlier, in full or in part, for any other degree or diploma in this or any other university.

I further declare that no part(s) of the thesis is /are a reproduction from any other source, published or unpublished, without acknowledgement.

Place: Madurai
Date:

Signature of the candidate
(V. JEYALAKSHMI)

ACKNOWLEDGEMENT

At first, I owe my thanks to GOD Almighty for sustaining me with his grace and strength while doing my research work.

I express thanks to my beloved guide **Dr. R. MAHALAKSHMY**, Assistant Professor, Department of Chemistry, Thiagarajar College, Madurai, for her excellent guidance and constant encouragement throughout my research period. Her mentorship provided me with the perfect balance of research independence and support. I would like to acknowledge the efforts taken and moral support rendered during my research work.

I take immense pleasure in expressing my deep sense of gratitude and heartfelt thanks to my research supervisors **Prof. B. VISWANATHAN** and **Prof. K. R. KIRSHNAMURTHY**, National Centre for Catalysis Research, IIT-Madras, for their excellent guidance, constant and consistent encouragement, good advice and caring with ever smiling face throughout my research period. I would like to acknowledge them for their efforts and moral support at every instance, without which, this would not have reached this state. Their sincerity, untiring support and creative ideas made my research experience challenging and stimulating. I have been truly lucky to be a part of NCCR research group for their fruitful discussions which broadened my perspective on the field of catalysis.

I am thankful to the Department of Science & Technology, Government of India, New Delhi and Indian Institute of Technology, Madras, Chennai, for allowing me to carry out experimental work in NCCR laboratories and extending all infrastructure facilities in NCCR.

I would like to express my grateful thanks to HPCL management for the funding the collaboration project on “Chemical mitigation of Carbon dioxide” between NCCR-IITM and Hindustan Petroleum Corporation limited (HPCL), Mumbai.

I sincerely thank the former Principal and Head, Department of Chemistry, Prof. Dr. A. Thamaraichelvan and Head, Department of Chemistry Dr. A. Suganthi and Dr. R. Sayee Kannan for their constructive suggestions, parental care, constant encouragement during every stage of my research work.

I would like to offer my heartfelt thanks to the teaching staff members of the Department of Chemistry, Thiagarajar College specially, Dr. P. Tharmaraj, Dr. A. Elangovan, Dr. P. Prakash, who offered their support in various ways.

Words are inadequate to express heartfelt gratitude to my friends, Ms. G. Saranya, Mr. K. Seetharaman, Mrs. Arthi Vijayakumar, Mr. P. Jayachandran, without whom I would not have been at this positive pedestal of my life.

I would like to thank Mrs. K. Rajalakshmi, with whom I have started this research problem and encouraged me throughout this thesis.

I am always thankful to Mrs. R. Vijayashanthi, for her timely help, friendship, who was with me day and night during my experiments in IITM.

I thank my colleagues Mrs. K. Devaki, Dr. G. Magesh, Dr. N. Vamsi Krishna, Dr. Thirunavukkarasu, Mr. K. Suthagar, Mr. Sourav Khan, Mr. Ariharan, Mr. Mahendran, Ms. A. Saranya, Mr. P.S. Ramesh, Ms. S. Tamilmani, Ms. Anbu anjugam, Mr. Vinayagamoorthy, Mr. P. Tamil Durai, Dr. M. Banu, Dr. Ramanamurthy, Mr. Anil Kumar, Mr. Rama Mohan, Mr. R. Shanmugam, Mr. M.G Prakash, Mr. Sanjeev Gupta, Mr. Suryakumar, Mr.Rajasekar for their help in many aspects.

Finally, I express my deepest gratitude to my parents (S. Velu, V. Muthumari), Teacher (Mrs. Mary), Brothers (V. Senthilkumar, V. Ananth, A. Vijay), Aunty (A. Ramayee) and A. Viji for their unrivaled love, constant support and encouragement that make my life happy and meaningful.

(V. JEYALAKSHMI)

CONTENTS

CHAPTER 1 INTRODUCTION

CHAPTER 2 EXPERIMENTAL METHODOLOGY

CHAPTER 3 STUDIES ON TITANIA BASED CATALYSTS FOR PHOTO CATALYTIC REDUCTION OF CO_2

3.1 Influence of doping/co-doping with anions (N&S) and meso porous structure of Titania

3.2 Effect of supporting tri-doped meso-porous titania on Sepiolite clay matrix

CHAPTER 4 STUDIES ON SODIUM TANTALATE BASED CATALYSTS FOR PHOTO CATALYTIC REDUCTION OF CO_2

4.1. Photo catalytic reduction of carbon dioxide on La modified sodium tantalate with different co-catalysts under UV-visible radiation

4.2 Modifications in $Na_{(1-x)}La_xTaO_{(3+x)}$: Influence of doping with Nitrogen and Iron (Fe^{3+}) on photo catalytic reduction of CO_2

4.3 Modifications in $Na_{(1-x)}La_xTaO_{(3+x)}$: Effect of addition of MgO on photo catalytic reduction of Carbon dioxide

4.4. Modifications in $Na_{(1-x)}La_xTaO_{(3+x)}$: Effect of sensitization with Cobalt Tetra Phenyl Porphyrin on photo catalytic reduction of CO_2

CHAPTER 5 STUDIES ON STRONTIUM TITANATE BASED CATALYSTS FOR PHOTO CATALYTIC REDUCTION OF CO_2

5.1. Modifications in $Sr_3Ti_2O_7$ catalyst to enable visible light absorption

5.2 Layered perovskite titanates ($SrTiO_3$, $Sr_3Ti_2O_7$ and $Sr_4Ti_3O_{10}$) as catalysts for photo reduction of CO_2

CHAPTER 6 SUMMARY AND CONCLUSIONS

LIST OF FIGURES

LIST OF TABLES

LIST OF SCHEMES

ABBREVIATIONS

AR - Analytical Reagent
atm - atmosphere
BE - Binding Energy
deg - degrees
DOS - Density of density
EDS - Energy Dispersive Spectra
FID - Flame Ionization Detector
GC - Gas Chromatography
TCD - Thermal Conductivity Detector
Hz - Hertz
FT-IR - Fourier Transform Infrared Spectroscopy
ml - milliliter
mmol - millimoles
ppm - partsper million
MPa - Mega Pascal
HOMO - Highest Occupied Molecular Orbital
LUMO- Lowest Unoccupied Molecular Orbital
VBM - Valence Band Maximum
CBM - Conduction Band Minimum
SEM - Scanning Electron Microscopy
TEM - Transmission Electron Microscopy
UV-Vis- Ultra violet - Visible
XRD - X-ray diffraction
XLBA - X-ray Line Broadening Analysis
XPS - X-ray photoelectron Spectroscopy

NOTATIONS

eV - electron Volt
m^2/g - Square meter per gram
e^- - electron
h^+ - hole
K - Kelvin
g - gram
Ȧ - Angstrom
d - Interplanar spacing planar
r - Radius
λ - Wavelength
cm - centimeter
nm - nanometer
mA - milli Amps
V - Volts
wt - Weight
kJ - Kilo Joule
hr - hour
θ - Bragg angle
υ - Frequency
% - Percentage
ºC - Degree Celsius
kCal - Kilo Calories
µmol - Micromole

CHAPTER 1

INTRODUCTION

1.1 Role of carbon dioxide

Presence of carbon dioxide is essential for the photo synthesis process, which forms the lifeline for all the flora and fauna that define the ecology of this earth. In fact, all other forms of life, including human beings, survive on the oxygen which is the by-product of photo synthesis. However, atmospheric CO_2 level has to be within certain limits. The optimum concentration of CO_2 necessary for the bio-network on earth is 300 ppm [1]. In earlier days, as shown in Fig. 1.1, CO_2 level in the atmosphere and the carbon cycle was maintained by a series of natural processes as described below.

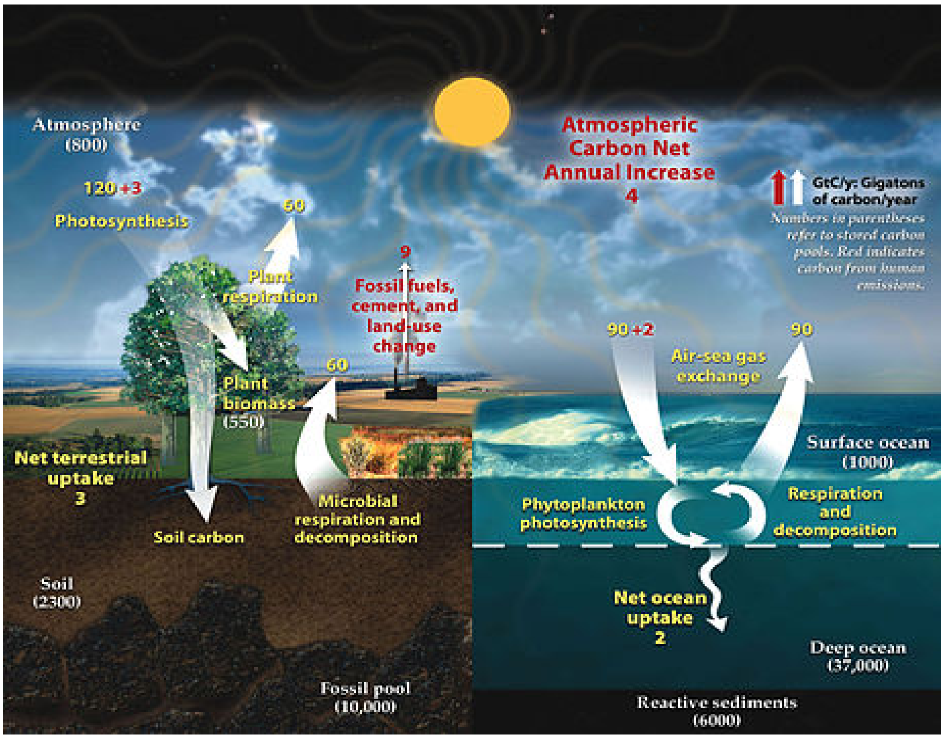

Fig. 1.1 Carbon cycle shows the movement of carbon between land, atmosphere, and oceans in billions of tons of carbon per year. Yellow numbers are natural fluxes; red are human contributions in billions of tons of carbon per year. White numbers indicate stored carbon. (Reproduced from https://en.wikipedia.org/wiki/Carbon_cycle)

In modern days, this delicate carbon cycle has been disturbed and atmospheric CO_2 level is gradually increasing. According to the data [2] published by International Energy Agency (IEA), CO_2 emission is exponentially increasing since the year 1870, mainly from the combustion of fossil fuels as shown in Fig. 1.2, in order to meet our energy requirements. Global Total Primary Energy Supply (TPES) has almost doubled, from 1971 to 2012, and 82% of TPES is derived by burning fossil fuels, emitting large quantities of CO_2 [2]. Since energy is essential for economic growth and overall development, increase in atmospheric CO_2 level is expected to remain high. CO_2 emissions from the fossil fuels pose serious environmental issues like green-house gas effect and unusual weather patterns. Even though CO_2 is the least effective green-house gas per kilogram emitted, it is considered as significant green-house gas due to large amount released to the atmosphere from human activities and industrial revolution [3].

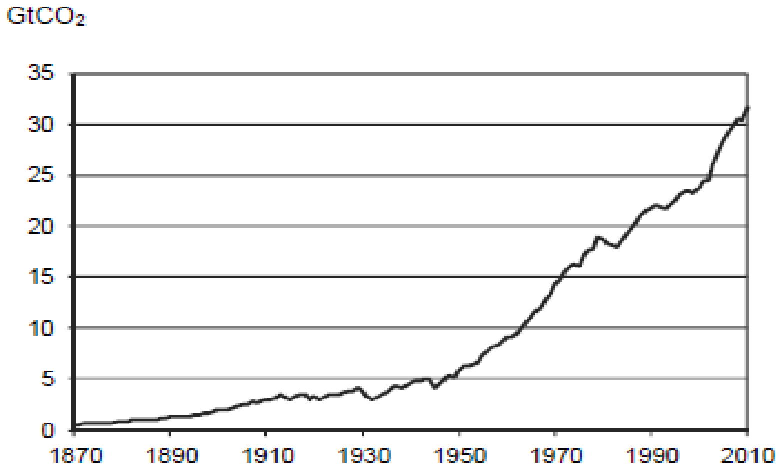

Fig. 1.2 Trend in CO_2 emission from fossil fuel combustion (Reproduced from ref. 2).

Fossil fuels could continue to be our primary source of energy, possibly till the turn of 21st century. Hence globally, serious efforts are on, to keep CO_2 level under control. On one hand, renewable sources of energy like solar, wind, tidal, bio-mass, and geothermal are being harnessed, though to a limited extent as of now, so as to minimize the carbon foot print/ CO_2 emission.

Table 1.1 Reactants and their Products with CO_2 [Reproduced from Ref. 4]

Reactants	Products with CO_2
Alkane	Syngas, acids, esters, lactones
Cycloalkane	Acids, esters, lactones
Active-H compound	Acids, esters, lactones
Monoalkene	Acids, esters, lactones
Diene[a]	Acids, esters, lactones[b]
Cycloalkene	Acids, esters, lactones, (co)polymers
Substituted hydrocarbon[c]	Acids, esters, lactones, polycarbonates
Alkyne	Lactones, unsaturated organic carbonates
Epoxide	Carbonates, (co)polymers (polycarbonates)
NH_3 and amine	Symmetrical ureas, aminoacids, (co)polymers
Diamine	Ureas, carbamates, (co)polymers (polyureas)
Imines	Carbamates, (Co)polymers (urethane)

[a]Allenes and 1,3-dienes, [b]with longer C-C chain than the original monomer. [c]Dihalogen substituted.

Simultaneously, viable means of capture, storage and sequestration of CO_2 and its conversion to fuels and chemicals are being explored. The task indeed is a challenging one. Conversion of CO_2 by reaction with different organic molecules could result in variety of highly useful products for the fine chemicals industry and is shown in Table 1.1 [4]. However, use of CO_2 as reactant by the chemical industry is only about 0.5 wt% (~128 Mt y^{-1}) of the total anthropogenic CO_2 emissions every year [1]. Hence, several simultaneous approaches are needed to convert CO_2 to fuels and chemicals, so that atmospheric CO_2 level could be maintained at near optimum levels. Such an approach would ultimately lead to the use of CO_2 as sustainable source of energy as well. Considering such a dual benefits, several CO_2 conversion processes, other than those for chemicals manufacture, are being studied with great interest. A discussion on such CO_2 conversion processes to yield fuels, is presented in the following section.

1.2 Processes for CO_2 conversion

CO_2 is the most oxidized form of carbon and therefore, the only chemical transformation at normal energies, that would be possible, is to reduce it. A wide range of CO_2 conversion / reduction techniques are under investigation [5] which include,

i. Chemical Reduction by metals which occur at relatively at high temperatures

$$2Mg + CO_2 \longrightarrow 2MgO + C \qquad (1)$$

$$Sn + 2CO_2 \longrightarrow SnO_2 + 2CO \qquad (2)$$

$$2Na + CO_2 \longrightarrow Na_2C_2O_4 \qquad (3)$$

ii. Thermo-chemical Conversion

$$CO_2 \xrightarrow{Ce^{4+,}\ T>900^{o}C} CO + 1/_2\ O_2 \qquad (4)$$

iii. Radio chemical Conversion

$$CO_2 \xrightarrow{\gamma - \text{Radiation}} HCOOH, HCHO \qquad (5)$$

iv. Photo-chemical Conversion

$$CO_2 \xrightarrow{h\nu} CO, HCHO, HCOOH \qquad (6)$$

v. Bio-Chemical Conversion

$$CO_2 + 4H_2 \xrightarrow{\text{Bacteria}} CH_4 + 2H_2O \qquad (7)$$

vi. Electro-chemical Conversion

$$CO_2 + xe^- + xH^+ \xrightarrow{eV} CO, HCOOH, (COOH)_2 \qquad (8)$$

vii. Bio-photochemical conversion

The bio part of the energy consists in catalysis and information content of an enzyme

$$CO_2 + \text{oxogluric acid} \xrightarrow{h\nu} \text{isocitric acid} \qquad (9)$$

viii. Electro-photochemical conversion

$$CO_2 + 2e^- + 2H^+ \xrightarrow{h\nu,\ eV} CO + 2H_2O \qquad (10)$$

Conventional catalytic reduction of CO_2 to chemicals (formic acid, methanol, methane etc.) with external hydrogen is feasible [6] but hydrogen from renewable resources is to be utilized, to render the process viable and sustainable.

Amongst the processes listed above, photochemical conversion processes (direct photochemical, photo-electrochemical and photo-biochemical conversions), that utilize abundantly available solar energy, qualify as sustainable processes and hence being pursued with tremendous interest. A brief account of photo-catalysis and photo-synthesis, which form the basis for all types of photo-catalytic conversions in general, and CO_2 photo reduction in particular, is presented in the following section.

1.3 Photo-catalysis and Photo-synthesis

Photo-catalysis involves an additional means of activation of molecules, besides the normal thermal and chemical catalytic action that facilitate any typical chemical reaction. In simple terms, photo-catalysis refers to any reaction that requires simultaneous presence of a photo-active catalyst and light energy source [7] and can be expressed as

$$R \xrightarrow{h\nu,\ \text{Catalyst}} P\ (\Delta G_{R\rightarrow P} < \text{or} > 0) \qquad (11)$$

Photo-generated electrons and holes react with adsorbed reactant molecules on a photo-active semiconducting catalyst surface, bringing about the reduction or oxidation of the adsorbed species. The reaction pathways in both processes according to Ravelli et al [8] are illustrated in Fig. 1.3A & B below:

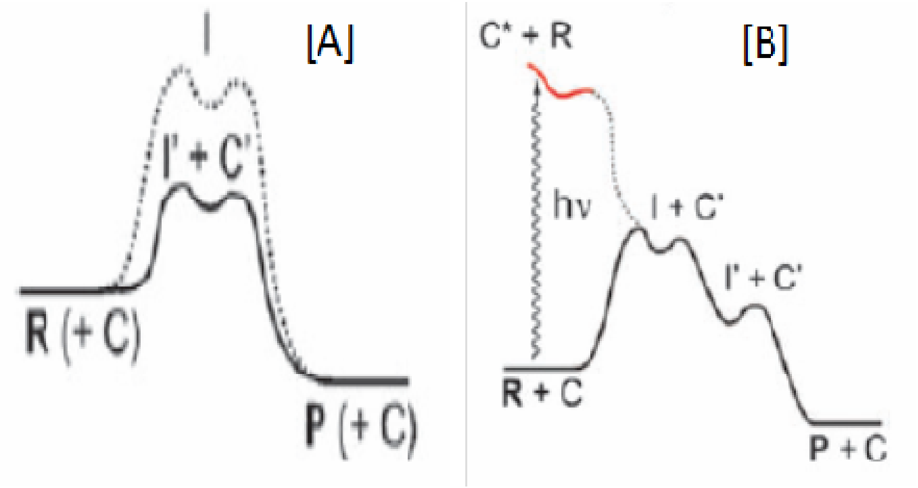

Fig. 1.3 Reaction path ways followed [A] in a thermal reaction (R-P) catalyzed by C via intermediate I'; [B] in a photo-catalyzed reaction (the catalyst C is active only in the excited state, but the chemical transformation of R occurs entirely on the ground state surface [Reproduced from Ref. 8].

The overall reaction cycle in a typical photo-catalytic conversion is depicted as shown in Scheme.1.1.

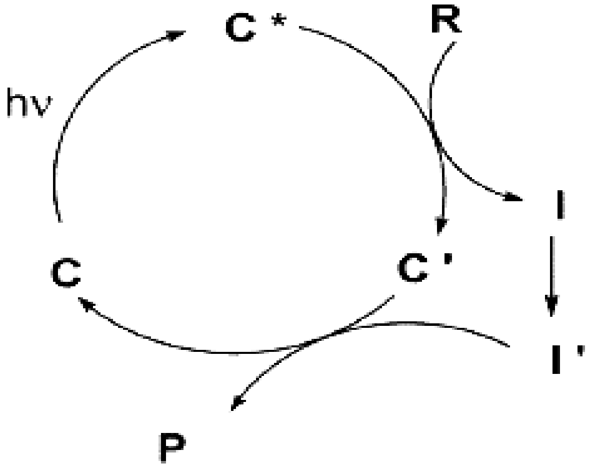

Scheme 1.1. Photo catalytic conversion of R to P by catalyst C [Reproduced from Ref.8].

Historically, photo catalysis has played a pivotal role in the evolution of life on earth. Photo- synthesis, the process so vital for the plant life, is essentially a photo-catalytic process, involving the conversion of CO_2 and water to carbohydrates, with the release of oxygen into the atmosphere. Chlorophyll acts as collector of solar energy and the conversions take place with the help of a series of enzyme catalysed redox process steps. This phenomenon of photo-synthesis marked the beginning of process of evolution of various forms of life on earth that survive on oxygen. Both photo-catalysis and photo-synthesis processes utilize the sustainable source of energy, the sunlight, available abundantly at zero cost (Scheme.1. 2).

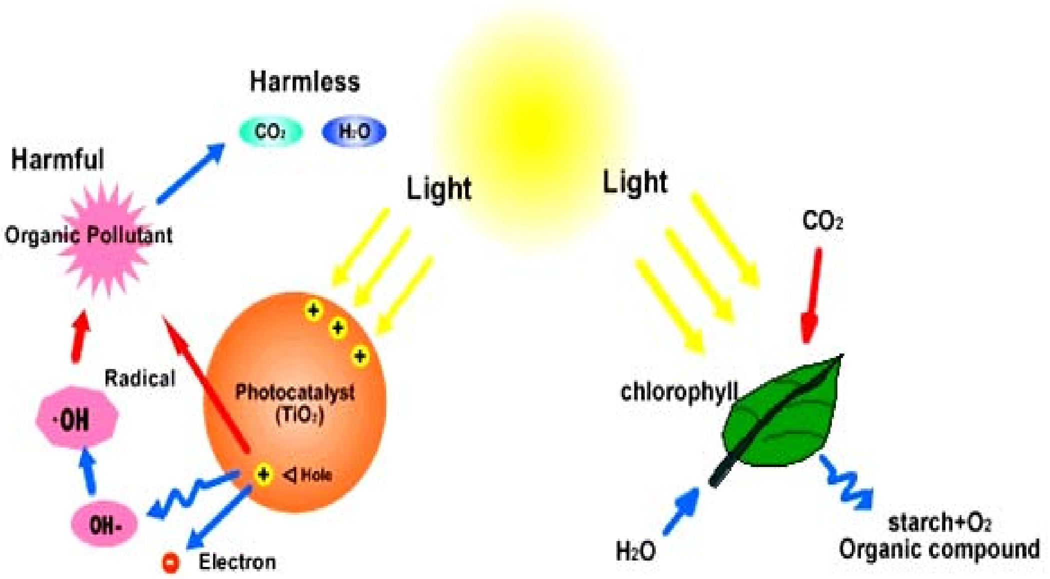

Scheme 1.2 Photo-catalysis and Photo-synthesis [Reproduced from http://www.tipe.com.cn/ library/kb2501.htm]

Photo catalytic reduction of carbon dioxide (PCRC) by water to yield hydrocarbons, the process commonly referred to as “artificial photo-synthesis”, dates back to nearly nine decades, in 1921-22. The process has now attained tremendous importance on global level, since it is considered as one of the means of controlling the current atmospheric carbon dioxide levels (green-house gas effect) by converting it into to fuels and chemicals and the role of CO_2 as source of energy.

1.3.1 Applications of photo-catalysis

It is known that earth receives nearly around 4.3 x 10^{20} J/h of energy while the requirement of energy for the earth is around 4.7 x 10^{16} J/h and thus showing that if one can harness 1 h energy from sun, it will be sufficient for nearly 9,200 h of energy needs of the earth or nearly the energy need for more than 1 year [5].

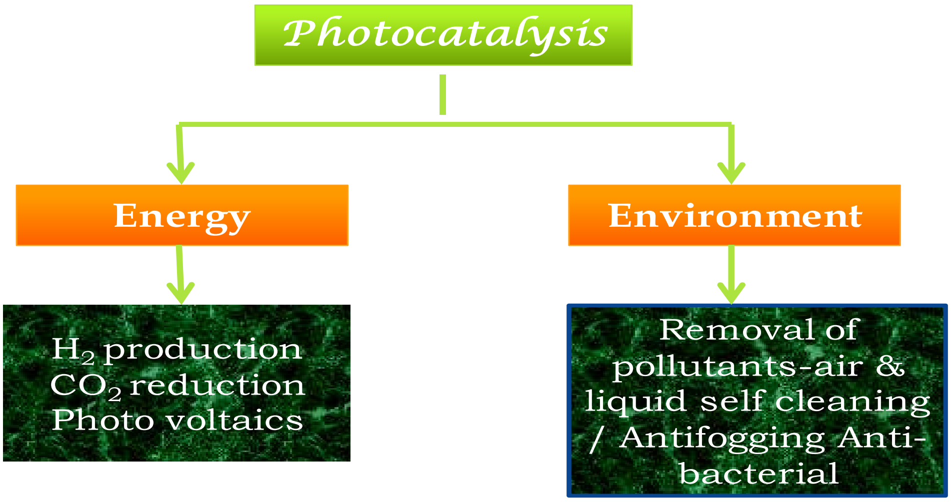

Scheme 1.3. Major application of photo-catalysis

In the current energy starved scenario on the earth, studies on the science and technology of photo-catalytic processes that utilize sunlight, have gained tremendous importance and hence being explored for a variety of applications. Photo-catalysis is emerging as one of the possible means of providing viable solutions to the challenges related to two major issues on the global front, energy and environment. Solutions in the form of different photo-catalytic conversions/ processes are represented in Scheme.1.3.

These applications are at various stages of development, with few of them like, self-cleaning, anti-fogging and anti-bacterial applications being practiced already on large scale. Photo-catalytic processes could be utilized for converting solar energy into other useful forms of energy like, hydrogen via splitting of water and hydrocarbons (methane, methanol etc.) which are now collectively termed as “solar fuels”, by photo-catalytic reduction of CO_2 with water. Besides, photo-catalytic oxidation/

degradation processes help in the elimination of harmful pollutants in air/liquid/water streams in a safe manner, resulting in the conservation of environment. There has been an explosive growth of applications of photo-catalysis as evidenced by the fact that from the year 2000 onwards around 1300 international patents per year have been filed, most of them pertaining to the application of titania as photo-catalyst for pollution control.

While the practical applications of photo catalysis in the area of pollution control has been demonstrated successfully, the applications on energy front, for hydrogen production by water splitting and hydrocarbons from CO_2 and water are still at infant stages of development.

1.4 CO_2 photo reduction with water- Process features

The CO_2 reduction is a thermodynamically uphill process as illustrated by its standard free energy of formation ($\Delta G° = -394.359$ kJ/mol) [9]. Economical CO_2 fixation is possible only if renewable energy, such as solar energy is used as the energy source. Equally difficult is the reduction/ splitting of water using solar radiation to yield hydrogen and hence requires similar combination of activation steps. We can now consider two different processes for CO_2 reduction namely,

- Direct photo-reduction of CO_2 using water as a reductant
- Photo-catalytic splitting of water to generate hydrogen and further reaction of this hydrogen with carbon dioxide forming C_1–C_2 fuels.

The most ideal and desirable process would then be the simultaneous reduction of CO_2 and water to yield hydrocarbons, which essentially works out to artificial photosynthesis. As shown in Fig. 1.4, photo-catalytic process occurs via the direct absorption of photons with energy greater than or equal to the band gap of the photo-catalyst, resulting in the generation of electron-hole pairs. The initial excitation and electron energy transfer to the adsorbed reactants on the photo-catalyst make surface chemical reactions in the photo-catalytic process possible.

The utilization of solar energy via chemical storage can be achieved by photo-catalytic or photo-electrochemical activation of light-sensitive catalytic surfaces. When comparing the two systems, photo-catalytic system is simpler, easy to construct and operate. The primary steps involved in the photo-catalytic reduction of CO_2 to hydrocarbons include:

- Photo-generation of charge carriers by excitation
- Bulk diffusion and interfacial transfer of charge carriers to surface species
- Reduction/oxidation and further conversion of surface species to different hydrocarbons

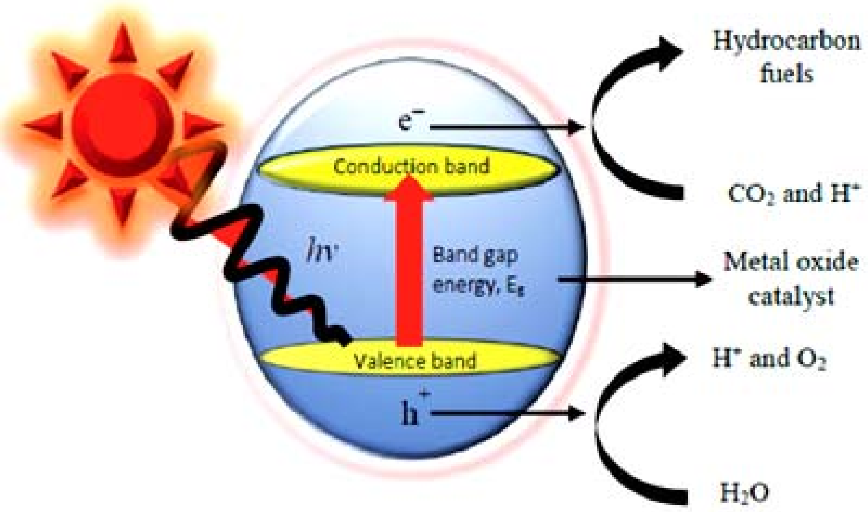

Fig. 1.4 Transformations during photo-catalytic reduction CO_2 with water [Reproduced from Ref. 10]

Photo-generated electrons bring out the reduction of CO_2 to hydrocarbons and holes facilitate oxidation of water. While the elementary process steps/ mechanism of photo-catalytic water splitting have been established to an acceptable level, there is little clarity on the reaction pathways that lead to the conversion of CO_2 to hydrocarbons.

1.4.1 Thermodynamic features and challenges

Hydrogen formation from water involves a free energy change (ΔG_0) of 237 kJ/ mol and an enthalpy change (ΔH_0) of 285 kJ/mol; the corresponding values for CO formation from CO_2 are 257 and 283 kJ/mol at 25°C (1atm). Hence, the minimum energy required for water and CO_2 splitting processes are 1.229 and 1.33 eV (per photon) respectively. In theory, the band gap of a photo-catalyst used for splitting/ reduction of water /CO_2 should be at least 1.33 eV [11]. One, two, four, six and eight electron reduction potentials (vs. NHE) for CO_2 reduction and H_2O oxidation at pH 7 and at 25°C, assuming unit activities for all gaseous and aqueous species are given below [9].

Reaction	E^0_{redox} V vs NHE at pH 7	
$2H^+ + 2e^- \longrightarrow H_2$	-0.41	(12)
$H_2O \longrightarrow 1/_2\, O_2 + 2H^+ + 2e^-$	-0.82	(13)
$CO_2 + e^- \longrightarrow CO_2^-$	-1.9	(14)
$CO_2 + H^+ + 2e^- \longrightarrow HCO_2^-$	-0.49	(15)
$CO_2 + 2e^- + 2H^+ \longrightarrow CO + H_2O$	-0.53	(16)
$CO_2 + 4H^+ + 4e^- \longrightarrow HCHO + H_2O$	-0.48	(17)
$CO_2 + 6H^+ + 6e^- \longrightarrow CH_3OH + H_2O$	-0.38	(18)
$CO_2 + 8H^+ + 4e^- \longrightarrow CH_4 + 2H_2O$	-0.24	(19)

From the above scheme it is clear that CO_2 photo reduction is not a single-step reaction. Upon transfer of one electron, the structure changes from linear to bent configuration, which results in irreversible reduction [5]. Additionally, single electron transfer to CO_2 is highly endergonic, because of the negative adiabatic electron affinity of CO_2. A simple comparison between photo-catalytic decomposition of water and the reduction of CO_2 with water are shown in Table 1.2 [5].

The initial step in the photo-catalytic reduction of CO_2 is the generation of electron-hole pairs upon absorption of photons of energy greater than or equal to the band gap of the photo catalyst. Subsequently, photoelectrons are utilized for the reduction of CO_2 and hole for oxidation of water. However, electron-hole recombination process, which is two to three orders of magnitude faster, competes with the desirable redox processes. Therefore, electron-hole recombination process has to be minimized by some means, to increase the efficiency and improve the rates of CO_2 photo-reduction. Besides the recombination, many other factors such as incident light intensity, fraction of the incident light absorbed by the photo-catalyst, the type of the catalyst and its particle size, specific surface area, structural and photo-physical properties etc. are known to influence the kinetics of CO_2 photo-reduction.

Table 1.2 Comparison of photo-catalytic decomposition of water and the reduction of carbon dioxide [Reproduced from ref. 5b]

S. No	Photo-catalytic decomposition of water	Photo-catalytic reduction of CO_2
1.	The products of the reaction are simple - hydrogen and oxygen only.	Multiple products are formed like CO, HCHO, CH_3OH and CH_4.
2.	The number of electrons transferred are limited (Maximum 4)	The total number of electrons involved can be a variable number (>8)
3.	The mechanistic pathway of the decomposition is simple	The mechanistic pathway has yet to be completely elucidated
4.	The products being gases diffuse out of the reaction centres	The products formed may be adsorbed on the catalyst
5.	Thermodynamically uphill reaction with the free energy of formation of water being - 228.4 kJ/mol	Thermodynamically less favouable with free energy of formation of CO_2 is - 394 kJ/mol
6.	Electrons reduce the protons to molecular hydrogen	Initital electron transfer to CO_2 requires high (-1.9 V) over-potential
7.	Water photo-catalytic decomposition is an independent reaction	Water decomposition can be a prerequisite for CO_2 reduction

1.4.2 Choice of catalysts - Guiding principles

It is again essential that the photo-generated electrons should possess requisite energy, as indicated by the thermodynamic criteria, to facilitate the reduction of CO_2. The chemical potentials of the photo-generated electrons and holes highly depend on the band edge positions of the semiconductor. This means that the conduction band bottom energy level of the photo- catalyst has to be more negative with respect to the energy for CO_2 reduction and the valence band top has to be more positive with respect to the energy for oxidation of water. Thus, the choice of the catalyst for CO_2 photo-reduction with water is determined by the relationship between energy levels of conduction and valence bands vis-a-vis the energies for CO_2 reduction and water oxidation. Pioneering studies on photo electro catalytic reduction of CO_2 on various semiconducting oxides has brought out the basic criteria for the catalytic activity. This guiding principle has been illustrated effectively by Inoue et al. [12] in the relationship between the energy levels of conduction and valence bands and those of the redox couples as depicted in Fig. 1.5.

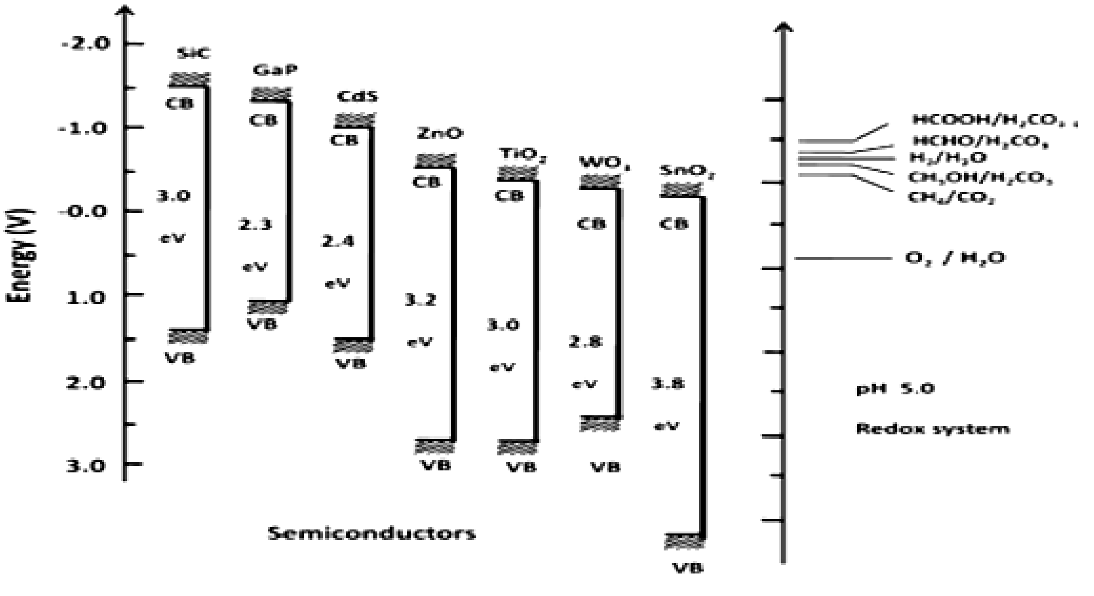

Fig. 1.5 Conduction band and valence band potentials for photo catalysts relative to the Energy levels of redox couples in water [12].

Semiconductors like SiC, GaP, CdS, ZnO and TiO_2, which satisfy the above criteria and are active for photo reduction of CO_2 while oxides like WO_3 and SnO_2 whose conduction band levels are below that for CO_2 reduction, have failed to perform. Energy levels of conduction and valence band Vs those for redox couple and the life time of charge carriers, prolonged by reduced recombination, are the two fundamental criteria to be considered for the selection of the efficient photo catalyst for CO_2 photo reduction.

1.5 Catalysts for photo reduction of CO_2 with water

A remarkable feature of PCRC is that it could emerge as a carbon neutral process [13], where in carbon emissions are recycled back as useful fuels/chemicals. The process involves two major steps; photo catalytic splitting of water to yield hydrogen, which in turn, helps in the photo reduction of carbon dioxide to different hydrocarbon products in the second step. Design of effective catalysts for such a complex process, involving multi-electron transfer steps, holds the key for the viability of the process.

Although many semiconductors have smaller band gaps and absorb in the visible range (e.g. CdS and Fe_2O_3 with band gap values of 2.4 and 2.3 eV, respectively), just a few of them are catalytically active because the energy levels of either the conduction or valence bands are unsuitable for CO_2 reduction and/or water oxidation (Fig. 1.5). This limitation, together with poor photo-corrosion stability of many semiconductors, limits significantly the number of potential photo-catalytic materials for PCRC.

Large-band-gap semiconductors are the most suitable photo-catalysts for CO_2 reduction, because they provide sufficient negative and positive redox potentials in conduction bands and valence bands, respectively. The disadvantage of using wide band-gap semi-conductors is the requirement of high energy input [14-18].

1.5.1 The need for modifications in the catalysts

The photo catalytic activity of a typical semiconductor like titania is initiated by the absorption of light energy corresponding to or higher than the band gap energy, resulting in the generation of electrons and holes. The electron-hole pair, on migration to the semiconductor surface, interacts with the adsorbed reactants to facilitate reduction and oxidation process respectively. In the absence of such an energy transfer, the pairs recombine with the loss of energy. Electron-hole recombination process, which is two to three orders of magnitude faster, competes with the desirable redox processes. Therefore, the recombination process needs to be minimized by suitable modifications, to increase the efficiency. Hence modifications in wide band gap semiconductor (band gap engineering) are aimed at dealing with the two major issues, namely, extending light absorption range beyond UV region and arresting the recombination of charge carriers.

By suitable modification of the band gap, i.e., reduction in band gap by creation of additional impurity energy levels, light absorption range/wavelength could be increased. In the case of titania, light absorption range is increased to cover part of visible region [16, 17]. Arresting the recombination rate increases the life time of photo-electrons and holes, thus leading to a corresponding increase in photo-catalytic activity.

1.5.2 Major types of modifications in the catalysts

A number of strategies have been devised to bring about the modifications in wide band gap semiconductors, which can be broadly classified as:

- Doping with metal cations and anions
- Coupling with other semiconducting oxides
- Sensitization with light harvesting compounds/dye molecules
- Plasmon resonance induced by specific metals

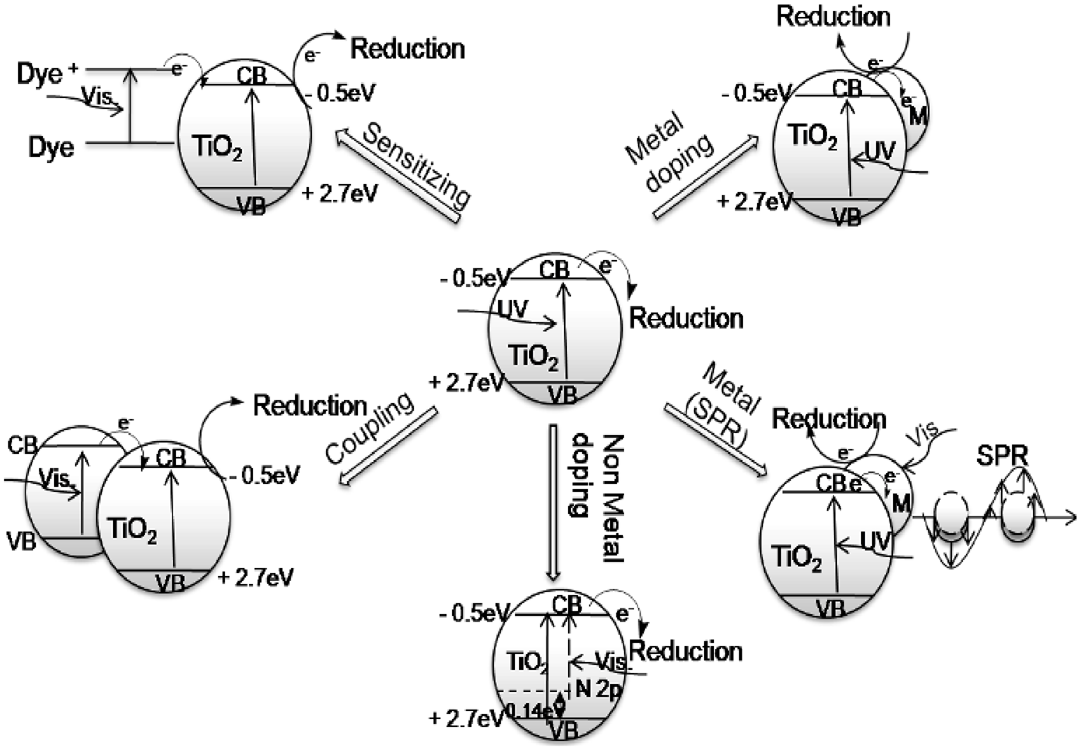

Fig. 1.6 Implications of modifiers on the electronic structure of Titanium dioxide [20]

Excellent and exhaustive reviews describing the changes brought about by these means in the photo-physical properties of the photo-catalysts and the consequent improvements observed in the photo-catalytic properties have been compiled [5, 9, 18-29]. The main features of these modifications and the implications in the properties of semiconductors, especially for titania, are summarized in the Table. 1.3, and presented graphically Fig. 1.6

Table 1.3 Implications of different modifications in titania [20]

Modifications	Implications/Mode of action
Doping of metals/metal ions	• Act as electron traps and facilitate charge carrier separation • Introduce impurity states and induce visible light absorption • Absorb visible light via surface plasmon resonance (SPR)
Doping of anions	• Narrowing of band gap due to mixing of p states of dopants (N, S) with O 2p states in the valance band of TiO_2. • Introduce impurity states above the valence band of titania • Both states induce visible light absorption
Coupling with semi-conductors	• A narrow band gap semiconductor, with appropriate energy levels, absorbs visible light and transfers excited electrons into the conduction band of titania. UV light source not needed • Besides visible light activity, effective separation of charge carriers is achieved
Sensitization with light harvesting components /dyes	• Light absorbing components can absorb visible light and inject photo-excited electrons into the conduction band of titania. • Besides visible light activity, effective separation of charge carriers is achieved

1.6 Influence of experimental parameters

Photo-catalytic activity depends on the experimental conditions such as, the amount of catalyst, light intensity, lighting area, reactor volume, type of reactor, temperature and pressure. Intrinsic properties of semiconductor photo-catalyst like, particle/ crystallite size [30], phase composition [31], surface area, surface hydroxyls, lattice defects and the type and level of dopants (metals and non-metals), morphology (powder, nano particles, nano tubes, nano rod and hollow nano spheres), structural features and photo-physical properties influence its performance [15-29]. Photo catalytic activity and phase transition behaviour of TiO_2 are significantly influenced by the preparative conditions and methods [32-34]. This explains the wide variations in activity and product patterns observed for the same photo catalyst by different authors. For example, a standard/reference catalyst Degussa P-25 (TiO_2) shows wide difference in efficiency in the results published by different authors during the period 1993 to 2009 as shown in Table. 1.4. Different experimental conditions adopted could be the other major factor that affects yield data, which shows variations in total yield as well as the product patterns. Hence, rationalization of activity and product patterns in terms of photo-physical properties has been a difficult task.

Table 1.4 CO_2 photo reduction with water on P-25 TiO_2 - Literature reports

S. No	**Products ***	**CH_4**	**CH_3OH**	**Reactor type**	**Reactants**	**Light source**	**T (K)**	**Ref.**
1	CH_4, C_2H_6 CH_3OH	0.9	Trace	Quartz cell	CO_2 in H_2O	500W Hg > 310 nm	278	35
2	H_2, CO, CH_4	2.0	Trace	Quartz cell	CO_2 in H_2O	1000W Hg<700 nm	343	36
3	H_2, CH_4, C_nH_m	4.74 5.68 6.42		Miniaturized reactor	CO_2 in H_2O	200W Hg /Xe <900 nm	278 373 473	37
4	CH_4, HCOOH	0.43		SS vessel	CO_2/ IPA	4200W, Xe		38
5	CH_4, CH_3OH	0.35		Quartz cell	CO_2: H_2O 1:5	75W Hg 254 nm	323	39
6	CH_3OH	-	6.37	Inner irradiator cell	CO_2 in NaOH	8W Hg 250 nm	323	40
7	CH_4, CH_3OH		93.75	Inner irradiator cell	CO_2 in $NaHCO_3$	15 W Hg 365 nm		41
8	CH_3-COOH		1.8	Quartz window	Liq. CO_2	990W Xe Arc lamp		42
9	CH_4	0.33	-	Quartz cell	CO_2: H_2O 1:5	100W Hg >250 nm	323	43

10	CH_4	0.001		Top illumination	CO_2: H_2O 1:5	4.8W 253.7 nm	311	44
11	CH_4	14.6		Glass plate	CO_2: H_2O 1:5	15W 365 nm	296	45
12	CH_4	3.51		Annular reactor	CO_2in $NaHCO_3$/ IPA	450WHg	293-298	31
13	CH_3OH		430	Inner irradiator cell	CO_2 in NaOH	400W halide 300-600 nm	315	46

* Products – in micro moles per hour per gram of catalyst

1.6.1 Effect of wavelength, band gap and light intensity

Semiconductors absorb light radiation with the threshold wavelength that provides sufficient photon energy to overcome the band gap between the valence and conduction bands. This threshold wavelength, required to promote electrons to the excited state, corresponds to the minimal photon energy and depends on the band-gap energy, e.g. for TiO_2 anatase with band gap energy 3.2 eV, it is about 387.5 nm. Irradiation using the light with shorter wavelength (254 nm) is significantly more effective for the CO_2 reduction using TiO_2 than that with the longer wavelength (350 nm) [47, 48]. The wavelength (λ) of the light used influences the yield of products as observed by Fan et.al [49] in their studies on N (4% w/w) and Ni (6% w/w) co-doped titania for CO_2 reduction with water. For this catalyst formulation, Fan et al [49] observed methanol yields of 482, 253.5 and 120.5 (all in μ moles/g-cat) with radiations of wavelength 254 nm, 365 nm and 400-780 nm respectively, thus clearly bringing out the influence of the wavelength of the light used. Electrons in excited states are produced via electronic transitions the probability of which depends on the light intensity. The CO_2 reduction rate increases linearly with the light intensity and at mid-range light intensities, the photo catalytic reaction rate is dependent on the square root of light intensity. At high light intensities the rate is independent of the light intensity [18].

Table 1.5 Rates of methanol and ethanol formation with radiations of different wavelengths [Reproduced from Ref. 50]

$BiVO_4$	Production rate [a]/μmol h^{-1}	300W Xe arc lamp with UV cut off filter	300 W Xe arc lamp without UV cut off filter	36W fluorescent lamp
Monoclinic	Ethanol	21.6	406.6	2.3
	Methanol	0	0	1.8
Tetragonal	Ethanol	1.1	4.9	0.6
	Methanol	0	0	0.6

[a] The rate was determined on the basis of the average production rate after 80 min of irradiation

Variations in the wavelength of radiation used can also affect the rate of formation of products as observed by Liu et al [50] on $BiVO_4$ catalysts (Table.1.5). Monoclinic $BiVO_4$ is found to be more active than the tetragonal form. Selective formation of ethanol is observed using 300 W UV radiations, with and without UV cut-off filter. But with 36 W lamp, both alcohols are formed at nearly same.

1.6.2 Influence of reaction pressure

Mizuno et al [51] observed that CO_2 photo reduction with water containing dispersed TiO_2 increased with increase in CO_2 pressure. Increase in the solubility of CO_2 in the liquid phase (water as well as aqueous 0.2N NaOH solution) at elevated pressure and the consequent increase in the concentration CO_2 in the solution phase is responsible for the observed increase in CO_2 reduction (Fig. 1.7).Similar observations on the effect of pressure have been observed by H. Hori et al [52].

Kaneco et al [53, 54] studied the CO_2 photo reduction using TiO_2 powders in liquid CO_2 medium. Carbon dioxide has limited solubility in water. Also reduction of CO_2 is competitive with hydrogen formation via water. To overcome this disadvantage, liquid CO_2 system has been explored. The protonation reaction was performed using water after the end of illumination. The main reduction product was exclusively formic acid. Tan et al [44, 55] studied the photo-catalytic reduction of carbon dioxide using TiO_2 pellets. Pellet increased the contact areas and adsorption capacity. Their yield was significant when compared to thin film coating technique.

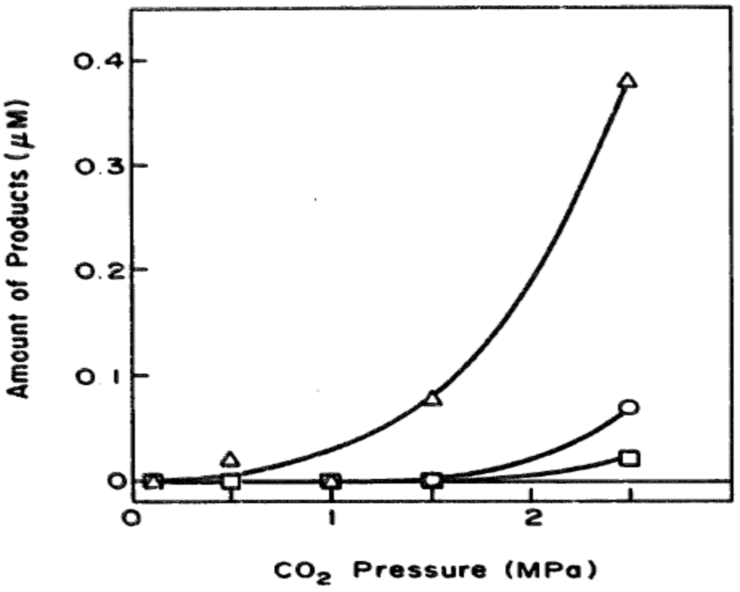

Fig. 1.7 Effect of CO_2 pressure on its photo reduction (medium, purified water; irradiation time, 24 h; catalyst, TiO_2): Δ- CH_4, ○-C_2H_4, □- C_2H_6. [Reproduced from Ref. 51]

1.6.3 Influence of titania particle size

Koci et al. [30] studied the effect of TiO_2 particle size on photo catalytic reduction of carbon dioxide. As the particle size decreased, higher yields of methanol and methane over the TiO_2 nano particles under the illumination of light were obtained. The optimum particle size corresponding to the highest yields of both products was 14 nm (Fig. 1.8). For particles with crystallite sizes < 14 nm, conversions dropped due to a combination of electronic (increase in recombination rates) and optical properties. The observed optimum particle size effect was a result of competing effects of specific surface area, charge–carrier dynamics and light absorption efficiency.

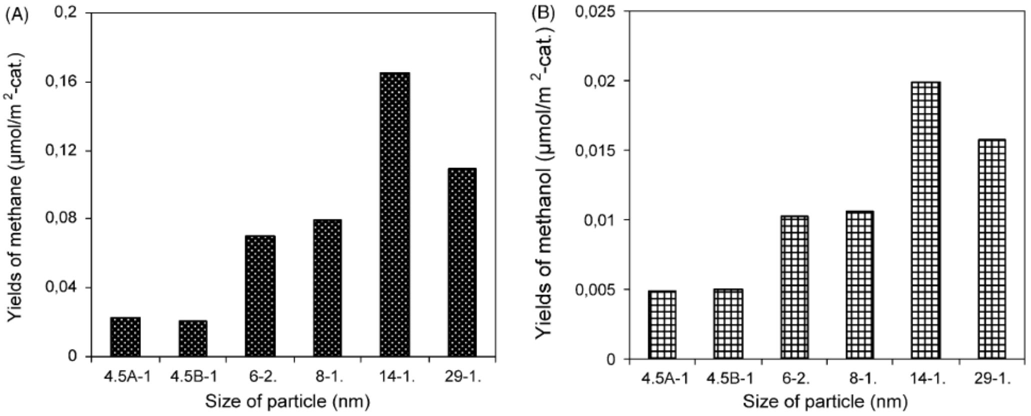

Fig. 1.8 A & B Dependence of product yields on particle size of titania (after 24 hrs of irradiation) [Reproduced from Ref. 30]

1.6.4 Influence of type of photo reactors and reaction media

The design of photo reactor is an important aspect in CO_2 photo-reduction process with water, which could significantly influence the selectivity of products and efficiency of the photo catalyst/process. As stated by O. Ola et al [56], an ideal photo reactor must have uniform light distribution throughout the entire system in order to achieve optimum results. The two parameters which determine the type of photo reactors utilized in CO_2 photo reduction are the phases involved i.e., multiphase, gas-solid, liquid-solid, gas-liquid-solid etc, and the mode of operation i.e., batch, semi-batch or continuous flow of reactants. The photo-catalyst can be used in either suspended or immobilized forms in different reactor configurations. Schematic representation of three types of reactor geometry are shown in Fig. 1.9, which are, A. Slurry reactor design with top illumination, B. optical fiber reactor design with side illumination C. internally illuminated reactor with top illumination [56].

Koci et al [46] studied the influence of reactor geometry on photo reduction of carbon dioxide using two annular batch reactors. The dependence of product yields on the reactor diameter and on the volume of the liquid phase confirmed the fact that the requirement of perfect mixing is difficult with the annular configuration of the reactor. The highest yields of the photo catalytic reduction were achieved in a configuration where the lamp just touches the surface of the liquid in the reactor and the configuration of the reactor was not annular. As shown in Table 1.6, different types of photo reactors and reaction medium significantly alter the product selectivity for a commercial P-25 TiO_2 photo catalyst. Advantages and disadvantages of different types of photo reactors for application in CO_2 photo reduction are given in Table 1.6.

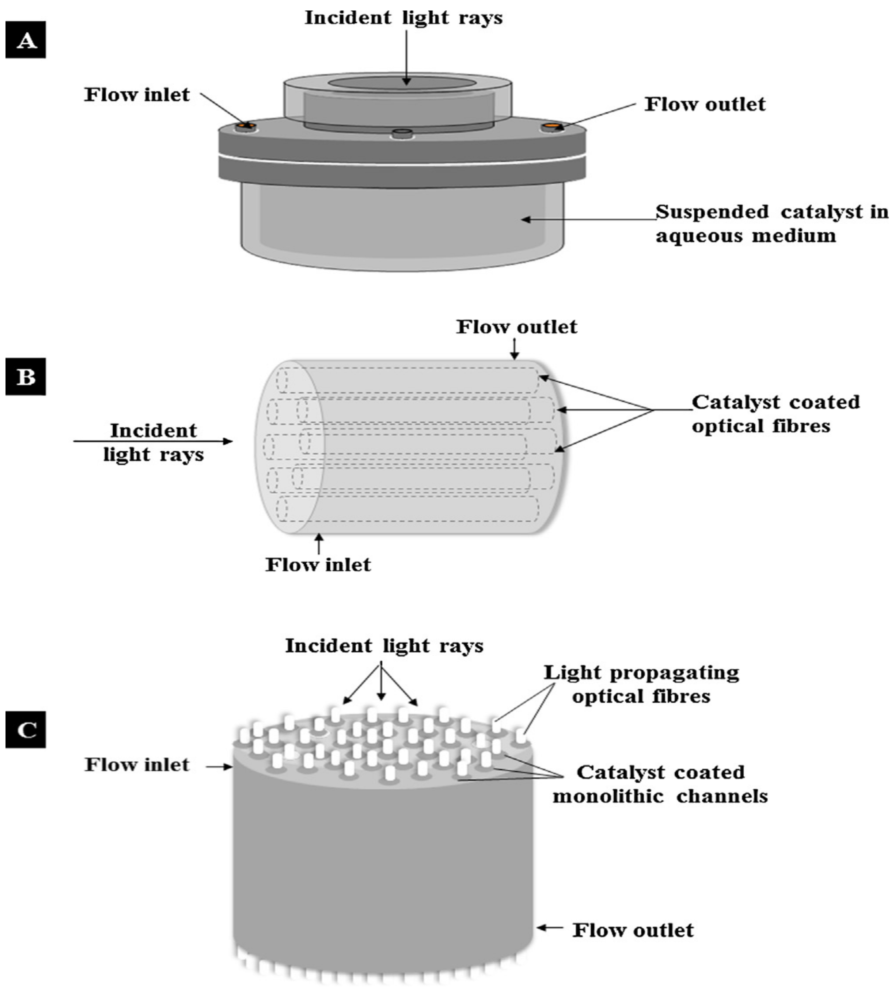

Fig. 1.9 Schematic diagram for different types of photo reactors (A) slurry reactor design with top illumination, (B) optical fiber reactor design with side illumination and (C) internally illuminated reactor with top illumination. (Reproduced from Ref. 56).

Wu et al [64-67] applied an optical fibre reactor to the photo reduction of CO_2 with H_2O using TiO_2, Cu/TiO_2, Ag/TiO_2, Cu–Fe/TiO_2–SiO_2 and dye-sensitized Cu–Fe/P25 catalysts coated on optical fibres. Compared with a traditional packed-bed reactor, an optical fibre reactor provides a medium to transmit light uniformly throughout a reactor and hence higher conversion (Table. 1.7) is achieved. In addition, a higher processing capacity is possible because the photo catalyst can be dispersed on the optical fibers with large surface area in a given reactor volume.

Table 1.6 Advantages and disadvantages of photo reactor systems [Reproduced from Ref. 56]

Reactor design	Advantages	Disadvantages	Ref.
Fluidized and slurry reactor (multiphase)	(I) Temperature gradients inside the beds can be reduced through vigorous movements caused by the solid passing through the fluids (II) Heat and mass transfer rates increase considerable due to agitated movement of solid particles. (III) High catalyst loading	(I) Filters (liquid phase) and scrubbers (gas) are needed. (II) Flooding tends to reduce the effectiveness of the catalyst. (III) Difficulty of separating the catalyst from the reaction mixture (IV) Low light utilization efficiency due to absorption and scattering of the light by the reaction medium (V) Restricted processing capacities due to mass transport limitations	19 [57, 58]
Fixed bed reactor	(I) High surface area (II) Fast reaction time (III) The conversion rate per unit mass of the catalyst is high due to the flow regime close to plug flow (IV) Low operating costs due to low pressure drop **Variants of fixed bed designs**	(I) Temperature gradient between gas and solid surface is common	[59, 60]

Monolith reactor	(I) High surface to volume ratio and low pressure drop with high flow rate can be achieved. (II) Configuration can be easily modified	(I) Low light efficiency due to opacity of channels of the monolith	[61, 62]
Optical fiber reactor	(I) High surface area and light utilization efficiency. (II) Efficient processing capacities of the catalyst	(I) Maximum use of the reactor volume is not achieved. (II) Heat build-up of fibers can lead to rapid catalyst	[62, 63]

When CO_2 present in the atmosphere dissolves in water it is mostly present in the form of carbonate. Many authors have studied photo-catalytic reduction of carbonate to form various chemicals. Ku et al. [41] studied the photo-catalytic reduction of carbonate in aqueous solution by the UV/TiO_2 process. The photo catalytic reduction of carbonate proceeded faster in acidic solutions than in alkaline solutions. The main products of the photo-catalytic reduction of carbonate by the UV/TiO_2 reduction process were found to be methanol and methane. A Langmuir–Hinshelwood type kinetic equation was developed for modelling the photo catalytic reduction of carbonate.

Table 1.7 Production rate of methane and ethylene over TiO_2 based-catalysts under artificial light- Influence of the type of photo reactor on reaction rate [64-67]

	Production rate[a] [μmol (gcat)$^{-1}$ h^{-1}]	
	Ethylene	Methane
Cu(0.5 wt%)-Fe(0.5 wt%)/TiO_2/glass plate	0.049	0.060
Cu(0.5 wt%)-Fe(0.5 wt%)/TiO_2/optical fiber	0.575	0.914
N3-dye- Cu(0.5 wt%)-Fe(0.5 wt%)/TiO_2/glass plate	0.033	0.148
N3-dye- Cu(0.5 wt%)-Fe(0.5 wt%)/TiO_2/optical fiber	0.562	0.847

[a] Production rates were determined on the basis of the average value after 4h of irradiation. The artificial light was in the wavelength range of 320-500 nm with intensity of 225 mW cm^{-2}.

Sayama et al [68] investigated the effect of carbonate salt addition on the photo catalytic decomposition of liquid water over Pt–TiO_2 catalyst. It has been found that an addition of carbonate salts to Pt-loaded suspensions led to highly efficient stoichiometric photo catalytic decomposition of liquid water into H_2 and O_2. Neither the pH nor cation directly contributes to the water splitting. The presence of a high concentration of carbonate ions is essential for the catalytic photo decomposition of water. The carbonate ion affects both the Pt particles and the TiO_2 surface. The Pt was covered with some titanium hydroxide compounds and therefore, the rate of the back reaction (H_2O formation from H_2 and O_2) on the Pt was suppressed effectively in the presence of carbonate ions. On the other hand, the TiO_2 surface was readily covered with several types of carbonate species. It is considered that these carbonate species aid desorption of O_2 from the TiO_2 surface.

In the place of pure water as the medium for dispersion of the catalysts, in some cases aqueous solution of $KHCO_3$ [46] or NaOH has been used. Martin Reli et al [46, 69] studied different reaction media, such as, NaOH, NaOH + Na_2SO_3, NH_4OH, NH_4OH + Na_2SO_3 to understand the influence of reaction medium on the PCRC process. It was found that NaOH was better reaction medium than NH_4OH for the yields of both gas phase [CH_4, CO] and liquid phase [CH_3OH] products. Some authors tried with organic reaction media like methanol, propan-2-ol which itself get oxidized during reaction and hence not favorable for the potential separation of products from CO_2 reduced products [69]. The use of NaOH as reaction medium is also beneficial since OH^- ions act as hole scavengers, thereby retarding electron-hole recombination and simultaneously, alkaline solution increases solubility of CO_2 vis-à-vis pure water [40]

1.6.5 Photo reduction with other reductants

Some researchers have attempted to replace water with other reductants [70]. This provides a high reaction yield and high selectivity to desired products by changing the mechanism. Liu et al. [71] conducted an experiment with CdS in various solvents including water, methanol, ethanol, and 1-propanol with dielectric constants of 80, 33, 24.3, and 20.1, respectively. The results indicated that, if low-dielectric constant solvents or low-polarity solvents are used, CO_2^- anion radicals can be strongly adsorbed on the surface through the carbon atom of another CO_2^- anion radical pre-sorbed on surface Cd sites because these radicals are not completely solvated by low-polarity solvents. Here, CO is produced as the major reduction product of CO_2. If a high-dielectric-constant solvent is used (e.g., water), the CO_2^- anion radicals can be greatly stabilized by the solvent, resulting in weak interactions with the photo catalyst surface. Similar effects of solvents have been observed on titania embedded in SiO_2 matrices [72]. Subsequently, the carbon atom of the radical tends to react with a proton to produce formic acid. Kaneco et al. [38] and later Dey [73] showed that photo-catalytic reduction of CO_2 using TiO_2 suspension in aqueous solutions containing 2-propanol as a hole scavenger leads to the preferential formation of methane.

1.7 Classification of catalyst systems

For the sake of clarity and meaningful comparative study, the catalyst systems studied so far for PVRC process have been grouped in the following manner:

i. Catalysts based on pure titania
ii. Titania catalysts modified with metals/metal oxides
iii. Titania catalysts modified with anions
iv. Titania catalysts dispersed on meso porous materials
v. Titania catalysts modified with sensitizers
vi. Metal oxide catalysts-mono, binary & ternary oxides

Details on the application of these catalysts towards CO_2 photo reduction with water have been compiled in the Tables 1.8 to Table 1.15.

Table 1.8 Studies on pure titania based catalysts

S. No.	Catalyst	Reactor used	Conditions		Light Source/ Intensity	Product formation	Ref.
			Reactant	Temp. (K)		(µmol/g cat)	
1.	TiO_2	SS Autoclave (Batch mode)	98 kPa - 2.5 MPa CO_2 in NaOH	293	340 nm	HCOOH, CH_3OH, CH_3CHO, C_2H_5OH	51
2.	TiO_2 liq.CO_2 medium	SS vessel (batch mode)	6.5 MPa CO_2	293	Xe /(990W)	HCOOH – 0.08	53
3.	TiO_2 (Degussa P25)	SS vessel (batch mode)	2.8 MPa CO_2 in 1M IPA	293	Xe / (4.2 kW)	CH_4 – 1.3.	38
4.	TiO_2 in CO_2Sc	SS vessel	9 MPa CO_2	308	Xe-990 W/0.96 kWm^{-2}.	HCOOH	54
5.	TiO_2	Rayonet photo reactor	CO_2 in IPA	308	350 nm	CH_4 – 0.3	74
6.	TiO_2 Pellets	Cylindrical quartz tube	$CO_2 + H_2O$	308	253.7 nm UVC, 3 x 1.6 W	CH_4 - 200 ppm	55
7.	TiO_2	Top – illuminated cell	$CO_2 + H_2O$	311	253.7nm. UVC/4.8W	CH_4 – .001, H_2,CO	75
8.	Mixed phase TiO_2	Annular glass	CO_2 in aq. $NaHCO_3$ +IPA	293–298	UV-Vis 450 W Hg	CH_4 - P-25- 5, A- 20, A+R - 50	31
9.	TiO_2 (14 nm)	Stirred batch annular	CO_2 in NaOH.	308	254 nm Hg 8W	CH_3OH - 0.16	30
10.	P-25, RM-TiO_2, UV100	glass reactor with quartz window	Satd CO_2 in NaOH	298	Hg/300-700 nm, 250 W	CH_4, CH_3OH, C_2H_5OH	76

11.	TiO_2 rod	Stainless steel with quartz window	(CO_2 + H_2O) vapor	RT	300 W Xe lamp	CH_4 – 5.7/h	77
12.	1D TiO_2	Cylindrical with quartz window	(CO_2 + H_2O) vapor	RT	400 W Xe lamp	CH_4- 1361/h	78
13.	TiO_2 ultrathin nanosheets	Glass reactor	CO_2 + H_2O vapor	RT	300 W UV Xe lamp	CH_4 - 5.8 ppm/h	79
14.	Meso TiO_2	Airtight circulation system	CO_2 + H_2O vapor	RT	300 W Xe lamp	CH_4 - 1.75, CO - 2.75	80

Table 1.9 Studies on metal doped titania catalysts

S. No.	Catalyst	reactor Used	Conditions		Light Source/ Intensity	Product formation (μmol/g cat)	Ref.
			Reactant	Temp. (K)			
1.	RuO_2 doped with TiO_2	Borosilicate glass reactor	CO_2 + H_2O	333	75 W Hg	HCOOH – 1.47, HCHO – 0.13, CH_3OH– 0.22, Q E - 0.04%	81
2.	Pd/ TiO_2	Pyrex glass cuvette	CO_2 in 0.05M $NaHC0_3$ & $Na_2C_2O_4$	299	450W Xe/360-nm, cutoff filter	$HCOO^-$ – 4.5	82
3.	Cu/ TiO_2	SS vessel with a quartz window	28 kgf/cm^2 CO_2 at pH 5.45.	308	450 W UV Xe	CH_4 – 21.8, C_2H_4 – 26.2, C_2H_6 – 2.7	83
4.	Cu(II)5wt%/ JRC-TiO-4	Flat-bottomed quartz cell.		275	75 W Hg > 290 nm	CH_4- 1.5, CH_3OH-6.0	84
5.	Cu_2O/TiO_2	Slurry phase quartz reactor	135.6 kPa, CO_2 in 0.2N	323	8 W Hg/254 nm	CH_3OH – 118.5	85

			NaOH				
6.	Cu/TiO_2	Cylindrical quartz reactor	CO_2 in 0.2 N NaOH	308	Hg/365 nm	CH_3OH - 1000	40
7.	3wt%CuO/ TiO_2	Horizontal SS vessel	CO_2 in 1M $KHCO_3$	373	10 W UV 2450 lW/cm^2	CH_3OH – 2655	86
8.	1.2wt% Cu(I)/ TiO_2	Continuous optical fiber	1.29 bar CO_2: 0.026 bar H_2O	348	365 nm	CH_3OH - 0.45	65
9.	TiO_2, Cu/TiO_2, Ag/TiO_2	optical-fiber	pCO_2 (1.19 bar), pH_2O (0.03 bar)	348	UV/365 nm, 10W/cm^2	CH_3OH - TiO_2- 2.0. Cu/TiO_2- 3.8 Ag/TiO_2-4.2	64
10.	Cu-Fe/TiO_2	Continuous circular Pyrex glass	CO_2 + H_2O	348	250–450 nm, 225 mW/cm^2	CH_4 – 0.9, C_2H_4 – 0.6, QE - 0.024%	87
11.	Cu & Pt on N doped TiO_2	SS chambers with quartz window	CO_2 + H_2O	317	Natural sun light AM 1.5 Illumination	CH_4-75*, Alkane - 25*, H_2 - 155*. *ppm cm^{-2} h^{-1}.	88
12.	Pt/TiO_2 nanotube	Fixed bed quartz reactor	CO_2 in H_2O vapor	308	300W Hg/365 nm.	CH_4 - 3.9	89
13.	7% Ag doped TiO_2	Annular Reactor	110 kPa CO_2 in 0.2 M NaOH	308	8W Hg/254 nm	CH_3OH - 1.9, H_2 – 120, CO - 0.9.	90
14.	2 wt% Cu/TiO_2	SS 316 high- temp. chamber		298	100W Hg/ 365 nm	In-situ IR spectroscopic study	91
15.	N-Ni/TiO_2		CO_2 (200 mL/ min)	348	λ=365nm 254nm. (15W) 400-780nm	CH_3OH – 254nm- 482. 365 nm- 253.5 400-700 nm- 120.5	49
16.	Ag doped TiO_2	Batch stirred Annular reactor	CO_2 in 0.2 N NaOH	308	8 W Hg/254 & 365 nm, 8	254 nm light more effective than	48

					W Hg filled with Ar (400 nm)	365 nm. 400 nm ineffective	
17.	23.2% $AgBr/TiO_2$	SS vessel	7.5 MPa CO_2 in 0.2M $KHCO_3$.	308	150W Xe/UV cutoff filter	CH_4-128.56, CH_3OH-77.87. C_2H_4OH-13.28. CO - 32.14	92
18.	Cu/Ce–TiO_2	High-press reaction	CO_2in 0.2 M NaOH.	323	125 W UV	CH_3OH - 180.3	93
19.	1wt% CuO–TiO_2	slurry reactor	CO_2 in CH_3OH	300	250W Hg/ 365 nm	$HCOOCH_3$ – 1600	94
20.	Au /TiO_2	SS reactor with a quartz window	CO_2 in H_2O	348	254, 365 nm 20 mW/cm^2. 532 nm - 350 mW/cm^2	CH_4 – 20, AQY = 6.9 *10^{-4}%	95
21.	Noble metal/N Meso TiO_2	Quartz tubular reactor	CO_2: H_2O/ 0.06:1.	333	34.8 mW cm^{-2}	CH_4 - 5.7	96
22.	Ag/Au on TiO_2	Batch Reactor (Quartz window)	CO_2 in H_2O	300	1000 W Xe	CH_4-503* *ppm	97
23.	Cu-I-TiO_2	SS reactor with quartz window	(CO_2+H_2O) vapor	RT	450 W Xe lamp	CO – 9.4	98
24.	0.1 wt% Y–TiO_2	Quartz reactor	CO_2 in 0.2 M NaOH	RT	300 W Hg lamp	HCHO - 384.62	99
25.	3 wt% Ag–TiO_2	Steel with borosilicate window	CO_2 + H_2O vapor	RT	8 W Hg lamp	CH_4 - 6, H_2 - 100	100
26.	Ni–TiO_2 (0.1 mol%)	Circulated liquid photoreactor	CO_2 + H_2O	303	6 (3W/cm^2) UV lamps	CH_4 - 14	101
27.	La_2O_3/TiO_2	Circular glass reactor	CO_2 + H_2O	RT	300 W Xe Lamp	CH_4 - 4.57	102
28.	CeF_3–TiO_2	Circulated	CO_2 +	RT	500 W Xe	CH_3OH - 162	103

		quartz reactor	H_2O		lamp		
29.	1.5 wt% NiO–TiO_2	Cylindrical pyrex glass reactor	CO_2 + H_2O	RT	200 W Hg lamp	CH_3OH - 19.51	104
30.	Pt-Cu/TiO_2	Stainless steel reactor with quartz window	CO_2 + H_2O	RT	AM 1.5G solar simulator	H_2 - >180* CH_4 - 49* CO - <25 *ppm/cm^2 h	105
31.	Ce–TiO_2	Stirred batch annular reactor	CO_2 in 0.2 N NaOH	RT	8 W Hg lamp	CH_4 - 16 H_2 - 750	106
32.	Pt/TiO_2	Stainless steel reactor with quartz window	(CO_2 + H_2O) vapor		500 W Xe Lamp	CH_4 - 277.2* C_2H_6 - 12.4 H_2 - 389.2 *ppm	107
33.	Pt/MgO/ TiO_2 nanotubes	Flat closed reactor	0.1 mol/L $KHCO_3$	RT	300 W Hg lamp	CH4 - 100.22 ppm/h cm^2 CO - 10.4 ppm/h cm^2	108
34.	In/TiO_2	Rectangular cell with quartz window	(CO_2 + H_2O) vapor	RT	500 W Hg lamp	CH_4 - 244 CO - 81	109
35.	TiO_2/ZnO mesoporous "french fries"	Glass reactor	CO_2 + H_2O vapor	RT	300 W UV Xe lamp	CH_4 - 250	110
36.	hollow anatase TiO_2 single crystals with {101} facets	Stainless steel reactor with quartz window	CO_2 + H_2O vapor	RT	UV Xe lamp	CH_4 - 250	111
37.	Pt@Cu_2O/ P25	Stainless steel reactor with quartz window	CO_2 + H_2O vapor	RT	UV Xe lamp	CH_4 - 33, CO - 8.3, H_2 - 25	112
38.	Cu/TiO_2	Stirred batch annular quartz reactor	CO_2+H_2O vapor	RT	UV lamp	CH_4 - nmol	113
39.	NaOH/TiO_2	Quartz reactor	CO_2+H_2O	RT	300 W Xe lamp	CH_4 - 52, H_2 - 59	114
40.	Au/TiO_2	High	CO_2+H_2	293	125 W Hg	CH_4 - 1.7*, H_2	115

		pressure reactor	O at 11 bar		lamp	- 53*, * mmol/h//kg	
41.	Au@TiO_2 yolk-shell hollow sphere	Glass reactor	CO_2+H_2O	RT	300 W Xe lamp	CH_4 - 26 , C_2H_6 - 17.5	116
42.	Fe–TiO_2	Batch type pyrex glass	CO_2+H_2O	303	6.0-W/cm^2 Hg lamp	CH_4 - 0.92/L	117
43.	Cu–TiO_2 paste	Batch type pyrex glass	CO_2+H_2O	303	6.0-W/cm^2 Hg lamp	CH_4 - 175/L	118
44.	CeO_2-TiO_2	Pyrex glass reactor	CO_2 in NaOH	RT	500 W Xe lamp	CH_3OH - 18.6	119
45.	Ag or Pt/TiO_2	Self-assembled reactor with quartz window	CO_2 + H_2O vapor	RT	UV light (3.25 mW cm^{-2})	CH_4 - 16 ppm for Ag, 10.8 ppm for Pt.	120
46.	M/TiO_2, (M=V, Cr, Co)	Pyrex glass	CO_2 + H_2O vapor	RT	500 W Halogen lamp	CH_3OH, C_2H_5OH, CH_3CHO, H_2.	121
47.	Mg/TiO_2	Cylindrical stainless steel	CO_2 + H_2O vapor	RT	550 W Xe-lamp	CH_4 - 1, CO - 0.125, H_2 - 0.3	122
48.	Cu-Zn/TiO_2	Quartz reactor	CO_2 in NaOH	298	Hg lamp	CH_4 - 126-184	123
49.	Au/TiO_2	Gas closed circulation system	CO_2 + H_2O	298	300 W Xe lamp	CH_4 - 23.1	124

Table 1.10 Studies on anion doped titania catalysts

S. No	catalyst	Reactor used	Conditions		Light Source/ Intensity	Product formation	Ref.
			Reactant	Temp. (K)		µmol/g cat	
1.	S doped TiO_2.	batch type reactor	CO_2 + H_2O	Sun light	8 mW·cm^{-2} UV lamp	CH_3OH, C_2H_5OH	125
2.	N doped TiO_2 nanotubes	quartz reactor	CO_2 in 0.1 N NaOH	308	500W W-Halogen lamp	HCOOH - 12475.8±266.7, CH_3OH - 1132.6±45.4, HCHO -921.6±24.1	126
3.	N-doped mesoporous TiO_2 with cocatalyst Pt,	Quartz tubular reactor	CO_2 + gaseous H_2O	333	350W Xe lamp	CH_4 - 5.7 in 2 h	127

	Ag, Au						
4.	I doped TiO_2	Stainless steel with quartz window	$(CO_2$+$H_2O)$ vapors	RT	450W Xe lamp		128
5.	N/100	Semi batch	CO_2 + H_2O	RT	-	CH_3OH - 23/h	129
6.	g-C_3N_4–N–TiO_2 (CT–70)	Gas closed circulation system	(CO_2 +H_2O) vapors	303	300 W Xe arc lamp	CO - 14.73	130
7.	N–TiO_2/spirulina	Slurry reactor	CO_2 + H_2O	RT	13 W lamp	H_2 - 144.99* CH_4-0.48 C_2H_4 - 0.12 C_2H_6 - 0.17 *mmol/g	131

Table 1.11 Studies on titania supported on different materials

S. No	Catalyst	Reactor used	Conditions		Light Source /Intensity	Product formation µmol/g cat	Ref.
			Reactant	Temp (K)			
1.	TiO_2- loaded Nafion films	Cylindrical high Press. optical cell with quartz window	2000 psia CO_2.		990 W Xe	HCOOH –190, CH_3OH- 280, CH_3COOH –30	132
2.	MW-CNT supported TiO_2	SS reactor.	CO_2 ,H_2O vapor	308	UV 365 nm	CH_4- 58.7, HCOOH- 93.4, C_2H_5OH- 149.4	45
3.	CdSe/Pt/TiO_2 hetero structure	Custom-built photo catalysis cell	3 Torr H_2O vap. 0.3 Torr CO_2	308	visible light 420 nm	CH_4, CH_3OH, CO, H_2 (CO_2 conv. rate 0.8 ppm g^{-1} h^{-1})	133
4.	Graphene - TiO_2nano Comp.				UV - 365 nm	CH_4 – 8.5	134
5.	CdS–(Bi_2S_3), TNT	Continuous-flow reactor	CO_2 in NaOH, Na_2SO_3	308	500 W Xe	CH_3OH - TNT - 102.5, TNTs - CdS - 159.5, TNTs–Bi $_2S_3$ - 224.6	135
6.	Nafion coated Pd–TiO_2	Quartz reactor	CO_2 in Na_2CO_3	RT	300 W Xelamp	CH_4 - 7 C_2H_6 - 0.7	136
7.	mesoporous TiO_2 /graphitic carbon	Stainless steel reactor	CO_2+H_2O vapor	303	300 W Xe lamp	CH_4 - 10.3	137

	microspheres						
8.	CNTs@Ni-doped TiO_2	Quartz reactor	CO_2+H_2O vapor	RT	visible light λ 400 nm	CH_4 - 0.145/h	138
9.	graphene-$Ti_{0.9}O_2$ hollow spheres	Cylindrical stainless steel quartz window	CO_2+H_2O vapor	RT	450 W Xe lamp	CO, CH_4	139
10.	graphene-TiO_2nanosheets	Glass reactor	CO_2+H_2O vapor	RT	300 W Xe lamp	CH_4 - 8 C_2H_6 - 16.8	140

Table 1.12 Studies on titania dispersed on porous materials

S. No	Catalyst	Reactor used	Conditions		Light Source /Intensity	Product formation	Ref.
			Reactant	Temp (K)		µmol/g cat	
1.	Q-TiO_2 embedded in SiO_2	Quartz cell	CO_2 in IPA	308	500 W Hg	CO, Formate	72
2.	Pt on (a) Ti-ionexchanged (b) Ti in MCM-48 framework	Flat bottom quartz cell.	734Pa CO_2	328	75 W Hg/λ> 280 nm	CH_4 – 12, CH_3OH- 2.	141
3.	Pt/TiO_2 in Zeolites	Quartz cell	CO_2 in H_2O	328	Hg/λ>280 nm.	Ti in O_h sites- CH_4, T_d sites- CH_3OH	142
4.	Ti- silicalite mol. sieve		CO_2,H_2O vapor		UV laser 266 nm	CO, HCHO, CH_3CHO.	143
5.	Fluorination of Ti- FSM-1	Quartz cell with a flat bottom.	CO_2 in H_2O	323	100 W Hg/λ> 250 nm	Fluorination increases selectivity towards CH_3OH	39
6.	TiO_2 in porous SiO_2 thin film.	-	CO_2 in H_2O	323	100 W Hg/λ > 250 nm	CH_4- 70, CH_3OH-10	144
7.	Ti –MCM- 41	IR vacuum cell, 3.4 ml	0.1 MPa CO_2	298	266 nm	CO, O_2, H_2O confirmed as a e-donor.	145
8.	Ru/TiO_2, TiO_2/SiO_2	Inner irradiation type (Batch mode)	CO_2 in IPA	308	1000 W Hg/365 nm.	CH_3OH - 250, CH_4 – 75.	146
9.	Cu, Fe substitution in TiO_2– SiO_2.	Packed bed, circulated reactor 216	CO_2 + H_2O vapor	348	150 W Hg/ 320–500 nm, &500–800	Cu– Fe/TiO_2 favors C_2H_4 formation, Cu–	147

		fibers			nm	Fe/TiO_2–SiO_2 favored CH_4	
10.	0.5%Cu/Ti O_2–SiO_2	SS wall & quartz window. (continuous-flow).	CO_2 in H_2O vapour	308	Xe arc source, λ < 650 nm	CO - 60, CH_4 – 10	148
11.	Cu_2O/SiC	XPA-II photochemical reactor	CO_2 in NaOH& Na_2SO_3 solns.	308	500W Xe/200 to 700 nm	CH_3OH - 191	149
12.	Ti-SBA-15	Combinatorial photo reactors.	CO_2 in H_2O		120W Hg/280 to 650.	CH_4, C_2H_4, C_2H_6.	150
13.	Cu/TiO_2-SiO_2	SS wall with quartz window (continuous flow)	(CO_2 + H_2O) vapour	RT	Xe arc lamp	CO - 10/h CH_4 - 60/h	151
14.	2 wt% Cu-TiO_2-SBA 15	Inner irradiation (continuous mode)	CO_2 in NaOH + H_2O	315	500 W halide lamp	CH_4 - 627/h	152
15.	Kaolinite/ TiO_2	Stirred batch annular reactor	NaOH	RT	8 W Hg lamp	CH_4 - 4.5 CO - 2.5	153
16.	1, 3 wt% Ce–TiO_2/ SBA 15	Stainless steel with quartz window	CO_2 + H_2O	RT	450 W Xe lamp	CO - 1	154
17.	Ti-KIT-6/Si-Ti = 100	Pyrex glass reactor	CO_2 + H_2O	RT	300 W UV lamp	CH_4 - 4.4/h H_2 - 2.2/h	155
18.	TiO_2 (20%)/KIT6	Pyrex glass reactor	(CO_2 + H_2O) vapor	RT	300 W lamp	CH_4 - 44.56 CH_3OH - 1.09 CO - 120.54 H_2 - 44.56	156
19.	Mesoporous g-C_3N_4 flakes	Closed gas circulation system	CO_2 in NaOH	RT	300 W Xe lamp, visible light λ 420 nm	CH_3OH, C_2H_5OH	157
20.	Si/TiO_2nanosphere	Stainless steel cell with quartz window	(CO_2 + H_2O) vapor	RT at 50 psi	355 nm Laser lamp	CH_3OH - 197 μM/100 mL	158
21.	Cu/TiO_2 monoliths	Pyrex glass reactor	(CO_2 + H_2O) vapor	RT	200 W Hg/500 W halogen lamp	H_2 - 12.5, CH_3OH - 4, C_2H_5OH - 3, CH_3CHO - 3	159
22.	TiO_2/SiO_2	Quartz reactor	(CO_2 + H_2O)	298	300 W Xe lamp	CO - 3/h	160

			vapor				
23.	Cu/GO	Cylidrical reactor	(CO_2 + H_2O) vapor	303	300 W halogen lamp	CH_3OH - 3/h, CH_3CHO - 4/h	161
24.	Ag-MWCNT @ TiO_2	Quartz reactor	(CO_2 + H_2O) vapor	333	15 W energy saving light	CH_4 - 6.34, C_2H_6 - 0.68	162
25.	Au-In/TiO_2	Cylidrical stainless steel with quartz window	CO_2 + H_2	RT	200 W Hg lamp	CO - 8982/h	163
26.	Pt-RGO/TiO_2	Quartz reactor	(CO_2 + H_2O) vapor	333	15 W energy saving light	CH_4 - 1.7	164
27.	Cu–TiO_2/ZSM-5	-	CO_2 in $NaHCO_3$ soln.	298	254 nmUV-lamp	CH_3OH - 50.05	165
28.	Ca/Ti_xSi MCM-41	Quartz reactor	CO_2 + H_2O (1:2)	303	6 W cm^{-2}Hg lamp	CH_4 - 82/L	166

Table 1.13 Studies on different metal oxides

S. No	Catalyst	Reactor used	Conditions		Light Source /Intensity	Product formation µmol/g cat	Ref.
			Reactant	Temp (K)			
1.	Cu/ZrO_2	Inner irradiation quartz reactor	CO_2 in $NaHCO_3$ (pH 2.3)	308	400-W Hg UV Hg	CO - 2.5	167
2.	TiO_2 (P25), ZrO_2	Circulating Pack.bed quartz reactor	1.1 atm CO_2	316	UV/365 & 254 nm.	TiO_2- CH_4- .21, CO-0.28, C_2H_6 - 0.2, ZrO_2- CO- 1.24 With H_2+H_2O	168
3.	Pd, Cu on Mixed oxides of MgO, ZnO Al_2O_3,TiO_2, SiO_2.	Batch reactor	CO_2 in 0.5M $KHCO_3$ (pH = 7.5)	308	250 mW Hg.	C_1-C_3 products. Acidic supports- CH_4, HCHO, HCOOH. Basic supports- C_2H_6, C_2H_5OH, Acetone	169
4.	MgO	Closed static system	CO_2 & H_2	308	500 W Hg	CH_4,CO.	170
5.	Ga_2O_3	Closed	CO_2: H_2:	308	200W Hg–	CO – 2.1	171

		circulating system- Quartz	(150:50 μmol).		Xe.		
6.	ZrO_2	Quartz reactor	$CO_2 : H_2$ or CH_4 = 150:50 (μmol).	308	500W Hg	CO – 9.5	172
7.	Meso Ga_2O_3	Quartz window- closed chamber	CO_2 in H_2O	300	300 W Xe	CH_4 – 2.9	173
8.	WO_3 nanosheets	Pyrex glass cell	$CO_2 + H_2O$ vapor	RT	300 W Xe arc, visible light λ 420 nm	CH_4 - 16	174
9.	rectangular sheet- WO_3	Stainless steel reaction chamber	$CO_2 + H_2O$ vapor	RT	UV Xe lamp	CH_4 - 0.34	175
10.	$W_{18}O_{49}$ nanowires	-	$CO_2 + H_2O$ vapor	RT	visible light λ 420 nm	CH_4 - 4000* * ppm/g	176
11.	Porous MgO/TiO_2	Continuous flow glass reactor	$CO_2 + H_2O$ vapor	423	400 W Xe lamp	CO - 30/h	177
12.	g-C_3N_4 nanosheet	Stainless steel with quartz window	$CO_2 + H_2O$ vapor	RT	300 W Xe lamp	CH_4 - 0.5, CH_3CHO - 0.05	178
13.	g-C_3N_4/ Bi_2WO_6	Glass reactor with quartz window	$CO_2 + H_2O$ vapor	RT	300 W Xe lamp	CO - 5.19/h	179
14.	CNTs–TiO_2	Quartz reactor	$CO_2 + H_2O$	RT	15 W energy saving light bulb	CH_4 - 1.2	180
15.	CuO nanowire/ ZnO	Cylindrical stainless steel with quartz window	(CO_2 + H_2O)vapor	RT	400 W Xe lamp	CO - 1980/h	181
16.	Fe_2O_3/Cu_2O	Cylindrical stainless steel reactor	(CO_2 + H_2O)vapor	RT	300 W Xe lamp	CO - 5	182
17.	Rh/Cr_2O_3/GaN	Pyrex cell	(CO_2 + H_2O)vapor	RT	300 W Xe lamp	CH_4 - 85, CO - 100, H_2 - 3.8	183
18.	ZnS	Fused silica reactor	CO_2 in Na_2S	288	1 kW high-press. Hg (Xe) arc lamp	$HCOO^-$ - 440 μM	184
19.	g-CN	Schlenk flask	CO_2 in Co-$(bpy)_3C_{l2}$ and TEOA	333	300 W Xe lamp	CO - 10.2, H_2 - 2.8	185

20.	ZnO/ZnTe	Quartz reactor	mixture $CO_2 + H_2O$	-	300 W Xe lamp	CH_4 - 356.51	186

Table 1.14 Studies on mixed metal oxide catalysts

S. No	Catalyst	Reactor used	Conditions		Light Source /Intensity	Product formation µmol/g cat	Ref.
			Reactant	Temp (K)			
1.	$SrTiO_3$ in aq. suspension	UHV surf. Anal. chamber -batch	$CO_2 + H_2O$	Sun light	Natural sunlight	HCOOH, HCHO, CH_3OH. QE=0.011%	16
2.	$CaFe_2O_4$	Quartz beaker	CO_2/0.01 M NaOH (pH 5.8)	308	500-W Hg	CH_3OH, HCHO.	187
3.	Pt/ $K_2Ti_6O_{13}$ + Fe-Cu- K/DAY	Photoreactor with quartz window	$CO_2 + H_2O$	308	300W Xe& 150W Hg.	CH_4 -0.014 HCOOH- 3.88 CH_3OH - 1.45 C_2H_5OH- 0.35	188
4.	Pt/ $K_2Ti_6O_{13}$ with Cu/ZnO.	Photo reactor with flat quartz window.	$CO_2 + H_2O$	308	300W Xe- or 150W Hg.	CH_4 - 0.86, HCOOH- 43.47, CH_3OH - 18.93 HCHO - 10.97.	189
5.	$ATaO_3$ (A= Li, Na, K)	Closed circulating reactor	CO_2 : H_2 = 150:50 (µmol)	303	200W Hg–Xe	The order of activity- $LiTaO_3$> $NaTaO_3$> $KTaO_3$. CO - 0.42 on $LiTaO_3$	190
6.	Bi_2WO_6 square nanoplates	230 mL glass reactor	$CO_2 + H_2O$		300 W Xe	CH_4 - 6	191
7.	Pt-$NaNbO_3$	Pyrex glass	$CO_2 + H_2O$	308	300-W Xe	CH_4–653*, *ppm/h/g	192
8.	Pt/ $NaNbO_3$	Closed Pyrex cell	80 kPa CO_2 in H_2O.	308	300 W Xe	CH_4 - 0.486	193

9.	Pt/Meso Zn-Ge (ZGON)				(λ> 400 nm)	CH_4 - 26.8*, *ppm/h/g	194
10.	Ag- $ALa_4Ti_4O_{15}$ (A = Ca, Sr, & Ba)	Inner irradiation quartz cell	CO_2 flow system (15 mL min^{-1}).		400W Hg	$BaLa_4Ti_4O_{15}$ >$SrLa_4Ti_4O_{15}$>$CaLa_4Ti_4O_{15}$. CO, HCOOH	195
11.	Ni@NiO on $InTaO_4$	Pyrex glass (continuous flow)	CO_2(3 kg cm^{-2}) in H_2O	298	100 mW Xe	Methanol - $InTaO_4$< $InTaO_4$-N<Ni@NiO/ $InTaO_4$-N.	196
12.	NiO–$InNbO_4$, Co_3O_4–$InNbO_4$	Pyrex glass (continuous flow)	CO_2 in 0.2 M $KHCO_3$	308	500W halogen H-500; 143µ W/cm^2; λ500–900nm	CH_3OH NiO-$InNbO_4$ - 1.577 Co_3O_4-$InNbO_4$ - 1.503.	197
13.	HNb_3O_8 nanobelts	Quartz tubular reactor	H_2O+CO_2	318	350 W Xe	CH_4 – 3.58	198
14.	Zn-Al LDH, Zn-Cu-Ga	Quartz reactor	2.3 kPa of CO_2 + 21.7 kPa of H_2	305–313	500-W Xe arc lamp	CO – 0.62, CH_3OH – 0.17.	199
15.	$FeTiO_3$/ TiO_2	Pyrex glass	CO_2 in $NaHCO_3$	RT	500W Xe (with cut off)	CH_3OH - 0.46	200
16.	$CuGaO_2$, $CuGa_{1-x}$ Fe_xO_2	SS cell	CO_2 in H_2O	RT	300WXe arc	CO - 9*, *ppm g^{-1} $_h$-1	201
17.	SiO_2- Pillared HNb_3O_8	Quartz tubular reactor	H_2O/CO_2 = 0.14	333	34.8mW cm^{-2} Xe arc	CH_4 - 2.9	202
18.	Pt/$SrTiO_3$–Rh/ Pt/$CuAlGaO_4$ WO_3	H- Twin reactor	2 mM $FeCl_2$/$FeCl_3$	RT	AM 1.5G	CH_3OH - 0.52 H_2 - 0.12	203
19.	Pt/$SrTiO_3$–Rh/ Pt/$CuAlGaO_4$ WO_3	H- Twin reactor	2 mM $FeCl_2$/$FeCl_3$	-	AM 1.5G	CH_3OH - 8 H_2 - 1	204
20.	Pt/self-doped $SrTiO_{3\square\delta}$	-	CO_2+H_2O water	-	300 W Xe, visible light λ 400 nm	CH_4 - 0.26/cm^2	205
21.	Ag/ $SrTiO_3$	Batch slurry reactor	CO_2 in CH_3OH	298	Hg lamp	HCOOH	206
22.	Au/ leaf-architectured	Pyrex reaction cell	CO_2+H_2O vapor	RT	300 W Xe	CO, CH_4	207

	$SrTiO_3$						
23.	$Pt/Fe_2V_4O_{13}$ nanoribbons		CO_2+H_2O vapor		visible light λ 420 nm	CH_4	208
24.	Pt and RuO_2/ $Na_2V_6O_{16}$ nanoribbons	Circular glass reactor	CO_2+H_2O vapor		300 W Xe lamp, visible light λ 420 nm	CH_4 - 2	209
25.	$Bi_6Mo_2O_{15}$ sub-microwires	-	CO_2+H_2O vapor	RT	UV Xe	CH_4 - 17* O_2- 250	210
26.	Bi_2WO_6 hollow microspheres	-	(CO_2+H_2O) vapor	RT	visible light λ 420 nm	CH_3OH - 33 *ppm,	211
27.	Pt/mesoporous $In(OH)_3$	Gas closed circulation pump	(CO_2+H_2O) vapor	RT	UV Xe	CH_4 - 25	212
28.	RuO_2/meso $ZnGa_2O_4$	Glass	(CO_2+H_2O) vapor	RT	UV Xe	CH_4 - 145 ppm	213
29.	$RuO_2/ZnGa_2O_4$nanocubes	Glass reactor	(CO_2+H_2O) vapor	-	UV Xe	CH_4 - 2, O_2 - 21	214
30.	Pt/ $ZnAl_2O_4$ -modifiedmesoZnGaNO	-	(CO_2+H_2O) vapor	-	visible light λ 420 nm	CH_4 - 40	215
31.	Pt/ZIF-8/Zn_2GeO_4nanorods	-	CO_2 bubbled Na_2SO_3	RT	UV Xe	CH_3OH - 3	216
32.	Pt &RuO_2/ sheaf-like, hyperbranched $Zn_{1.7}GeN_{1.8}O$	Pyrex glass	(CO_2+H_2O) vapor	RT	visible light λ 420 nm	CH_4 - 55	217
33.	4.5($ZnGa_2O_4$):(Zn_2GeO_4)	Glass reactor	(CO_2+H_2O) vapor	RT	UV Xe	CH_4 - 2.75, O_2 - 17	218
34.	$Pt/In_2Ge_2O_7$ (En) nanowires	Pyrex glass cell	(CO_2+H_2O) vapor	RT	300 W Xe	CO - 4, O2	219
35.	Pt/Zn_2SnO_4	Pyrex glass cell	(CO_2+H_2O) vapor	RT	UV Xe	CH_4 - 350	220
36.	layered Mg-In LDH	Closed circulation system	(CO_2+H_2O) vapor	RT	UV Hg-Xe	CO - 3, O2	221
37.	layered Zn–Cu–Ga LDH	Quartz reactor	(CO_2+H_2) vapor	RT	500 W UV Xe	CH_3OH, CO	222
38.	$Ag/KTaO_3$	Glass reactor	CO_2+H_2O	RT	300 W Xe	CO - 152.6, H_2 - 1134, O_2 - 499.9	223
39.	(MgAl)-LDO grafted TiO_2	Quartz tube reactor	(CO_2+H_2O) vapor	423	100 W He/ 450W Xe	CO - 4/h	224

40.	ZnGaNOnanorod	Glass reactor	CO_2+H_2O	RT	300 W Xe	CH_4 - 0.19	225
41.	$NiCo_2O_4$ with $[Ru(bpy)_3]Cl_2$. $6H_2O$	Schlenk reactor	TEOA/ water/acetonitrile	303	300 W Xe	CO - 35, H_2 - 5	226
42.	$SnNb_2O_6$	Schlenk reactor	CO_2+H_2O	RT	300 W Xe	CH_4 - 110 µL/h	227
43.	$MTaO_3$ (M = Li, Na, K)	Pyrex glass cell	CO_2+H_2O	RT	200 W Hg–Xe arc lamp	CH_4 - 1.9 nmol/h CO - 4	228
44.	$Ag/BaZrO_3$	Cylindrical quartz reactor	(CO_2+H_2O) vapor	RT	300 W Xe	CH_4 - 4	229
45.	$MnCo_2O_4$	-	CO_2 in TEOA	303	300W Xe	CO - 27, H_2 - 8	230
46.	Cu_xO_y-$ZrOCo^{II}$ SBA-15	Stainless infrared vacuum cell	CO_2 in diethylamine	RT	laser	CO	231
47.	Cr doped $SrTiO_3$	-	(CO_2+H_2O) vapor	RT	300W Xe	CH_4 - 8.8	232
48.	$Ca_xTi_yO_3$	Quartz reactor	CO_2+H_2O	303	6 W cm^{-2} , UV lamp	CH_4 - 17	233
49.	C, N/sodium titanate	Stainless steel	(CO_2+H_2O) vapor	RT	100 W Xe solar simulator	CH_4 - 9.75/h	234

Table 1.15 Studies on dye sensitized photo catalysts

S. No	Catalyst	Reactor used	Conditions		Light Source /Intensity	Product formation µmol/g cat	Ref.
			Reactant	Temp (K)			
1.	Metal porphyrin / phthalo cyanine on Nafion	Glass cell with an optical window.	CO_2 in TEA	308	500 W tungsten-halogen	HCOOH.	235
2.	Dye($[Ru(Bpy)_3]^{2+}$perylene Di- Imide based) sensitized, Q- yield:Pt onTiO_2	Glass chamber connected to a vacuum line	0.09 MPa CO_2 inH_2O	298	75 W visible daylight lamp, 150 W UV	CH_4 - 0.6.	236
3.	Ruthenium dye (N_3)- sensitized Cu–Fe/TiO_2	Continuous circulating Pyrex glass	CO_2 + H_2O (vapor)	348	Solar 20 mW cm^{-2}, UV lamp 225 mW cm^{-2}	CH_4 - 0.617	237
4.	CoPc/TiO_2	Pyrex glass cell (batch mode).	CO_2 in 0.1N NaOH.	308	500W tungsten-halogen	HCOOH - 300, CH_3OH – 10, HCHO – 50.	238

5.	0.7 wt.% In-situ CoPc/TiO_2	Pyrex glass cell	CO_2 in 0.1N NaOH.	308	500W tungsten-halogen	HCOOH-1487.6 CH_3OH – 93 HCHO - 134.3.	239
6.	Ru/RuOx sensitized TiO_2	-	CO_2+ H_2O	-	Solar simulator	CH_4 - 900 µL h^{-1}	240
7.	Dye sensitized (perylenediimide derivatives) Pt impregnated on TiO_2	-	CO_2 + H_2O	RT	75 W daylight lamp	CH_4 - 0.74	241
8.	N719/TiO_2	H type reactor	CO_2 + H_2O/ 2 M NaOH	RT	300 W Xe	CH_3OH - 178.1/cm^2 HCHO - 129.2/cm^2	242
9.	IrOx/SiGe-jn/CC/p-RuCP	Stainless steel Monolithic tablet shaped device	CO_2 + H_2O	RT	Simulated solar light	HCOOH - 50.2, H_2 - 3.6, O_2 - 26.4	243
10.	Zinc porphyrin/TiO_2	Pyrex glass reactor	(CO_2 + H_2O) vapor	RT	300 W Xe	CO - 8.07/h CH_4 - 1.01/h	244

1.8 Kinetics and mechanism of CO_2 photo-reduction with water

Understanding of CO_2 reduction pathway on semiconductor surfaces is at an infant stage. However, based on detailed experiments, researchers have put forward plausible pathways for CO_2 reduction on TiO_2 surfaces. Three different reaction pathways depending on the binding mode of $CO_2^{\cdot -}$ radical anion on the semiconductor surface have been proposed [245], which are i) The formaldehyde pathway, ii) The carbene pathway, iii) The glyoxal pathway as shown in Fig. 1.9

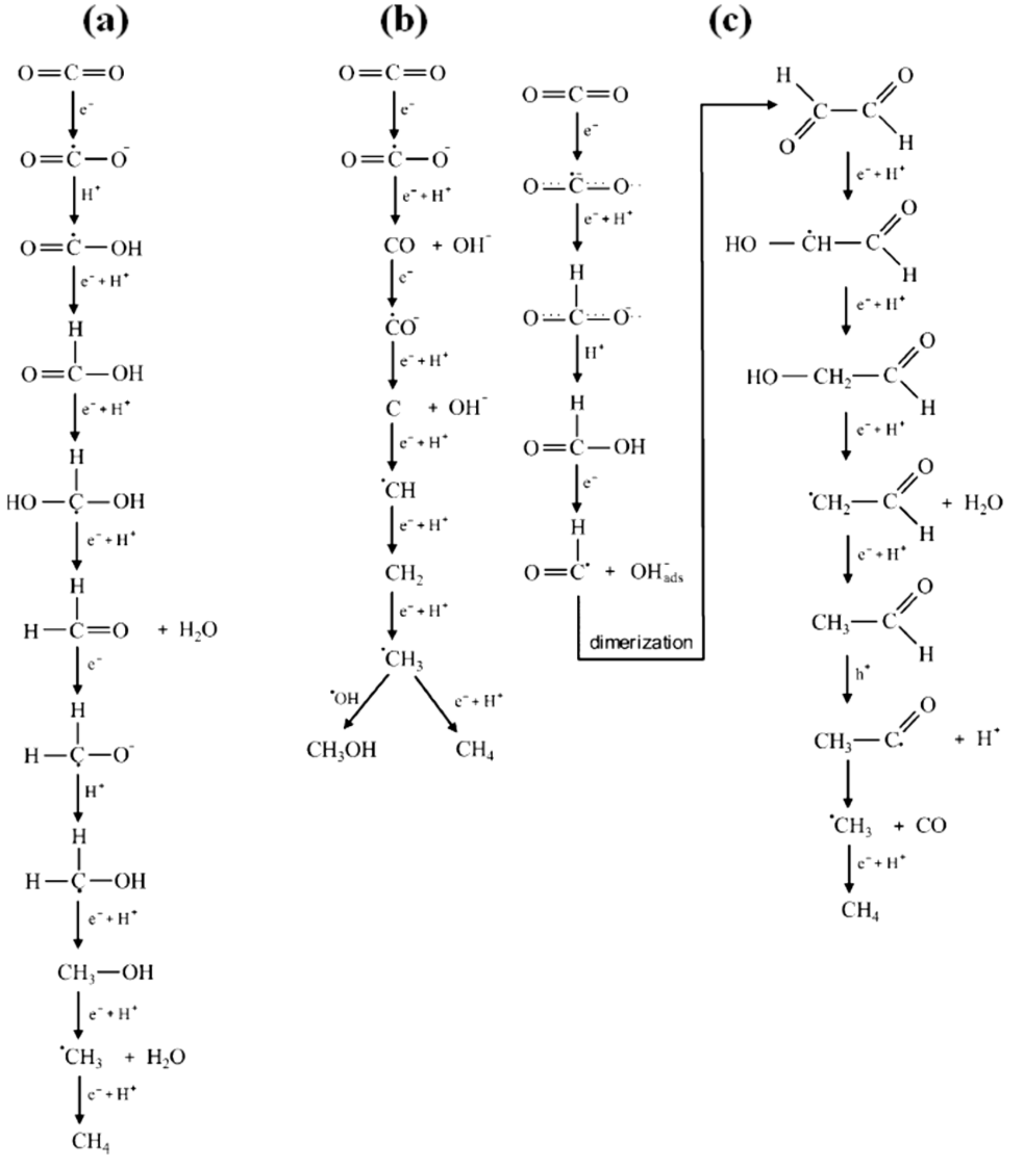

Fig. 1.10 Proposed mechanisms for the reduction of CO_2 to methane: (a) formaldehyde pathway (b) carbene pathway (c) glyoxal pathway [245]

In the case of Formaldehyde pathway, binding mode of CO_2 through one of the oxygen atoms on titanium ion or carbon atom through surface oxygen atom of TiO_2, favors the formation of .COOH radical, which further combines with .H to form formic acid. As shown in Fig. 1.9 a, final 8 e- reduction product CH_4 was obtained from consecutive reduction of formic acid through HCHO and CH_3OH as intermediate products. These observations find support in a recent publication by Dimitrijevic et al [246], wherein detailed low temperature ESR measurements on TiO_2 nano particles dispersed in aqueous alkaline solutions, have indicated the formation of H atoms and OH radicals in addition to methyl ($.CH_3$) and methoxy ($.CH_3O$) radicals on the surface. However the formation of surface formate species is proposed as the initial step according to the Scheme. 4 below:

$CO_2 + 2e^- + H^+ \longrightarrow HCOO^-$ ------------ (20)

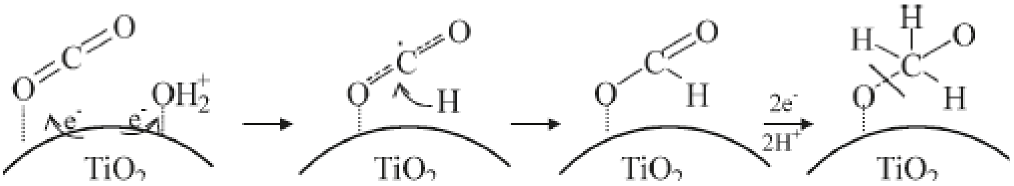

Scheme 1.4 Proposed mechanism of photo catalytic transformation of CO_2 to methoxy radical over TiO_2 in the presence of dissociated/ bound water [246]

Ulagappan and Frei [145] carried out a mechanistic study of the reaction with methanol as electron donor on Ti silicalite using in-situ FT-IR spectroscopy and traced the reaction pathway using isotopic labelling studies with $C^{18}O_2$, $^{13}CO_2$ and $^{13}CH_3OH$. HCOOH was identified as the primary product, which on pyrolysis gives CO. In the absence of methanol, water was confirmed as the electron donor.

Koci et al studied kinetic model for CO_2 photo-reduction with respect to the formaldehyde pathway [247] the result shows that the formation of methane did not correspond to the consecutive reduction of formic acid and methanol. Hence they have proposed carbene pathway for CO_2 photo reduction shown in Fig. 1.9 b, in this pathway, anion radical bind through carbon on the semiconductor surface, formation of CO and O occur in the first step. Then adsorbed CO reduced with two electrons to form carbon residue on the semiconductor surface, which further combines with .H to form carbene and methyl radicals and finally CH_4. Formation of different transient surface species and their transformations on TiO_2 during photo catalytic reduction of

CO_2 by water was traced by Anpo et al [43, 248] using ESR, EXAFS and other spectroscopic techniques. Ti^{3+}, H, C and CH_3 radicals were detected by ESR studies carried out at 77K. The charge transfer excited state, $(Ti^{3+}\text{-}O^{-})^{3*}$ with Ti in tetrahedral co-ordination, formed by absorption of light energy, was proposed as the active site on which CO_2 get s reduced to CO and C, which on addition of active surface hydrogen forms hydrocarbons. Further mechanistic pathways in this case, have been elucidated in Scheme. 5.

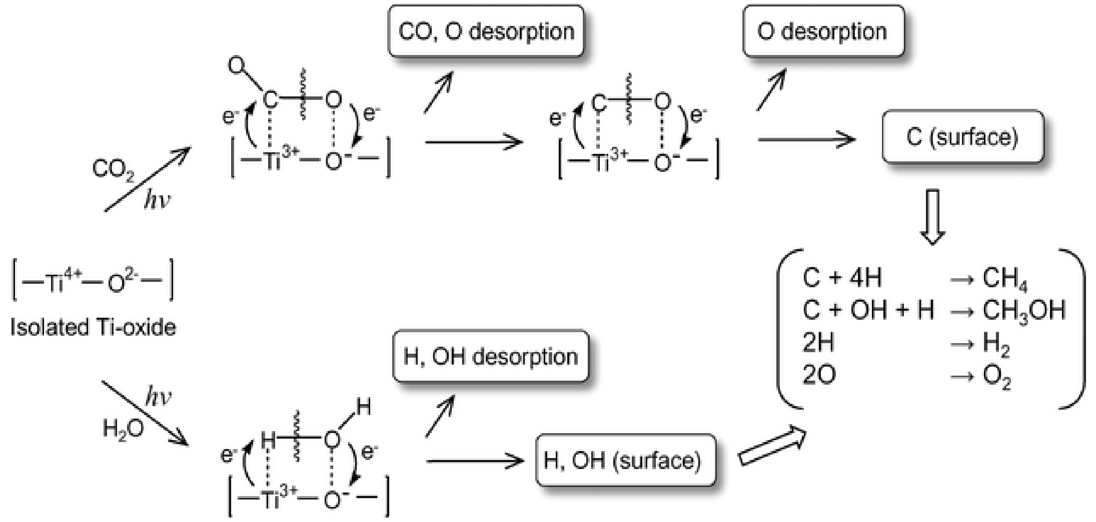

Scheme 1.5 Schematic representation of the photo catalytic reduction of CO_2 with H_2O on anchored titanium dioxide [43, 248]

Yang et al [249] studied the photo catalytic reduction of CO_2 using Ti-SBA-15 on the effects of varying feed composition on the product patterns, with a view to understand the reaction mechanism. In particular, addition of CO, H_2 in the place of H_2O, methanol and formaldehyde was studied in detail. While CH_4, C_2H_4 and C_2H_6 could be observed with CO + H_2O with reasonable rates, with CO+H_2 mixture, the reaction rates were very low. It was concluded that H_2O was a more efficient reductant with CO_2 or CO than H_2. CH_3OH was not a significant product and when added with the feed and it did not increase the reaction rate. Similarly added formic acid also did not enhance product formation. These observations rule out methanol or formic acid as intermediates in the formation of hydrocarbons on Ti-SBA-15. However, added formaldehyde underwent facile conversion to hydrocarbon products. Based on the detailed analysis of the products it was proposed that CO_2 photo- reduction proceeds through the formation of CO in the initial stages followed by its conversion to formaldehyde, which in turn gets converted to other hydrocarbon products as shown in scheme 6. Ti-OH site, which on photo activation gets converted to [Ti (III)-O]* is considered as the active site [145].

$$\begin{array}{lcl}
\text{-Ti-OH} + CO_2 & \rightarrow & \text{-Ti-OOH} + CO \\
[\ \text{-Ti-OH} + H_2O & \rightarrow & \text{-Ti-OOH} + H_2\ ] \\
\text{-Ti-OOH} + CO + H_2O & \rightarrow & \text{-Ti-OH} + H_2CO + O_2 \\
\text{-Ti-OH} + H_2CO + H_2O & \rightarrow & \text{-Ti-OH} + H_2CH_2 + O_2 \\
\hline
CO_2 + 2\ H_2O & \rightarrow & CH_4 + 2\ O_2
\end{array}$$

$$\begin{array}{lcl}
\text{-Ti-OH} + H_2CO + H_2CO & \rightarrow & \text{-Ti-OH} + H_2C{=}CH_2 + O_2 \\
\text{-Ti-OH} + H_2CO + H_2CO + H_2O & \rightarrow & \text{-Ti-OH} + H_3C\text{-}CH_3 + {}^3/_2\ O_2
\end{array}$$

Scheme 1.6 Proposed mechanism of photocatalytic reduction of CO_2 with H_2O over Ti-SBA-15 [Reproduced from 249]

Kinetic models for photo catalytic reduction of CO_2 with water on titania have been reported by Lo et al [168] and Tan et al [250]. Both authors have applied single site Langmuir- Hinshelwood [L-H] type kinetic model to simulate the process. Lo et al. [168] could successfully validate their model with the experimental data with a pseudo first order reaction rate equation. Tan et.al [250] adopted the reaction scheme involving the formation of surface carbon radicals as proposed by Anpo et al [43, 248] and could predict rates of formation of methane and hydrogen. Koci et al. [247] while applying the L-H model have checked the suitability of the two reaction mechanisms proposed, i.e., one by Anpo [43, 248] and the other by Wu [67] and observed that their model supports Anpo's mechanism wherein CO is proposed as the primary intermediate. Hence carbene reaction pathway is a more plausible reaction pathway for CO_2 reduction.

Shkrob et al [245, 251, 252] have proposed Glyoxal reaction pathway for CO_2 photo reduction by adopting EPR study, which includes both oxidation and reduction reactions. In the previous reaction pathway authors were interested in reduction reactions (electrons), but highly oxidative holes are also present in the system. The formation of oxidized products from formaldehyde and methanol is more favorable compared to reduced product from it. Hence Shkrob et al proposed C2 complex reaction pathway shown in Fig. 1.9c, in which dimerization of formyl radical to gives glyoxal, further reduced to form acetaldehyde through vinoxyl radical. CH_3CHO easily oxidized to form unstable acetyl radical which further undergoes decarbonylation to form methyl radical, and then combine with .H to form CH_4.

While the formation of C_1 hydrocarbons could be explained to a reasonable level of acceptability, the understanding on the pathways leading to the formation of C_2 and $>C_2$ hydrocarbons was not clear. Dimerization of surface C_1 species was proposed as the possible route for the formation of C_2 hydrocarbon products [253], though direct experimental evidence to this effect was lacking.

Yang et al [249] observe that the backward reaction ie, oxidation of hydrocarbons back to CO_2 and water, proceeds to a significant extent. This implies that the oxygen produced by the splitting of water, which is responsible for the backward reaction, has to be removed effectively to increase hydrocarbon yields. Means of separating physically the oxidation and reduction sites would be crucial in this respect. It is clear that the reaction mechanism is quite complex and depends on the type of the catalysts/active sites.

1.9 Deactivation of photo-catalysts

In some cases [146, 89, 133, 135, 151] the catalysts reported for photo-reduction of CO_2 tend to get deactivated within short period, while in few cases activity beyond 20 hrs. has been reported. Transformation of photo-activated CO_2 to hydrocarbons proceeds through several hydrocarbon intermediates, whose identity or nature is yet to be established. Accumulation of these intermediates on the catalyst surface and blocking of the active sites is one of the major reasons for the catalyst deactivation. In the case of catalyst nano particles dispersed in liquid media, coagulation and reduction in light absorption power [146] and changes in the oxidation state of metal ions [133] may lead to catalyst deactivation. Regeneration with air helps in restoring the activity. However, the phenomenon of catalyst deactivation in this process needs further study, especially when large scale applications of this process are desired.

An in-depth understanding of the reaction mechanism and the fast deactivation of the photo catalyst would be helpful in the development of superior catalysts for this process that has the potential to emerge as a sustainable route for the production of fuels and chemicals.

1.10 Future trends and research directions

Photo catalytic reduction of carbon dioxide with water to fuels/chemicals (methane, methanol, etc.,) is an emerging area of research towards utilizing the abundant sunlight. Though the process has the potential to become a viable and sustainable alternative energy source to fossil fuels, it has thrown up several tough challenges to the scientists and technologists, which are yet to be tackled, namely,

- Facilitating the activation of two thermodynamically most stable molecules, CO_2 and H_2O
- Conversions achieved so far are extremely small, < 1 %, occurring at very slow rate
- Catalysts tend to get deactivated over short period which needs further studies
- CO_2 photo reduction process is highly complex, involving multi electron transfer and non- selective, leading to a range (C1-C3) of hydrocarbon products and reaction pathways have not been established yet

- Design of catalysts consisting of photo active phase/support and co-catalysts aided by metal ion and /or anion doping and light harvesting components/sensitizers, as a functionally integrated composite, is equally complex.
- Ideal catalysts are expected to display maximum efficiency towards solar energy absorption and possess requisite band energy level characteristics to drive the redox reactions.
- The process involves two steps, spitting of water and reduction of carbon dioxide, which is thermodynamically more favourable. Since the second step involves multi-electron transfer, the rates are very slow relative to the first. These two steps are to be synchronized to achieve higher yields of hydrocarbons.
- Multiple and complex surface reaction pathways that involve several carbon containing ion radicals, render the selective formation of methane or methanol a difficult task.
- Further decomposition of the products and promotion of backward reactions also contribute towards lower yields.
- Catalyst deactivation proceeds through the formation of carbonaceous species on the surface. This implies that the metal function responsible for the hydrogenation of carbonaceous species needs to be improved though availability of hydrogen via water splitting may not be the issue.
- Titania, subjected to a wide range of modifications, in the form of titania based composites and in different morphological forms has been explored to enhance the activity for photo-catalytic reduction of CO_2 with water with respect to pristine titania. Primary objectives behind the modifications, namely, promoting visible light activity, retarding the recombination of charge carriers by effective physical separation (by doping with metals, anions & cations), facilitating their transport through titania surface, isolation of titania sites by dispersion on high surface area supports and incorporation of suitable active elements to bring out required redox reactions, have been realized to a significant extent. However, the expected

improvement in activity has been moderate, an increase by 2-4 times, which is too low for any possible practical applications.

- In-depth investigations on the surface reaction pathways by *in-situ* spectroscopic methods, supported by sound theoretical studies on the activation and surface transformations of CO_2 and other aspects for investigation, as detailed in the earlier section, would be helpful in controlling deactivation and achieving higher conversions.

Nevertheless, research efforts on these fronts are being pursued with the objectives of designing of efficient catalyst systems to achieve higher yields of desired products and improving catalyst life. Efforts in future have to be towards the development of alternative catalysts, based on various semiconducting metal oxides/sulfides/nitrides/phosphides, layered titanates, binary and ternary oxides of Nb, Ta, Ga & In in conjunction with alkaline, alkaline earth and rare earth oxides and with a host of co-catalysts and sensitizers.[9, 10, 74-244, 254, 255]

Especially, the following areas/aspects are worth exploring further:

- A number of binary and ternary oxides of Bi, V, Nb& Ta with Gr IIIA elements like, Al, Ga & In are known to be efficient catalysts for photo-catalytic splitting of water in the visible region [256, 257]. These systems with suitable co-catalysts like NiO could be excellent catalysts for CO_2 photo reduction
- Most of these oxides are synthesized by high temperature solid state reaction with very low surface area. Soft chemistry routes could be explored to get high surface area samples. However, in such cases, the contribution due to residual carbon on the catalysts is to be accounted for.
- These compounds possess well-defined crystal structure and hence their solid state and photo- physical properties could be fine-tuned to derive maximum performance

- Performance of such photo catalysts could be improved further by forming composites with advanced materials like CNT, graphene [258-261] and Nafion [262] which facilitate free and fast transfer of charge carriers could be another way to improve performance.
- Studies on modes of adsorption and activation of CO_2 on metals, metal oxides, which act as co-catalysts- experimental as well as theoretical approaches are to be pursued.
- Use of different co-catalysts, single as well as bi-component systems
- Elucidation of the mechanistic pathways for the transformation of transient surface species and formation of C_2 and higher carbon number products
- Modes of deactivation of catalysts and possibilities for regeneration

It is expected that the use of photo electrochemical cells (PEC) for conversion of CO_2 to methanol [263-266] would add another dimension to the process, to get improved yields of hydrocarbons. Additionally, development of novel and more efficient catalyst systems and prevention of re-oxidation of products could help in improving the efficiency of the process.

1.11 Scope of the present investigation

CO_2 is one of the cheapest and most abundant carbon containing raw material in the earth. But the usage of CO_2 as raw material is thermodynamically not favourable due its stability and chemically inert nature. Hence thermodynamically uphill reactions can be solved by developing a good catalyst system. The production of fuels from green-house gas CO_2 and abundantly available water in the presence of natural sunlight is an attractive research, because it will give remedy to both energy and environmental issues which we are facing in the present context. There is some relief from green-house effect by using CO_2 as reactant and its conversion to fuel (for energy) from natural sources such as solar light and water would help to contain green house gas effect. The challenge is to activate thermodynamically most stable molecules CO_2 and H_2O. Photo catalytic reduction with water has the potential to emerge as a viable process in such an effort, since, photo-catalysts can convert solar energy into chemical energy and also have the ability to promote non-spontaneous reactions ($\Delta G>0$). Hence design of photo catalysts is an important and challenging task.

The primary objective of the present investigation is to design novel photo catalysts for CO_2 reduction. Detailed literature survey on different types of catalysts investigated so far reveal that two perovskite type catalysts, $NaTaO_3$ and $Sr_3Ti_2O_7$, which display significant activity for splitting of water and possess conduction and valance band energy levels suitable for CO_2 photo reduction have not been exploited so far. Both oxides, being wide band gap semi-conductors, are to be suitably modified to enable visible light absorption. Attempts have been made to modify these oxides and explore their activity for CO_2 photo reduction. Besides, meso-porous character of the photo-catalysts is known to improve the activity as shown in Table 1.11. In order to explore this aspect, a comparative study of standard titania P-25 and a lab-made mesoporous titania in pristine and doped (N,S & Fe) forms have been investigated. Accordingly, investigations covering several other aspects, as detailed below, around these three main catalyst systems (TiO_2, La-$NaTaO_3$ and $Sr_3Ti_2O_7$) have been planned:

- Studies on titania based catalysts:
    - Comparison of meso porous titanium dioxide with standard P-25 titania
    - Influence of doping/co-doping with N and S
    - Effect of supporting N, S & Fe co-doped TiO_2 samples on sepiolite
- Studies on La modified $NaTaO_3$ based photo catalysts:
    - Influence of different co-catalysts: Ag, Au, Pt, Pd, NiO, CuO and RuO_2 and bi-metallic co-catalysts, Pt-CuO & Pt-NiO
    - Effect of metal–non metal (Fe, N) co- doping
    - Effect of addition of basic component, MgO
    - Sensitization with Cobalt tetra phenyl porphyrin (CoTPP)

- Studies on layered perovskite type titanates based on $Sr_3Ti_2O_7$ as photo catalysts:
    - Comparison of strontium titanates- $SrTiO_3$, $Sr_3Ti_2O_7$ and $Sr_4Ti_3O_{10}$
    - Effect of doping/co-doping $Sr_3Ti_2O_7$ with N,S & Fe

Hydrothermal and polymer complex methods have been adopted for the preparation of the tantalates and titanates. All catalysts have been subjected to comprehensive characterization studies, using XRD, DRS-UV, photo luminescence, XPS, Raman spectroscopic techniques, SEM, EDAX, TEM, and surface area analysis. Photo catalytic efficiency of the prepared catalysts for CO_2 reduction with water has been studied in a lab-made photo reactor, with UV-visible radiation. Observed activity patterns have been rationalized in terms of structural, morphological, electronic and photo-physical properties of the catalysts, so as to arrive at a basis for the design of effective photo catalysts for this application.

1.12 Organization of the thesis

Chapter 1. Introduction
Chapter 2. Experimental methods
Chapter 3. Studies on titania based catalysts
Chapter 4. Studies on La modified sodium tantalite based catalysts
Chapter 5. Studies on strontium titanate based catalysts
Chapter 6. Summary and Conclusions

1.13 References

1. W. Wang, S. Wang, X. Ma, J. Gong, Chem. Soc. Rev., 2011, 40, 3703.
2. International Energy Agency “CO_2 emissions from fuel combustion highlights 2014”
3. M. A. Wojtowicz, J. R. Pels, J. A. Moulijn, Fuel Process. Technol. 1993, 34, 1.
4. R. W. Steiner, Chem. Eng. 1993, 100, 114.

5. M.A. Scibioh, B. Viswanathan, Proc. Indian National Science Academy, 2004, 70A, 407. B. Viswanathan, Materials and processes for solar fuel production, 174, 2014, 211-233.
6. S. S. Kim, G. Kishan, M. J. Choi,K. W. Lee, Appl. Catal. A. Gen., 1999, 179, 155.
7. N. Serpone, E. Pelizzetti, Wiley-Interscience, New York, 1989; N. Serpone, A. V. Emeline, Int. J. Photoenergy, 2002, 4, 91.
8. D. Ravelli, D. Dondi, M. Fagnoni and A. Albini, Chem. Soc. Rev., 2009, 38, 1999.
9. V. P. Indrakanti, J. D. Kubickib,H. H. Schobert, Energy Environ. Sci., 2009, 2, 745.
10. S. Das, W.M.A. Wan Daud, RSC Adv., 2014, 4, 20856
11. V. Jeyalakshmi, K. Rajalakshmi, R. Mahalakshmy, K.R. Krishnamurthy, B. Viswanathan, Res. Chem. Intermed. 2013, 39, 2565.
12. T. Inoue, A. Fujishima, K. Honda, Nature, 1979, 277, 637.
13. Z. Jiang, T. Xiao, V. L. Kuznetsov, P. P. Edwards, Phil. Trans. R. Soc. A, 2010, 368, 3343.
14. M. Halmann, Nature, 1978, 275, 115.
15. Y. Izumi, Coord. Chem. Rev. 2013, 257, 171.
16. M. Halmann, M. Ulman, B. A. Blajeni, Sol. Energy,1983, 31, 429.
17. B. A. Blajeni, M. Halmann, J. Manassen, Solar Energy, 1980, 25, 165.
18. K. Koci, L. Obalova, Z. Lancy, Chem. Papers, 2008, 62, 1.
19. P. Usubharatana, D. McMartin, A. Veawab, P. Tontiwachwuthikul, Ind. Eng. Chem. Res, 2006, 45, 2558.
20. V. Jeyalakshmi, R. Mahalakshmy, K.R. Krishnamurthy, B. Viswanathan, Indian J. Chem., Sect. A: Inorg., Bio-inorg., phys., Theor. Anal. Chem., 2012, 51, 1263

21. M. Pengfei Ji, Takeuchi and T M Cuong, J. Zhang, M. Matsuoka, M. Anpo, Res. Chem. Intermed, 2010, 36, 327.
22. Y. Yang, H. Zhong, C. Tian, Res Chem. Intermed, 2011, 37, 91.
23. C. M. Teh, A. R. Mohamed, J Alloys Compd, 2011, 509, 1648.
24. A. Zaleska, Recent Pat Engg,2008, 2, 157.
25. A. Fujishima, X. Zhang, D.A. Tryk, Surf Sci Rep, 2008, 63, 515.
26. M. Anpo and M. Takeuchi, J. Catal, 2003, 216, 505.
27. M. R. Hoffmann, S.T. Martin, W. Chi and W. Detlef, Chem Rev, 1995, 95, 69.
28. M. A. Malati, W. K. Wong, Surf. Tech, 1984, 22, 305.
29. B. Viswanathan, K. R. Krishnamurthy International Journal of Hydrogen Energy, 2012, Article ID 269654 (10pages)
30. K. Kocˇ, L. Obalova, L. Mateˇjova´, D. Placha´, Z. Lacny´, J. Jirkovsky´, O. Sˇolcova´, Appl. Catal. B: Environ. 2009, 89, 494.
31. G. Li, S. Ciston, Z. V. Saponjic, L. Chen, N. M. Dimitrijevic, T. Rajh, K. A. Gray, J. Catal., 2008, 253, 105.
32. M. Gopal, W. J. Moberly Chan, L. C. De Jonghe, J Mater Sci, 1997, 32, 6001.
33. S. Ito, S. Inoue, H. Kawada, M. Hara, M. Iwasaki, H. Tada, J Colloid Interf. Sci, 1999, 216, 59.
34. K. Terabe, K. Kato, H. Miyazaki, S. Yamaguchi, A. Imai, Y. Iguchi, Mater Sci, 1994, 29, 1617.
35. O. Ishitani, C. Inoue, Y. Suzuki, T. Ibusuki, J. Photochem. Photobiol A, 1993, 72, 269.
36. F. Saladin, L. Fross, I. Kamber, J. Chem. Soc. Chem. Commun., 1995, 533.
37. F. Saladin, I. Alxneit, J. Chem. Soc. Faraday Trans, 1997, 93, 4159.

38. S. Kaneco , Y. Shimizu, K. Ohta, T. Mizuno, J. Photochem. Photobiol. A: Chem. 1998, 115, 223.
39. K. Ikeue, H. Yamashita, M. Anpo, T. Takewaki, J Phys Chem B, 2001, 105,8350.
40. I.H. Tseng, W.C. Chang, J. C. S. Wu, Appl. Catal. B: Environ, 2002, 37, 37.
41. Y. Ku, W-H Lee, W-Y Wang,J. MolCatal. A: Chemical, 2004, 212, 191.
42. P. Pathak, M. J. Meziani, L. Castillo, Y. P. Sun, Green Chem.2005, 7, 667.
43. J. Hwang, J. Chang, S. Park, K. Ikeuen, M. Anpo, Topics in Catal, 2005, 35, 311.
44. S. S. Tan, L. Zou, E. Hu, Sci. Technol. Adv. Mater. 2007, 8, 89.
45. X-H. Xia, Z-J. Jia, Y. Yu, Y. Liang, Z. Wang, L-L. Ma, Carbon, 2007, 45,717.
46. K. Kocí, Martin Reli, O. Kozák, Z. Lacny, DanielaPlachá, PetrPraus, LucieObalov, Catal. Today (2010) doi:10.1016/j.cattod.2010.12.054
47. R. W. Matthews,S. R. McEvoy, J. Photochem. Photobiol.A: Chem, 1992, 66, 355.
48. K. Koˇcí, K. Zatloukalova, L. Obalova, S. Krejcikova, Z. Lacny, L. Capek, A. Hospodkova, O. Solcova, Chinese J. Catal., 2011, 32, 812.
49. J. Fan, E.Z. Liu, L. Tian, X.Y. Hu, Qi He, T. Sun, Am. Soc. Civil Eng., 2010, Doi:10.1061/(ASCE)EE.1943-7870.0000311.
50. Y. Liu, B. Huang, Y. Dai , X. Zhang, X. Qin ,M. Jiang, M. Whangbo, Catal. Commun, 2009, 11, 210.
51. T. Mizuno, K. Adachi, K. Ohta, A. Saji, J. Photochem. Photobiol. A: Chem. 1996, 98, 87.
52. H. Hori, K. Koike, Y. Suzuki, M. Ishizuka, J. Tanaka, K. Takeuchi, Y. Sasaki, J. Mol.Catal. A: Chem. 2002, 179, 1.

53. S. Kaneco, H. Kurimoto, K. Ohta, T. Mizuno, Akira, J. Photochem. Photobiol. A: Chem., 1997, 109, 59.
54. S. Kaneco, H. Kurimoto, Y. Shimizu, K. Ohta, T. Mizuno, Energy, 1999, 24, 21.
55. S. S. Tan, L. Zou, E. Hu,Catal. Today, 2006, 115, 269.
56. O. Ola, M. M. Maroto-Valer, J. Photochem. Photobiol. C:Photochem. Reviews, 2015, 24, 16.
57. T.V. Nguyen, J.C.S. Yu, Appl. Catal. A, 2008, 335, 112.
58. P. Du, J.T. Carneiro, J. A. Moulijn, G. Mul, Appl. Catal. A. 2008, 334, 119.
59. C. Perego, S. Peratello, Catal. Today, 1999, 52, 133.
60. P.S. Mukherjee, Ray, Chem. Eng. Technol., 1999, 22, 253.
61. T. Van Gerven, G. Mul, J. Moulijn, A. Stankiewicz, Chem. Eng. Process., 2007, 46, 781.
62. H. Lin, AIChE J., 2006, 52, 2271–2280.
63. R.D. Sun, A. Nakajima, I. Watanabe, T. Watanabe, K. Hashimoto, J. Photochem.Photobiol. A, 2000, 136, 111.
64. J. C. S. Wu, T.H. Wu, T. Chu, H. Huang, D. Tsai, Topic in Catal., 2008, 47, 131.
65. J.C.S Wu, H. M. Lin, C-H. Lai, Appl. Catal. A: Gen, 2005, 296, 194.
66. J. C. S. Wu, H.M. Lin, International J. Photoenergy, 2005, 7, 115.
67. J.C.S. Wu, Catal. Surv. Asia, 2009, 13, 30.
68. K. Sayama, H. Arakawa, J. Chem. Soc. Faraday Trans. 1997, 93, 1647.
69. M. Reli, M. Sihor, K. kočí, P. prau, O. kozák, L. obalová, GeoScience Engineering, 2012, LVIII, 34. ISSN 1802-5420.
70. J. D. Graham. N. I. Hammer, Handbook of climate change mitigation pp. 1755-1780. DOI 10.1007/978-1-4419-7991-9_46,

71. B. J. Liu, T. Torimoto, H. Yoneyama,J. Photochem. Photobiol. A: Chem.,1998, 113, 93.
72. B.J. Liu, T. Torimoto, H. Matsumoto,H. Yoneyama, J. Photochem. Photobiol. A: Chem., 1997, 108, 187.
73. G.R. Dey, J. Natural Gas Chem, 2007, 16, 217.
74. G.R. Dey, A. D. Belapurkar, K. Kishore, J. Photochem. Photobiol. A: Chem, 2004, 163, 503.
75. S. S. Tan, L. Zou, E. Hu, Sci. Technol. Adv. Mater. 2007, 8, 89.
76. K. Rajalakshmi, V. Jeyalakshmi, R. Mahalakshmy, K.R. Krishnamurthy, B. Viswanathan, Indian J. Chem., Sect. A: Inorg., Bio-inorg., phys., Theor. Anal. Chem., 2012, 51A, 411.
77. J. Pan, X. Wu, L. Wang, G. Liu, G. Qing (Max) Lu, H-M Cheng, Chem. Comm. 2011, 47, 8361.
78. W-NWang, W-J An, B. Ramalingam, S. Mukherjee,D. M. Niedzwiedzki, S. Gangopadhyay, P. Biswas, J. Am. Chem. Soc. 2012,134, 11276.
79. H. Xu, S. Ouyang, P. Li, T. Kako, J. Ye, ACS Appl. Mater. Interfaces, 2013, 5, 1348.
80. T. Wang, X. Meng, P. Li, S. Ouyang, K. Chang, G. Liu, Z. Mei, J. Ye, Nano Energy, 2014, 9, 50.
81. M. Halmann, E. KatzirBorgarello, J. Kiwi, Sol. Energy Mater., 1984, 10, 85.
82. Z. Goren, I. Willner, A. J. Nelson, J Phys Chem, 1990, 94, 3784.
83. K. Adachi, K. Ohta, T. Mizuno, Solar Energy, 1994, 53, 187.
84. H.Yamashita, H. Nishigushi,N. Kamada, M. Anpo, Res ChemInterm. 1994, 20, 815-823.
85. I-H. Tseng, J C S. Wu, H-Y. Chou, J. Catalysis, 2004, 221, 432.
86. Slamet, H W. Nasution, E. Purnama, S. Koesla, Gunlauardi, J Catalysis Commun., 2005, 6, 313.

87. T-V. Nguyen, J.C. S. Wu, Appl. Catalysis A:General 2008, 335, 112.
88. O.K. Varghese, M.Paulose,T. J. Latempa, C.A.Grimes, Nano Letters, 2009, 9, 731.
89. Q-H. Zhang, W-D. Han, Y-J. Hong, J-G. Yu,Catalysis Today, 2009, 148, 335.
90. K. Koci, K. Mateju, L. Obalova, S. Krejcikova, Z. Lacny, D. Placha, L.Capek, A.
    Hospodkova, O. Solcova, Appl. Catal. B: Environ., 2010, 96, 239.
91. J. C. S. Wu, C. W. Huang, Front. Chem. Eng. China 2010, 4, 120.
92. M. A. Asi, C. He, M. Su, D. Xia, L. Lin, H. Deng, Y. Xiong, R. Qui, X. Li, Catal. Today, 2011, 175, 256.
93. D. Luo, Y. Bi, W. Kan, N. Zhang, and S. Hong, J. Mol. Structure, doi: .1016/j. molstruc. 2011.03.044.
94. S. Qin, F. Xin, Y. Liu, X. Yin, W.Maa, J. Colloid &Surf.Sci., 2011, 356, 257.
95. J-J Chen, J. C. S. Wu, P. C. Wu, D. P. Tsai, J Phys Chem C, 2011, 115, 210.
96. X. Li, Z. Zongjin, W. Li, H. Pan, Appl. Catal. A: Gen. 2012, 429– 430, 31.
97. A. Cybula, M. Klein, A. Zielinska-Jurek, M. janczarek, A. Zaleska, Physicochem. Probl. Miner. Process. 2012, 48, 159.
98. Q. Zhang, T. Gao, J. M. Andino, Y. Li, Appl.catal. B: Environ., 2012, 123-124, 257.
99. W. Jing, T. Xin, Y. Tao, Z. Lin, Appl. Mech. Mater. 2011, 55, 1506.
100. L. Collado, P. Jana, B. Sierra, J.M. Coronado, P. Pizarro, D.P. Serrano, V.A. de la PenaO'Shea, Chem. Eng. J. 2013, 224, 128.
101. B. S. Kwak, K. Vignesh, N-K Park, H-J Ryu, J-I Baek, M Kang, Fuel 2015, 143, 570.

102. Y. Liu, S. Zhou, J. Li, Y. Wang, G. Jiang, Z. Zhao, B. Liu, X Gong, A. Duan, J. Liu, Y Wei, L. Zhang, Appl. Catal. B 2015, 168–169, 125.
103. C. Tang, W. Hou, E. Liu, X. Hu, J. Fan, J. Lumin. 2014, 154, 305.
104. O. Ola, M. M. Maroto-Valer, J. Catal. 2014, 309, 300.
105. S. Rani, N. Bao, S.C. Roy, Appl.Surf. Sci. 2014, 289, 203.
106. L. Matˇejová, K. Koˇcí, M. Reli, L. Capek, A. Hospodková, P. Peikertová, Z. Matˇej, L. Obalová, A. Wach, P. Ku´strowski, A. Kotarba, Appl. Catal B:Environ., 2014, 152-153, 172.
107. Y. Wang, Q. Lai,F. Zhang, X Shen, M. Fan, Y. He, S. Ren, RSC Adv. 2014, 4 (84) 44442.
108. Q. Li, L. Zong, C. Li, J. Yang, Appl. Surf. Sci. 2014, 314, 458–463.
109. M. Tahir, N.S. Amin, Appl. Catal. B:Environ., 2015, 162, 98.
110. G. Xi, S. Ouyang, J. Ye, Chem. Eur. J. 2011, 17, 9057.
111. W. Jiao, L. Wang,G. Liu, G. Qing (Max) Lu, H-M. Cheng, ACS Catal. 2012, 2,1854.
112. Q. Zhai, S. Xie, W. Fan, Q. Zhang, Y. Wang, W. Deng, Y. Wang, Angew. Chem. Int. Ed. 2013, 52, 5776.
113. D. Liu , Y. Fernandez , O. Ola , S. Mackintosh , M. Maroto-Valer, C. M. A. Parlett , A. F. Lee , J. C. S. Wu , Catal. Commun. 2012 , 25 , 78.
114. X. Meng, S. Ouyang, T. Kako, P. Li, Q. Yu, T. Wang, J. Ye Chem. Commun., 2014, 50, 11517.
115. I. Rossetti, A. Villa, C. Pirola, L. Prati. G. Ramis, RSC Adv., 2014, 4, 28883.
116. W. Tu, Y. Zhou, H. Li, P. Li, Z. Zou, Nanoscale, 2015, 7, 14232.
117. J. Y. Do, Y. Im, B. S. Kwak, J-Y. Kim, M. Kang, Chem. Eng. J. 2015, 275, 288.
118. M. Park, B. S. Kwak, S. W. Jo, M. Kang, Energy Conversion and Management., 2015, 103, 431.

119. H. Abdullah, M. R. Khan, M. Pudukudy, Z. Yaakob, N. A. Ismail, Journal Of Rare Earths, 2015, 33, 1155.

120. Q. Wang, P. Dong, Z. Huang, X. Zhang Chemical Physics Letters, 2015, 639, 11.

121. O. Ola, M. M. Maroto-Valer, Appl. Catal. A: General, 2015, 502, 114.

122. M. Manzanares, C. Fabrega, J. O. Osso, L. F. Vega, T. Andreu, J. R. Morante, Applied Catalysis B: Environ., 2014, 150– 151, 57– 62.

123. P.N. Paulino, V.M.M. Salim, N.S. Resende, Appl. Catal. B: Environ., 2015, doi:10.1016/j.apcatb.2015.12.037

124. J. Jiao, Y. Wei, Z. Zhao, W. Zhong, J. Liu, J. Li, A. Duan, G. Jiang, Catal. Today., 2015, 258, 319.

125. S. T. Hussain, K. Khan & R. Hussain, J Nat. Gas Chem, 2009, 18, 383.

126. Z, Zhao, J.Fan, J.Wang and R.Li, Catal. Commun., 2012, 21, 32.

127. X. Li, Z. Zhuang, W. Li, H. Pan, Appl. Catal. A: General., 2012, 429–430, 31.

128. Q. Zhang, Y. Li, E. A. Ackerman, M. Gajdardziska-Josifovska, H. Li, Appl. Catal. A: Gen., 2011, 400, 195–202.

129. B. Michalkiewicz, J. Majewska, G.Kądziołka, K. Bubacz, S. Mozia, A.W. Morawski, J. of CO_2 Utilization 2014, 5, 47.

130. S. Zhou, Y. Liu, J. Li, Y. Wang, G. Jiang, Z. Zhao, D. Wang, A. Duan, J. Liu, Y. Wei, Appl. Catal. B Environ., 2014, 158–159, 20.

131. T. Phongamwong, M. Chareonpanich, J. Limtrakul, Appl. Catal. B:Environ., 2015, 168–169, 114.

132. P.Pathak, M. J. Meziani, Y. Li, L.T. Cureton, Y-P Sun, Chem. Commun., 2004, 1234.

133. C. Wang, R.L Thompson,J.Baltrus, C.Matranga, J.Phys. Chem. Lett. 2010, 1, 48.

134. Y T. Liang, B K.Vijayan, K A.Gray, M C. Hersam, Nano Lett, 2011, 11, 2865.

135. X.Li, H. Liu, D. Luo, J.Li, Y.Huang, Y.Fang, Y.Xu, L.Zhu, Chem. Engg. Journal, 2012, 180, 151-158.

136. W. Kim, T. Seok, W. Choi, Energy Environ. Sci. 2012 , 5 , 6066 .

137. C. L. Zhang, Q. Y. Zhang , S. F. Kang, B. Li , X. Li , Y. G. Wang , ECS Solid State Lett. 2013, 2, M49 .

138. W. J. Ong, M. M. Gui, S. P. Chai, A. R. Mohamed , RSC Adv., 2013, 3, 4505 .

139. L. J. Liu, H. L. Zhao, J. M. Andino , Y. Li, ACS Catal2012, 2, 1817.

140. W. G. Tu, Y. Zhou, Q. Liu, S. C. Yan, S. S. Bao, X. Y. Wang, M. Xiao, Z. G. Zou, Adv. Funct. Mater. 2013, 23, 1743 .

141. M.Anpo, H. Yamashita, Y.Ichihashi, Y.Fujii, M. Honda, J Phys Chem B, 1997, 101, 2632.

142. H. Yamashita, Y. Fujii, Y. Ichihashi, S. G. Zhang, K. Ikeue, D. R. Park, K. Koyano, T. Tatsumi, M. Anpo, Catal Today, 1998, 45, 221.

143. N. Ulagappan, H. Frei, J. Phys. Chem. A, 2000, 104, 7834.

144. K. Ikeue, S.Nozaki, M. Ogawa, M. Anpo, Catal. Lett, 2002, 111.

145. Ulagappan, H.Frei, J. Phys. Chem. A, 2000, 104, 7834; W. Lin, H. Han H. Frei, J. Phys.Chem. B 2004, 108, 18269.

146. N. Sasirekha, S.J.S. Basha, K. Shanthi, Appl. Catal. B, 2006, 62, 169.

147. The-Vinh Nguyen, J.C.S. Wu, Solar Energy Mat. Solar cells, 2008, 92, 864.

148. Y. Li, W. Wang, Z. Zhan, M. Woo, C. Wu, P. Biswas, Appl. Catal B:Environ., 2010, 100, 386.

149. H. Li, Y. Lie, Y. Huang, Y. Fang, Y. Xu, L. Zhu, Z. Li, J. Nat. Gas Chem., 2011, 20, 145.

150. C-C. Yang, J. Vernimmen, V. Meynen, P. Cool and G. Mul, J. Catalysis, 2011, 284, 1.

151. W. Wang, J. Park, P. Biswas, Catal Sci. Technol., 2011, 1, 593.

152. H. C. Yang, H.Y.Lin, Y.S. Chien,J.C.S.Wu and H. H. Wu, Catal.Lett., 2009, 131, 381.

153. K. Koˇci, V. Mateˇjka, P. Kovar, Z. Lacny, L. Obalova, Catal. Today 2011, 161, 105.

154. C. Zhao, L. Liu, Q. Zhang, J. Wang, Y. Li, Catal. Sci. Technol., 2012, 2, 2558.

155. P. Akhter, M. Hussain, G. Saracco, N. Russo, Nanoscale Res. Lett. 2014, 9, 1.

156. M. Hussain, P. Akhter, G. Saracco, N. Russo, Appl. Catal. B: Environ., 2015, 170–171, 53.

157. J. Mao , T. Peng , X. Zhang , K. Li , L. Ye , L. Zan , Catal. Sci. Technol. 2013, 3, 1253.

158. Y. Liu, G. Ji, M. A. Dastageer, L. Zhu, J. Wang, B. Zhang, X. Chang, M. A. Gondal, RSC Adv., 2014, 4, 56961.

159. O. Ola, M. M. Maroto-Valer, Catal. Sci. Technol., 2014, 4, 1631.

160. L. Yuan, C. Han, M. Pagliaro, Y-J Xu, J. Phys. Chem. C, DOI: 10.1021/acs.jpcc.5b08893.

161. I Shown, H-C Hsu, Y-C Chang, C-H Lin, P Kumar Roy, A Ganguly, C-H Wang, J-K Chang, C-I Wu, L-C Chen, K-H Chen, Nano Lett. 2014, 14, 6097.

162. M. M. Gui, W. M. Ping Wong, S-P Chai, A. R. Mohamed, Chemical Engineering Journal 2015, 278, 272.

163. B. Tahir, M. Tahir, N. Saidina Amin, Appl. Surf. Sci., 2015, 338, 1.

164. L. L. Tan, W-J. Ong, S-P. Chai, A.R. Mohamed, Appl. Catal. B: Environ., 2015, 166–167, 251.

165. J-J Wang, Y-H. Jing, T. Ouyang, Q. Zhang, C-T Chang, Catal. Commun., 2015, 59, 69.
166. S. Won Jo, B. S. Kwak, K. M. Kim, J. Y. Do, N-K. Park, S. O Ryu, H-J Ryu, J-I Baek, M. Kang, Appl. Surf. Sci., 2015, 355, 891.
167. K. Sayama, H. Arakawa, J. Phys. Chem. 1993, 97, 531.
168. C.C. Lo, C.H. Hung, C.S. Yuan, J.F. Wu, Sol. Energy Mater. Sol. Cells, 2007, 91, 1765.
169. M. Subrahmanyam, S. Kaneco, N. Alonso-Vante, Appl. Catal B:Environ., 1999, 23, 169.
170. K. Teramura, T. Tanaka, H. Ishikawa, Y. Kohno, T. Funabiki, J. Phys. Chem. B., 2004, 108, 346.
171. K. Teramura, H. Tsuneoka, T. Shishido, T. Tanaka, Chem. Phys. Lett., 2008, 467, 191.
172. S. Yoshida, Y. Kohno, Catal. Surveys from Japan, 2000, 4, 107.
173. H. Park, J. H. Choi, K. M. Choi, D. K. Lee, J. K. Kang, J. Mater. Chem., 2012, 22, 5304.
174. X.Y. Chen, Y. Zhou, Q. Liu, Z. D. Li, J. G. Liu, Z. G. Zou, ACS Appl. Mater. Interfaces 2012, 4, 3372 .
175. Y. P. Xie, G. Liu, L. C. Yin, H. M. Cheng, J. Mater. Chem. 2012 , 22 , 6746 .
176. G. C. Xi, S. X. Ouyang, P. Li, J. H. Ye, Q. Ma, N. Su, H. Bai, C. Wang, Angew. Chem. Int. Ed. 2012, 51, 2395 .
177. L. Liu, C. Zhao, D. Pitts, H. Zhao, Y. Li, Catal. Sci. Technol., 2014, 4, 1539.
178. P. Niu, Y. Yang, J. C. Yu, G. Liu, H-M Cheng, Chem. Commun., 2014, 50, 10837.
179. M. Li, L. Zhang, X. Fan, Y. Zhou, M. Wu, J. Shi J. Mater. Chem. A, 2015, 3, 5189.

180. M. M. Gui, S-P Chai, B-Q. Xu, A. R. Mohamed RSC Adv., 2014, 4, 24007.

181. W-N. Wang, F. Wu, Y. Myung, D. M. Niedzwiedzki, H S Im, J Park, P Banerjee, P Biswas ACS Appl. Mater. Interfaces 2015, 7, 5685.

182. J-C Wang, L Zhang, W-X Fang, J Ren, Y-Yu Li, H-C Yao, J-S Wang, Z-J Li, ACS Appl. Mater. Interfaces 2015, 7, 8631.

183. B. Alotaibi, S. Fan, D. Wang, J. Ye, Z. Mi, ACS Catal. 2015, 5, 5342.

184. R. Zhou, M. I. Guzman J. Phys. Chem. C 2014, 118, 11649.

185. J. Lin, Z. Pan, X. Wang, ACS Sustainable Chem. Eng. 2014, 2, 353.

186. F. Ehsan, T. He, Applied Catalysis B: Environ., 2015, 166–167, 345.

187. Y. Matsumoto, M. Obata, J. Hombo, J. Phy. Chem., 1994, 98, 2950.

188. G. Guan, T. Kida, A. Yoshida, App. Catal., B:Environ., 2003, 41, 387.

189. G. Guan, T. Kida ,T. Harada, M. Isayama, A.Yoshida, App. Catal. A: Gen. 2003, 249, 11.

190. K. Teramura, H. S-I. Okuoka, H. Tsuneoka, T. Shishido, T. Tanaka, Appl. Catal. B: Environ., 2010, 96, 565.

191. Y. Zhou, Z. Tian, Z. Zhao, Q. Liu, J. Kou, X. Chen, J. Gao, S. Yan, Z. Zou, ACS Appl. Mater. Interfaces, 2011, 3, 3594.

192. H. Shi, T. Wang, J. Chen, C. Zhu, J. Ye, Catal Lett, 2011, 141, 525.

193. Peng Li, S. Ouyang, G. Xi, T. Kako, J. Ye, J. Phys. Chem. C, 2012, 116, 7621.

194. N. Zhang, S. Ouyang, T. Kako, J. Ye, Chem. Commun., 2012, 48, 1269-1271.

195. K. Iizuka, T. Wato, Y. Miseki, K. Saito, A. Kudo, J. Am. Chem. Soc. 2011, 133, 20863.

196. C. W. Tsai, H. M. Chen, R. S. Liu, K. Asakura, T. S. Chan, J. Phys. Chem. C, 2011, 115, 10180.

197. D.S. Lee, H. J. Chen, Y. W. Chen, J. Phys. Chem. Solids 2012, 73, 661.
198. X. Li, H. Pan, W. Li, Z. Zhuang, Appl. Catal. A: Gen, 2012, 413– 414, 103.
199. A. Ahmed , Y. Shibata ,T. Taniguchi T, Izumi, J. Catal. 2011, 279, 123.
200. Q.D. Truong, J. Y. Liu, C. C. Chung, Y. C. Ling, Catal. Commun., 2012, 19, 85.
201. J. W. Lekse, M. K. Underwood, J. P. Lewis, C. Matranga, J. Phys. Chem. C, 2012, 116, 1865.
202. X. Li, W. Li, Z. Zhuang, Y. Zhong, Q. Li, L. Wang, J. Phys. Chem. C. 2012, DOI:10.1021/jp303365z.
203. W-H Lee, C-H Liao, M-F Tsai, C-W Huang, J. C.S. Wu, Appl. Catal. B:Environ., 2013, 132, 445.
204. Y-H Cheng, V-H Nguyen, H-Y Chan, J.C.S. Wu, W-H. Wang, Appl. Energy, 2015, 147, 318.
205. K. Xie, N. Umezawa, N. Zhang, P. Reunchan , Y. Zhang , J. Ye, Energy Environ. Sci. 2011 , 4 , 4211.
206. D. D. Sui, X. H. Yin, H. Z. Dong, S. Y. Qin, J. S. Chen, W. L. Jiang, Catal. Lett. 2012, 142, 1202 .
207. H. Zhou, J. J. Guo, P. Li, T. X. Fan, D. Zhang, J. H. Ye , Sci. Rep. 2013, 3, 1667.
208. P. Li, Y. Zhou, W. G. Tu, Q. Liu, S. C. Yan, Z. G. Zou, Chem Plus-Chem, 2013, 78, 274 .
209. S. Feng, X. Chen, Y. Zhou, W. Tu, P. Li, H. Li , Z. Zou, Nanoscale 2014, 6, 1896.

210. P. Li, Y. Zhou, W. G. Tu , R. Wang, C. F. Zhang, Q. Liu, H. J. Li, Z. D. Li, H. Dai, J. J. Wang, S. C. Yan, Z. G. Zou, Cryst. Eng. Comm.,2013 , 15 , 9855 .

211. H. F. Cheng, B. B. Huang, Y. Y. Liu, Z. Y. Wang, X. Y. Qin, X. Y. Zhang, Y. Dai, Chem. Commun.,2012 , 48 , 9729 .

212. J. J. Guo, S. X. Ouyang, T. Kako, J. H. Ye, Appl. Surf. Sci. 2013, 280, 418 .

213. S.C. Yan, S.X. Ouyang, J. Gao, M. Yang, J.Y. Feng, X.X. Fan, L.J. Wan, Z.S. Li, J.H. Ye, Y. Zhou, Z.G. Zou, Angew. Chem. Int. Ed., 2010, 49, 6400.

214. S. C. Yan, J. J. Wang, H. L. Gao, N. Y. Wang, H. Yu, Z. S. Li, Y. Zhou, Z. G. Zou, Adv. Funct. Mater. 2013, 23, 758.

215. S. Yan, H. Yu, N. Wang, Z. Li, Z. Zou, Chem. Commun., 2012 , 48 , 1048

216. Q. Liu, Z. X. Low, L. X. Li, A. Razmjou, K. Wang, J. F. Yao, H. T. Wang, J. Mater. Chem. A. 2013, 1, 11563 .

217. Q. Liu, Y. Zhou, Z. P. Tian, X. Y. Chen, J. Gao, Z. G. Zou, J. Mater. Chem. 2012, 22, 2033.

218. S. C. Yan, J. J. Wang , H. L. Gao, N. Y. Wang, H. Yu, Z. S. Li, Y. Zhou, Z. G. Zou, Adv. Funct. Mater. 2013, 23, 1839 .

219. Q. Liu, Y. Zhou, Y. Ma, Z. G. Zou, RSC Adv. 2012, 2, 3247 .

220. Z. D. Li, Y. Zhou, J. Y. Zhang, W. G. Tu, Q. Liu, T. Yu, Z. G. Zou, Cryst. Growth. Des. 2012, 12, 1476 .

221. K. Teramura, S. Iguchi, Y. Mizuno, T. Shishido, T. Tanaka, Angew Chem. Int. Ed. 2012, 51 , 8008 .

222. N. Ahmed, M. Morikawa, Y. Izumi, Catal. Today. 2012, 185, 263 .

223. K. Li, A. D. Handoko, M. Khraisheh, J. Tang, Nanoscale, 2014, 6, 9767.

224. C. Zhao, L. Liu, G. Rao, H. Zhao, L. Wang, J. Xua, Y. Li, Catal. Sci. Technol., 2015, 5, 3288.
225. P. Zhou, S. C. Yan, Z. G. Zou, CrystEngComm, 2015, 17, 992.
226. Z. Wang, M. Jiang, J. Qin, H. Zhou, Z. Ding, Phys. Chem. Chem. Phys., 2015, 17, 16040.
227. S. Zhu, S. Liang, J. Bi, M. Liu, L. Zhou, L. Wu, X. Wang, Green Chem. 2015, DOI: 10.1039/C5GC02308D.
228. H. Zhou, P. Li, J. Guo, R. Yan, T. Fan, D. Zhang, J. Ye, Nanoscale, 2015, 7, 113.
229. X. Chen, J. Wang, C. Huang, S. Zhang, H. Zhang, Z. Li, Z. Zou, Catal. Sci. Technol., 2015, 5, 1758.
230. S. Wang, Y. Hou, X. Wang ACS Appl. Mater. Interfaces 2015, 7, 4327.
231. W. Kim, H. Frei, ACS Catal. 2015, 5, 5627.
232. Y. Bi, M. Fahad Ehsan, Y. Huang, J. Jin, T. He, J. of CO_2 Utilization, 2015, 12, 43.
233. B. S. Kwak, M. Kang, Appl. Surf. Sci., 2015, 337, 138.
234. S. K. Parayil, A. Razzaq, S-M. Park, H. R. Kim, C. A. Grimes, S-Il In, Appl.Catal. A: General, 2015, 498, 205.
235. J. Premkumar, R. Ramaraj, J. Photochem. & Photobiol A:Chem., 1997, 110, 53.
236. O. Ozcan, F. Yukruk, E.U. Akkaya, D. Uner, Applied Catalysis B: Environ., 2007, 71, 291.
237. T.-V. Nguyen, J. C. S. Wu and C-H.Chiou, Catal. Commun., 2008, 9, 2073.
238. Z. Zhao, J. Fan, S. Liu, Z. Wang, Chem. Eng. Journal, 2009, 151, 134.
239. Z. Zhao, J. Fan, M. Xie&Z.Wang, J Cleaner Prodn, 2009, 17, 1025.
240. K.R. Thampi, J. Kiwi, M. Graetzel, Nature 1987, 327 (6122), 506.

241. O. Ozcan, F. Yukruk, E.U. Akkaya, D. Uner, Appl. Catal. B Environ., 2007, 71, 291.

242. G. Qin, Y. Zhang, X. Ke, X. Tong, Z. Sun, M. Liang, S. Xue, Appl. Catal. B:Environ., 2013, 129, 599.

243. T. Arai, S. Sato, T. Morikawa, Energy Environ. Sci., 2015, 8, 1998.

244. K. Li, L. Lin, T. Peng, Y. Guo, R. Li, J. Zhang, Chem. Commun., 2015, 51, 12443.

245. L. Schmidt-Mende, J. K. Stolarczyk, S. N. Habisreutinger, Angew. Chem. Int. Ed. 2013, 52, 7372.

246. N.M. Dimitrijevic, B. K.Vijayan, O. G. Poluektov, T. Rajh, K. A. Gray, H. He, P. Zapol, J. Amer. Chem. Soc., 2011, 133, 3964.

247. K. Kocˇ, L. Obalov, O. Sˇ olcov, Chem. Process Eng. 2010, 31, 395.

248. M. Anpo, H. Yamashita, Y. Ichihashi,S. Ehara, J. Electroanal.Chem., 1995, 396,21.

249. C-C. Yang, J. Vernimmen, V. Meynen, P. Cool, G. Mul, J. Catalysis, 2011, 284, 1; C-C. Yang, Ph.D Thesis, University of Twente, Twente, The Netherlands 2011.

250. S. S. Tan, L. Zou, E.Hu, Catal. Today, 2008, 131, 125.

251. I. A. Shkrob, N. M. Dimitrijevic, T. W. Marin, H. He, P. Zapol, J. Phys. Chem. C, 2012, 116, 9461.

252. I. A. Shkrob, T.W. Marin, H. He, P. Zapol, J. Phys. Chem. C 2012, 116, 9450.

253. M.R. Hoffmann, J.A. Moss, M.M. Baum, Dalton Trans. 2011, 40, 5151.

254. G. Palmisano, E. Garcı´a-Lo´ pez, G. Marcı´, V.Loddo, S. Yurdakal, V. Augugliaro, L.Palmisano, Chem. Comm., 2010, 46, 7074.

255. K. Li, D. Martin, J. Tang, Chinese J. Catal., 2011, 32, 879.

256. J. Ye , Z. Zou, H. Arakawa, M. Oshikiri, M. Shimoda, A. Matsushita, T. Shishido, J. Photochem.&Photobiol. A: Chemistry, 2002, 148, 79.
257. W. Junhu , Z. Zhigang , Ye. Jinhua, J. Alloys and Compds., 2004, 377, 248.
258. Q. Xiang, J. Yu, M. Jaroniec, Chem. Soc. Rev., 2012, 41, 782.
259. M-Q Yang, Y-J. Xu, Phys. Chem. Chem. Phys., 2013, 15, 19102.
260. M-Q Yang, N. Zhang, M. Pagliaro, Y-J. Xu, Chem. Soc. Rev., 2014, 43, 8240.
261. X. Xie, K. Kretschmer, G. Wang, Nanoscale, 2015, 7, 13278
262. W. Kim, T. Seok and W. Choi, Energy Environ. Sci., 2012, 5, 6066.
263. J. Morris, G. J. Meyer and E. Fujita, Acc. Chem. Res., 2009, 42, 1983.
264. G. Seshadri, C. Lin and A. B. Bocarsly, J Electroananl. Chem, 1994, 372, 145.
265. Ganesh, Mater Sci. and Applns., 2011, 2, 1407.
266. Y.R. Smith, V. Subramanian, B. Viswanathan,“ Photo-electrochemical and Photocatalytic conversion of carbon dioxide, Chapter 9, in “Photo-electrochemistry and photobiology for sustainability”, 2010, 1, 217. (Eds. S. Kaneco, B. Viswanathan and H Katsumata), Bentham Science.

CHAPTER 2

EXPERIMENTAL METHODOLOGY

2.1 Chemicals used

Titanium tetrakis (butoxide), Hexa chloro platinic acid, Nickel(II) nitrate hexa hydrate, Copper(II) nitrate hexa hydrate, Magnesium nitrate hexa hydrate, Ruthenium (III) chloride, Iron (III) oxide, Gold (III) chloride hydrate and Sepiolite clay were obtained from Sigma Aldrich. Tantalum (V) oxide was purchased from Alfa Aesar. Silver nitrate, Strontium nitrate anhydrous were procured from SD fine chemicals. Lanthanum oxide was procured from Loba chemie. P25 (commercial TiO_2) was obtained from Evonik, Germany. Hombikat UV 100 (commercial TiO_2-anatase) was supplied by M/s Sachtleben, Germany. Urea and Thiourea were purchased from Merck. All other chemicals used in the investigation were of analytical (AR) grade and were obtained from Sisco Research Laboratories Pvt. Ltd. or S.D. Fine Chemicals, India.

2.2 Preparation of catalysts

2.2.1 Preparation of meso porous titanium dioxide

Meso-porous titanium dioxide was prepared by hydrothermal method [1]. In a typical synthesis, titanium glycolate formed in the first step was subjected to by hydrothermal treatment. Titanium glycolate precursor was synthesized by the addition of 4.26 mL Titanium tetrakis (butoxide) into a 14 mL of ethylene glycol kept in a 100 mL flask with continuous stirring, under inert atmosphere by bubbling nitrogen for about 30 min. to remove moisture from the reaction mixture. Then the flask was sealed and kept stirring for 12 h at room temperature. The resulting mixture was poured into a 200 mL of acetone (2% water in acetone solution) and stirred for an hour. The obtained white precipitate was centrifuged and washed with ethanol. The resulting white sample was dried at 50 ºC to get titanium glycolate powder.

$$\mathbf{Ti(OBu)_4 + 2HOCH_2CH_2OH \longrightarrow Ti(OCH_2CH_2O)_2 + 4HOBu}$$

1g of titanium glycolate powder was dispersed in 80 mL of water under ultrasonication. The resulting mixture was transferred into a teflon lined autoclave and kept in an oven at 180^0 C for 4h. The resulting product was washed with water followed by ethanol and dried at 60^0 C. The obtained mesoporous titanium dioxide was denoted as TiO_2-MP in subsequent discussions.

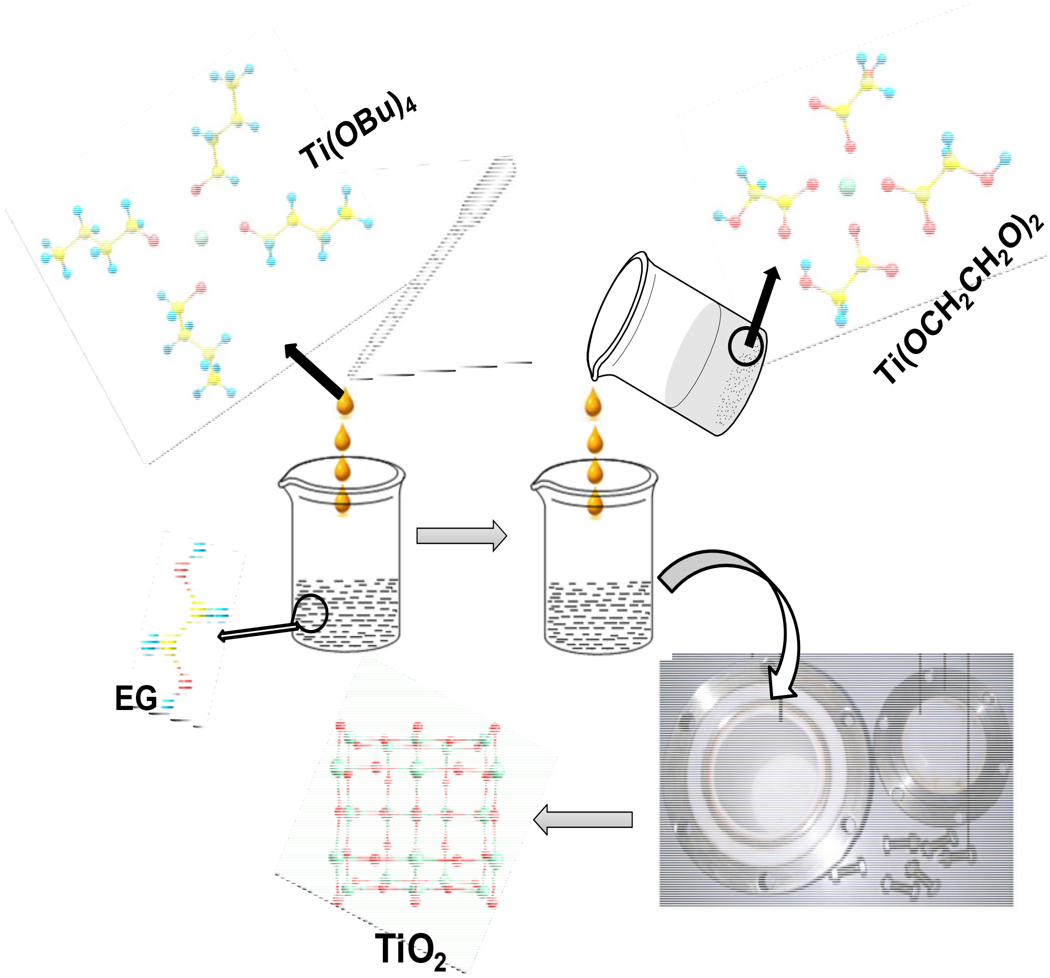

● - Titanium, ● - Oxygen, ● - Carbon, ● - Hydrogen.

Scheme 2.1 Flowchart representation for the synthesis of meso-porous titanium dioxide

2.2.2 Preparation of doped meso-porous titania

Similar procedure was followed for titanium glycolate synthesis as mentioned in the above method [1]. Then, urea or thio-urea (2 moles in each case) as precursors for N doping and N-S co-doping were introduced along with titanium glycolate prior to hydrothermal treatment to get N doped and N-S co-doped TiO_2-MP samples.

2.2.3 Preparation of doped titania-P-25

N doped or N-S co-doped TiO_2-P25 were prepared by dispersing the pristine sample in aqueous solutions of urea or thiourea, dried at 100 °C followed by calcination in air at 300 ºC for 2 h and denoted as N/P25 and N-S/P25.

2.2.4 Preparation of meso Fe-N-S/TiO_2 supported on sepiolite

Sepiolite was dry ground for 30 min. to get fine particles and avoid structural alteration. Fe-N-S tri-doped meso-porous TiO_2 was synthesized by adopting the method as described in Section 2.2.1. To the prepared titanium glycolate powder, thiourea as N-S precursor and iron(III) oxide as Fe precursor were added prior to the hydrothermal treatment to get Fe-N-S tri-doped meso- porous TiO_2 and denoted as FNST. To prepare FNST/sepiolite with different loading of FNST, appropriate amounts of FNST precursors and sepiolite were added to titanium glycolate prior to hydrothermal treatment to get 10%, 25%, 50%, 75% FNST loaded on sepiolite.

2.2.5 Preparation of $NaTaO_3$ and modification with La

$NaTaO_3$ and 2.0% (w/w) lanthanum promoted catalysts were prepared by hydrothermal route [2, 3]. To prepare $NaTaO_3$, 0.6 g of NaOH dissolved in 20 mL of water (0.75M) and 0.442 g of Ta_2O_5 were added into a teflon lined stainless steel autoclave. After hydrothermal treatment at 140 °C for 12 h, the precipitate was collected, washed with deionized water and ethanol, finally several times with water and dried at 80 °C for 5 h.

La modified $NaTaO_3$ ($Na_{(1-x)}La_xTaO_{(3+x)}$ with x= 0.00014 for 2.0% w/w of La) was prepared by the same procedure, by adding 0.0117 g of La_2O_3 along with NaOH and Ta_2O_5 in the autoclave.

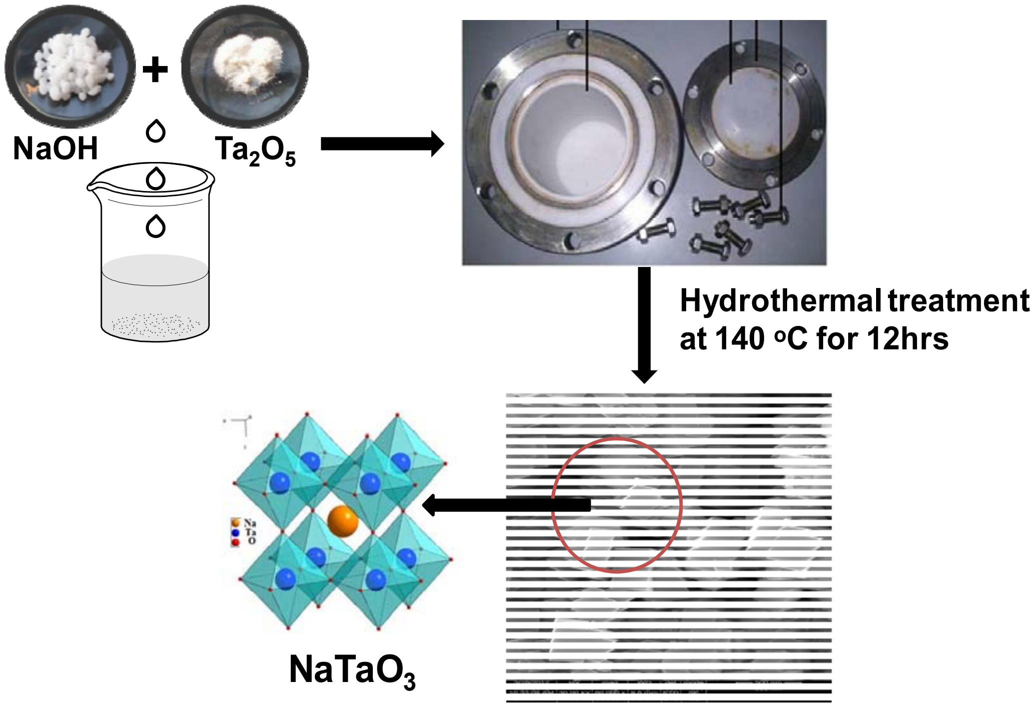

Scheme 2.2 Flowchart representation for the synthesis of $NaTaO_3$

2.2.6 Preparation of $Na_{(1-x)}La_xTaO_{(3+x)}$ loaded with different co-catalysts

NiO (0.2% w/w) as co-catalyst was loaded on to the synthesized $Na_{(1-x)}La_xTaO_{(3+x)}$ powder by wet impregnation from an aqueous solution of $Ni(NO_3)_2$. $6H_2O$, dried at 100 °C followed by calcination in air at 270 °C for 2 h. Loading of La and NiO was based on the optimization study carried out by Kato et.al. [4]. Similarly, 0.15 w/w% Pt (as H_2PtCl_6) and 1% w/w each of Au (as $HAuCl_4$), Ag (as $AgNO_3$), CuO (as $Cu(NO_3)_2.6H_2O$) and RuO_2 (as $RuCl_3.$ XH_2O) were loaded on $Na_{(1-x)}$ $La_xTaO_{(3+x)}$ by wet impregnation and dried. Pt and Au salts were reduced in hydrogen at 450 °C and 200 °C for 2 h respectively, prior to use. Ag, RuO_2 and CuO loaded samples were calcined in air at 300 °C.

2.2.7 Preparation of Fe-N modified $Na_{(1-x)}La_xTaO_{(3+x)}$

In order to ensure the incorporation of Fe and N into the tantalate lattice, the respective precursors were added to La_2O_3 and Ta_2O_5 dispersed on NaOH solution prior to hydrothermal treatment. Rest of the preparation steps was the same as in

Section 2.2.5. The same procedure was adopted for doping of N and Fe separately and for co-doping N & Fe. Fe_2O_3 and urea were added as precursors for iron and nitrogen respectively.

2.2.8 Loading of MgO on Fe-N/$Na_{(1-x)}La_xTaO_{(3+x)}$

$MgO/Na_{(1-x)}La_xTa_{(1-y)}Fe_yO_{(3-z)}N_z$ was prepared by impregnation method [5]. Briefly, appropriate amount (0.3 wt%, 0.5 wt%, 1 wt%) MgO as $Mg(NO_3)_2.6H_2O$ was dissolved in water, followed by 1g of $Na_{(1-x)}La_xTa_{(1-y)}Fe_yO_{(3-z)}N_z$ (Fe-N/NTO) support with stirring. The resulting mixture was dried and calcined in air at 500 ºC for 4hr, denoted as MgO/FeN-NTO.

2.2.9 Preparation of CoTPP sensitized $Na_{(1-x)}La_xTaO_{(3+x)}$

5,10,15-20-Tetra phenyl porphinato cobalt(II), (CoTPP) was synthesised using reported procedures [6, 7]. $Na_{(1-x)}La_xTaO_{(3+x)}$ was synthesized using the procedure described in Sec. 2.2.5.

1.0 w/w%-CoTPP / $Na_{(1-x)}La_xTaO_{(3+x)}$ composite was prepared by adopting previous report [8]. Briefly, 10 mg of CoTPP was dissolved in 20 mL of ethanol, followed by 1g of $Na_{(1-x)}La_xTaO_{(3+x)}$ support with stirring. The resulting solution was refluxed at 80 °C for 130 min. The solvent was removed by evaporation under vacuum and the solid sample was dried at 60 ºC for 6h.

2.2.10 Preparation of $Sr_3Ti_2O_7$ and doping with N, S & Fe

Neat $Sr_3Ti_2O_7$ was prepared by adopting polymer complex method, (Pechini's method) reported by Yoshino et al [9] after some modifications at our end. Ethylene glycol and methanol ratio and pH of the medium were further optimized to get phase pure $Sr_3Ti_2O_7$. Titanium tetra butoxide (2 moles) was added to a mixture of ethylene glycol and methanol (1:2 mole ratio) with vigorous stirring. To this mixture, citric acid (to get 1:0.5 mole ratio of ethylene glycol : citric acid) and strontium nitrate (3 moles as per the stoichiometry) were added. Heating the mixture at 130 °C for 20 h resulted in a polymer complex gel, which was pyrolized in air at 350 °C, followed by calcination at 900 °C for 2 hrs. Urea or thio-urea (2 moles in each case) as precursors for N doping and N-S co-doping and Fe_2O_3 powder (3wt% of Fe with respect to $Sr_3Ti_2O_7$) as such, were introduced along with strontium nitrate, prior to polyester formation to obtain doped $Sr_3Ti_2O_7$. Doped catalysts are represented by the general formulae-$Sr_3Ti_2O_7$ (neat), $Sr_3Ti_2O_{(7-x)}N_x$, $Sr_3Ti_{(2-x)}S_xO_{(7-y)}N_y$, $Sr_3Ti_{(2-x)}Fe_xO_7$, $Sr_3Ti_{(2-x)}Fe_xO_{(7-y)}N_y$, $Sr_3Ti_{(2-x-y)}Fe_xS_yO_{(7-z)}N_z$ signifying different dopant compositions.

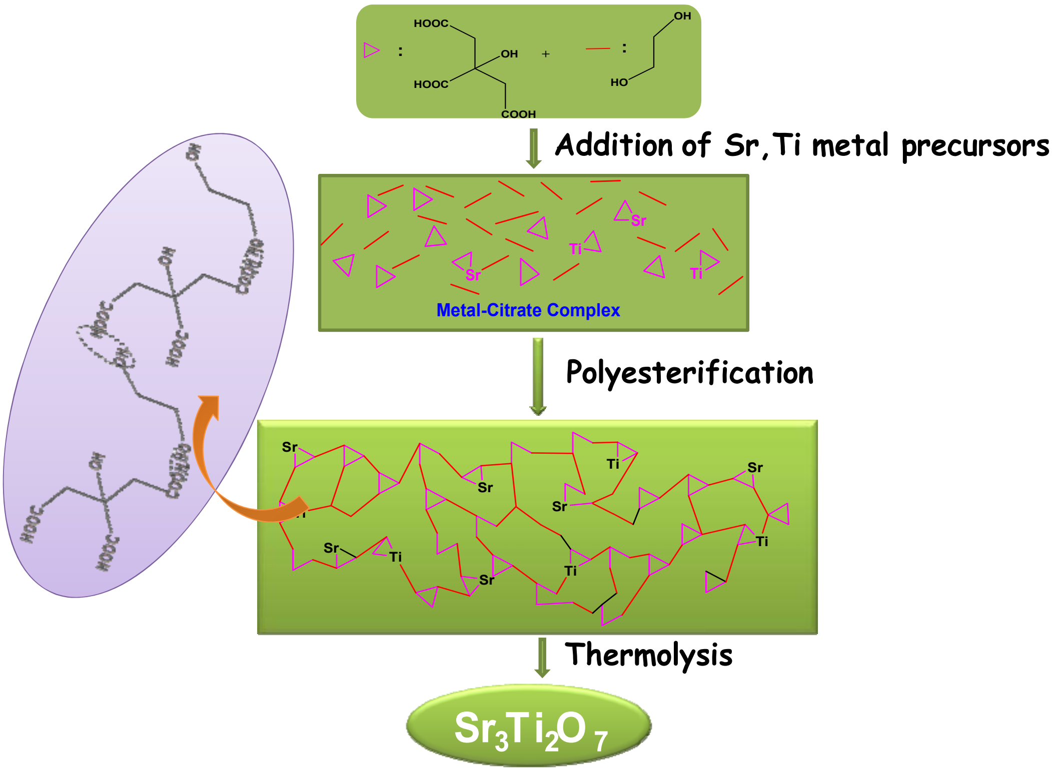

Scheme 2.3. Flowchart representation for the synthesis of $Sr_3Ti_2O_7$ by Polymerized Complex Method.

2.3 Characterization of catalysts

2.3.1 X- Ray Diffraction

The crystal phase of the catalysts was analysed by X-ray diffractometer (Rigaku-MiniFlex-II) using Cu Kα radiation (λ=1.54056 Å) in the scan range of 2θ = 5-90° at a speed of 3°/min. The crystallite sizes were calculated by the Scherrer's formula, $t = K\lambda/\beta \cos\theta$, where t is the crystallite size, K is the constant dependent on crystallite shape (0.9 for this case) and λ = 1.54056 Å, β is the FWHM (full width at half maximum) and θ is the Bragg's angle.

The phase composition of TiO_2 was analyzed using the relative peak intensity of anatase and rutile and using the formula, $FA = 1/ [1+1.26(I_R/I_A)]$, where IR – Intensity of Rutile peak, IA – Intensity of Anatase peak.

Lattice parameters for the catalyst having tetragonal crystal system were calculated using the formula

$1/d^2 = [h^2+k^2]/a^2 + l^2/c^2$,

Lattice parameters for the catalyst having orthorhombic crystal system was calculated using the formula

$1/d^2 = h^2 / a^2 + k^2 / b^2 + l^2 / c^2$

where h, k, l are miller indices, d is the inter planar distance and a, b, c are lattice parameters.

2.3.2 DRS UV- Visible Spectroscopy

Diffuse reflectance absorption spectra of the catalysts in the UV-Visible region were recorded using a Thermo Scientific Evolution 600 spectrophotometer equipped with a Praying Mantis diffuse reflectance accessory.

2.3.3 Photoluminescence Spectroscopy

Photoluminescence spectra were recorded under the excitation with a 450W Xenon Lamp and the spectra were collected using JobinYvon Fluorolog-3-11 spectro fluorimeter.

2.3.4 Surface Area measurement

Surface area and pore volume of the catalysts were measured using Micromeritics ASAP 2020. Samples were degassed at 373 K for 2 h and at 423 K for 3 h. Pure nitrogen at liquid nitrogen temperature (77K) was used.

Assuming spherical morphology of the synthesised materials, the average crystallite size values can be calculated from surface area measurements using the formula,

$SA = 6 * 10^3/ (L * Density)$

Where SA – Surface area

L – Particle size

Density of the Anatase - 3.84 g cm^{-3}

2.3.5 Transmission electron microscopy

Transmission electron micrographs were recorded using JEOL 3010 model. Few milligrams of the samples (1-2 mg) were dispersed in few mL (1-2 mL) of ethanol by ultra-sonication for 15 minutes and a drop of the dispersion was placed on a carbon coated copper grid and allowed to dry in air at room temperature.

2.3.6 Scanning Electron Microscopy

Scanning electron micrographs were recorded using FEI, Quanta 200, equipped with EDXA attachment for elemental analysis. The samples in the powder form were taken on the carbon tape and mounted on the SEM sample holder.

2.3.7 X-Ray photoelectron spectroscopy

The X-ray photoelectron spectra of the catalysts were recorded using Omicron Nanotechnology instrument with Mg Ka radiation. The base pressure of the analysis chamber during the scan was 2×10^{-10} millibar. The pass energies for individual scan and survey scan are 20 and 100 eV, respectively. The spectra were recorded with step width of 0.05 eV. The data were processed with the Casa XPS program (Casa Software Ltd, UK), and calibrated with reference to the adventitious carbon peak (284.9 eV) in the sample. Peak areas were determined by integration employing a Shirley-type background. Peaks were considered to be a 70:30 mix of Gaussian and Lorentzian functions. The relative sensitivity factors (RSF) were obtained from literature.

2.3.8 Temperature Programmed Desorption

CO_2-TPD profile was recorded by Micromeritics chemisorb 2750 TPD unit. Few milligrams of samples were heated to 600 ºC at the rate of 20 ºC/min in 30 mL of high pure Helium flow. Pretreatment was continued for 1h at 600 ºC and then cooled to 30 ºC in helium flow. Gas changed to 10.2% CO_2 in Helium at the rate of 30 mL/min flow. CO_2 adsorbed for 30 min. at 30 ºC. Gas changed to Pure Helium (30ml/min) and physisorbed CO_2 is removed for stable baseline status. CO_2-TPD started from 30 ºC to 600 ºC.

2.3.9 Raman Spectroscopy Analysis

Raman spectra of the prepared catalyst were measured by using Bruker RFS27 operating with 1064 nm line of Nd:YAG Laser source in rock solid interferometer in the range of 100–800 cm^{-1} using liquid nitrogen cooled germanium detector with the resolution of 2 cm^{-1}.

2.4 Photo catalytic activity

2.4.1 Photo catalytic reduction of carbon dioxide with water

Activity of the catalysts in UV visible region (300-700 nm) was evaluated in batch mode, using jacketed, all glass reactor (620 ml), shown in Fig. 2.1, fitted with quartz window (5 cm dia) and filled with 400 ml of aqueous 0.2 N NaOH solution. Besides increasing the solubility of CO_2, alkaline water acts as hole scavenger. 0.4 g of catalyst was dispersed in the alkaline solution with vigorous stirring (400 rpm). Increasing the stirring rate beyond 400 rpm did not increase the conversion, indicating that under the present experimental conditions, the mass transfer limitations are overcome at this speed. Aqueous alkaline solution (pH 13.0) was saturated with CO_2 by continuous bubbling for 30 min. after which pH reduced to 8.0. In order to remove trace amounts of hydrocarbon and moisture in the CO_2 cylinder, the CO_2 gas was passed through molecular sieve and activated carbon before purging CO_2 into the reaction mixture. Reactor in-let and out-let valves were then closed and irradiation with Hg lamp with 77W power (from WACOM HX-500 lamp house) was started.

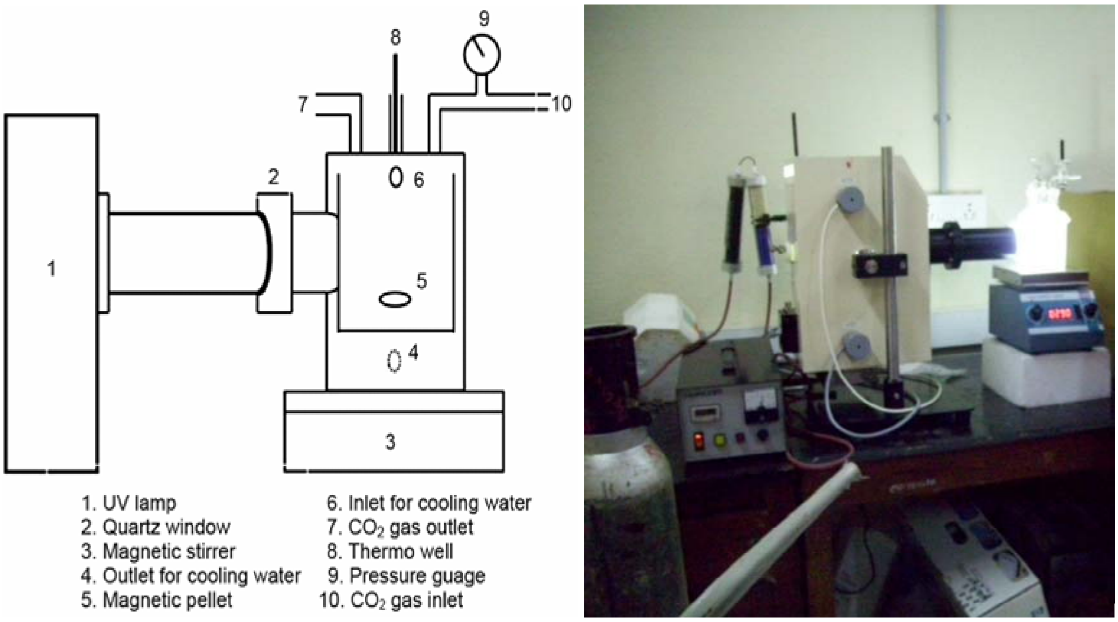

Fig. 2.1 Schematic diagram and photograph of the photo reactor

The intensity of the lamp was measured by lux meter and it was found to be 77000 lux which was then converted into Watts with the help of the spectral distribution of the lamp. Using fibre optics spectra analyzer (Ocean optics), the spectral distribution of Hg lamp was found.

Blank experiments (reaction with irradiation without catalyst and reaction in dark with catalyst) were conducted to ensure that the products formed were only due to photo reduction of CO_2. When the solution with dispersed catalyst was purged, saturated with nitrogen and irradiated very small quantities of hydrocarbons, possibly due to the conversion of residual carbon on catalyst surface, was observed up to certain period of time depends on the surface carbon impurities, after which no product could be detected. Based on these observations, with each catalyst composite, the solution saturated with nitrogen was first irradiated for 12 h to remove hydrocarbons formed from carbon residues and then saturated with CO_2 so that photo catalytic reduction of CO_2 on clean catalyst could be followed further for 20 h.

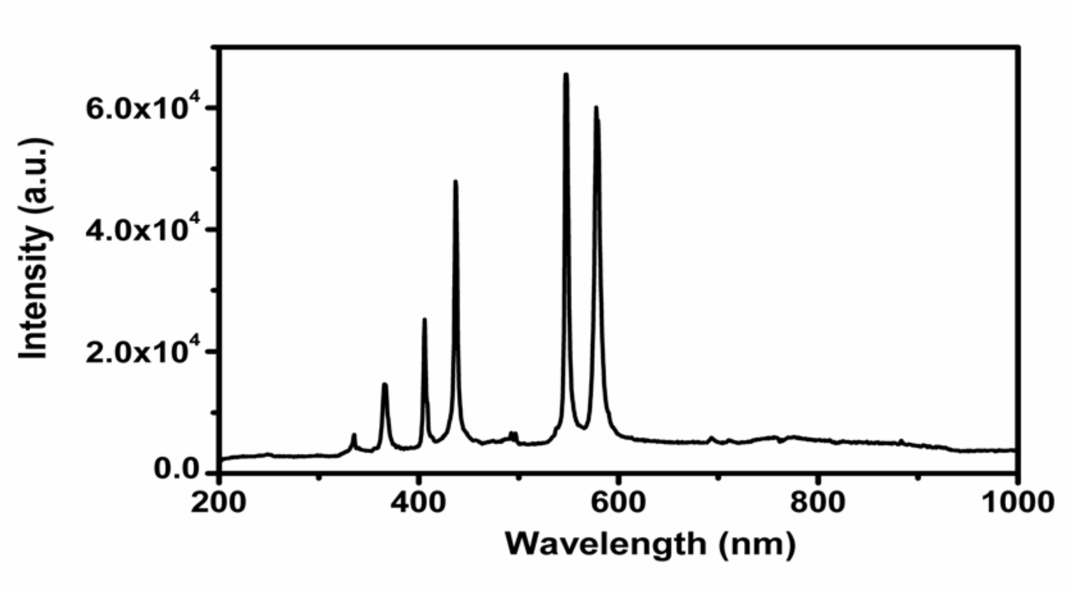

Fig. 2.2 Spectral distribution of Mercury Lamp

Gas and liquid phase samples were taken out at periodic intervals with gas-tight/liquid syringes and analyzed by GC. Liquid phase products (hydrocarbons) were analysed on PoroPlot Q capillary column with FID and gas phase products on Molecular Sieve 13X column with TCD.

The products were analyzed using Clarus 580 Perkin Elmer Gas chromatography - using Poroplot Q, 30 m and the detector is FID.

Injector Temperature: 250 °C

Column Temperature: 150 °C isothermal, Hold – 20 min

Detector Temperature: 250 °C

Carrier Gas: Nitrogen, 1.5 mL/min.

All the standard gas such as Methane (10 % in N_2), ethylene, ethane, propylene and liquid standards such as formaldehyde, formic acid, methanol, acetone, acetaldehyde, ethanol were injected and their retention time were noted. Some of the liquid compounds were detected in gas phase, hence all the liquid compound were taken, purged with N_2 and then the gas phase which now contains both the compound and N_2 were injected into the GC for calibration.

Gaseous products other than hydrocarbon such as H_2 and O_2 have been analyzed by TCD detector with molecular sieve 13X column

Injector Temperature: 150 °C

Column Temperature: 50 °C isothermal for 8 min.

Detector Temperature: 110 °C

Carrier gas: Nitrogen, 30 mL/min.

2.4.2 Quantum efficiency calculation

As mentioned earlier, photo-catalytic activities highly depends on the experimental conditions such as, the amount of catalyst, light intensity, lighting area, reactor volume, temperature and pressure. Hence we cannot be compare activities of the same photo-catalyst with different experimental conditions. Therefore calculation of quantum yield is an important parameter as per photo-catalyst concern. Potassium ferric oxalate was used as standard for actinometry. Apparent quantum yield (AQY) was calculated based on the quantities of different products formed per hour per gram of the catalyst and using the formula

$$\mathrm{AQY(\%)} = \frac{\text{Number of reacted electrons}}{\text{Number of incident photons}} \text{ X } 100$$

The estimated AQY (%) value considered as smaller value than real QY, because the absorbed light by the photo catalyst should be smaller than the actual incident photons due to scattered light was not taken for calculation. Number of reacted electrons can be calculated from the obtained product from CO_2 reduction. Amount of incident photons has been calculated by actinometry. Brief experimental details are given below

The light energy emitted from any source is measured in the units of Einstein [10]. One Einstein is equal to the energy absorbed or emitted by one mole of reactants. Light energy absorption is the primary process in any photochemical reaction. The photochemical reaction for this actinometric experiment is

$$2Fe^{3+} + C_2O_4^{2-} \rightarrow 2Fe^{2+} + 2CO_2$$

The amount of ferrous ions formed from the irradiated solution is determined as 1,10-phenanthroline complex which absorbs at 510 nm. This complex requires that Fe ion to be in +2 state not in +3.

Standard solutions of 0.2 N Ferric sulphate and 1.2 M potassium oxalate were prepared. Equal volumes of ferric sulphate and potassium oxalate solution were pipette out make upto the reactor volume (610 mL). Then the prepared $K_3Fe(C_2O_4)_3$ solution was irradiated with same experimental condition which we have followed for CO_2 photo reduction. Mixed well the irradiated solution and pipette out 1 mL of the actinometer solution into a 10 mL of flask, added 2 mL of 0.2% 1,10 Phenanthroline and buffer solution and mixed well to form ferrous- phenanthroline complex. The same complex mixture was prepared using the $K_3Fe(C_2O_4)_3$ solution without irradiation. The absorbance of both the solutions was measured at 510 nm.

Intensity of light is calculated using the formula

I (in Einstein/min) = $AV_2V_3/\varepsilon\phi^{\wedge}LTV_1$

Here, V_1 – The volume of irradiated actinometer solution taken

V_2 – The volume of actinometer solution originally irradiated

V_3 – The volume to which the aliquot of the irradiated solutions is diluted

ε (~ 1.11 x 10^4) – Extinction coefficient of ferrous phenanthroline complex at 510 nm

$\phi^{\wedge}$ (~ 1) - Quantum yield of Fe^{2+} production at wave length of light used

T - The time of irradiation

A – Optical difference in absorbance between the irradiated solution and that taken in dark.

2.5 References

1. C. C. Li, Y. P. Zheng, T. H. Wang, J. Mater. Chem., 2012, 22, 13216–13222.
2. X. Li, J. Zang, J. Phy. Chem.C 2009), 113, 19411.
3. J.W. Liu, G. Chen, Z.H. Lia, Z.G. Zhang Int. J. Hydrogen Energy 2007, 32, 2269.
4. H. Kato, K. Asakura, A. Kudo, J. Am.Chem.Sec. 2003, 125, 3082.

5. S. Xie, Y. Wang, Q. Zhang, W. Deng, Y. Wang, ACS Catal. 2014, 4, 3644.
6. J.S. Lindsey, R.W. Wagner, J. Org. Chem. 1989, 54, 828.
7. A. Adler, F.R. Longo, F. Kampas, J. Kim, J. Inorg. Nucl. Chem. 1970, 32, 2443.
8. J. Niu, B. Yao, Y. Chen, C. Peng, X. Yu, J. Zhang, G. Bai, App. Surface sci 2013, 271, 39.
9. M. Yoshino, M. Kakihana, W.S. Cho, H. Kato, A. Kudo, Chem. Mater. 2002, 14**,** 3369
10. B. Viswanathan, P.S Raghavan, Practical Physical Chemistry,Viva books Private Limited, 2005.
11. M.J. Frisch, Gaussian 09, Revision B.01; Gaussian, Inc.: Wallingford, CT, 2010
12. R. Kumar, M. Sankar, Inorg. Chem 2014, 53, 12706.

CHAPTER 3

STUDIES ON TITANIA BASED CATALYSTS FOR PHOTO CATALYTIC REDUCTION OF CARBON DIOXIDE

3.1 Influence of doping/co-doping with anions (N & S) and meso porous structure of Titanium Dioxide

3.1.1 Introduction

Eversince the discovery of titania as photo catalyst by Fujishima and Honda in 1972 [1], TiO_2 continues to be the preferred and hence extensively studied catalyst system due to its inherent and versatile photo-catalytic activity, low toxicity, chemical inertness, ability to resist photo-corrosion, high stability under photo-irradiation, abundant availability at low cost. Titania is a versatile catalyst that finds wide application as photo-catalyst for both energy conversion and environmental issues. The key applications of photo-catalysis on the energy front, utilizing abundantly available sunlight, are production of hydrogen by splitting of water, generation of electricity using solar cells (photo-voltaic cells) photo-catalytic production of methane and other hydrocarbons (solar fuels) from CO_2 and water (artificial photosynthesis). Titania has been studied extensively for the removal of pollutants from the industrial effluents and drinking water (Advanced Oxidation Processes), purification of air, self-cleaning, anti-fogging and anti-bacterial applications towards environmental protection [2-6].

TiO_2 based materials with high surface area are believed to favour heterogeneous photo-catalytic reactions due to its more number of active sites which will increase the availability of reactant molecules on the surface. A major drawback of high surface area photo-catalytic materials is the difficulty in removing it from the reaction mixture after the reaction for recyclability [7-9]. This can be overcome by using porous TiO_2, which can give high surface area and easy to remove from reaction mixture. Meso porous structure shortens diffusion length of the reactants and migration distance of charge carriers to the surface. However, efficient utilization of

TiO_2 is limited with UV region which is only <5% of natural solar light, due to its wide band gap (3.2 eV). Hence, intensive research effects are being pursued to modify the electronic energy levels (band structure) of TiO_2 so as to extend its light absorption in visible region [6]. Modification/doping with non metals has been extensively studied on TiO_2. Though a number of anions [7-28] C, N, F, P, B and S have been used for doping on titania, doping with nitrogen the most effective strategy and hence studied extensively [29]. Dopant nitrogen in TiO_2 lattice, can be substitutional nitrogen which creates N 2p states just above the valence band and also can be interstitial nitrogen which forms impurity energy level as shown in Fig. 3.1. These newly generated additional energy levels within the wide band gap of the TiO_2 not only promote absorption of visible light photons, which also gives alternate pathways for the electron-hole recombination, thus altering their life times which is essential for an effective photo catalyst [29].

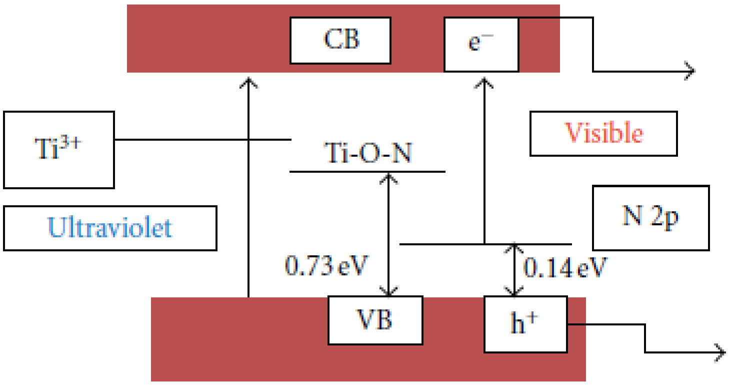

Fig. 3.1 Schematic energy level diagram for nitrogen substituted TiO_2 [Bare semiconductor absorbs UV radiation while localized energy levels of nitrogen above valence band facilitate the visible light absorption].(Reproduced from Ref. 29)

Recently co-doping on TiO_2 with two anions is reported to be highly effective in improving photo-catalytic activity due to changes in the electronic energy levels brought out by synergetic effect caused by the dopants. Introduction of anions like N and S in TiO_2 results in narrowing of band gap (band gap engineering) due to mixing of p states of dopants (N, S) with valence band O 2p states of TiO_2 or creation of impurity states above the valence band of TiO_2, to facilitate visible light absorption [30-36].

In this Chapter the influence of meso porous TiO_2 (TiO_2-MP) and the effect co-doping with N, S on photo catalytic activity have been investigated. Co-doping (N & S) induces visible light absorption of TiO_2, while meso-porous structure enhances the efficiency by reducing diffusion length and recombination of charge carriers. Photo-catalytic efficiency of the doped TiO_2-MP was tested by CO_2 photo-reduction with H_2O. In order to highlight the influence of meso porous character of TiO_2, similar levels of doping/co-doping with N & S was carried out on commercial TiO_2-P-25. Photo-physical properties and photo-catalytic activity of anion modified P-25 TiO_2 were evaluated and compared with those for modified TiO_2-MP.

3.1.2 Electronic energy levels of TiO_2

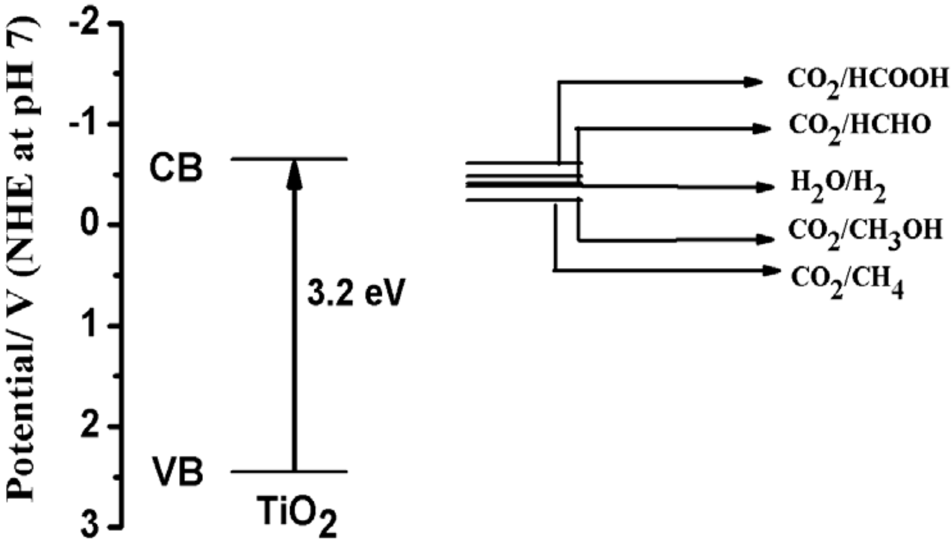

Fig. 3.2 VB and CB energy levels of TiO_2 with respect to the potential for reduction of CO_2 and oxidation of water.

As shown in Fig. 3.2, the conduction band edge (-0.7 V vs NHE pH 7) of TiO_2 is more negative with respect to the potential for reduction of CO_2 to various reduction products. Its valence band energy level is suitable for oxidation of water as well. Hence, it is a suitable semiconductor for CO_2 photo-reduction with H_2O. Details on the preparation of neat and N & S co-doped meso porous TiO_2 and TiO_2-P-25 are given in Chapter 2.2.1 - 2.2.3.

3.1.3 Results and Discussion

3.1.3.1. X-ray Diffraction Study

X-ray diffraction patterns were recorded to investigate the structure and phase composition of the TiO_2-MP & TiO_2-P25 and their anion modified versions. XRD pattern for TiO_2-MP is shown in Fig. 3.3A. Peaks at 2Θ values of 25.28 (101), 37.98 (004), 48.38 (200), 53.98 (105), 62.78 (204), 68.98 (116), 70.18 (220) and 75.58 (215) correspond to polycrystalline anatase phase (JCPDS Card No. 21-1272) of TiO_2.

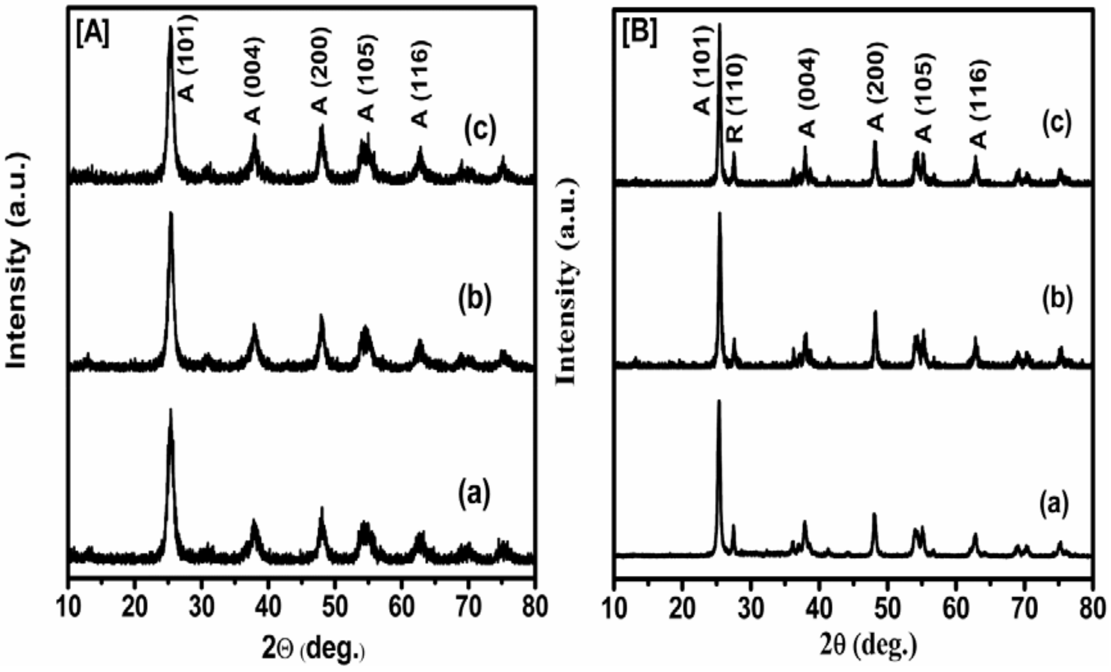

Fig. 3.3 XRD patterns for neat and doped TiO_2. [A] TiO_2-MP, (a) Pristine TiO_2-MP, (b) N/TiO_2, (c) N,S/TiO_2. [B] Commercial P25-TiO_2 (a) P25, (b) N/P25, (c) N,S/P25. A- Anatase, R- Rutile.

TiO_2-MP photo catalyst mainly consists of anatase. There are no significant changes in the phase composition and crystal structure after modifications with anions. XRD patterns for TiO_2-P25 and its anion modified versions are shown in Fig. 3.3B. In addition to the above mentioned peaks due to anatase phase, some extra peaks at 2θ values, 27.58 (110), 36.18 (101) and 41.38 (111), corresponding to rutile structure (JCPDS Card No. 89-4920 and 89-4921) of TiO_2 are observed.

In the case of TiO_2-P25 photo catalyst, anatase and rutile phase compositions were analyzed by the relative intensities of peaks of anatase and rutile d-lines, using the formula, $F_A = 1/ [1+1.26(I_R/I_A)]$. Nearly 85% of anatase and 15% of rutile phases were observed in TiO_2-P25. Anion modified TiO_2-P25 also has d-lines similar to those observed for the pristine material, indicating no structural and phase composition with modified photo catalyst. The crystallite size of the synthesized materials, calculated by using Scherer's formula, and lattice parameters for tetragonal crystal system calculated using the formula $1/d^2 = [h^2+k^2]/a^2 + l^2/c^2$, where h, k, l are miller indices, d is the inter planar distance, a and c are lattice parameters, are tabulated in Table 3.1. As evidenced from Table 3.1, small changes observed in the lattice parameter values with modified TiO_2 samples imply the incorporation of the anions into TiO_2 crystal lattice [30].

Table 3.1 Structural and textural properties of TiO_2 based photo catalysts

Catalyst	Phase	Lattice parameter (Ȧ)		Cell volume	Average crys. Size (nm)		Textural Properties			Band gap
		a=b	c	(Ȧ)^3	D^a	D^b	S_{BET} (m^2 g^{-1})	V_p (cm^3 g^{-1})	D_p (nm)	(eV)
TiO_2-MP	A	3.78	9.368	133.854	8.5	10.1	153	0.38	9.8	3.1
N/TiO_2	A	3.796	9.540	137.468	11.9	12.2	126	0.29	9.2	2.93
N,S/TiO_2	A	3.772	9.472	134.768	9.9	10.3	149	0.25	6.8	2.9
P25	A+R	3.78	9.472	135.339	20.8	29	53	0.23	21.5	3.11
N/P25	A+R	3.781	9.480	135.526	22.2	39	39	nd	nd	2.91
N,S/P25	A+R	3.782	9.516	136.112	24.8	43	35	0.23	28.1	2.9

a- Average crystallite size calculated using Scherer's equation

b- Average crystallite size calculated using SA= $6*10^3/$ (L*density) [SA = BET surface area, L = Average crystallite size, density = 3.9 g/cm^3]. nd - not determined.

3.1.3.2 UV-Visible Diffuse Reflectance Spectra

Fig. 3.4A shows DRS in UV visible region for the pristine and anion doped TiO_2-MP catalysts. Absorption maximum at 390 nm corresponds to intrinsic absorption peak for TiO_2. Non-metal (N, S) doped photo catalysts extended the absorption edge towards the visible region. This could have arisen due to mixing of the nitrogen 2p states with oxygen 2p states on the top of the valence band and/or by the creation of N-induced mid gap energy levels [29]. The red shift with anion modified TiO_2-MP follows the order TiO_2< N/TiO_2< N,S/TiO_2(Fig. 3.4A-curves a to c). Corresponding changes in the band gap energy values are given in Table 3.1. The enhanced shift observed for N, S co-doped TiO_2 may be due to the synergetic effect of co-doping on the electronic structure of TiO_2 and are in line with literature reports [31-38]. With respect to Ti-O bond, Ti-N and Ti-S bonds are more covalent in character due to reduced electro-negativity difference and hence a reduction in the band gap is observed [26]. In comparison, the spectra for TiO_2-P25 and its anion modified versions, shown in Fig. 3.4B (curves a-c), also reveal similar red shift towards visible region with respect to TiO_2 P25 (Table 3.1).

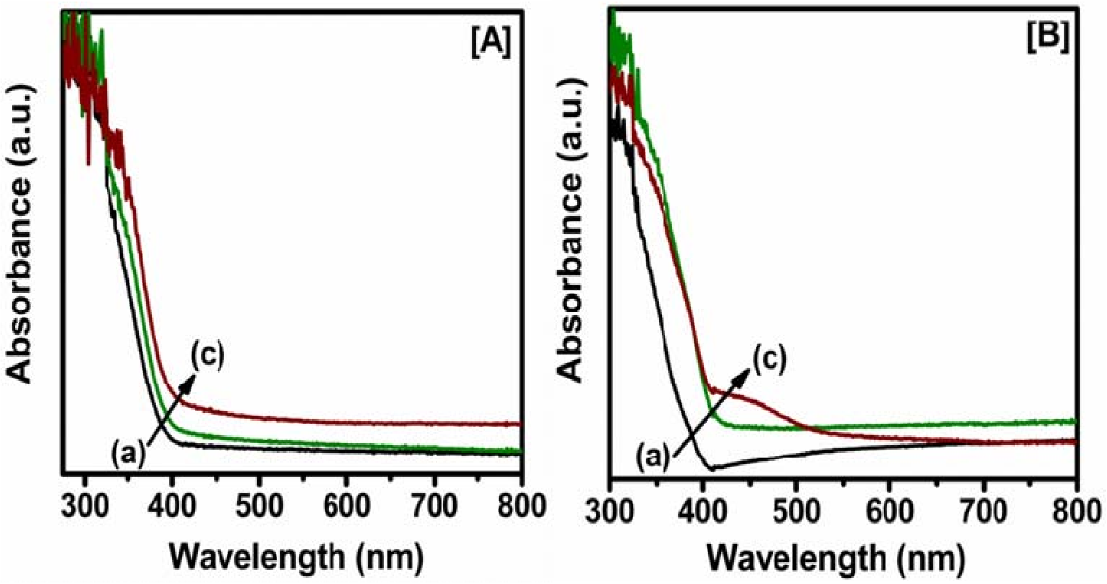

Fig. 3.4 Diffuse Reflectance spectra for neat and doped TiO_2. [A] TiO_2-MP, (a) Pristine TiO_2-MP, (b) N/TiO_2, (c) N-S/TiO_2. [B] TiO_2-P25 (a) P25, (b) N/P25, (c) N-S/P25.

3.1.3.3 Textural Analysis

N_2 adsorption and desorption isotherms and corresponding pore size distribution curves for TiO_2-MP and its anion modified versions are presented in Fig. 3.5. All three isotherms belong to Type IV as per IUPAC classification. The presence of H1 type hysteresis loop in P/P_0 range of 0.5-0.9 suggests mesoporous character with high degree of porosity [39-41].

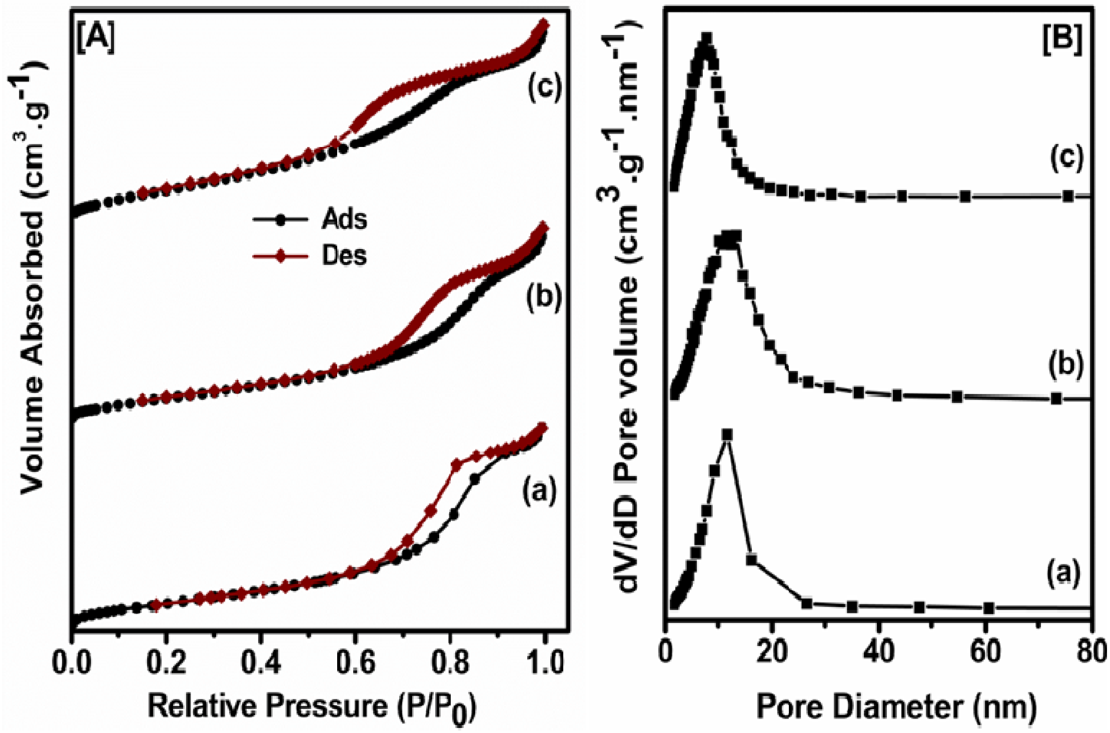

Fig. 3.5 [A] N_2 adsorption desorption isotherms, [B] pore size distribution curves of neat and doped TiO_2-MP, (a) TiO_2-MP, (b) N/TiO_2-MP, (c) N,S/TiO_2-MP.

Textural properties such as specific surface area, pore size and pore volume are listed in Table 3.1. Specific surface area and pore volume values decrease upon the addition of N or N, S in the TiO_2. Specific surface area of the anion modified TiO_2-P25 catalysts also decrease due to the minor blocking of pores in the TiO_2 by the addition of anions. Average crystallite size, calculated from specific surface area (BET) data by assuming the particles are in spherical morphology, using the formula, SA= $6*10^3$/ (L*density) [SA = Surface Area, L = Average Crystallite size, density = 3.9 g/cm^3]

are listed in Table 3.1. Average crystallite size values calculated using BET surface area and by XLBA using Scherer's equation are fairly comparable.

3.1.3.4 Raman Spectra

Fig. 3.6 shows Raman spectra of the neat and modified TiO_2. Six Raman active fundamental peaks were observed with neat and modified samples, with peaks centered at 144 cm^{-1} (E_g), 197 cm^{-1} (E_g), 397 cm^{-1} (B_{1g}), 518 cm^{-1} (A_{1g} + B_{1g}) and 640 cm^{-1} (E_g). All these peaks are characteristic of TiO_2 anatase phase, in line with the XRD pattern Fig. 3.3A. Intensity of the Raman peak is related to the degree of crystallinity of the material. An increase in intensity was observed with the anion doped mesoporous TiO_2 catalyst, implying increase in crystallinity as evidenced from XRD pattern.

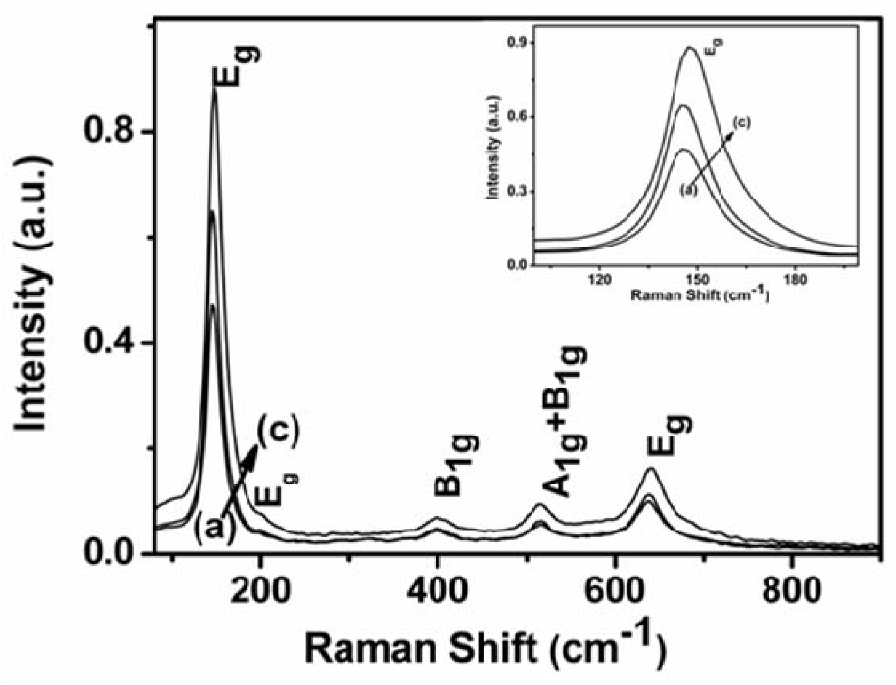

Fig. 3.6 Raman spectra of neat and doped TiO_2-MP, (a) TiO_2-MP, (b) N,S/TiO_2-MP, (c) N/TiO_2-MP.

The slight shift observed (inset Fig. 3.6) towards higher wave number, can be ascribed due to changes in the force constants of Ti-O-Ti structure, indicating that doped anions have been incorporated into the TiO_2 crystal lattice [42-47].

3.1.3.5 Scanning Electron Microscopic Analysis

Scanning Electron Micrograph for the neat and anion modified TiO_2-MP are given in Fig. 3.7a-c. TiO_2-MP displays spherical morphology. Anion modified TiO_2-MP undergoes a change its morphology and also a decrease in crystallite size as evidenced from XRD line broadening analysis (Table 3.1). TiO_2-P25 samples also show similar changes in morphology and crystallite size on doping, as shown in Fig. 3.7d-e.

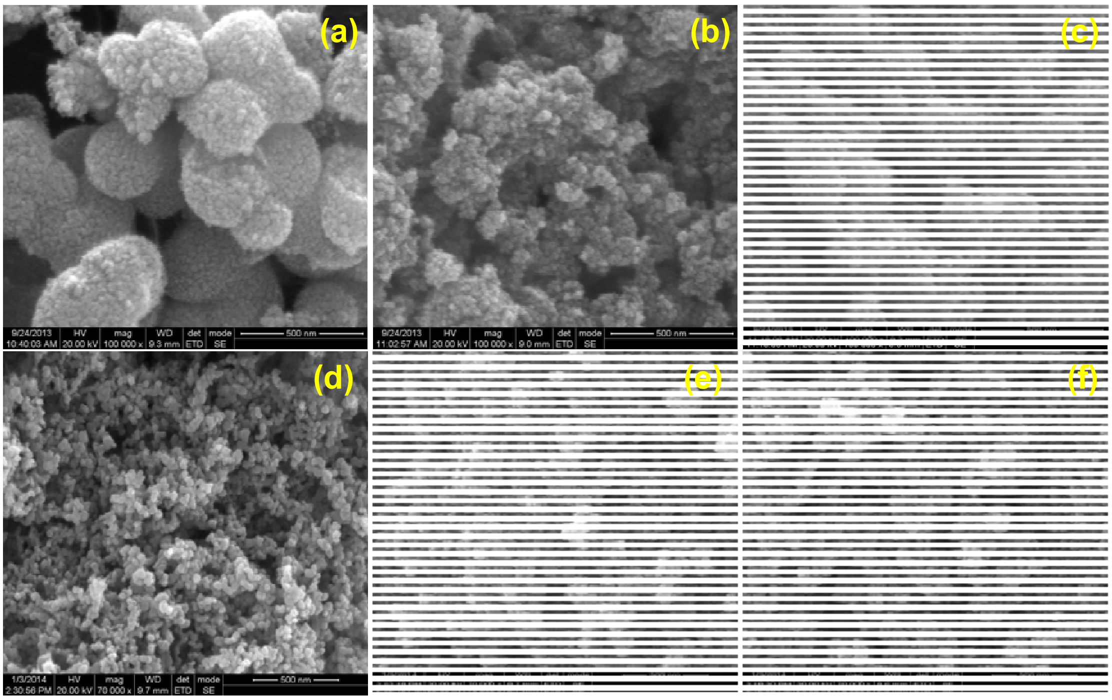

Fig. 3.7 Changes in the morphology of doped TiO_2 (a) TiO_2-MP, (b) N/TiO_2-MP, (c) N-S/TiO_2-MP, (c) TiO_2 P25, (d) N/P25, (f) N-S/P25.

3.1.3.6 EDAX spectra

Addition of dopant precursor during hydrothermal treatment has ensured the incorporation of doped elements into the TiO_2 crystal structure. This can be confirmed by the qualitative EDAX spectral data presented in Fig. 3.8. In Fig. 3.8b,c and e, f EDAX spectra indicate the presence of N and S in addition of Ti and O elements confirming the doped elements have been incorporated in the synthesized material.

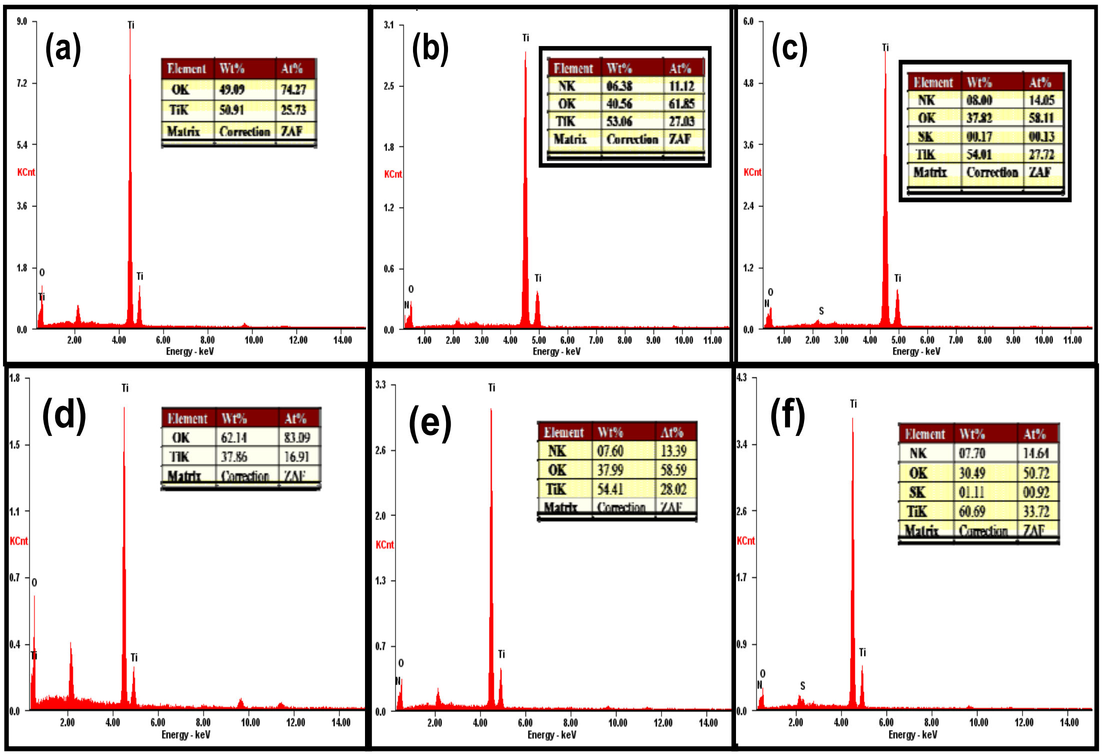

Fig. 3.8 EDAX spectra for neat and doped TiO_2 (a) TiO_2-MP, (b) N/TiO_2-MP, (c) N,S/TiO_2-MP, (c) TiO_2 P25, (d) N/P25, (f) N,S/P25.

3.1.3.7 Transmission Electron Microscopy Images

TEM observations further confirm the presence of spherical particles in the synthesized TiO_2-MP and its anion modified catalysts. The well resolved lattice fringes observed from HRTEM (Fig. 3.9 (b)), measured d-value of 0.34 nm corresponds to (101) anatase TiO_2 crystal planes. SAED shown in Fig. 3.9 (c), reveals that poorly crystalline structure of anatase, with rings that can be ascribed to (101), (004), (200) and (105) reflections of TiO_2.

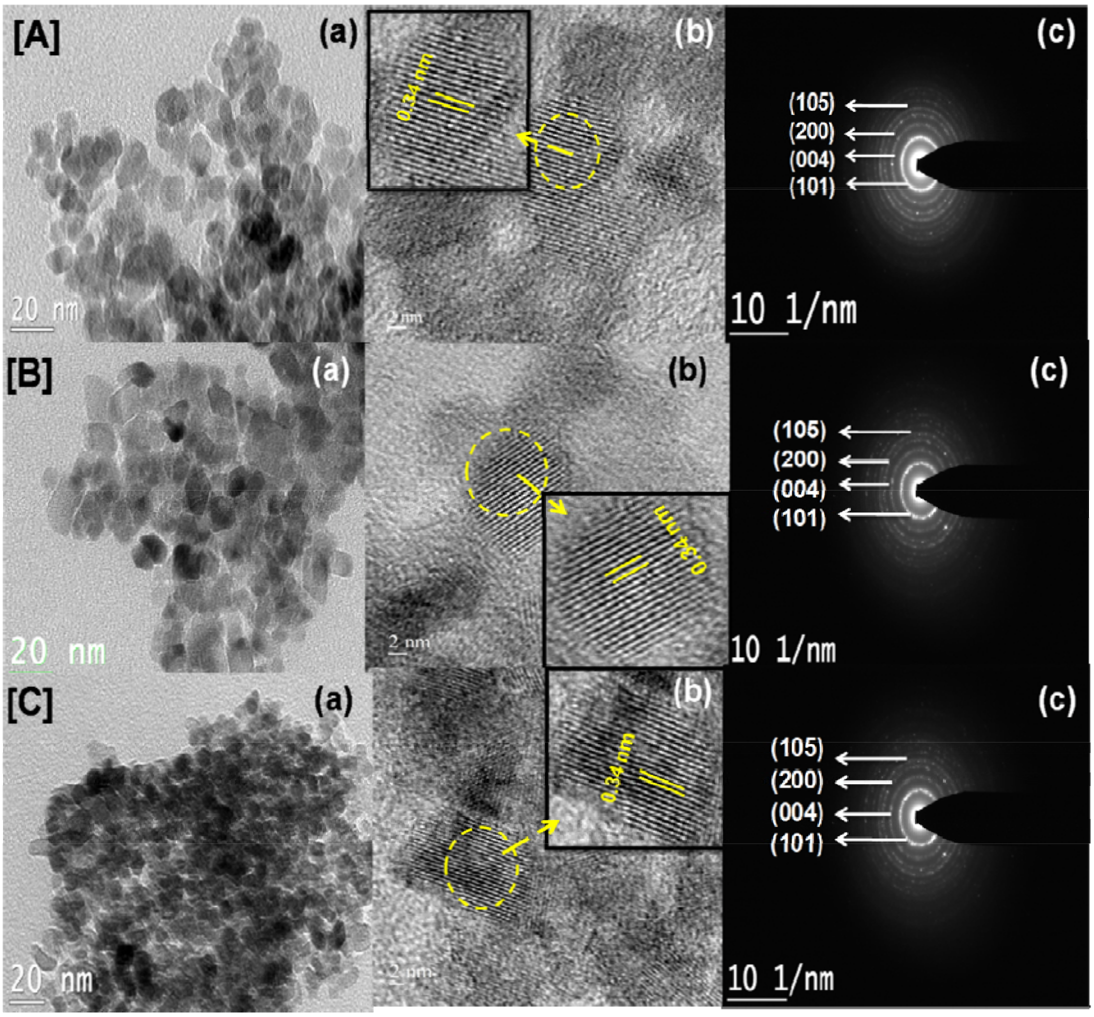

Fig. 3.9 TEM micrographs of [A] TiO_2-MP, [B] N/TiO_2-MP, [C] N,S/TiO_2-MP; (a) TEM images, (b) HRTEM images, (c) SAED pattern.

3.1.3.8 X-ray Photoelectron Spectra

XPS measurements were carried out to analyze chemical composition and identify chemical states of the dopant elements present in the synthesized photo catalysts. Typical XPS survey spectra of the synthesized photo catalysts are shown in Fig. 3.10 and binding energy values for main XPS peaks for possible elements present in the synthesized materials are tabulated in Table 3.2. Surface chemical composition of the catalysts possible elements are tabulated in Table 3.3. Survey spectrum for pristine TiO_2 shows the presence of Ti 2p and O 1s with binding energies at 458 eV, 530 eV respectively. Presence of C peak at 285 eV may be due to carbon from the instrument itself. Anion modified TiO_2 (Fig. 3.10b, 3.10c) has extra peaks except those for Ti and O, at 399.5 eV and 169 eV corresponding to N 1s and S 2p respectively, indicating the presence of dopant elements in the TiO_2 surface.

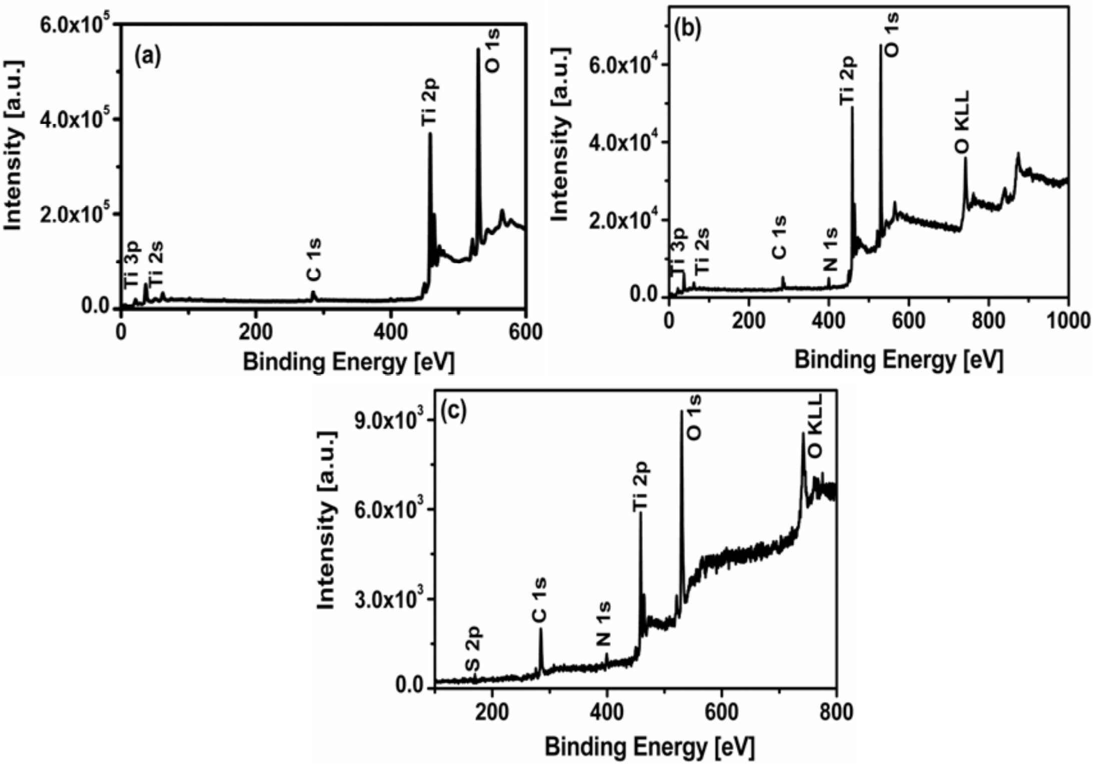

Fig. 3.10 XPS survey spectra of (a) TiO_2-MP, (b) N/TiO_2-MP, (c) N,S/TiO_2-MP.

Table 3.2 Binding energy of main XPS peaks for pristine and modified TiO_2-MP.

Photo catalysts	Binding Energy (eV)						
	Ti		**O**		**N**		**S**
	($2p_{3/2}$)	($2p_{1/2}$)	Bulk (O^{2-})	OH	Ti-N	Ti-N-O_x	SO_x
TiO_2	458.9	464.8	529.8	531.6	-		
N/TiO_2	458.1	463.9	530.0	531.8	399.1	400.0	-
N-S/TiO_2	458.2	464.0	530.2	532.0	399.7	-	168.5

Table 3.3 Elemental composition for neat and modified TiO_2-MP from XPS data.

Photo catalysts	Composition (%)			
	Ti	**O**	**N**	**S**
TiO_2	31.5	68.5	-	-
N/TiO_2	28.85	58.78	5.42	-
N-S/TiO_2	25.3	57.6	13.9	3.2

High resolution XP spectra of Ti 2p (Fig. 3.11 [A]), O 1s (Fig. 3.11 [B]) for the neat and modified photocatalyst are shown in Fig. 3.11. The main peaks centered at 458.8 eV and 464.3 eV correspond to Ti^{4+} $2p_{3/2}$ and Ti^{4+} $2p_{1/2}$ of TiO_2. Similar peaks with small shift towards lower binding energy were observed with modified catalysts. Such shifts can be ascribed to the slight distortion of the TiO_2 crystal structure, brought about by added dopant elements. As reported earlier, substitution of nitrogen in the place of oxygen creates more electron density on Ti, due to the less electro negativity of nitrogen compared to oxygen [16, 35, 48-50]. It is known that as the electro negativity of the anion decreases, the % ionic character of Ti-hetero atom will decrease. Consequently net positive charge on Ti^{4+} also decreases with anion modified photo catalyst [51, 52], resulting in binding energy shifts towards lower energy region.

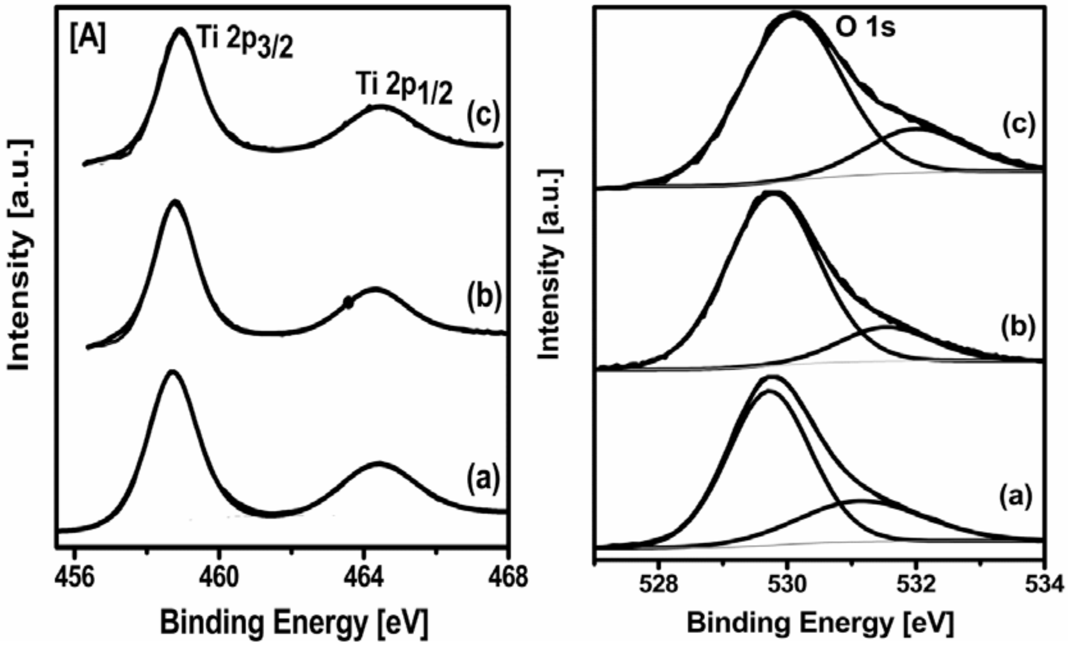

Fig. 3.11 High resolution XPS spectra for [A] Ti 2p, [B] O 1s of neat and modified meso TiO_2. (a) TiO_2-MP, (b) N/TiO_2-MP, (c) N, S/TiO_2-MP.

Two types of O 1s peak observed in all the neat and modified catalysts (Fig. 3.11 [B]), peak centered at 529 eV corresponds to lattice oxygen of Ti-O-Ti in octahedral TiO_6 crystal lattice and another small area peak centered at 531 eV can be ascribed to surface hydroxyl group or adsorbed oxygen [30-38]. The observed lower binding energy shift with anion modified TiO_2 confirms the incorporation of anions in the TiO_2 lattice.

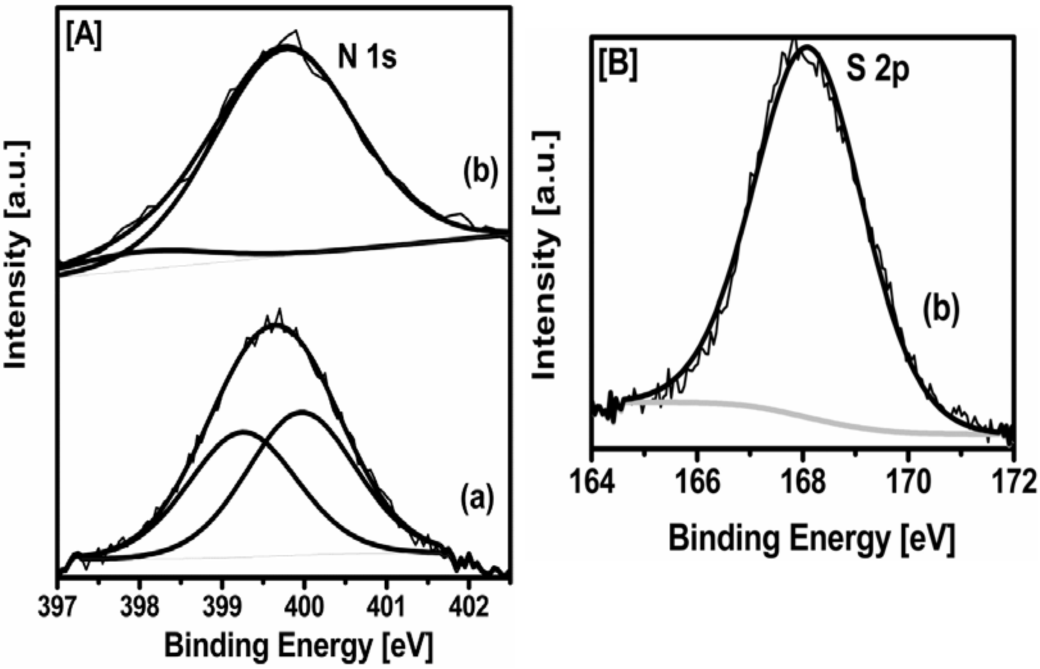

Fig. 3.12 High resolution XPS spectra for [A] N1s, [B] S 2p of anion modified TiO_2-MP. (a) N/TiO_2-MP, (b) N, S/TiO_2-MP.

High resolution XP spectra of N 1s for the N doped and N, S co-doped TiO_2 photo catalysts are shown in Fig. 3.12A. It is clearly seen that there are two deconvoluted peaks at 398.8 eV and 400.3 eV. The peak at 400.3 eV corresponds to the presence of surface oxidized form nitrogen such as Ti-N-O or nitrogen in interstitial locations in the TiO_2 crystal structure and the peak at 398.8 eV can be attributed to the presence of substitutional/anionic nitrogen in the form of N-Ti-O bond and there is no indication for the formation of N-Ti-N bond (394.5 eV). Observed results implies that at least a part of the doped nitrogen has been incorporated into TiO_2 in substitutional as well as interstitial locations in TiO_2 crystal structure [16, 22, 31, 32, 35, 38, 49-54]. Even though, part of the doped N is located in the interstitial position of the TiO_2 lattice, it doesn't affect the crystalline structure as evidenced from Table 3.1. Also, the observed higher binding energy shift (398.8 eV) for anionic N (Fig. 3.12A) compared to N-Ti-

N (<397 eV), suggest that doped N would have some strong interaction with nearby oxygen in the TiO_2 lattice [52].

High resolution XP spectra of S 2p for N, S co doped TiO_2 are shown in Fig. 3.12B. Apeak detected at 168 eV, corresponds to the cationic form of sulphur, in the state of S^{6+} ion. Peak at 163 eV corresponding to anionic S (S^{2-}) ion is not observed. This observation implies that at least a part of the doped sulphur is located at Ti^{4+} ion sites in TiO_2 crystal structure, since ionic radii of S^{6+} and Ti^{4+} ions are closer, Whereas,anionic form of S (S^{2-}) with higher ionic radii (1.84 Å) vis-a-vis that of O^{2-} ion (1.4 Å) could not be accommodated into the TiO_2 crystal structure [22, 31, 32, 35, 38, 52].

3.1.3.9 Photoluminescence Spectra

Photoluminescence studies were carried out to determine the fate of charge carriers, since PL emission occurs from the recombination of photo generated electrons and holes. Surface charge transfer and reduced recombination rate of charge carriers and diffusion of reactants are key factors for improving photocatalytic efficiency [22].

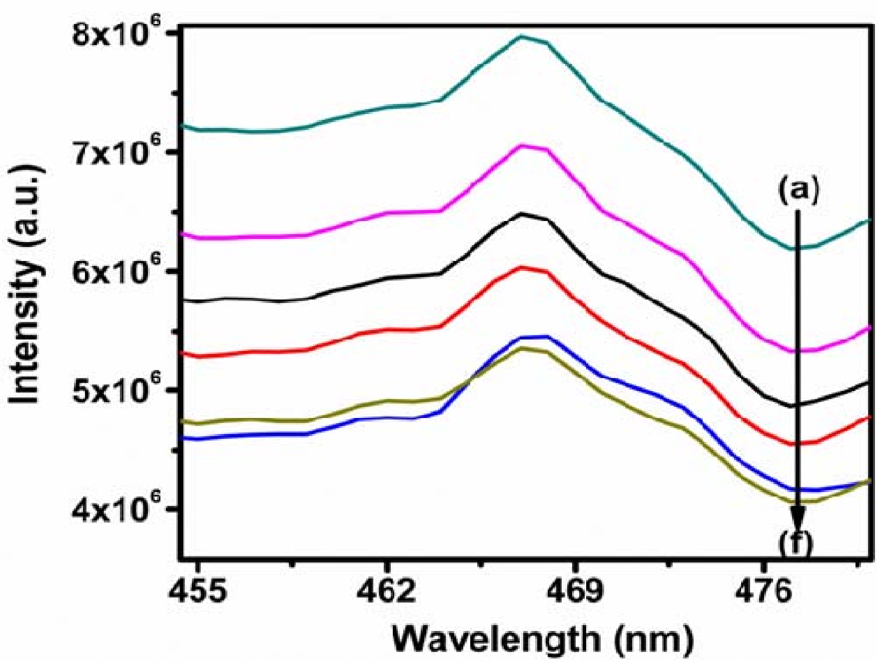

Fig. 3.13 Photo luminescence spectra for neat and doped TiO_2 photo catalysts (a) P25, (b) N/P25, (c) TiO_2-MP, (d) N/TiO_2-MP, (e) N,S/TiO_2-MP, (f) N,S/P25.

It is clearly seen that, PL spectra (Fig. 3.13) of the anion modified photocatalyst show less intensity compared to pure TiO_2-MP, implying that there is an increase in life time of charge carriers with anion modified photocatalysts, due to the incorporation of N and S into the TiO_2 crystal structure. Similar trend was observed with modified TiO_2-P25 catalysts, but not as effective as TiO_2-MP. Mesoporous structure facilitates charge transfer to active surface due to increase in diffusion rate of charge carriers.

3.1.4 Photo catalytic reduction of Carbon dioxide

All the experiments were carried out upto 20 hrs. Trends in the formation of major products, methanol and ethanol, with respect to time of irradiation up to 20 hrs, are given in Fig. 3.14. Besides hydrogen and oxygen, methane, ethylene and ethane were formed in very small quantities (~0.1-10 micromoles/g) and hence not considered in the plots. CO and formic acid were detected at trace levels and hence could not be quantified. As shown in Fig. 3.15, considerable amounts of methanol is formed when the aqueous alkaline is saturated with carbon dioxide compared to very small quantities formed after saturation with nitrogen, indicating that the observed methanol/products were obtained from CO_2 photo reduction and not from surface carbon impurities on the catalyst.

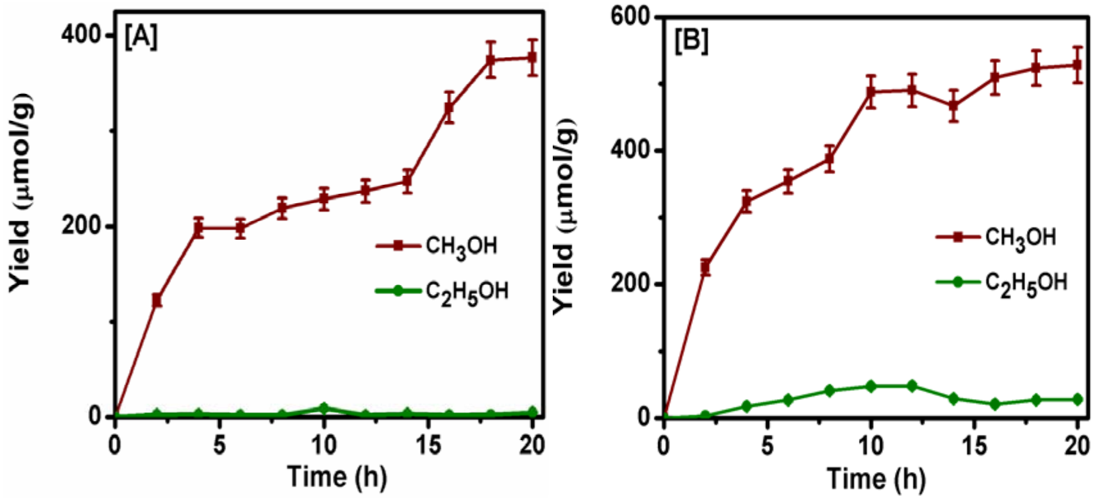

Fig. 3.14 Trends in products distribution during CO_2 photo reduction [A] TiO_2-MP, [B] N,S/TiO_2.

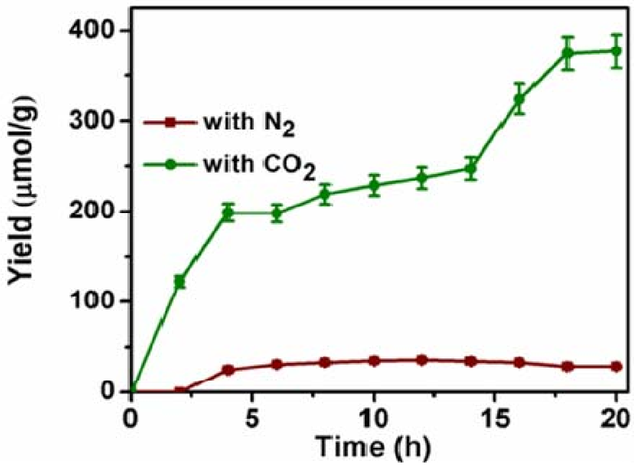

Fig. 3.15 Methanol yield with meso TiO_2 after purging with N_2 and CO_2 in similar experimental condition.

Rate of formation of products are high during initial 8 hrs, beyond which the product formation tends to slow down. Based on the initial rates (µmol g^{-1} h^{-1}) for the formation of different products, and the number of photo electrons involved in each case, apparent quantum yields (AQY) for all the photo catalysts have been calculated and presented in Table. 3.4

Table 3.4 Product distribution and quantum yield data for neat and modified TiO_2 catalysts.

Catalyst	Products formed after 20 hrs of irradiation (µ mol g^{-1} h^{-1})							AQY x10^{-3} (%)
	CH_4	C_2H_4	C_2H_6	CH_3OH	C_2H_4O	C_2H_5OH	C_3H_6	
P25	0.004	0	0.01	5.5	0	0.64	0	0.8
N/P25	0.1	0	0.02	5.9	0	2.3	0	1.2
N,S/P25	0.12	0.16	0.07	22.2	0.7	2.6	0.06	3.3
TiO_2-MP	0.08	0.07	0.11	28.0	2.1	1.2	0.02	3.9
N/TiO_2-MP	0.04	0.02	0.3	32.8	0.3	6.2	0.02	5.2
N,S/TiO_2-MP	0.04	0.02	0.05	53.8	0.3	5.2	0.01	7.3

In general, when the CO_2 photo reduction is carried out in aqueous phase, methanol and in some cases ethanol are formed as main reduced products [55-66]. CH_3OH/CH_4 considered as a preferred solar fuel, since the energy density per volume or mass unit of the CH_3OH/CH_4 is higher than H_2, and also liquid products has advantages over handling [65]. In the present case, aqueous phase for CO_2 has been employed for photo reduction and hence observed methanol/ethanol as main products as mentioned in above literature reports. The main drawback for using aqueous phase for CO_2 photo reduction is that most of active sites of photo catalysts are covered by H_2O molecules, whose adsorption is strong compared to CO_2. The solubility of CO_2 in water is less. Consequently, the quantity reduction products formed is less, due to less population of CO_2 molecules on reaction medium [67]. Hence, aqueous alkaline solution (0.2N NaOH) has been used to enhance solubility of CO_2 in reaction medium. NaOH has been used as the preferred and appropriate reaction medium for CO_2 photo reduction by M. Reli et al [63] and other previous reports [55-64]. Besides OH^- act as an effective hole scavenger, which reduces the recombination of photo generated charge carriers, thus enhancing the effective utilization of electrons for CO_2 reduction and resulting in the formation of multi-electron transfer products like ethanol [55, 60-64].

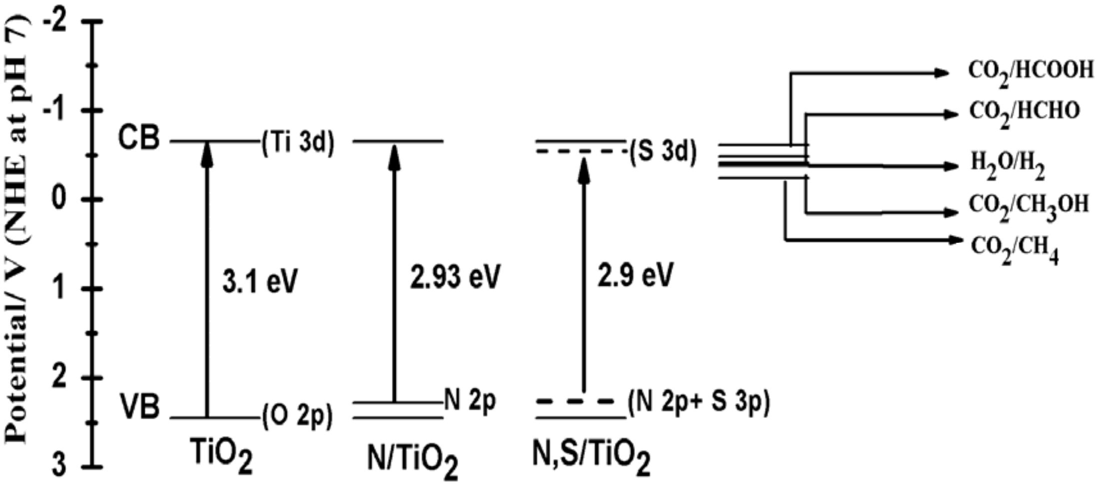

Fig. 3.16 VBM & CBM energy levels of TiO_2 and its anion modified catalysts vis-a-vis potential for reduction of CO_2 and oxidation of water.

In a typical photo catalytic reaction, when the photo-catalyst absorbs light equal to or greater than the band gap energy, photo generated electrons move to the conduction band resulting in the formation of holes in the valence band of the semiconducting photo catalyst. Reduction capability of semiconductor depends on the energy of photo-generated electron (conduction band edge), whereas oxidizing power depends on the energy of hole (valence band edge) present in the semiconductor. As shown in

Fig. 3.16, conduction band edge (-0.7 V vs NHE at pH 7) for TiO_2 is more negative compared to the subsequent reduction of CO_2 after initial activation to form CO_2^- and valence band edge (+2.5 V vs NHE at pH 7) is more positive compared to water oxidation potential. Hence, TiO_2 is an ideal candidate for CO_2 photo reduction with water [68-70]. In the present case, the pH of the alkaline reaction medium is reduced from 14 to 8-9 on saturation with CO_2. As shown in Fig. 3.17a, bicarbonate/carbonate species are predominant at this pH [71]. The reduction potential of these species are lower than that of CO_2 as shown in Fig. 3.17b and hence undergoes facile reduction, mainly to methanol and methane [58, 71]. Formation of CH_3OH/CH_4 from adsorbed bicarbonate and directly from adsorbed CO_2 on titania dispersed in aqueous/alkaline solutions have been reported earlier [72-74].

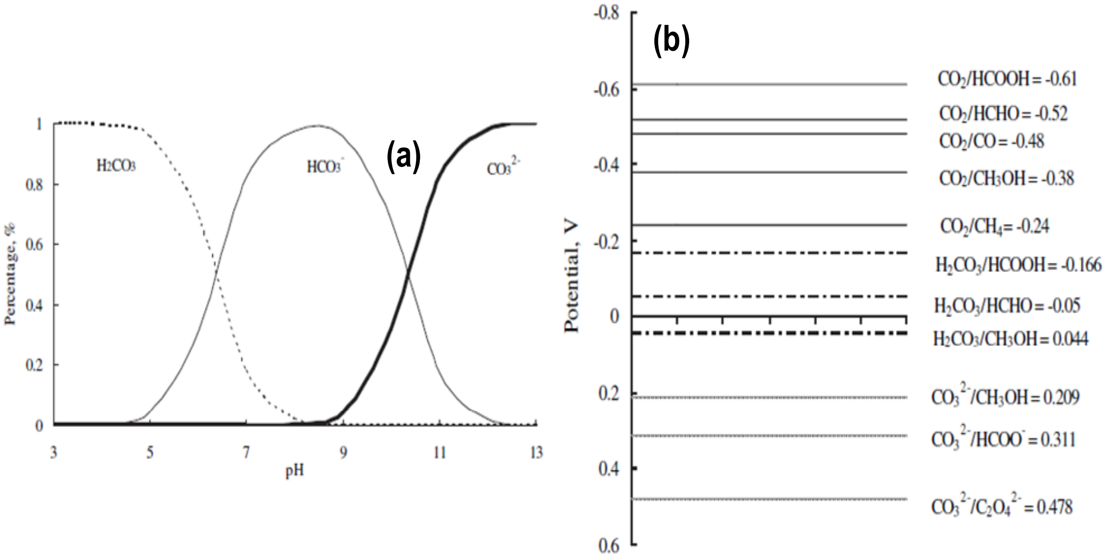

Fig. 3.17 (a) variation of carbonate ion species with solution pH, (b) Thermodynamic potential versus normal hydrogen electrode(NHE) for possible CO_2 photo reduction products [Reproduced from ref. 71]

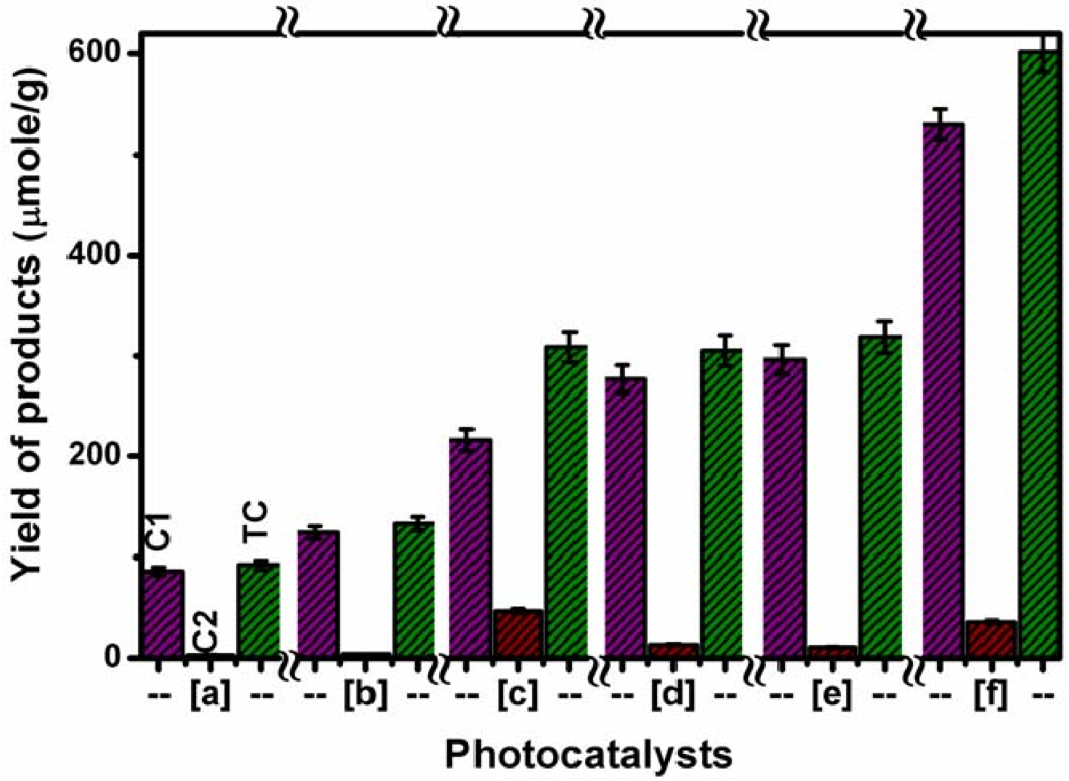

[C1- C1 carbon products, C2 - C2 carbon products, TC-Total carbon products]

Fig. 3.18 Comparison of photo catalytic activity for neat and modified TiO_2 after 20 hrs of irradiation : (a) P25, (b) N/P25, (c) N,S/P25, (d) TiO_2-MP, (e) N/TiO_2-MP, (f) N,S/TiO_2-MP.

Main carbon products obtained from CO_2 photoreaction under our experimental conditions with 20 hrs of illumination are shown in Fig. 3.18 and Table 3.4. TiO_2-MP gives almost five times higher activity than P25 TiO_2. In case of anion modified photo catalysts too, TiO_2-MP gives better activity compared to P25 TiO_2. Meso-porous structure generates more surface active sites and consequently, adsorption of reactant molecules is more compared to P25 TiO_2 [7-9, 75-77]. Absorption of photon-flux is not uniform throughout the materials, for example a wavelength of 320 nm is reduced to 10% of its original intensity after penetrating a distance of 8.5 µm itself. But the meso-porous material is performing as an efficient light harvesting moiety, since its pores are acting as light transfer path, and can penetrate original waves throughout the structure even inside (bulk) to the surface too [76]. Subsequently more photoactive centers are generated, which are needed for efficient photoactive material. Porous structure reduces the diffusion length of photo generated charge carriers and reactant gas molecules and can easily reach the surface active sites where photoreaction takes place [7-9]. Hence the creation of more number of photoactive sites for efficient absorption of light and reducing diffusion length of photo generated charge carriers and gas molecules are responsible for improved photo catalytic activity of TiO_2-MP compared to TiO_2-P25.

One can clearly visualize that N-S co-doped photo catalysts given better product yields compared to bare and mono doped TiO_2. Doping of nitrogen plays an important role towards photo catalytic activity, with some of doped N present in substitutional sites in the lattice of oxygen where as some of them in the interstitial position of TiO_2 as evidenced from XPS data (Fig. 3.12A). As stated by B. Naik et al, both substitutional and interstitial N have some important roles in photo catalytic activity [22, 77-81]. As shown in Fig. 3.16, doped N creates impurity energy levels above the valence band. Since VBM is mainly composed of O 2p orbital, with the mixing of N 2p orbitals of similar energy with O 2p, VBM (N 2p + O 2p) band width is increased. Consequently, the band gap is reduced, as evidenced from DRS-UV visible spectra (Fig. 3.4) [29]. The observed increased in photo catalytic activity with N doped TiO_2 compared to neat TiO_2 is in line with literature reports [82-85]. As reported earlier, the presence of nitrogen in the TiO_2 lattice alters the basicity of the TiO_2 surface [82]. Basic sites are essential for CO_2 adsorption due to the acidic nature of CO_2. Hence the availability of CO_2 molecules on the N and N,S modified TiO_2 surface is more compared to neat TiO_2. Sathish et al, reported that doped with N contributes to VBM whereas doped S mainly (9.16 % for CB and 2.36% for VB) contributes to CBM as shown in Fig. 3.16 and hence further reduction in band gap energy [52, 86] is observed. Such synergetic effect between N and S causes significant increase in the life time of photo generated charge carriers with mono doped and co-doped TiO_2 (as evidenced from PL spectra, Fig. 3.13) are responsible for the observed increase in photo catalytic activity [22, 87]. In the case of TiO_2-MP, a number of factors, like, high surface area, suitable particle size, efficient light harvesting porous structure, increased life time of charge carriers, reduction of diffusion length of both reactant and charge carriers and availability of large number of photoactive sites for adsorption of reactants are responsible for enhanced photo catalytic activity of pristine and N-S co-doped versions.

3.1.5 Conclusions

N, S co-doped TiO_2-MP was prepared by hydrothermal method for the application of CO_2 photoreduction with water. Anatase was the only phase obtained from this method. The presence of Type IV isotherm confirms the mesoporous structure of anatase TiO_2. Anion doping induces red shift in the UV-visible spectra. Doped N is incorporated into the lattice of TiO_2, with some of them present in the interstitial position with strong interaction with nearby oxygen of TiO_2, and the doped S is present as S^{6+} located in Ti^{4+} sites. PL spectra show that the recombination of charge carriers is retarded with anionic modified TiO_2. Similar trends are observed with doped TiO_2-P25 samples. CO_2 photoreduction with water was carried out to evaluate the prepared photo catalysts. The increase in activity observed with anion modified photocatalysts is mainly due to the highly available surface active sites, increased adsorption ability of reactants, favorable crystalline size, efficient absorption in visible region and longer life time of charge carriers. Compared to P25 TiO_2 nano particles, synthesized TiO_2-MP has given better activity, due to the availability of porous structure which enhances the diffusion of charge carriers to the surface active sites where the adsorbed reactants get reduced into products.

3.2 Effect of supporting tri-doped meso-porous Titania on Sepiolite Clay Matrix

3.2.1 Introduction

Even though TiO_2 is the versatile semiconductor for photo catalytic applications, its proficiency for practical application is lacking due to its high band gap and inadequate absorption in visible region which is the major part of the solar radiation. Indeed, the modifications on TiO_2 have been widely investigated to improve absorption in the visible region. An interesting and useful outcome of the extensive studies on the effect of doping on titania is the process of co-doping and the synergistic effects observed within the system of dopants. Existence of synergistic effect in metal-non metal co-doped systems has been established and supported with theoretical studies [6, 88-91]. W. Choi et al [92] studied the photo reactivity of 21 different metal ion doped quantum sized TiO_2 for both oxidation ($CHCl_3$ degradation) and reduction (CCl_4dechlorination) reactions and found that Fe doped TiO_2 significantly enhances the photo-activity for both the reactions. Roldan et al [93] observed that Fe doping strongly reduces the oxygen vacancy formation energy, especially on the surface, which favors the dissociative adsorption of reactant molecules. Fe doped TiO_2 can harvest longer part of wavelength in the visible region as compared to bare TiO_2 [88-99]. Co doping of Fe-N [100-103], Fe-S [104-107] and N-S [30-36] with TiO_2 has been widely studied due to its efficient photo catalytic activity in visible region [88-91]. B. Li et al [108, 109] found that Fe-N-S tri-doped TiO_2(FNST) exhibited higher visible light activity and is more efficient compared to neat TiO_2 due to the synergetic contribution of tri-doped species [108-110]. Hence, Fe-N-S meso-porous TiO_2 (TiO_2-MP) was chosen as active photo catalyst for further studies.

Anpo et al [111], ascertained that highly dispersed TiO_2 anchored on porous Vycor glass shows better photo-catalytic activity compared to bulk TiO_2. Hence researchers started to investigate on TiO_2 supported on porous materials because the unique porous structure and interesting physicochemical properties could improve the performance. TiO_2 dispersed on various porous materials displays significant enhancements in its photo-catalytic activity as shown in Table 1.11. Many porous materials such as zeolites, mesoporous carbon, mesoporous silica/alumina, graphene and clay or clay based matrix were employed disperse TiO_2. Matrix with less particle size, environmentally free, chemically inert, low cost, and with good adsorption capacity were used for photo catalytic and environmental applications [112-119].

J. Paul et al [120] have reported that alkali promoted surface facilitates a high probability of electron transfer to impinging neutral CO_2 molecules. M. Subrahmanyam et al [121] also suggested that, the conversion of CO_2 to C1-C3 compounds takes place preferentially on basic oxide supported systems compared to acidic oxides.

3.2.2 Sepiolite clay as support

In the present study, ~13% Mg containing silicate, Sepiolite, with specific pore structure was chosen as supporting material for the synthesized meso-porous FNST photo-catalyst. Sepiolite is an effective support for dispersion of TiO_2 for photo-catalysis applications [112-119, 122, 123]. Sepiolite has been studied for many applications including waste water treatment, catalyst support, rheological and catalytic properties, sieving of molecules/ions, adsorbents and pesticides which are based on the fibrous morphology, surface area, porosity, crystal morphology, structure and composition of the sepiolite [124-129].

Sepiolite, a hydrated magnesium silicate with micro fibrous morphology, is an important group of clay minerals. As shown in Fig. 3.19, Sepiolite clay [129-134] consists of blocks of octahedral magnesium sheets as layers between two tetrahedral silica layers with a theoretical half unit cell formula $Si_{12}O_{30}Mg_8(OH,F)_4(OH_2)_4 \cdot 8H_2O$. SiO_4 tetrahedra sheet can be easily interchanged, due to the irregular continuity of the SiO_4 sheets and structural cavities that are extended along the axis of the microfibers with the significant number of silanol groups present on the surface of the mineral. Therefore the surface adsorbed reactants can be easily converted into the activated complexes, which facilities different conversions. Typical properties of sepiolite are given in Table 3.5

Table 3.5 Properties of Sepiolite (Ref. 125)

Particle Shape	Needle like
Length (μm)	0.2-2.0
Width (Å)	100-300
Thickness (Å)	50-100
Channels dimensions (Å)	3.7 X 10.6
Specific gravity (g/cm^3)	2.0-2.3
Cation exchange capacity (mequiv./100 g)	<25
Melting point (°C)	1.550
Brookfield viscosity of a suspension at 6% in water at 5 rpm (cP)	30.00-50.00

Even though surface area of sepiolite increases with acid treatment, it destroys the minerals present in the structure and produces amorphous silica. In order to preserve minerals for this application, we have taken sepiolite as such, with simple dry grinding for 30 min. to get fine particles without structural alteration [124].

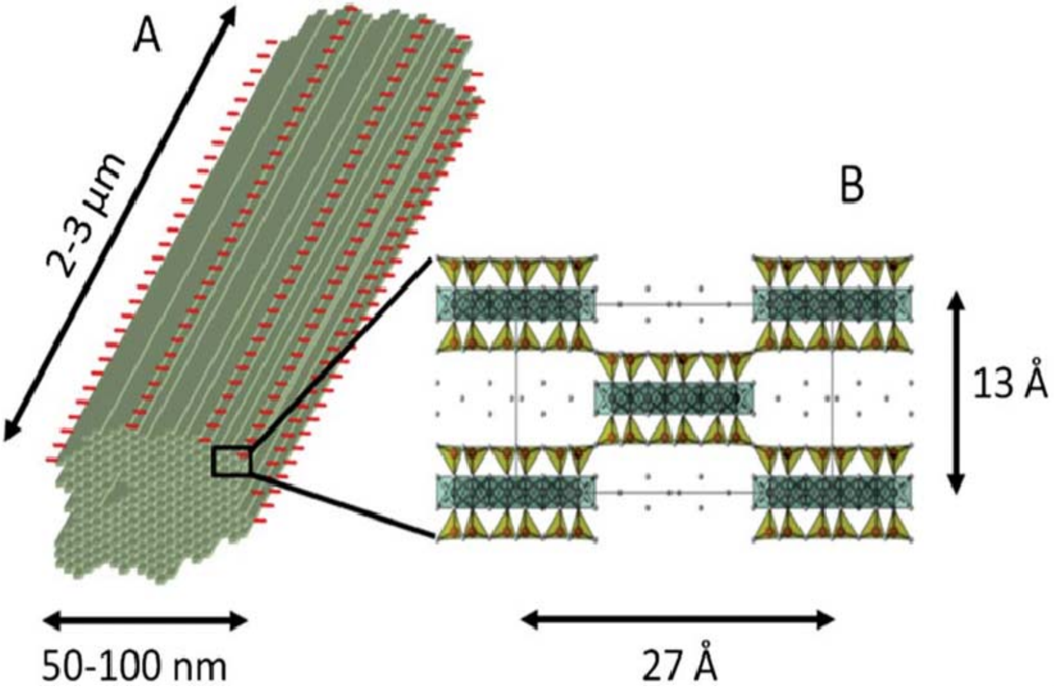

Fig. 3.19 (A) Microstructure of a sepiolite natural nanofibre; and (B) sepiolite crystalline structure showing Si tetrahedra (in yellow) and Mg octahedral (in green), viewed along the c axis according to Brunauer and Preisinger. Oxygen atoms (in grey) representing water molecules are visible within the channels and tunnels of the fibres.(Reproduced from ref. 134)

In this chapter, mesoporous FNST photo-catalyst with different loading (10%, 25%, 50%, 75% of FNST) has been supported on sepiolite clay matrix. Sepiolite has been added during the synthesis of tri-doped meso porous TiO_2 by hydrothermal method (Chapter. 2. Section 2.2.4). Sepiolite supported catalysts were characterized by XRD, DRS-UV, X-ray photoelectron spectroscopy, Raman spectra, nitrogen adsorption and desorption, BET surface area analysis, PL spectra, SEM and EDAX. Activity of the catalysts for PCRC was evaluated. Optimum amount of FNST loading on sepiolite, metal oxide support interactions and band structure of FNST are for factors responsible for this crucial application.

3.2.3 Results and discussion

3.2.3.1 X-ray diffraction

Fig. 3.20 shows X-ray diffraction patterns of unsupported FNST (Fe-N-S/TiO_2) photo-catalysts and when supported on sepiolite. Fig. 3.20a shows diffraction peaks at 2θ values- 25.2 (101), 36.9 (004), 48.0 (200) and 62.7 (204) which correspond to anatase phase of prepared FNST [108-110]. Fig. 3.20b shows the characteristic diffraction peaks of sepiolite at 2θ values - 7.4 (110), 17.7 (150), 20.2 (060), 26.7 (241) and 33.6 (371) [128, 135-138].

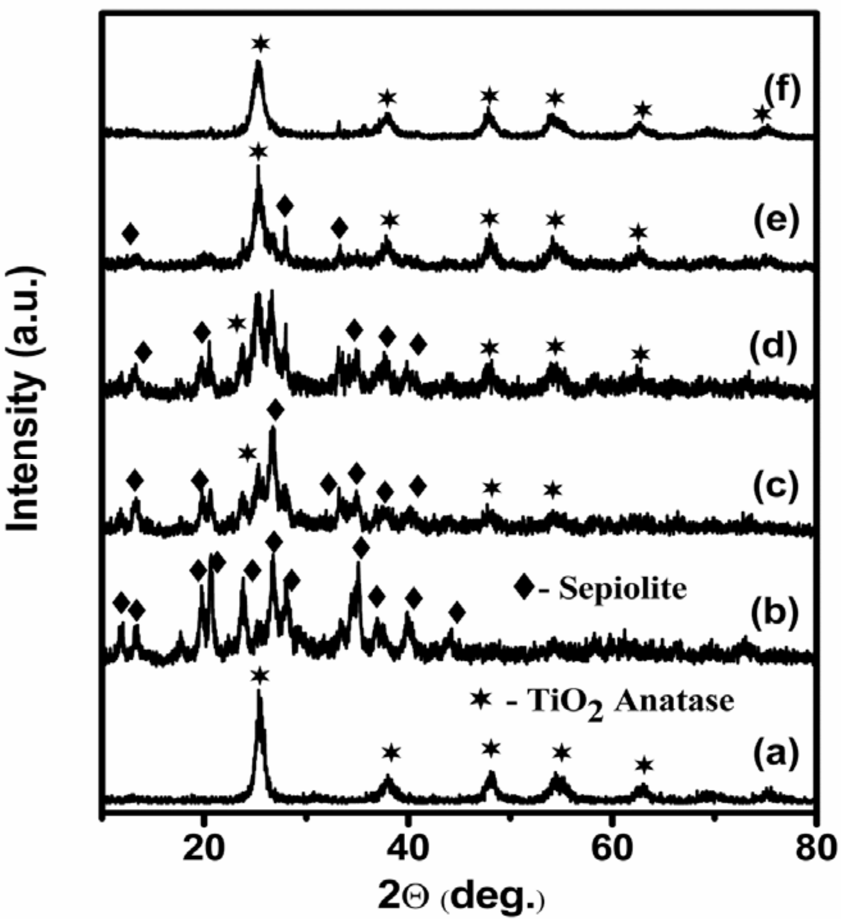

Fig. 3.20 XRD patterns for neat and sepiolite supported FNST (a) FNST, (b) pristine Sepiolite (c) 10% FNST/Sep. (d) 25% FNST/Sep. (e) 50% FNST/Sep. (f) 75% FNST/Sep.

In the case of Fe-N-S co-doped TiO_2 (FNST), there is no significant change in XRD patterns when compared to pristine TiO_2. No diffraction peak related to Fe_2O_3 was found, possibly due to low concentration of dopant element or may be a part of Fe has been incorporated into the TiO_2 lattice due to closer ionic radii of dopant Fe^{3+} (0.64 Å) and Ti^{4+} (0.61 Å). In Fig. 3.20c, and d, diffraction peaks corresponding to both FNST and sepiolite phases are observed, clearly showing that FNST particles are dispersed on the surface of sepiolite. Whereas in Fig. 3.20e and f, diffraction peaks mainly due to FNST particles are observed and no significant peak due to sepiolite was observed. This can be ascribed that the high quantity (50 wt% and 75 wt%) of crystalline FNST particles present in those systems as compared to sepiolite. The crystallite size of the prepared samples calculated using Scherrer's equation and lattice parameters calculated for tetragonal TiO_2 system are shown in Table 3.6. It can be seen that lattice parameters for FNST and cell volume have not significantly changed even when sepiolite content is high, implying that the components, FNST & sepiolite, exist as two distinct phases .

3.2.3.2 Raman Spectra

Raman spectra are useful indistinguishing various phases of titanium dioxide, due to its capability of elucidating structural complexity, as distinct peaks, clearly separated in frequency [41-47]. Fig. 3.21 shows the Raman spectra for the neat and sepiolite supported photo-catalysts. Six fundamental transition modes manifest as peaks, at 146 cm^{-1}, 199 cm^{-1}, 397 cm^{-1}, 519 cm^{-1} and 640 cm^{-1}, corresponding to E_g, E_g(weak), $B1_g$, A_{1g}+B_{1g} and E_g respectively. The observed results suggest that anatase is the predominant phase formed by the synthesis method adopted for titanium dioxide nanoparticles.

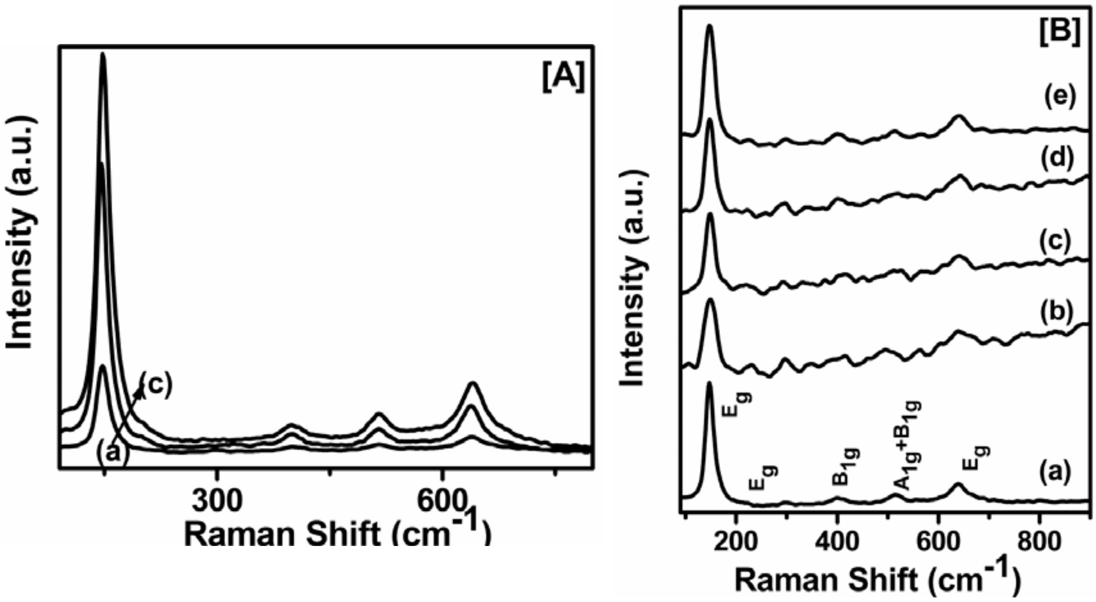

Fig. 3.21 Raman Spectra for [A] neat and modified TiO_2- (a) TiO_2, (b) NS/TiO_2, (c) FNST. [B] Sepiolite loaded FNST catalyst- (a) FNST (b) 10% FNST/Sep. (c) 25% FNST/Sep. (d) 50% FNST/Sep. (e) 75% FNST/Sep.

It can be clearly seen from Fig. 3.21 [A] that, the peak intensity is increased with broadening of peak and also slight shift in frequency towards higher wave number is observed on modified TiO_2 photo-catalysts. These changes could be ascribed due to the effects of decreasing particle size on the force constant and vibrational amplitudes of the nearest neighbour bonds [42, 100]. Results indicate that on doping with Fe-N-S, TiO_2 crystallite size of the nanoparticles decreases doped elements have been incorporated into the titanium dioxide lattice as evidenced from XRD pattern. Fig. 3.21 [B] shows the Raman spectra for different loading of FNST on sepiolite, six foundational Raman modes for anatase phase TiO_2 are seen clearly. No significant peaks due to sepiolite is seen, since pristine sepiolite is Raman inactive due to strong fluorescence effect [139, 140].

3.2.3.3 DRS UV-Visible Spectra

DR spectra in UV-Visible region for neat FNST and sepiolite supported FNST catalysts are shown in Fig. 3.22. In Fig. 3.22e, the absorption band edge for FNST is observed at 458 nm, which represents the red shifted band edge as compared to pristine band edge of TiO_2 at 387.5 nm. This can be ascribed to the synergetic effect of Fe-N-S tri-doping, which leads to formation of impurity level between band gap, which is responsible for absorption in visible region.

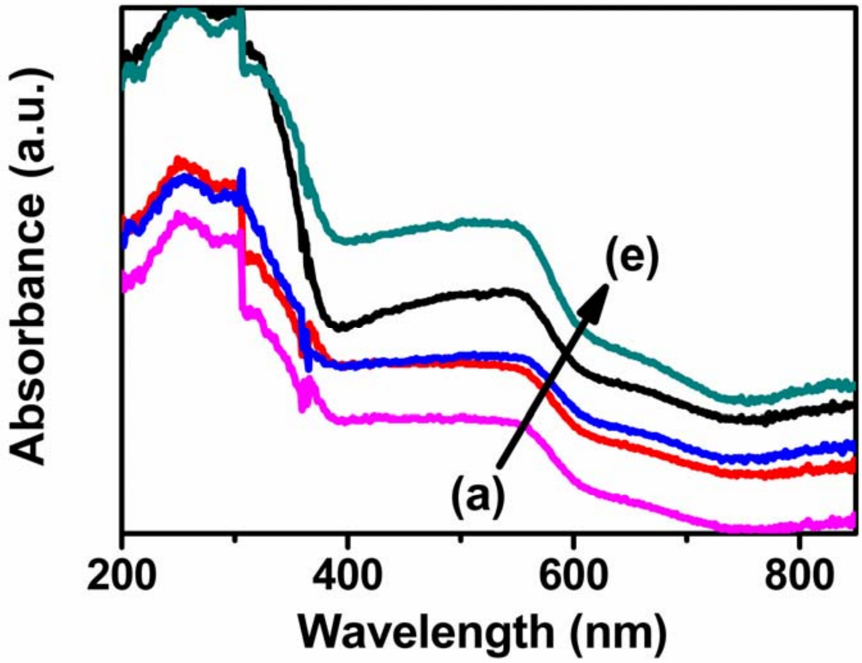

Fig. 3.22 Diffuse Reflectance spectra for sepiolite loaded FNST; (a) 10% FNST/Sep. (b) 25% FNST/Sep. (c) 50% FNST/Sep. (d) 75% FNST/Sep. (e) FNST.

A prominent peak at 510 nm could be due to d-d transition ${}^2T_{2g} \rightarrow {}^2A_{2g}$, ${}^2T_{1g}$ of Fe^{3+} or charge transfer transition between iron ions ($Fe^{3+} + Fe^{3+} \rightarrow Fe^{4+} + Fe^{2+}$). These results are consistent with the previously reported Fe doped and Fe-N-S tri-doped TiO_2 photo catalyst [100-110]. Fig. 3.22a-d shows absorption spectra for sepiolite containing different loadings of FNST. It can be clearly seen that there is no significant shift on either side of the wavelength region. Band gap energy values calculated using the formula 1240/λ, where λ is the wavelength of absorption, are listed in Table 3.6. These observations indicate that the optical characteristics of FNST photo catalyst have not been significantly affected by supporting on sepiolite.

Table 3.6 Structural and Textural Properties of photo catalysts

Photo catalyst	Lattice parameter (Ȧ)		Cell volume	Average crys. Size (nm)		Textural Properties			Band gap
	a=b	c	$(Ȧ)^3$	D^a	D^b	S_{BET} ($m^2\,g^{-1}$)	V_p ($cm^3\,g^{-1}$)	D_p (nm)	(eV)
FNST	3.762	9.42	133.318	8.7	12.4	124	0.28	9.1	2.71
Sepiolite	-	-	-	4.2	11.7	132	0.4	13.2	nd
10% FNST/ Sep.	3.489	10.95	133.318	7.6	11.6	133	0.44	13.4	2.8
25% FNST/ Sep.	3.792	9.508	136.718	12	12.1	127	0.36	13.2	2.76
50% FNST/ Sep.	3.794	9.508	136.862	9.6	12.3	125	0.34	10.9	2.76
75% FNST/ Sep.	3.812	9.496	137.989	8.1	10.1	151	0.37	9.2	2.78

[a] Crystalline size calculated using scherrer's equation

[b] Average crystalline size calculated using SA= $6*10^3$/ (L*density) [SA = Surface Area, L = Average Crystallite size, density = 3.9 g/cm^3]. nd - not determined.

3.2.3.4 Surface Area Analysis

Nitrogen adsorption and desorption isotherms and pore size distribution curves for neat FNST, neat sepiolite and FNST supported sepiolite samples are given in Fig. 3.23 and Fig. 3.24. All the prepared catalyst display (Fig. 3.23 a-f) Type IV isotherm with H1 type hysteresis loop at relative pressure range of 0.6-1.0, revealing the presence of mesoporosity. Fig. 3.24 represents the pore size distribution by BJH method for the prepared catalysts, from adsorption branch of the isotherms.

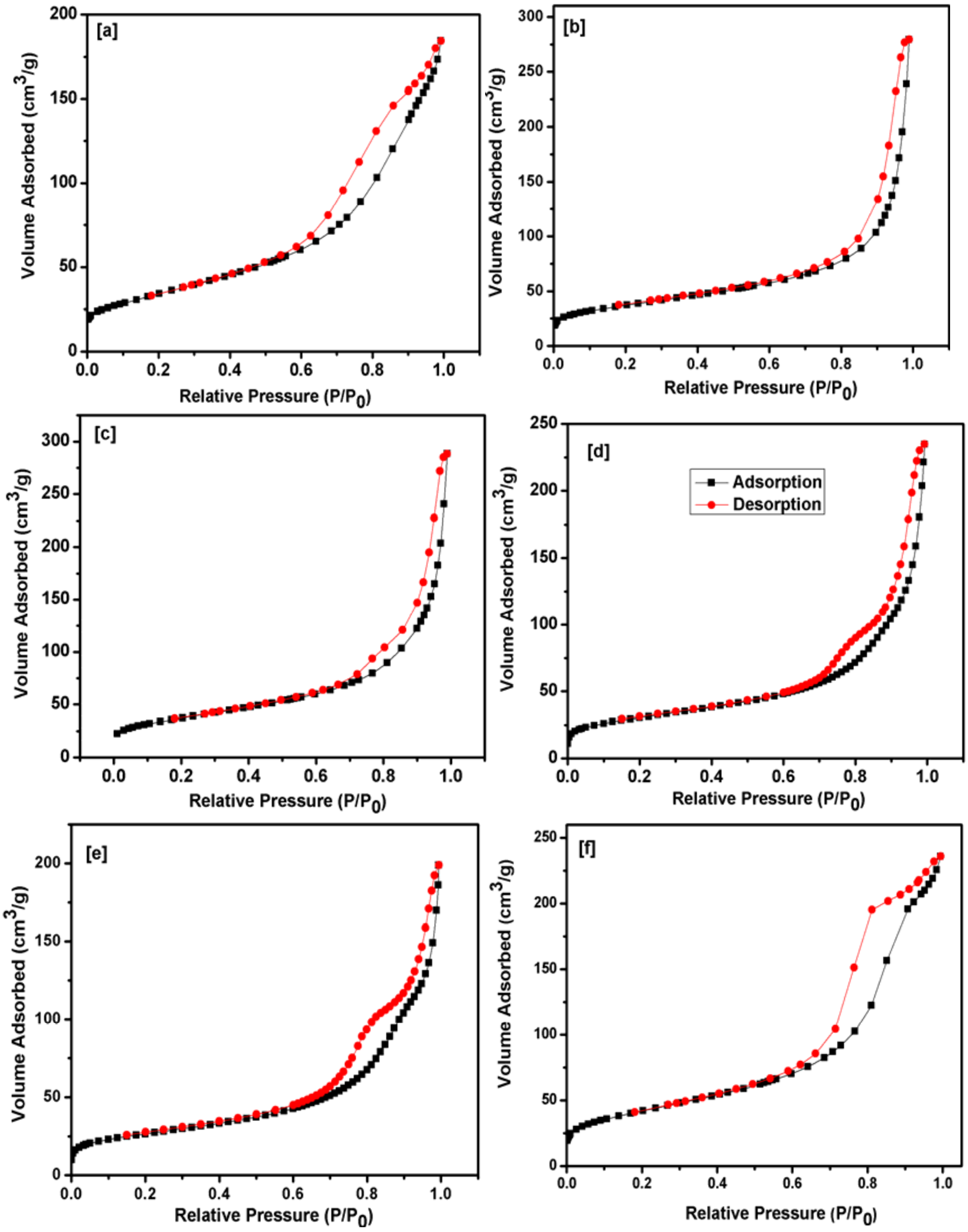

Fig. 3.23 N_2 adsorption desorption isotherms of FNST and sepiolite loaded photocatalysts; (a) FNST, (b) pristine Sepiolite (c) 10% FNST/Sep. (d) 25% FNST/Sep. (e) 50% FNST/Sep. (f) 75% FNST/Sep.

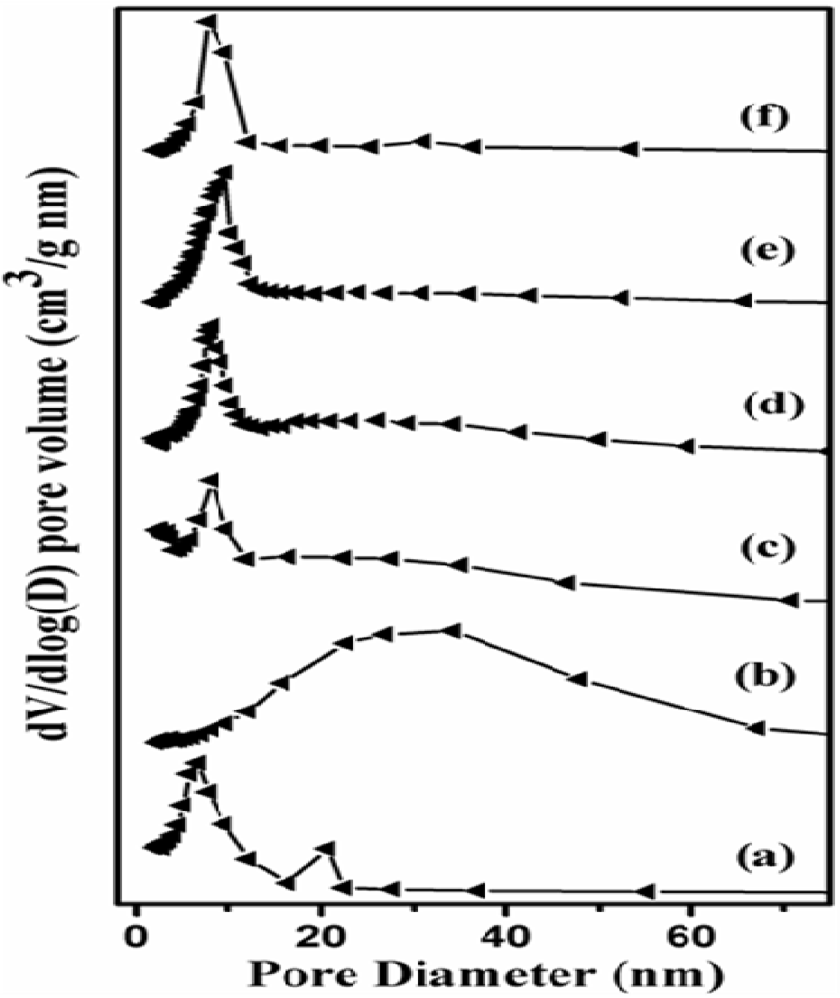

Fig. 3.24 Pore size distribution of FNST and sepiolite loaded photocatalysts; (a) FNST, (b) pristine Sepiolite (c) 10% FNST/Sep. (d) 25% FNST/Sep. (e) 50% FNST/Sep. (f) 75% FNST/Sep.

Narrow pore size distribution for both neat and supported systems of FNST/sepiolite are observed [39-41, 114-116]. Textural properties such as surface area, pore diameter and pore volume are listed in Table 3.6. Surface area of FNST decreased compared to neat TiO_2 as mentioned in previous chapter Table 3.1. Co doping of Fe, N-S into the TiO_2 might have blocked the pores of the parent material. It is clearly seen that, in Fig. 3.23c-d nitrogen adsorption-desorption isotherm curves are similar to that for sepiolite when the sepiolite content is high (90%, 75%), whereas the 75% FNST/Sep (Fig. 3.23f) shows textural characteristics of FNST. In the case of 50% FNST/Sepiolite (Fig. 3.23e) composite isotherm curve clearly indicates that it contains the porous characteristics of both FNST and sepiolite. Similar trend was observed with pore size distribution (Fig. 3.24) curves too. Hence the above results suggested that, pore structures of both FNST and sepiolite have been retained in the supported system.

3.2.3.5 Scanning Electron Microscopy Analysis

The morphology and dispersion of FNST particles on the sepiolite has been scrutinized by using SEM. The SEM images for the neat FNST and FNST/sepiolite samples are shown in Fig. 3.25. Fig. 3.25a clearly shows that fine spherical particles are present in the synthesized FNST. Fig. 3.25b image signifies the presence of fibrous morphology in sepiolite. whereas Fig. 3.25c-f SEM images reveal that the FNST active photo catalysts were finely dispersed on the external surface of sepiolite as spherical particles which increase with the increase in FNST (25%, 50%, 75%) content in supported system. In the case of 75% of FNST/Sep photo catalyst almost all the particles are spherical and it looks like neat FNST image, with very little fibrous morphology of sepiolite.

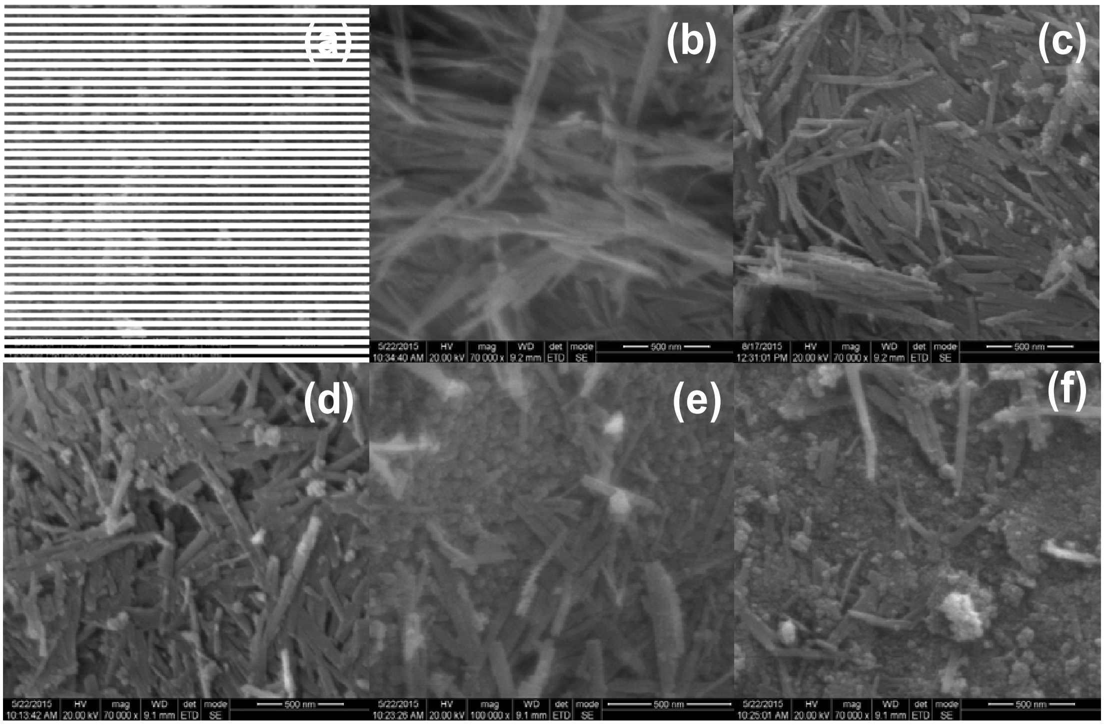

Fig. 3.25 SEM images for the FNST and sepiolite supported photo catalysts; (a) FNST, (b) pristine Sepiolite (c) 10% FNST/Sep. (d) 25% FNST/Sep. (e) 50% FNST/Sep. (f) 75% FNST/Sep.

3.2.3.6 EDAX Spectra

Elemental composition of the prepared photo catalysts has been analysed by energy-dispersive X-ray spectroscopy analysis. In Fig. 3.26a, the presence of signals due to Fe, N and S with Ti and O indicates that the doped elements (Fe, N and S) are present in the TiO_2 matrix. Fig. 3.26b shows the occurrence of many elements such as Si, Al, Mg, Fe, K and O in fibrous sepiolite matrix. Fig. 3.26c-f, the presence of both sepiolite and FNST elements are indicated. FNST supported on sepiolite has been prepared by hydrothermal method which has ensured the presence of all dopants, along with those present in sepiolite.

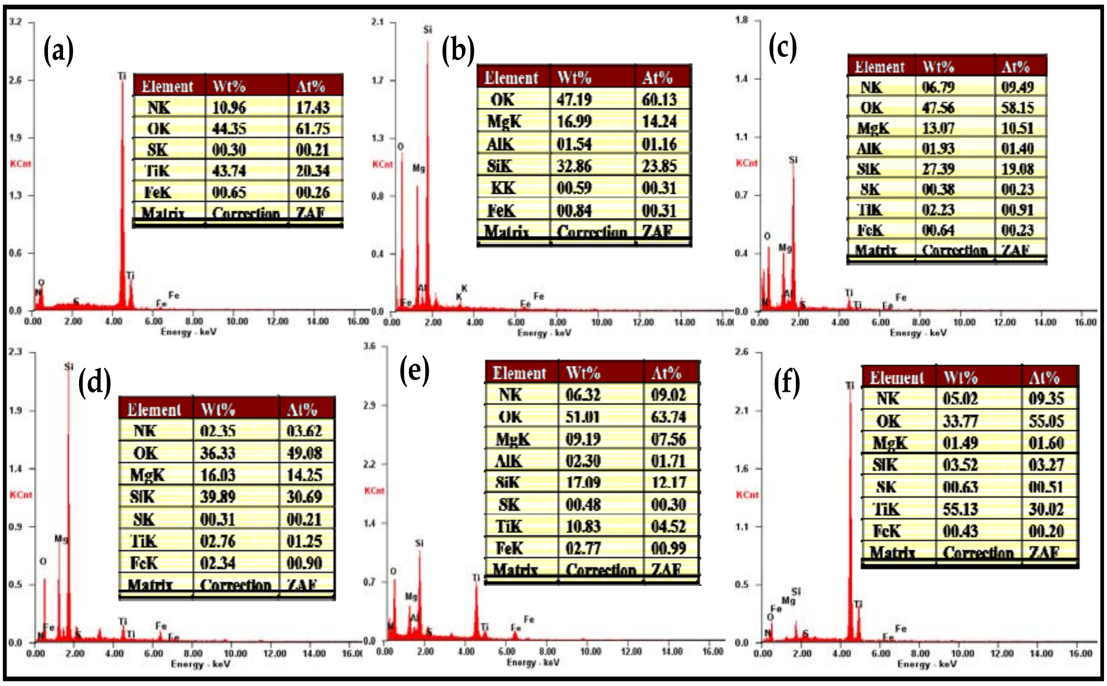

(a)

Element	Wt%	At%
NK	10.96	17.43
OK	44.35	61.75
SK	00.30	00.21
TiK	43.74	20.34
FeK	00.65	00.26
Matrix	Correction	ZAF

(b)

Element	Wt%	At%
OK	47.19	60.13
MgK	16.99	14.24
AlK	01.54	01.16
SiK	32.86	23.85
KK	00.59	00.31
FeK	00.84	00.31
Matrix	Correction	ZAF

(c)

Element	Wt%	At%
NK	06.79	09.49
OK	47.56	58.15
MgK	13.07	10.51
AlK	01.93	01.40
SiK	27.39	19.08
SK	00.38	00.23
TiK	02.23	00.91
FeK	00.64	00.23
Matrix	Correction	ZAF

(d)

Element	Wt%	At%
NK	02.35	03.62
OK	36.33	49.08
MgK	16.03	14.25
SiK	39.89	30.69
SK	00.31	00.21
TiK	02.76	01.25
FeK	02.34	00.90
Matrix	Correction	ZAF

(e)

Element	Wt%	At%
NK	06.32	09.02
OK	51.01	63.74
MgK	09.19	07.56
AlK	02.30	01.71
SiK	17.09	12.17
SK	00.48	00.30
TiK	10.83	04.52
FeK	02.77	00.99
Matrix	Correction	ZAF

(f)

Element	Wt%	At%
NK	05.02	09.35
OK	33.77	55.05
MgK	01.49	01.60
SiK	03.52	03.27
SK	00.63	00.51
TiK	55.13	30.02
FeK	00.43	00.20
Matrix	Correction	ZAF

Fig. 3.26 EDAX spectra for the FNST and sepiolite loaded photocatalysts; (a) FNST, (b) pristine Sepiolite (c) 10% FNST/Sep. (d) 25% FNST/Sep. (e) 50% FNST/Sep. (f) 75% FNST/Sep.

3.2.3.7 X-ray Photoelectron Spectroscopy

As stated in the previous section, chemical composition and chemical states of the doped elements can be identified by XPS analysis. The typical survey spectra for synthesized FNST and 50% FNST/Sep photo-catalysts are shown in Fig. 3.27. Binding energy values of main XPS peaks for the possible elements present in the synthesized materials are tabulated in Table 3.7 and chemical composition of the elements present in the prepared materials are listed in Table 3.8. In Fig. 3.27a, survey spectra show the presence of elements such as Ti, O, Fe, N and S. In Fig. 3.27b, along with the elements corresponding to FNST photo catalyst, an extra peak for Si present in sepiolite matrix is observed, suggesting that, all the doped elements and basic support matrix elements are available in the supported photo catalyst. High resolution XPS spectra for Ti 2p and O 1s are shown in Fig. 3.28. In Fig. 3.28a, Ti 2p peaks centered at 458.6 eV and 464.2 eV corresponding to Ti^{4+} $2p_{3/2}$ and Ti^{4+} $2p_{1/2}$ levels respectively are observed. No significant changes are observed with 50% FNST/Sep. system. In Fig. 3.28b, O 1s peak centered at 529.6 eV on deconvolution, shows a small peak centered at 531.4 eV due lattice oxygen of Ti-O-Ti in octahedral TiO_6 unit and surface OH groups or adsorbed oxygen on the surface respectively [30-38].

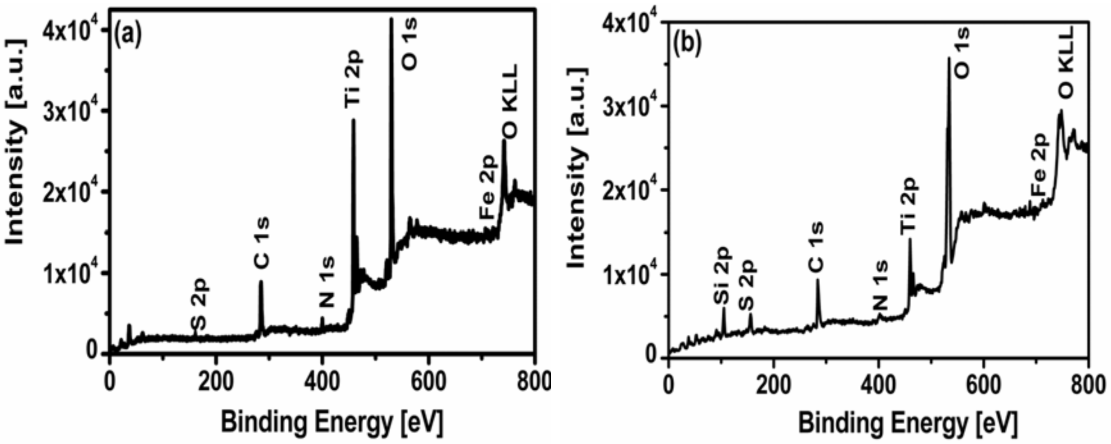

Fig. 3.27 XPS survey spectra of (a) FNST (b) 50% FNST/Sep.

Table 3.7 Binding energy of main XPS peaks for neat FNST and Sepiolite loaded.

Photo catalysts	Binding Energy (eV)									
	Ti		**O**		**N**		**S**	**Fe**		**Si**
	($2p_{3/2}$)	($2p_{1/2}$)	(O^{2-})	OH	Ti-N	Ti-N-O_x	SO_x	($2p_{3/2}$)	($2p_{1/2}$)	2p
FNST	458.5	464.3	529.7	531.0	399.6	-	168.4	710.96	720.9	-
50% FNST/Sep	458.7	464.4	531.4	532.0	397.1	398.9; 401.1	168.2	709.0	722.6	103.6

High resolution spectra of N 1s peak is centered at 399 eV for FNST, whereas for 50% FNST/Sep. composite, the N 1s peak appeared as a broad spectrum, which on deconvolution shows three peaks, centered at 396.7 eV, 399 eV and 400.8 eV as shown in Fig. 3.29[A]. The peaks centered at 396.7 eV and 399 eV correspond to binding energy for N-Ti-N bond and N-Ti-O bond respectively, suggesting that the doped nitrogen is substituted for the lattice oxygen in TiO_2 crystal structure. Whereas the peak at 400.8 eV corresponds to surface oxidized form of nitrogen such as Ti-N-O bond, suggesting that some of the doped nitrogen is also present in the interstitial position of TiO_2 lattice in the supported system [49-54].

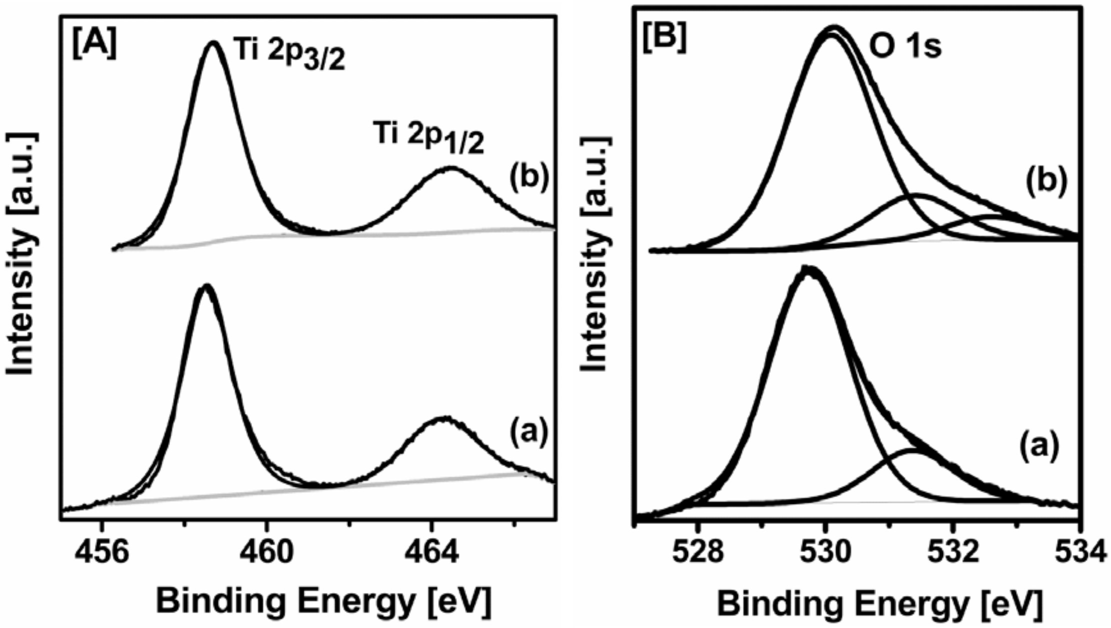

Fig. 3.28 High resolution XPS spectra for [A] Ti 2p, [B] O1s of (a) FNST (b) 50% FNST/Sep.

High resolution spectra of Fe 2p are shown in Fig. 3.29 [B]. The peaks centered at 711.8 eV and 723.9 eV correspond to Fe $2p_{3/2}$ and Fe $2p_{1/2}$ respectively, indicating that doped Fe is present predominantly in Fe^{3+} state. The observed binding energy of 711.9 eV for Fe^{3+} is higher compared to that for Fe^{3+} (710.7 eV) in precursor Fe_2O_3, suggesting some interactions in the Fe-N-S co-doped TiO_2[103]. XPS results for both FNST and FNST loaded sepiolite clearly reveal that Fe^{3+} has been incorporated into the Ti^{4+} site in the lattice of TiO_2 since ionic radii of Fe^{3+} (0.64 Å) and Ti^{4+} (0.61 Å) are closer [88-99]. Fig. 3.29 [C] shows high resolution spectra for S 2p centered at 168.1 eV both in neat FNST and 50% FNST/Sep, system corresponding to cationic form of S (as S^{6+} ion) as observed in the previous section. As mentioned in the earlier section, substitution of Ti^{4+} by S^{6+} is favorable as compared to substitution as S^{2-} into oxygen lattice, due to dissimilar ionic radii of O^{2-}(1.4 Å) and S^{2-}(1.84 Å)[22, 31, 32, 35, 38, 52]. Hence doped S exists in cationic state, with substitution of Ti^{4+} in titania lattice. Such substitutions are observed in the FNST photo catalyst as well as in FNST/Sep. supported systems.

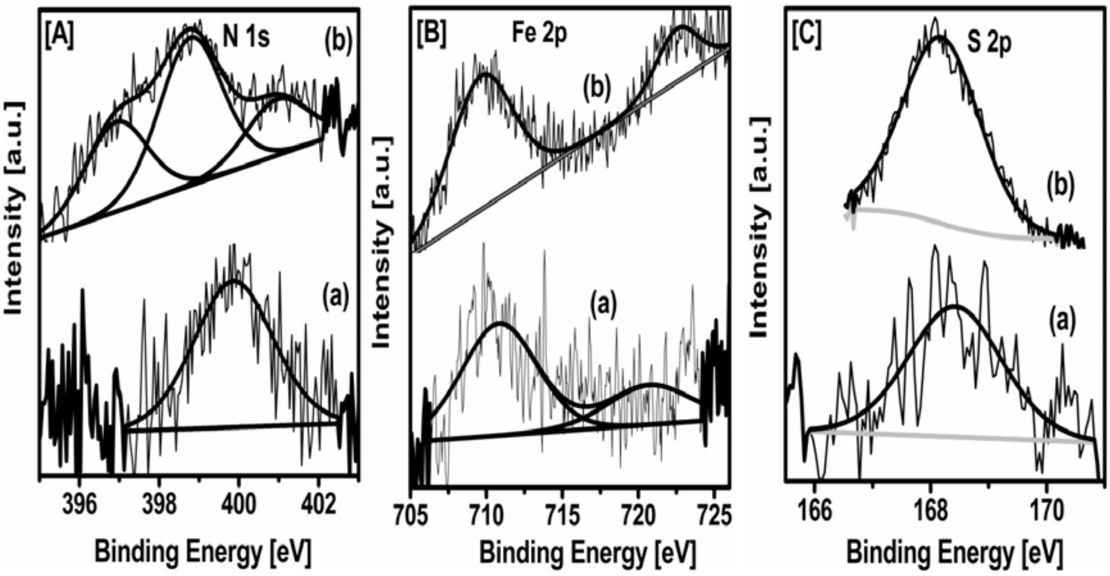

Fig. 3.29 High resolution XPS spectra for [A] N1s, [B] Fe 2p [C] S 2p of (a) FNST (b) 50% FNST/Sep.

Table 3.8 Elemental composition from XPS data

Photo catalysts	Composition (%)					
	Ti	**O**	**N**	**S**	**Fe**	**Si**
FNST	26.9	67.01	1.939	3.964	1.316	-
50% FNST/Sep.	12.14	51.23	2.54	1.402	0.256	15.47

3.2.3.8 Photoluminescence Spectra

Photoluminescence (PL) spectrum is an important tool to describe the recombination rate of charge carriers, since this spectrum is the result of recombination of excited charge carriers. Appearance of high intensity emission lines indicate high recombination rate while lower intensity peak represents slower recombination rate/prolonged life time of charge carriers. Fe-N-S tri-doped TiO_2 shows less intense peak compared to co-doped/mono/pristine TiO_2 as shown in Fig. 3.30A, indicating that Fe-N-S tri-doped elements significantly increase the life time of charge carriers. In Fig. 3.30B, PL spectra of FNST supported on sepiolite porous structure, shows less intense peaks compared to that for FNST photo-catalyst. As reported earlier, clay structured material can trap photo generated charge carriers and consequently retarded their recombination [112, 141]. Thus, FNST supported on sepiolite acts as efficient charge transfer material. This is necessary for efficient photo-catalytic process.

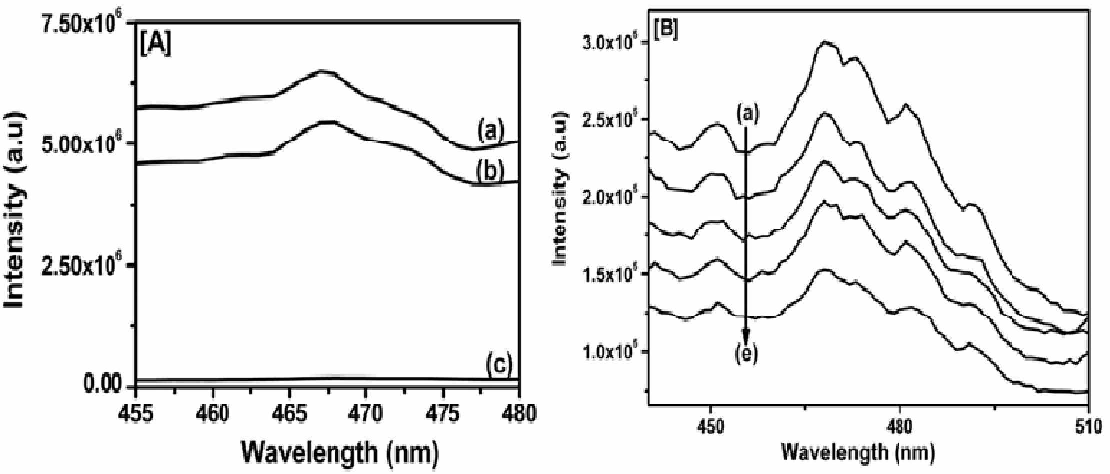

Fig. 3.30 Photoluminescence Spectra for neat and modified TiO_2 [A]; (a) TiO_2, (b) NS/TiO_2, (c) FNST. Sepiolite loaded FNST catalyst [B]; (a) 10% FNST/Sep. (b) 25% FNST/Sep. (c) FNST (d) 50% FNST/Sep. (e) 75% FNST/Sep.

3.2.4 Photo catalytic reduction of Carbon dioxide

Activity of all the prepared photo-catalyst composites was evaluated for PCRC with water. The experimental conditions for evaluation of activity have been described in Chapter 2 Section 2.4. Products obtained were mainly methanol with minor quantity of ethanol and trace quantities of methane, ethylene, ethane, propylene and hydrogen. CO and HCHO were also detected but could not be quantified. Trends in the formation of major products such as methanol and ethanol at different intervals up to 20 hrs of irradiation, are shown in Fig. 3.31. Formation rate of CO_2 photo-reduced products are calculated and listed in Table 3.9. Apparent quantum yields (AQY) for all the catalysts were calculated from the number of photoelectrons involved in the reduced products, shown in Table 3.9. As stated in the Chapter 3.1, in alkaline reaction medium, OH^- ions act as an efficient hole scavengers and increase the life time of photo-generated charge carriers, increases solubility of CO_2 and also the formation of HCO_3^- species in alkaline solution at the experimental condition.

Generally in aqueous phase reaction, suspended photo-catalyst surface is covered with large quantity of H_2O molecules, consequently more concentration of OH groups on the active surface, which facilitates selectivity towards CH_3OH [142].

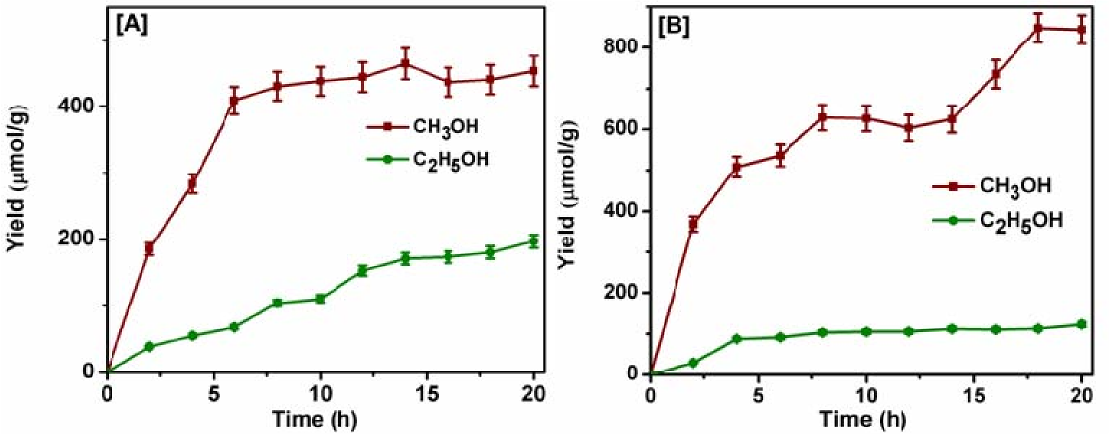

Fig. 3.31 Trends in products distribution during CO_2 photo reduction [A] FNST, [B] 50% FNST/Sep.

Table 3.9 Products distribution and quantum yield data for neat and sepiolite loaded FNST.

Photo catalyst	**Products formed after 20 hrs of irradiation (μmol g^{-1} h^{-1})**							**AQY x 10^{-3} (%)**
	CH_4	**C_2H_4**	**C_2H_6**	**CH_3OH**	**C_2H_4O**	**C_2H_5OH**	**C_3H_6**	
FNST	0.07	0.06	0.04	53.5	0.1	12.2	0.05	8.77
10% FNST/ Sep.	0.05	0.1	0.02	48.5	0.2	11.3	0.04	8.00
25% FNST/ Sep.	0.2	0.21	0.05	60.3	0.05	13.1	0.00	9.57
50% FNST/ Sep.	0.11	0.12	0.11	79.5	0.17	12.9	0.05	11.87
75% FNST/ Sep.	0.09	0.08	0.02	52.1	0.04	11.7	0.1	8.63

Total carbon products obtained from CO_2 photo-reduction by the synthesized photo-catalyst composites after 20 hrs of photo-irradiation are shown in Fig. 3.32. It is clearly seen that, FNST gives higher product yield compared to N-S co-doped TiO_2. Hence doped Fe plays crucial role in CO_2 photo-reduction as observed in the earlier literature reports [88-110]. Fe doping on TiO_2 significantly enhances visible light absorption, since the energy level of Fe^{3+}/Fe^{2+} (0.77 V vs NHE) lies close to that of Ti^{3+}/Ti^{4+} and consequently forming localized energy level below the conduction of

TiO_2 (-0.7 V vs NHE). Hence the band gap is reduced, as shown in Fig. 3.33 and also supported by the experimental evidence from DR spectra (Fig. 3.22).

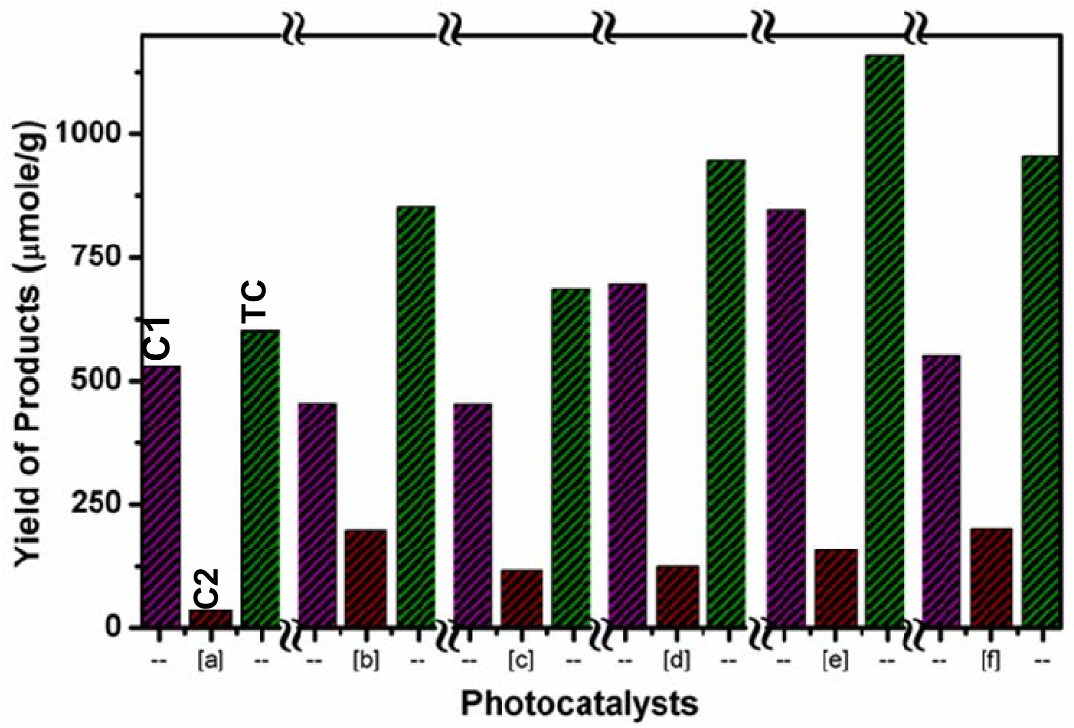

[C1- C1 carbon products, C2 - C2 carbon products, TC-Total carbon products]

Fig. 3.32 Comparison of photo-catalytic activity for neat and modified TiO_2 after 20 hrs of irradiation: (a) NS/TiO_2, (b) FNST, (c) 10% FNST/Sep. (d) 25% FNST/Sep. (e) 50% FNST/Sep. (f) 75% FNST/Sep.

The newly generated impurity energy level is below the conduction band. Fe^{3+} can trap holes, since Fe^{3+}/Fe^{4+} (2.2 V vs NHE) is more positive compared to VBM (2.43 V vs NHE) of TiO_2, and subsequently increases the life time of photo generated charge carriers as evidenced form PL spectra (Fig. 3.30). Doped Fe^{3+} having special kind of trapping and detrapping characteristics, when Fe^{3+} accepts (traps) hole from VBM it becomes Fe^{4+}, whereas Fe^{3+} accepts electrons to form Fe^{2+}. The formed Fe^{2+} and Fe^{4+} both are unstable according to crystal field theory, and consequently both have the tendency to become Fe^{3+} due to its stable d^5 configuration [94]. In this way, the life time of photo-generated charge carriers increase, by trapping/de-trapping mechanism of doped Fe^{3+}. Such a mechanism helps in the transfer of charge carriers to the active surface where adsorbed reactants get reduced/oxidized into products. From Table 3.9, it is noticeable that, the rate of formation of C1 products are similar, whereas C2 products are almost double with FNST compared to N-S co doped TiO_2. The observed increased in activity with Fe doped photo catalyst is mainly due to the visible light absorption, efficient utilization of light irradiation and increase in life of charge carriers, which facilitate multi-electron reduction products compared to anion doping.

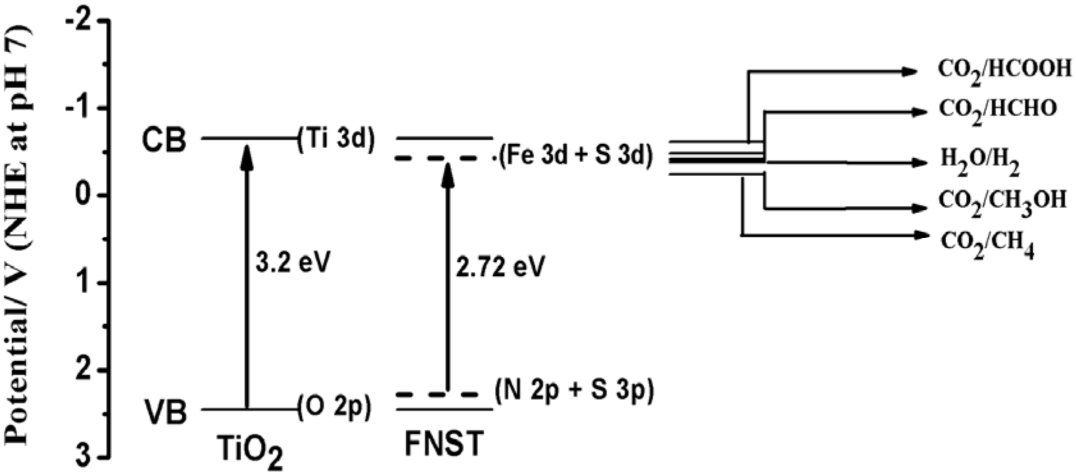

Fig. 3.33 VBM & CBM energy levels of TiO_2 and its Fe-NS modified catalysts vis-a-vis potential for reduction of CO_2 and oxidation of water.

In Fig. 3.32, it is clearly seen that, the photo-catalytic efficiency is increased when the loading of FNST increased from 10% to 50%, whereas 75%FNST/Sep. composite shows almost similar carbon product like bulk FNST photo-catalyst. The observed results reveal that FNST is the active photo-catalyst and there is synergism between active surface and clay structure which enhances the photo-catalytic efficiency of 50% FNST/Sep. composite. Such a trend and reduced product was obtained by H. C. Yang et al, who stated that, loading amount and dispersion of active TiO_2 on porous material has an impact on its efficiency and found that 45% of TiO_2 on SBA-15 shows optimum activity towards CO_2 photo reduction [143].

Generally photo-catalytic reaction mechanism involves five necessary steps, namely (i) adsorption of reactant molecules on the active surface, (ii) light absorption and creation of photo generated electron hole pairs, (iii) interaction of charge particles with adsorbed species/recombination of charge particles, (iv) reduction and oxidation on active surface, (v) desorption of products from the surface [141]. In Fig. 3.31, it is noticeable that, the initial rates of formation of reduced products are high with FNST/Sep. composite compared to FNST catalyst. This can be ascribed to the photo reduced products are adsorbed on the surface of active catalyst, result in decrease of photo reduction rate due to non-availability of pure active surface [144]. In heterogeneous catalysis reaction, the rate of particular reaction depends on the number of surface active sites and concentration of adsorbed species on its active surface. Dispersed FNST clay structure creates more active sites and also OH^- groups in clay structure facilitate adsorption of reactant molecules on the active surface. Photo generated electrons can be trapped by clay structure, which subsequently reduces electron hole recombination or charged particles reaches surface adsorbed species as shown in scheme 3.1. The increased in efficiency with 50% FNST/Sep. composite is mainly due to the enhancement of active surface which is favorable for CO_2 adsorption and prolong the life of charge carriers results in the formation of multi electron CO_2 reduced products.

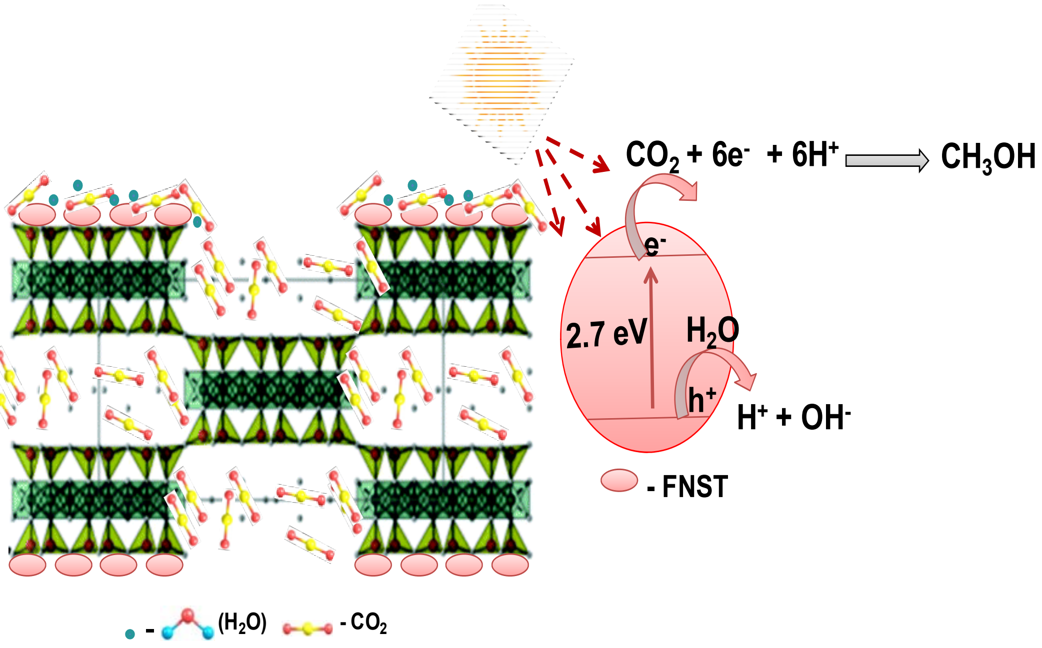

Scheme 3.1 Plausible mechanism for CO_2 photo reduction with water on FNST loaded on sepiolite.

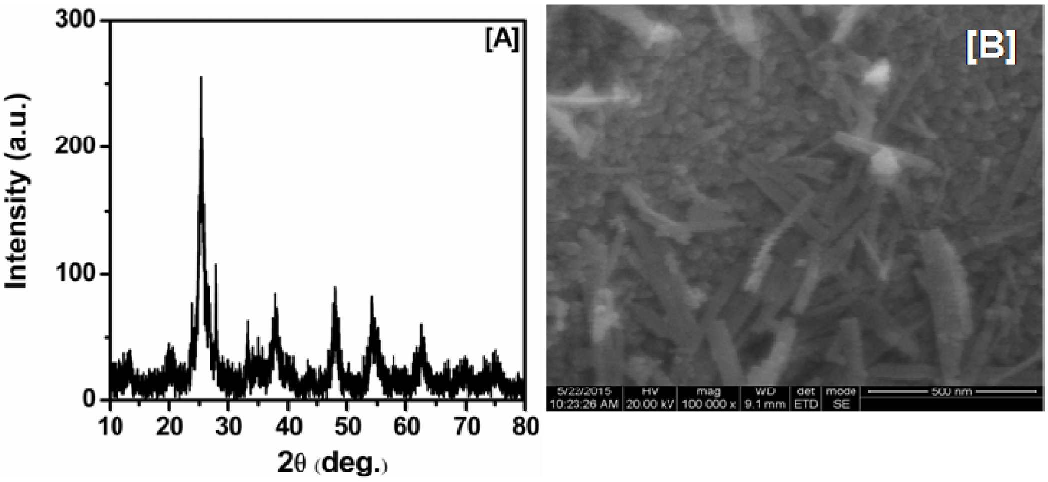

Fig. 3.34 XRD[A] data &SEM [B] for used after 20 hours of reaction50% FNST/Sep.

After 20 hrs of the irradiation, the used photo catalyst was centrifuged and dried at 373 K for 1 hr, characterized with XRD and SEM as shown in Fig. 3.34, the results reveal that photo catalyst structure and morphology were retained even after 20 hrs of irradiation. As stated earlier, NaOH as reaction medium plays multiple roles such as hole scavenger, increases solubility of CO_2 in reaction medium and facilitates formation of CO_2 reduced product, besides it helps to retain the clay structure even after 20 hrs of irradiation as evidenced from XRD (Fig. 3.34A) and SEM (Fig. 3.34B). When the reaction medium as water/acid medium, the minerals present in the sepiolite such as Ca, Mg and less amount of metals would be released from sepiolite structure [145].

3.2.5 Conclusions

Fe-N,S tri-doped titanium dioxide (FNST) and FNST loaded on sepiolite composite were synthesized by hydrothermal method. The effect of tri-doping on TiO_2 has been characterized by various techniques. Results imply that formed single phase anatase structure and also doped elements has been incorporated into the TiO_2 lattice as evidenced from XRD, Raman, EDAX and XPS data. DRS UV-Visible spectra reveal that, tri-doping causes band gap narrowing by creating impurity energy level below the CBM and above the VBM of Pristine TiO_2. PL spectra imply that retardation of charge carrier recombination rate by tri-doping as well as clay structured support.

Activity of the prepared composite materials was evaluated by photo catalytic reduction of carbon dioxide with water. Enhancement of photo catalytic efficiency with sepiolite composite compared to pristine FNST was observed. The synergetic effect of FNST and clay structure increases adsorption ability of reactant molecules, prolong life time of charge carriers by trapping and also better desorption of reduced product from active catalyst surface resulted in increasing photo catalytic activity. 50% FNST loaded on sepiolite is the optimum FNST loading which gives better photo catalytic activity compared to less/high concentration of FNST. Hence sepiolite can be employed as support for CO_2 photo reduction

3.3 References

1. A. Fujishima, K. Honda, Nature, 1972, 238, 37.
2. A. Fujishima, T. N. Rao, D. A. Tryk, J. Photochem Photobiol C Photochem Rev, 2000, 1, 1; O Carp, C L Huisman, A Reller, Prog Solid State Chem, 32 (2004) 33.
3. A. Fujishima, X. Zhang, C R Chim, 2006, 9, 750
4. A. Fujishima, X. Zhang, D. A. Tryk, Int. J. Hydrogen Energy, 2007, 32, 2664
5. F. E. Osterloh, Chem Mater, 2008, 20, 35.
6. V. Jeyalakshmi, R. Mahalakshmy, K.R. Krishnamurthy, B. Viswanathan, IJCA, 2012, 51A, 1263.
7. W. Zhou, H. Fu, Chem Cat Chem 2013, 5, 885.
8. D. G. Shchukin, J. H. Schattka, M. Antonietti, R. A. Caruso, J. Phys. Chem. B 2003, 107, 952.
9. X. Zhang, F. Zhang, K-Y Chan, Appl. Catal. A: General, 2005, 284, 193.
10. R. Asahi, T. Morikawa, T. Ohwaki, K. Aoki, Y. Taga, Science 2001, 293, 269.
11. T. Umebayashi, T. Yamaki, H. Itoh, K. Asai, Appl Phys Lett, 2002, 81, 454
12. S. U. M. Khan, M. Al-Shahry, W. B. Ingler, Science 2002, 5590, 2243.
13. J.C. Yu, J. Yu, W. Ho, Z. Jiang, L. Zhang, Chem Mater., 2002, 14, 3808
14. H. Irie, Y. Watanabe, K. Hashimoto, Chem Lett., 2003, 32, 772.
15. J.C. Yu, W. Ho, J. Yu, H. Yip, P. K. Wong, J. Zhao, Environ. Sci. Technol. 2005, 39, 1175.

16. M. Sathish, B. Viswanathan, R. P. Viswanath, C. S. Gopinath, Chem. Mater. 2005, 17, 6349.
17. K. Yang, Y. Dai, B. Huang, S. Han, J. Phys. Chem. B 2006, 110, 24011.
18. D.M. Chen, D. Yang, Q. Wang, Z.Y. Jiang, Chem Res., 2006, 45, 4110.
19. S. In, A. Orlov, R. Berg, F. Garcia, S. Pedrosa-Jimenez, M. S. Tikhov, D. S. Wright, R. M. Lambert, J. Am. Chem. Soc. 2007, 129, 13790.
20. L. Lin, W. Lin, J. L. Xie, Y. X. Zhu, B. Y. Zhao, Y. C. Xie, Appl. Catal., B 2007, 75, 52.
21. K. Yang, Y. Dai, B. Huang, J. Phys. Chem. C 2007, 111, 12086.
22. B. Naik, K. M. Parida, C. S. Gopinath, J. Phys. Chem. C 2010, 114, 19473.
23. F. Wei, L. Ni, P. Cui, J. Hazard. Mater. 2008, 156, 135.
24. J. Yu, M. Zhou, B. Cheng, X. Zhao, J. Mol. Catal. A: Chem. 2006, 246, 176.
25. J. Xu, J. Li, W. Dai, Y. Cao, H. Li, K. Fan, Appl. Catal., B 2008, 79, 72.
26. M. Satish, B. Viswanathan, R. P. Viswanath, C. S. Gopinath, J. Nanosci. Nanotechnol. 2009, 9, 423.
27. P. Xu, T. Xu, J. Lu, S. Gao, N.S. Hosmane, B. Huang, Y. Dai, Y. Wang, Energy Environ. Sci., 2010, 3, 1128.
28. K. Yang, Y. Dai, B. Huang, J. Phys. Chem. C 2007, 111, 18985.
29. B. Viswanathan, K. R. Krishnamurthy, Inter. J. Photo energy, 2012, Article ID 269654.
30. Y. Zhang, P. Liu, H. Wu, Applied Surface Science, 2015, 328, 335.
31. X. Li, R. Xiong, G. Wei, Catal Lett., 2008, 125, 104.
32. J.A. Rengifo-Herrera, E. Mielczarski, J. Mielczarski, N.C. Castillo, J. Kiwi, C. Pulgarin, Appl. Catal. B: Environ., 2008, 84, 448.
33. M. Ksibi, S. Rossignol, J-M Tatibouët, C. Trapalis, Materials Lett., 2008, 62, 4204–4206.
34. J.A. Rengifo-Herrera, K. Pierzchała, A. Sienkiewicz, L. Forro´, J. Kiwi, C. Pulgarin, Appl. Catal. B: Environ., 2009, 88, 398–406.
35. G. Yan, M. Zhang, J. Hou, J. Yang, Mater. Chem. & Phys., 2011, 129, 553.
36. M. Behpour, V. Atouf, Appl. Surf. Sci., 2012, 258, 6595.

37. P. Zhou, J. Yu, Y. Wang, Appl. Catal. B: Environ., 2013, 142– 143, 45.
38. Q. Xiang, J. Yu, M. Jaroniec, Phys. Chem. Chem. Phys., 2011, 13, 4853.
39. W-G Yang, F-R Wan, Q-W Chen, J-J. Li, D-S. Xu, J. Mater. Chem., 2010, 20, 2870.
40. C. C. Li, Y. P. Zheng, T. H. Wang, J. Mater. Chem., 2012, 22, 13216.
41. M. Gurulakshmi, M. Selvaraj, A. Selvamani, P. Vijayan, N.R. Sasi Rekha, K. Shanthi, Appl. Catal. A: General, 2012, 449, 31.
42. H.C. Choi, Y.M. Jung, S.B. Kim, Vib. Spectrosc., 2005, 37, 33.
43. Y. Xie, Q. Zhao, X. J. Zhao, Y. Li, Catal Lett., 2007, 118, 231.
44. X. Chen, S. S. Mao, Chem. Rev. 2007, 107, 2891.
45. Y. Cong, J. Zhang, F. Chen, M. Anpo, J. Phys. Chem. C 2007, 111, 6976.
46. H. Li , X. Zhang , Y. Huo , J. Zhu, Environ. Sci. Technol. 2007, 41, 4410.
47. M. Grandcolas, J. Ye, Sci. Technol. Adv. Mater., 2010, 11, 055001.
48. M. Kitano, K. Funatsu, M. Matsuoka, M. Ueshima, M. Anpo, J. Phys. Chem. B, 2006, 110, 25266.
49. X. Chen, C.B. urda, J. Phys. Chem. B, 2004, 108, 15446.
50. H. X. Li, J. X. Li, Y. I. Huo, J. Phys. Chem. B 2006, 110, 1559
51. B. Viswanathan.. Bull. Catal. Soc. India, 2003, 2, 71-74.
52. M. Sathish, Ph.D thesis 2006, IITM India
53. C. S Gopinath, J. Phys. Chem. B 2006, 110, 7079.
54. J.A. Rengifo-Herrera, C. Pulgarin, Solar Energy, 2010, 84, 37.
55. I-H. Tseng, W.C. Chang, J.C.S. Wu, Appl. Catal. B: Environ., 2002, 37, 37.
56. K. Ikeue, S. Nozaki, M. Ogawa, M. Anpo, Catal. Today, 2002, 74, 241.
57. I.-H. Tseng, J.C.S. Wu, H.-Y. Chou, J. Catal., 2004, 221, 432.
58. A.H. Yahaya, M.A. Gondal, A. Hameed., Chemical Physics Lett., 2004, 400, 206.
59. Slamet, H W. Nasution, E. Purnama, S. Koesla, Gunlauardi, Catal. Commun., 2005, 6, 313.
60. K. Koˇcí, K. Zatloukalova, L. Obalova, S. Krejcikova, Z. Lacny, L. Capek, A. Hospodkova, O. Solcova, Chinese J. Catal., 2011, 32, 812.

61. K. Kocí, M. Reli, O. Kozák, Z. Lacny, D. Plachá, P. Praus, L. Obalov, Catal. Today 2011, 176, 212.
62. C-W Tsai, H M Chen, R-S Liu, K. Asakura, T-S Chan., J. Phys. Chem. C 2011, 115, 10180.
63. M. Reli, M. Sihor, K. kočí, P. prau, O. kozák, L. obalová, Geo Science Engineering, 2012, LVIII, 34. ISSN 1802-5420.
64. X. Li, H. Liu, D. Luo, J. Li, Y. Huang, Y. Fang, Y. Xu, L. Zhu, Chem. Engg. Journal, 2012, 180, 151.
65. S. Naval, A. Dhakshinamoorthy, M. Alvaro, H. Garcia., Chem Sus Chem 2013, 6, 562.
66. E. Liu, L. Kang, F. Wu, T. Sun, X. Hu, Y. Yang, H. Liu, J. Fan, Plasmonics, 2014, 9, 61.
67. K. Li, A. D. Handoko, M. Khraisheh, J. Tang, Nanoscale, 2014, 6, 9767
68. B. Viswanathan, M. Aulice Scibioh, Photo electrochemistry principles and practices
69. Roland, Adv. Func. Mater., 2014, 24, 2421.
70. S. Kohtani, E. Yoshioka, H. Miyabe, Photocatalytic hydrogenation on semiconductor particles, http://dx.doi.org/10.5772/45732.
71. X. Yang, T. Xiao, P. P. Edwards, Inter. Journal of hydrogen energy, 2011, 36, 6546.
72. J.C.S. Wu, Catal. Surv. Asia, 2009, 13, 30.
73. N.M. Dimitrijevic, B.K. Vijayan, O.G. Poluektov, T. Raijh, K.A. Gray, H. He, P. Zapol, J. Am. Chem. Soc., 2011, 133, 3964
74. Y. Liu, B. Huang, Y. Dai, X. Zhang, X. Qin, M. Jiang, M.-H. Whangbo, Catal. Commun., 2009, 11, 210.
75. X-Y. Li, L-H. Chen, Y. Li, J. C. Rooke, C. Wang, Y. Lu, A. Krief, X-Y. Yang, B-L. Su, J. Colloid and Interface Sci., 2012, 368, 128.
76. Y. Li , Z-Y. Fu , B-L. Su, Adv. Funct. Mater. 2012, 22, 4634.
77. X. Li, Z. Zhuang, W. Li, H. Pan, Appl. Catal. A: General., 2012, 429, 31.

78. C. D. Valentin, G. Pacchioni, A. Selloni, S. Livraghi, E. Giamello, JPCB 2005, 109, 11414.
79. J-H. Xu, W-L Dai, J Li, Y Cao, H Li, H He, K Fan, Catalysis Comm., 2008, 9, 146.
80. C. Di Valentin, E. Finazzi, G. Pacchioni, A. Selloni, S. Livraghi, M.C. Paganini, E. Giamello, Chemical Phys., 2007, 339, 44.
81. H. Shen, L. Mi, P. Xu, W. Shen, P-N Wang, Appl. Surf. Sci., 2007, 253, 7024.
82. B. Michalkiewicz, J. Majewska, G. Kadziołka, K. Bubacz, S. Mozia, A. W. Morawski, J. CO_2 Utilization, 2014, 5, 47.
83. Z. Zhao, J. Fan, J. Wang, R. Li, Catal. Commun., 2012, 21, 32.
84. S. Zhou, Y. Liu, J. Li, Y. Wang, G. Jiang, Z. Zhao, D. Wang, A. Duan, J. Liu, Y. Wei, Appl. Catal. B Environ., 2014, 158–159, 20.
85. T. Phongamwong, M. Chareonpanich, J. Limtrakul, Appl. Catal. B:Environ., 2015, 168–169, 114.
86. M. Sathish, M. Sankaran, B. Viswanathan, R.P. Viswanathan, Indian J. Chem., 2007, 46a, 895.
87. H.X. Li, G.S. Li, J. Zhu, Y. Wan, J. Mol. Catal. A: Chem., 2005, 226, 93.
88. W. Choi, Catalysis Surveys from Asia, 2006, 10, 16.
89. X. Chen, S. S. Mao, Chem. Rev. 2007, 107, 2891.
90. S. Girish Kumar, L. Gomathi Devi, J. Phys. Chem. A, 2011, 115, 13211.
91. R. Daghrir, P. Drogui, D. Robert, Ind. Eng. Chem. Res. 2013, 52, 3581.
92. W. Choi, A. Termin, M. R. Hoffmann, JPC 1994, 98, 13669
93. A. Rolda´n, M. Boronat, A. Corma, F. Illas, J. Phys. Chem. C 2010, 114, 6511.
94. J. Yu, Q. Xiang, M. Zhou, Appl. Catal. B: Environ., 2009, 90, 595.
95. P. Goswami, J. N. Ganguli, Mater. Research Bulletin, 2012, 47, 2077.
96. Y. Wang, Z-H Jiang, F-J Yang, Mater. Sci. & Engi. B, 2006, 134, 76.
97. A.V. Vinogradov, V.V. Vinogradov, A.V. Agafonov, J. Alloys & Compds 2013, 581, 675.

98. X.H. Wang, J.G. Li, H. Kamiyama, M. Katada, N. Ohashi, Y. Moriyoshi, T. Ishigaki, J. Am. Chem. Soc. 2005, 127, 10982.
99. H. Yamashita, M. Harada, J. Misaka, M. Takeuchi, B. Neppolian, M. Anpo, Catal. Today, 2003, 84, 191.
100. Y. Cong, J.L. Zhang, F. Chen, M. Anpo, D. He, J. Phys. Chem. C, 2007, 111, 10618.
101. Z. Liu, Y. Wang, W. Chu, Z. Li, C. Ge, J. Alloys & Compds, 2010, 501, 54.
102. W-X. Liu, J. Ma, X-G. Qu, and W-B. Cao, Res. Chem. In-termed., 2009, 35, 321.
103. T-H. Kim, V. Rodríguez-González, G. Gyawali, S-H. Cho, T. Sekino, S-W. Lee, Catal. Today, 2013, 212, 75.
104. Y. Niu, M. Xing, J. Zhang, B. Tian, Catal. Today 2013, 201, 159.
105. Y. Yang, C. Tian, X. Zhao, Colloids and Surfaces A: Physicochem. Eng. Aspects, 2011, 389, 12.
106. Y. Yang, H. Zhong, C. Tian, Z. Jiang, Surface Sci., 2011, 605, 1281.
107. M. Hamadanian, A. Reisi-Vanani, M. Behpour, A.S. Esmaeily, Desalination, 2011, 281, 319.
108. C. Kaewtip, P. Chadpunyanun, V. Boonamnuayvitaya, Water Air & Soil pollution, 2012, 223, 1455.
109. C. Kaewtip, K. Accanit, N Chaowai, K. Areerat, P. Reanjaruan, V. Boonamnuayvitaya, Advances in Mater. Phys. & Chem., 2012, 2, 40.
110. B. Li, X. Cheng, X. Yu, L. Yan, Z. Xing, Advances in Materials Science and Engineering, Volume 2012, Article ID 348927, doi:10.1155/2012/348927
111. M. Anpo, H. Yamashita, Y. Ichihashi, S. Ehara, J Electroanal Chem., 1995, 396, 21.
112. M. Tahir, B. Tahir, N. Saidina Amin, Materials Research Bulletin, 2015, 63, 13.
113. A. Bhattacharyya, S. Kawi, M.B. Ray, Catal. Today, 2004, 98, 431.

114. D. Karamanis, A.N. Ökte, E. Vardoulakis, T. Vaimakis, Appl. Clay Sci., 2011, 53, 181.
115. D. Chen, H. Ji, J. Wang, J. Chen, Z. Wu, Z. Xia, Mater. Sci. Forum, 2011, 694, 85.
116. Y. Du, D. Tang, G. Zhang, X. Wu, Chinese J. of Catal., 2015, 36, 2219.
117. M. Ugˇurlu, Microporous and Mesoporous Materials 2009, 119, 276.
118. M. Ugˇurlu, M.H. Karaoˇglu, Chemical Engineering Journal 2011, 166, 859.
119. J. Liu, G. Zhang, Phys. Chem. Chem. Phys., 2014, 16, 8178
120. J. Paul, F.M. Hoffmann, Catal. Lett., 1988, 1, 445.
121. M. Subrahmanyam, S. Kaneco, N. Alonso-Vante, Appl. Catal. B: Environ., 1999, 23, 169.
122. M. Uğurlu, M. H. Karaoğlu, Fresenius Environ. Bulletin, 2010, 19, 2883,
123. S. Sua´rez, M. Yates, A.L. Petre, J.A. Martı´n, P. Avila, J. Blanco, Appl. Catal. B: Environ., 2006, 64, 302.
124. E. Galan, Clay Minerals, 1996, 31, 443.
125. A. Álvarez, J. Santarén, A. Esteban-Cubillo, P. Aparicio, Current Industrial Applications of Palygorskite and Sepiolite. In Emilio Galan and Arieh Singer, editors: Developments in Clay Science, Vol. 3, Amsterdam, The Netherlands, 2011, pp. 281-298,
126. M. Alkan, O. Demirbas, M. Dogˇan, Microporous and Mesoporous Materials, 2007, 101, 388–396, References therein.
127. A. Priesinger, Tenth National Conference On Clays And Clay Minerals.
128. H. Hattori, Applied Catalysis A: General, 2001, 222, 247.
129. V.G. Milt, E.D. Banús, E.E. Miró, M. Yates, J.C. Martín, S.B. Rasmussen, P. Ávila, Chemical Engineering Journal, 2010, 157, 530.
130. Q. Tang, F. Wang, M. Tang, J. Liang, C. Ren, Journal of Nanomaterials Volume 2012, Article ID 382603, 6 pages doi:10.1155/2012/382603
131. W.G. Xu, S.F. Liu, S.X. Lu, S.Y. Kang, Y. Zhou, H.F. Zhang, J.Colloid & Interface Sci., 2010, 351, 210.

132. M. Akcay, Journal of Molecular Structure, 2004, 694, 21.
133. S. Dikmen, G. Yilmaz, E. Yorukogullari, E. Korkmaz, The canadian journal of chemical engineering, 2011, 90, 785.
134. F. M. Fernandes, L. V´azquez, E. Ruiz-Hitzky, A. Carnicero, M. Castro, RSC Adv., 2014, 4, 11225
135. P. Aranda, R. Kun, M. Angeles, M. Luengo, S. Letaïef, I. Dékány, E. Ruiz-Hitzky, Chem. Mater. 2008, 20, 84.
136. Z. Wang, C. Zhao, D. Han, F. Gu, Anal. Methods, 2015, 7, 2779.
137. G. Zhang, Q. Xiong, W. Xu, S. Guo, Appl. Clay Sci., 2014, 102, 231.
138. Q. Zhua, Y. Zhanga, Fengzhu Lv, P. K. Chu, Z. Ye, F. Zhou, J. Hazardous Mater., 2012, 217– 218, 11.
139. D.A. Mckeown, J.E. Post Clays and Clay Minerals, 2002, 5, 667.
140. R. Giustetto, K. Seenivasan, S. Bordiga, Period. Mineral., 2010, Special Issue, 21- 37
141. M. Tahir, N.A.S. Amin, Chemical Engineering Journal, 2013, 230, 314.
142. Y. Shioya, K. Ikeue, M. Ogawa, M. Anpo, Appl. Catal. A: General, 2003, 254, 251.
143. H.-C. Yang, H.-Y. Lin, Y.-S. Chien, J. C.S. Wu, H.-H. Wu, Catal. Lett. 2009, 131, 381.
144. X. Yang, T. Xiao, P.P. Edwards, Inter. J. Hydrogen Energy, 2011, 36, 6546
145. S. Martinez-Ramirez, F. Puertas, M. T. Blanco-Varela, Clay Minerals, 1996, 31, 225.

CHAPTER 4

STUDIES ON SODIUM TANTALATE BASED CATALYSTS FOR PHOTO CATALYTIC REDUCTION OF CARBON DIOXIDE

4.1 Photo catalytic reduction of carbon dioxide on La modified sodium tantalate with different co-catalysts under UV-visible radiation

4.1.1 Introduction

Photo catalytic reduction of CO_2 by water (PCRC) to fuels/chemicals (methane/methanol) is considered as one of the means of mitigating green-house gas effect caused by the alarming levels of atmospheric CO_2 and hence is attracting global attention [1-10]. Several photo-active semiconductors like TiO_2, SiC, CdS, mixed metal oxides like $InNbO_4$, HNb_3O_8, Bi_2WO_6, promoted $NaNbO_3$, promoted Zn_2GeO_4 and a number of layered titanates have been explored for this process [10-15]. Layered perovskite type oxides, like $ALa_4Ti_4O_{15}$ (A=Ca, Sr, Ba) with Ag, Au, Ru, CuO and NiO as co-catalysts have been reported to be active for PCRC to CO and HCOOH [16]. Titanates with perovskite structure, $ATiO_3$ (A= Sr, Ca & Pb) with different co-catalysts are known to be active for PCRC to CO and CH_4 [17].

In this context, La modified sodium tantalate, $Na_{(1-x)}La_xTaO_{(3+x)}$ (La=2 wt%) with NiO (0.2 wt%) as co-catalyst, which is reported [18] to be highly effective for splitting of water, is an ideal catalyst of choice for PCRC. Tantalum based mixed oxides act as efficient photo catalysts. Shunsuke Sato et al. [19, 20] reported CO_2 photo reduction using N-Ta_2O_5 linked with Ru complexes, which showed high activity and selectivity towards HCOOH. Teramura et al [11] have observed that alkali metal tantalates, $ATaO_3$ (A=Li, Na & K) catalyse PCRC using external hydrogen as reductant, forming only CO and no hydrocarbons. $LiTaO_3$ yields maximum CO of 0.45 μmoles/g. Activity pattern follows the order, $LiTaO_3 > NaTaO_3 > KTaO_3$, which is consistent with the respective band gap energy and CO_2 uptake values. It is well-known that the nature of the reductant used influences the activity and product pattern. For example, PCRC under UV radiation by titania with hydrogen as reductant, yields CH_4, CO and C_2H_6, while with water, only CO and methane are formed, with relatively higher CO_2 conversion. On the other hand, photo catalytic reduction of CO_2 on ZrO_2 surface gives only CO with H_2 and H_2O, but the overall CO_2 conversion is high with H_2 [12].

However, $ATaO_3$ type tantalates have not been explored in detail so far, for PCRC with water as the reductant, except for a recent report by Li et al on $KTaO_3$ nanoflakes [21], and hence would be an interesting study, as it conforms to the criterion for sustainability and the process is simplified as a single one. In an effort to develop newer and efficient catalysts for PCRC, we have investigated in detail $NaTaO_3$ based catalysts in conjunction with different co-catalysts.

Choice of lanthanum modified $NaTaO_3$ with NiO as co-catalyst for the present investigation is based on its unique characteristics:

- Amongst the three tantalates, $NaTaO_3$ modified with lanthanum and NiO as co-catalyst, displays maximum activity for hydrogen production [18] by splitting of water with very high quantum efficiency of 56% with UV radiation (270 nm). Splitting of water is the necessary step in PCRC by water.
- $NaTaO_3$ with perovskite structure is the most active photo-catalyst among tantalates with corner-shared TaO_6 octahedra. Since the bond angle of Ta-O-Ta is close to 180°, facile transport of photo electron-hole pairs across the corner-shared octahedral framework is favoured [22].
- Conduction band bottom energy level of $NaTaO_3$ is suitable for reduction of CO_2 to form hydrocarbons.
- The substitution of La^{3+} ions for Na^+ ions in $NaTaO_3$ increases the n-type electrical conductivity and leads to the formation of nano steps structure on the surface [18] which separates oxidation and reduction sites, resulting in improved photo-catalytic activity.
- Location of the conduction band of $Na_{(1-x)}La_xTaO_{(3+x)}$ vis-à-vis that of NiO facilitates easy transfer of photo-generated electrons from $Na_{(1-x)}La_xTaO_{(3+x)}$ to conduction band of NiO, resulting effective charge separation and high activity [22]. Such a situation would be helpful for CO_2 reduction as well, though hydrogen production is favoured kinetically.

- Adsorption and activation of CO_2 on $NaTaO_3$ surface could also contribute to the activity.

Since the nature of co-catalysts influence the surface transformations leading to the formation of different hydrocarbons, the effect of other co-catalysts like Pt, Ag, Au, CuO, RuO_2 and bimetallic co-catalysts, such as, Pt-Ni and Pt-Cu, in the place of NiO, have been investigated.

4.1.2 Results and Discussions

4.1.2.1 X-ray diffraction patterns

XRD patterns of all the catalysts (Fig. 4.1) showed characteristic d-lines that can be attributed to orthorhombic phase of $NaTaO_3$ (JCPDS-25-0863) and no diffraction peaks due to the raw material Ta_2O_5 was found. Addition of La and co-catalysts like, NiO, Pt Au, Ag, CuO and RuO_2, being 2 w/w% maximum, did not result in any significant change in the XRD pattern of the parent material.

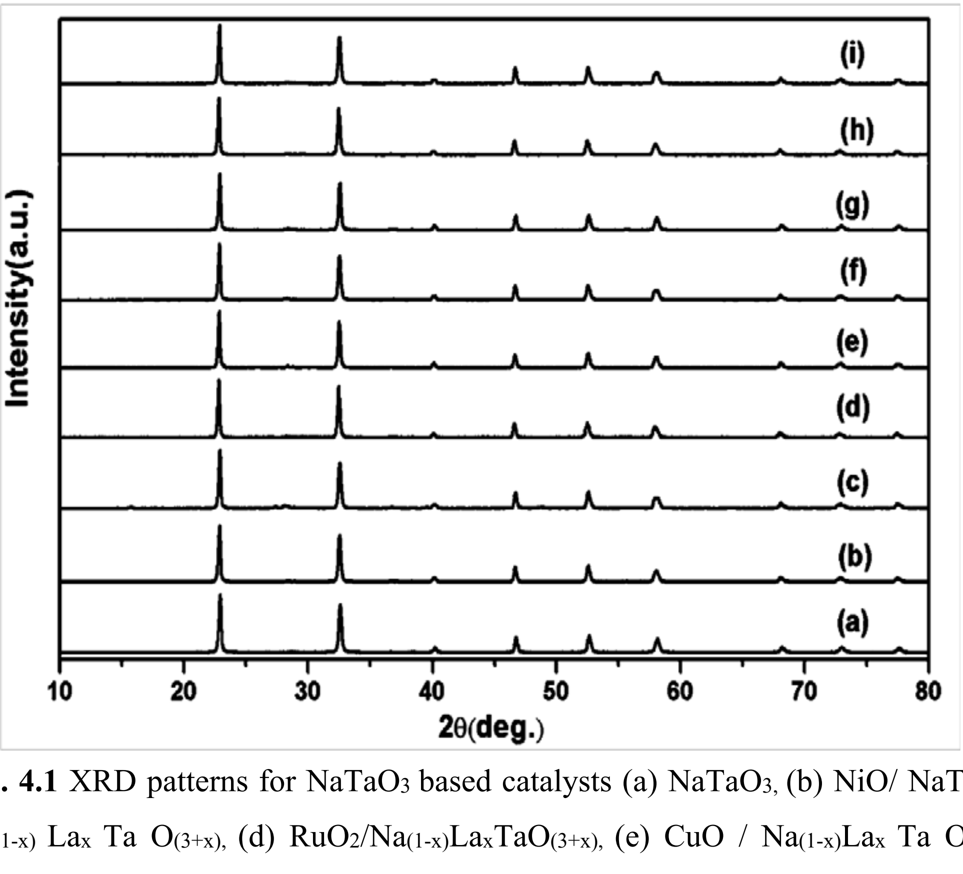

Fig. 4.1 XRD patterns for $NaTaO_3$ based catalysts (a) $NaTaO_3$, (b) NiO/ $NaTaO_3$, (c) $Na_{(1-x)} La_x Ta O_{(3+x)}$, (d) $RuO_2/Na_{(1-x)}La_xTaO_{(3+x)}$, (e) CuO / $Na_{(1-x)}La_x Ta O_{(3+x)}$, (f) $NiO/Na_{(1-x)}La_xTaO_{(3+x)}$, (g) $Pt/Na_{(1-x)} La_x TaO_{(3+x)}$, (h) $Ag/Na_{(1-x)}La_xTaO_{(3+x)}$, (i) Au/ $Na_{(1-x)} La_xTaO_{(3+x)}$.

However, as reported in literature [18] substitution of Na^+ (1.39Å) by La^{3+} (1.36Å in 12 co-ordinated site) in the lattice of $NaTaO_3$ resulted in small shift in d-lines as shown in Fig. 4.2. Surface area of $Na_{(1-x)}La_xTaO_{(3+x)}$ as measured by BET method was 2.9 m^2/g and no significant changes in the texture were observed on impregnation of the co-catalysts.

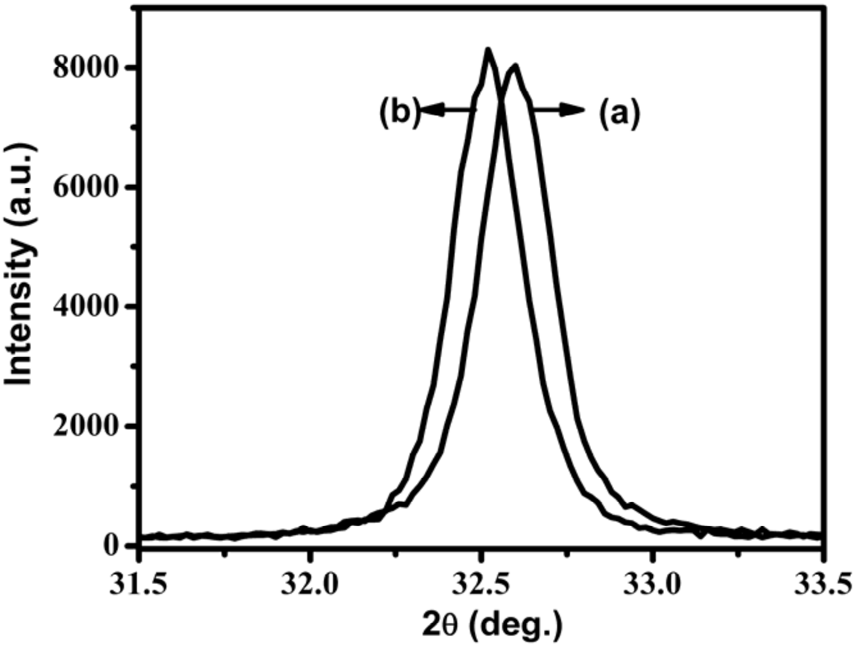

Fig. 4.2 Effect of substitution of Na^+ by La^{3+} on d-line of $NaTaO_3$ catalysts (a) $NaTaO_3$, (b) $Na_{(1-x)}La_xTaO_{(3+x)}$.

4.1.2.2 Diffuse reflectance spectra

Diffuse reflectance spectra for all $NaTaO_3$ based catalysts recorded in UV-Visible region are shown in Fig. 4.3. All modified formulations display small shifts in the light absorption edges towards visible region, which is reflected in the corresponding changes in band gap values. In the case of $Au/Na_{(1-x)}La_xTaO_{(3+x)}$ a prominent surface plasmon resonance band due to nano size Au is observed at 525 nm, which could possibly influence the photo activity of the catalyst. Band gap, calculated by standard method and crystallite size, calculated by adopting Scherer's formula, are tabulated in Table. 4.1.

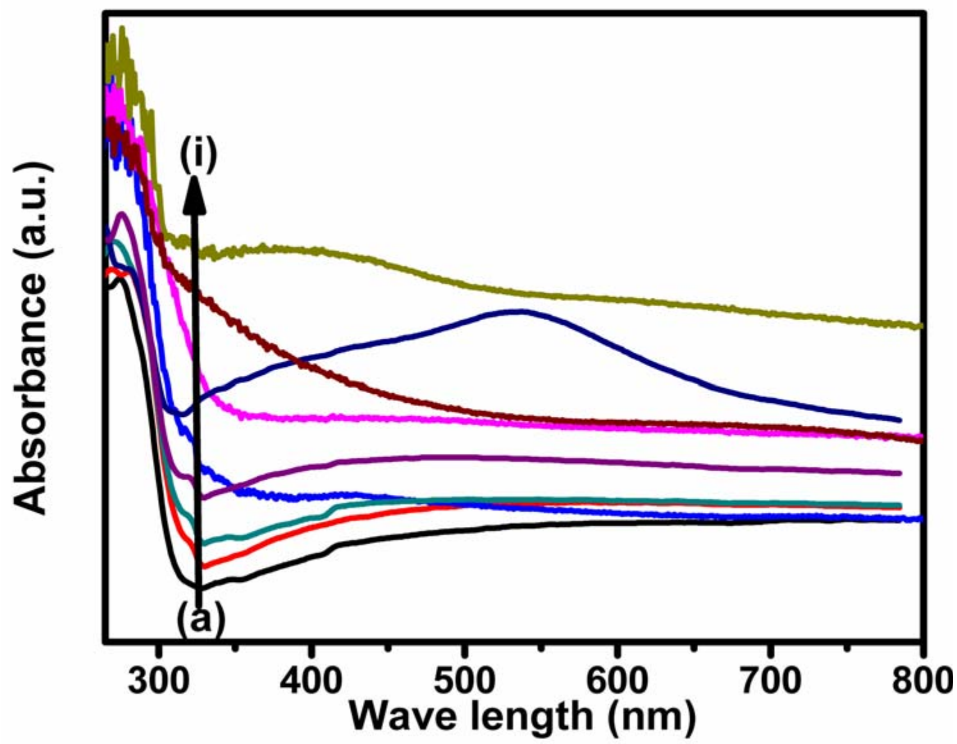

Fig. 4.3 Diffuse reflectance spectra of neat and modified $NaTaO_3$ catalysts

(a) $Na_{(1-x)}La_xTaO_{(3+x)}$, (b) $NaTaO_3$,(c) NiO/$Na_{(1-x)}$ $La_xTaO_{(3+x)}$, (d) Pt/$Na_{(1-x)}La_xTaO_{(3+x)}$, (e) NiO/$NaTaO_3$, (f) Au/$Na_{(1-x)}La_xTaO_{(3+x)}$, (g) Ag/ $Na_{(1-x)}$ $La_xTaO_{(3+x)}$, (h) CuO/ $Na_{(1-x)}La_xTaO_{(3+x)}$, (i) RuO_2/$Na_{(1-x)}La_xTaO_{(3+x)}$.

4.1.2.3 Electron Microscopic Analysis

Cubic morphology of $Na_{(1-x)}La_xTaO_{(3+x)}$ is clearly observed in the Scanning Electron Micrograph presented in Fig. 4.4a. TEM (Fig. 4.4b) further confirms the cubic architecture of the $Na_{(1-x)}La_x$ $TaO_{(3+x)}$. SAED (Fig. 4.4c) shows the highly crystalline nature of $NaTaO_3$ nano cubes, and d-value of 0.389 nm measured from HRTEM (Fig. 4.4d) corresponds to (002) planes of orthorhombic phase of $NaTaO_3$. STEM-EDS elemental mapping of Na(Kα), Ta(Lα), La(Lα), Ni(Kα), O(Kα) shown in Fig. 4.5, and EDAX data presented in Fig. 4.14 confirm the incorporation of La and co-catalyst NiO in the tantalate matrix.

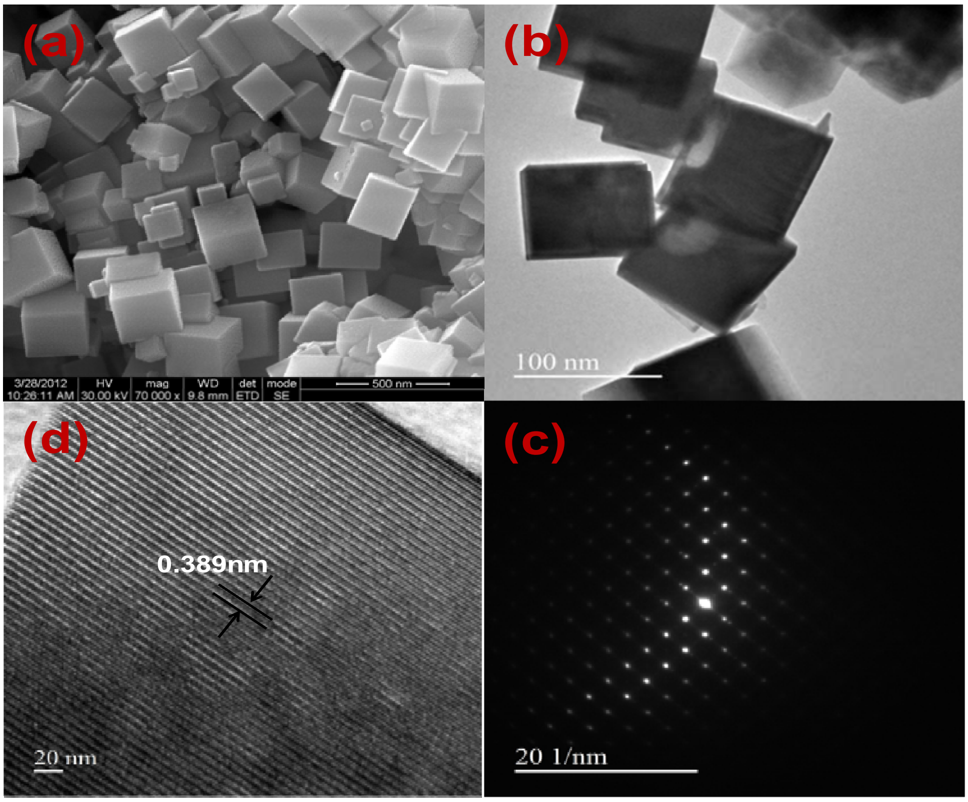

Fig. 4.4 Morphology of $Na_{(1-x)}La_xTaO_{(3+x)}$ (a) SEM image, (b) TEM image (c) SAED (d) HRTEM.

Table 4.1 Crystallite size and band gap energy data for neat and modified $NaTaO_3$

Photo catalysts	Crystallite Size (nm)	Band Gap (eV)
$NaTaO_3$	48.1	3.9
$NiO/NaTaO_3$	47.3	3.7
$Na_{(1-x)}La_xTaO_{(3+x)}$	47.2	4.1
$Au/Na_{(1-x)}La_xTaO_{(3+x)}$	46.6	3.9
$Ag/Na_{(1-x)}La_xTaO_{(3+x)}$	50.6	3.5
$RuO_2/Na_{(1-x)}La_xTaO_{(3+x)}$	49.4	3.6
$Pt/Na_{(1-x)}La_xTaO_{(3+x)}$	46.2	3.9
$CuO/Na_{(1-x)}La_xTaO_{(3+x)}$	45.4	3.5
$NiO/Na_{(1-x)}La_xTaO_{(3+x)}$	46.6	3.8

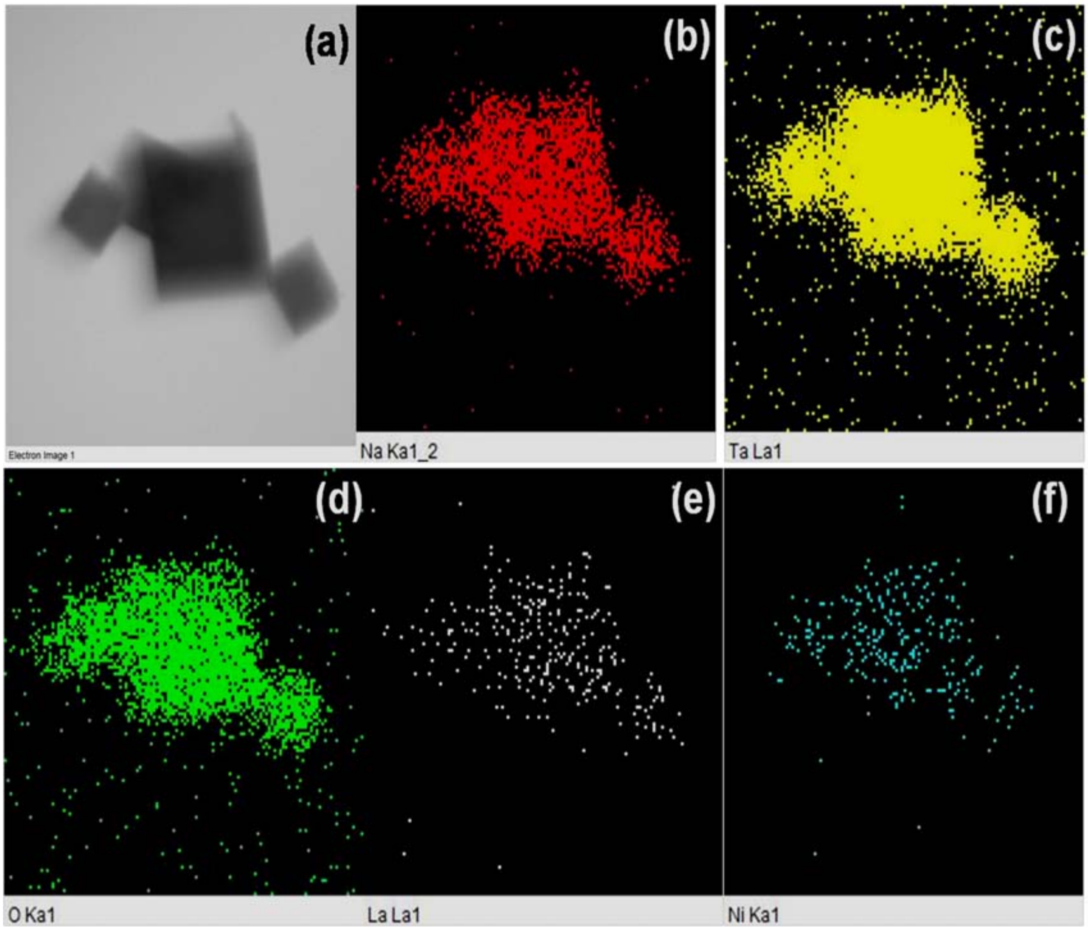

Fig. 4.5 STEM (a) and Elemental mapping (b) Na-Kα (c) Ta-Lα (d) O-Kα (e) La-Lα (f) Ni-Kα for 0.2 wt% NiO/$Na_{(1-x)}La_xTaO_{(3+x)}$.

4.1.2.4 Photoluminescence Spectra

Photo luminescence spectra of all the catalysts are presented in Fig. 4.6. With respect to neat $NaTaO_3$, all formulations modified by the addition of La and co-catalysts display perceptible decrease in the intensity of photo-luminescence, indicating a decrease in charge carrier recombination rates, which result in longer life time of the charge carriers. As indicated by DRS and photo-luminescence data, it is clear that the two factors which could influence the photo-catalytic activity of $NaTaO_3$ modified with co-catalysts are:

i) Increase in life time of charge carriers by decreased recombination rates

ii) Extension of light absorption edge towards visible region.

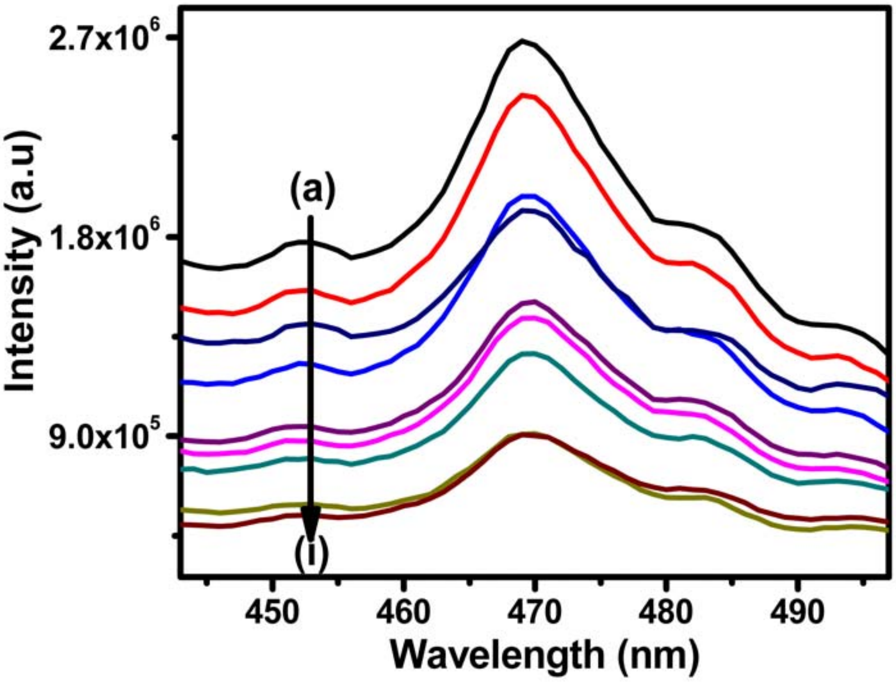

Fig. 4.6 Photo-luminescence spectra for neat and modified $NaTaO_3$ catalysts

(a) $NaTaO_3$, (b) $Na_{(1-x)}La_xTaO_{(3+x)}$, (c) NiO/ $NaTaO_3$, (d) $CuO/Na_{(1-x)}La_xTaO_{(3+x)}$, (e) $NiO/Na_{(1-x)}La_xTaO_{(3+x)}$, (f) $Ag/Na_{(1-x)}La_xTaO_{(3+x)}$ g) $Pt/Na_{(1-x)}La_xTaO_{(3+x)}$, (h) $RuO_2/Na_{(1-x)}La_xTaO_{(3+x)}$, (i) Au/ $Na_{(1-x)}La_xTaO_{(3+x)}$.

4.1.3 Activity for photo catalytic reduction of CO_2

All the experiments were carried out up to 20 hrs. Besides hydrogen and oxygen, methane, ethylene, ethane and acetaldehyde were formed in very small quantities (~0.1-10 micromoles/g) and hence not considered in the plots. CO and formic acid were detected at trace levels and hence could not be quantified. As shown in Fig. 4.7, large amounts of methanol is formed when the aqueous alkaline is saturated with carbon dioxide compared to very small quantities formed after saturation with nitrogen, indicating that the observed methanol/products were obtained from CO_2 photo reduction, not from surface carbon impurities on the catalyst. Trends in the formation of major products, methanol and ethanol, with respect to time of irradiation up to 20 hrs, are given in Fig. 4.8 and Fig. 4.9. Rates of formation of products are high during initial 6-8 hrs beyond which the product formation tends to slow down. Based on the initial rates (μmol g^{-1} h^{-1}) for the formation of different products, and the number of photo electrons involved in each case, apparent quantum yields (AQY) for all the catalysts have been calculated and presented in Table 4.2. Comparison of the hydrocarbons products formed on different catalysts after 20 hrs of irradiation are shown in Fig. 4.10.

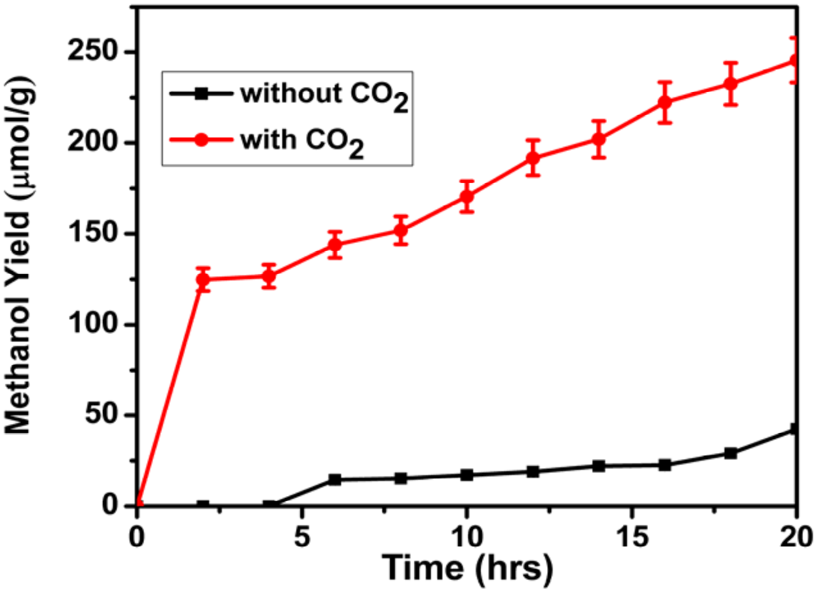

Fig. 4.7 Methanol yield with $NaTaO_3$ after purging with N_2 and CO_2

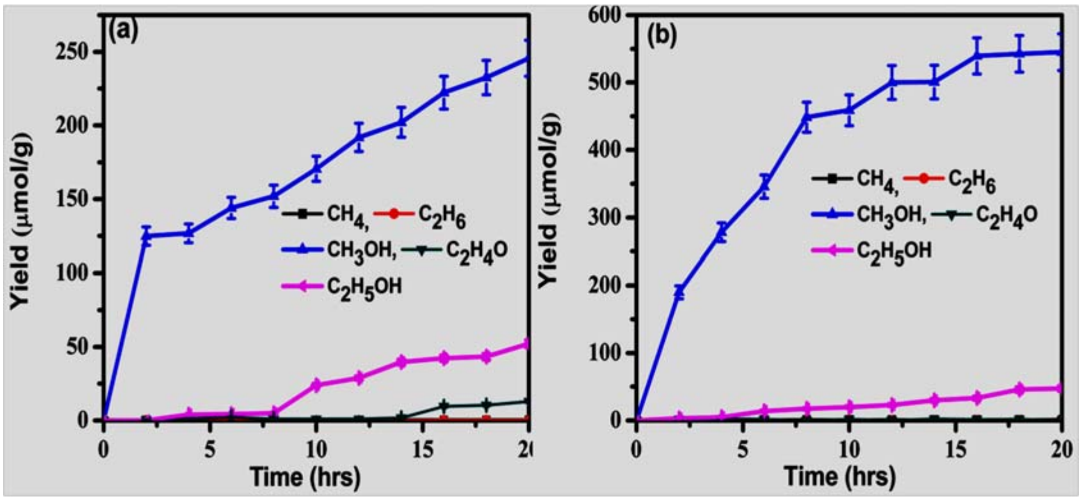

Fig. 4.8 Trends in photo catalytic activity for CO_2 reduction with alkaline medium - Time on stream plots - (a) $NaTaO_3$, (b) $Na_{(1-x)}La_xTaO_{(3+x)}$.

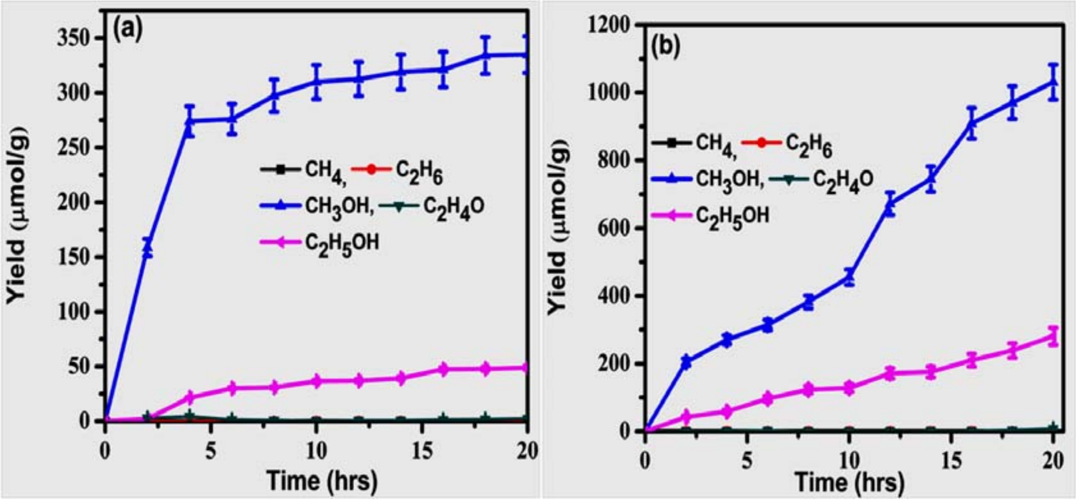

Fig. 4.9 Trends in photo catalytic activity for CO_2 reduction with alkaline medium - Time on stream plots (a) $NiO/NaTaO_3$, (c) 0.2 wt%$NiO/Na_{(1-x)}La_xTaO_{(3+x)}$.

Table 4.2 Products distribution and quantum yield data for neat and modified $NaTaO_3$ catalysts.

Photo catalysts	**Products obtained from CO_2 reduction (μmol g^{-1} h^{-1})**								**AQY (%)**
	CH_4	**C_2H_4**	**C_2H_6**	**CH_3OH**	**C_2H_4O**	**C_2H_5OH**	**C_3H_6**	**H_2**	$*10^{-3}$
$NaTaO_3$	0.01	-	0.01	20.6	0.6	2.5	-	0.13	2.99
$NiO/NaTaO_3$	0.02	-	0.02	35.6	0.76	2.9	-	0.3	4.79
NTO*	0.02	-	-	35.0	4.01	6.4	0.05	0.4	4.61
Au/NTO	0.03	-	0.02	29.8	0.39	7.9	0.01	1.0	5.22
Ag/NTO	0.21	-	0.01	28.4	0.68	5.5	0.17	0.2	4.51
RuO_2/NTO	0.06	-	0.01	49.6	0.24	16.2	0.04	0.2	9.24
Pt/NTO	0.41	0.13	0.02	40.6	1.44	1.5	0.03	0.3	5.22
CuO/NTO	0.01	0.03	0.04	60.5	0.91	15.9	0.15	0.2	10.50
NiO/NTO	0.02	0.14	0.01	59.6	2.15	18.8	0.42	0.2	11.29
Pt-Ni/NTO	0.43	0.020	0.20	73.3	0.14	3.21	3.71	0.43	10.3
Pt-Cu/NTO	0.06	0.30	0.10	60.7	2.51	2.83	2.80	0.60	8.95

* $Na_{(1-x)}La_xTaO_{(3+x)}$.

It is observed from Table. 4.2 that lanthanum and various co-catalysts incorporated in $NaTaO_3$ significantly influence the overall quantum yield as well as selectivity to various products. Addition of lanthanum and NiO separately to $NaTaO_3$ results in marginal increase in quantum yield. In the presence of both La and NiO, quantum yield increased by more than three times with respect to neat $NaTaO_3$. Amongst the co-catalysts employed, NiO and CuO display maximum increase in activity and relatively higher selectivity towards alcohols. Other co-catalysts like, Pt, Ag, Au and RuO_2 do promote CO_2 photo reduction but are not as effective as NiO and CuO. Initially methanol is formed at a higher rate and later, the rate tapers off, once ethanol formation by coupling of surface C1 species picks up.

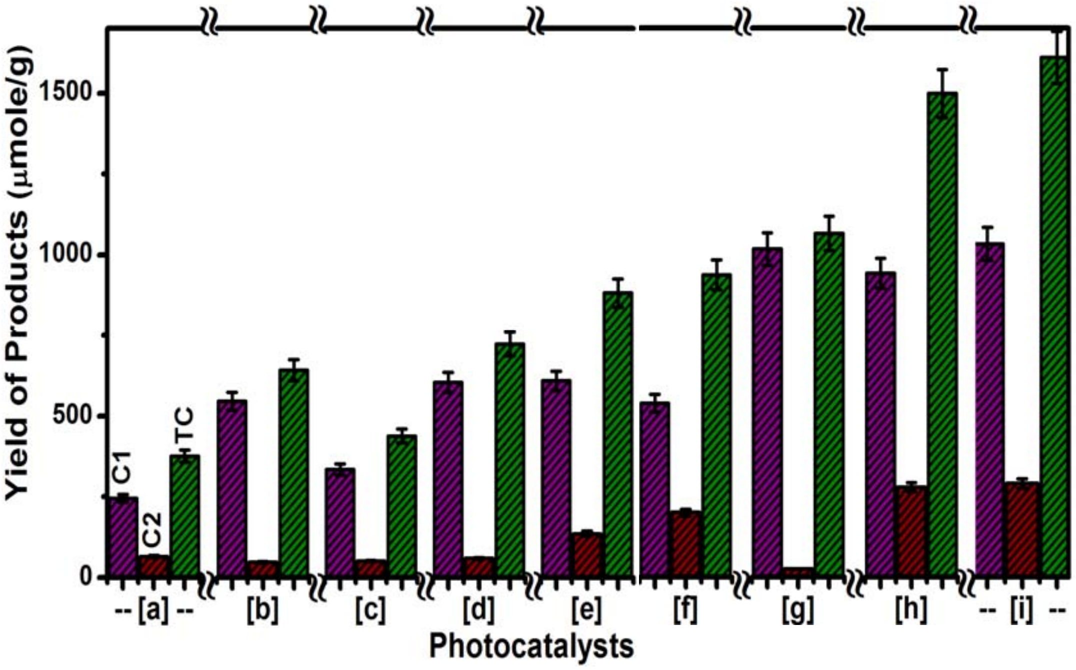

Fig. 4.10 Comparison of activity of neat and modified $NaTaO_3$ catalysts: (a) $NaTaO_3$, (b) $NiO/NaTaO_3$, (c) $Na_{(1-x)}La_xTaO_{(3+x)}$, (d) Au/ $Na_{(1-x)}La_xTaO_{(3+x)}$. (e) Ag/$Na_{(1-x)}La_xTaO_{(3+x)}$, (f) $RuO_2/Na_{(1-x)}La_xTaO_{(3+x)}$, (g) Pt/$Na_{(1-x)}La_xTaO_{(3+x)}$, (h) CuO/$Na_{(1-x)}La_x TaO_{(3+x)}$, (i) NiO/$Na_{(1-x)}La_xTaO_{(3+x)}$.

In general, when reduction is carried out in gas phase, CO and methane are the major products and in aqueous phase, mainly methanol, methane and in some cases ethanol and other C_2 hydrocarbons are reported, depending on the catalyst/co-catalyst used and reaction conditions like the medium (pure water or alkaline solution) and pressure [23, 24].

In aqueous alkaline medium, at pH 8-9, bicarbonate/carbonate species are dominant. Since the reduction potential of these species are lower than that for CO_2 [25] they undergo facile reduction, mainly to methanol and methane. As the surface concentration of surface monomeric hydrocarbon species increases, C_2 products like ethylene, ethane and ethanol are formed by coupling. Similar reaction pathways for the formation of ethanol have been proposed earlier [26-31]. Formation of ethanol starts only after a time lag, so that monomeric species $.CH_3$ and $.CH_2$ responsible for the formation of ethanol get sufficiently accumulated on the surface [28]. Hence the formation of ethanol continues after that stage. Methanol formation tends to slow down due to the competitive formation of ethanol and slow catalyst deactivation due to the carbonaceous species on the surface [32-34].

4.1.4. Role of lanthanum and co-catalysts

Lanthanum doped $NaTaO_3$ has been studied extensively in view of its promoting effect on splitting of water under UV radiation. According to Kato et al. [18, 22] doping with lanthanum increases the crystallinity and induces nano level step sites on the surface, which help to retard charge carrier recombination.

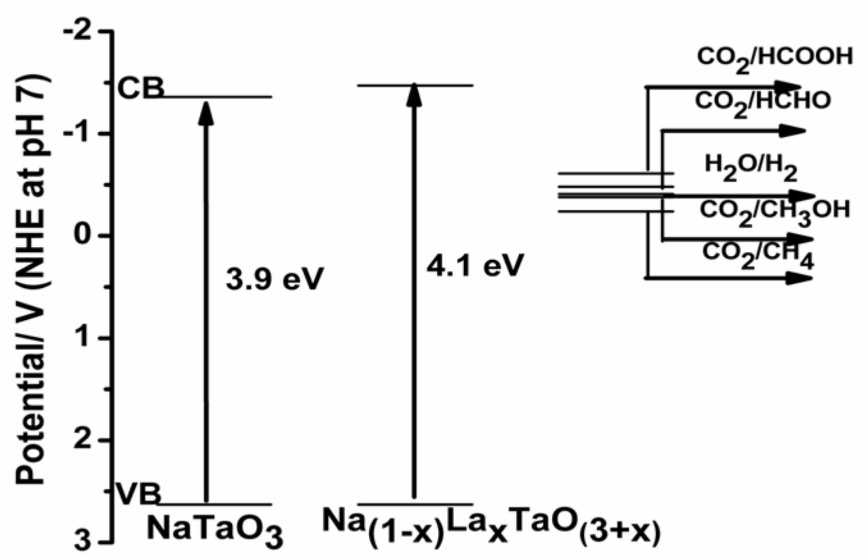

Fig. 4.11 Effect of La loading on conduction band energy level for $NaTaO_3$- vis-à-vis CO_2 reduction potential.

With an increase in the band gap value (3.9 to 4.1 eV) on lanthanum doping, the conduction band energy level becomes more negative (Fig. 4.11), thus favouring increase in activity towards CO_2 reduction. Finely dispersed NiO crystallites act as efficient centres for hydrogen generation. Such changes lead to increase in activity for water splitting as well as CO_2 photo reduction. As shown in Fig. 4.12, the relative location of the conduction band of NiO (at -0.96 V) with respect to that of $NaTaO_3$ (at -1.06 V) facilitates easy transfer of photo-generated electrons from $Na_{(1-x)}La_xTaO_{(3+x)}$ (at -1.26 V) to the conduction band of NiO [22].

Increase in the availability of photo-generated electrons in the conduction band of NiO facilitates deeper reduction of CO_2 to alcohols. Similar matching/coupling of the conduction band energy levels of $Na_{(1-x)}La_xTaO_{(3+x)}$ and CuO explains high activity observed with CuO as co-catalyst.

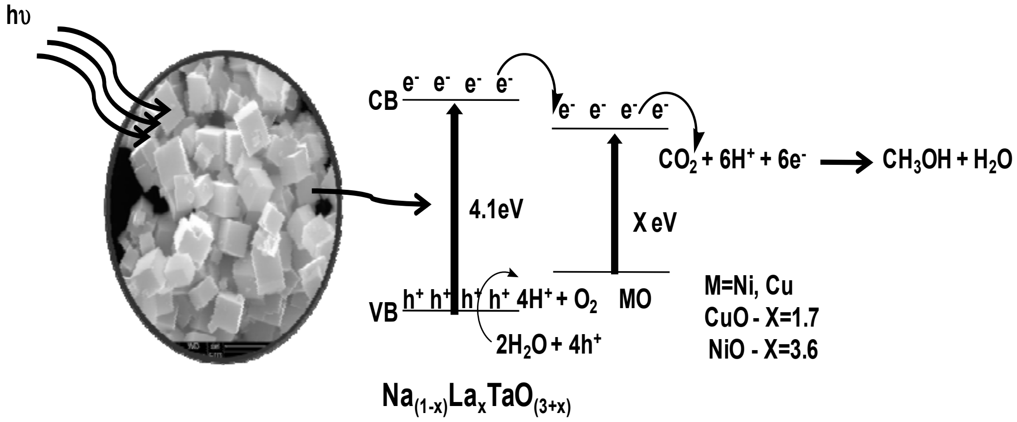

Fig. 4.12 Facile charge transfer between conduction band energy levels of $Na_{(1-x)}La_xTaO_{(3+x)}$ and metal oxides (CuO, NiO).

Other co-catalysts, Pt, Ag, Au and RuO_2 act as effective electron traps which help in hydrogen gas generation and CO_2 reduction (Fig. 4.13). However, these are not as effective as NiO/CuO. While H_2 formation is favoured by Pt as co-catalyst, CuO and NiO favour methanol formation and Ag, Au favour CO, CH_4. This trend is also supported by electrochemical reduction of CO_2 with these co-catalysts [36].

In our case, major pathway for hydrocarbons is through the facile reduction of bicarbonate species; hence formation of CO is remote and not identified in the products. H_2 generation with Pt co-catalyst is less due to the reverse reaction of water formation [17], carbonaceous deposits on the surface and consumption of protons for hydrocarbon formation. Wang et al [33] could not detect hydrogen during photo catalytic reduction of CO_2 on nano size Pt supported on single crystal TiO_2 since hydrogen generated was used for methane formation.

We have carried out reaction with bimetallic co-catalysts Pt/Cu and Pt/Ni and found out that activity is varying from Pt, CuO, NiO mono co-catalyst composition whereas selectivity towards hydrocarbon formation increases with methanol formation as shown in Table 4.2. Hence Co-catalyst Pt selectively improves hydrocarbon products not alcoholic products.

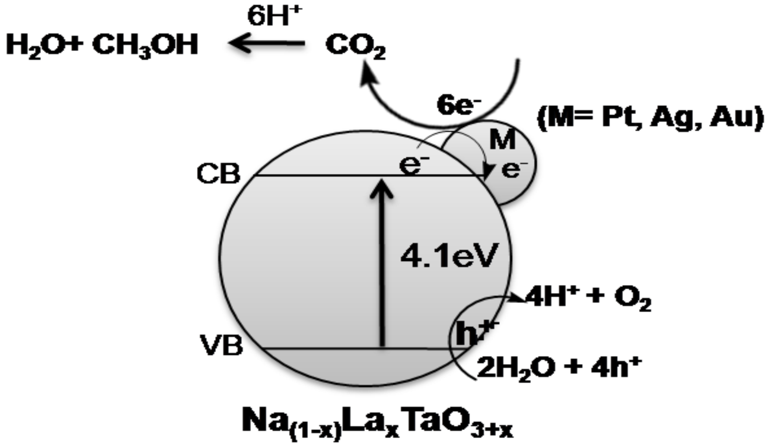

Fig. 4.13 Role of co-catalysts Pt, Ag and Au as electron traps towards charge separation.

Surface plasmon resonance (SPR) band due to nano size Au observed at 525 nm in Au/$Na_{(1-x)}La_xTaO_{(3+x)}$ induces additional light absorption in visible region resulting in perceptible improvement in activity compared to neat $NaTaO_3$, but less than that achieved with NiO/CuO as co-catalysts. Based on SPR maximum, Au crystallite size works out to 22 nm [35], which may be due to the method of preparation adopted in this work. Larger crystallite size of 22 nm and lower energy associated with visible light could be responsible for the moderate activity improvement observed with Au, as compared to NiO/CuO as co-catalysts. Zhou et al [17] have reported that, when Au is used as co-catalyst with $SrTiO_3$ for photo catalytic reduction of CO_2, the formulation with Au crystallite size of 2 nm shows higher activity compared to the one with the size of 5-7 nm. The difference in the crystallite size is attributed to the methods adopted for deposition of Au on $SrTiO_3$.

In aqueous media, electro reduction of CO_2 to CO [4, 36] is observed with Au, Ag, Zn, Pd and Ga as co-catalysts. Formic acid is generated during reduction with Pb, Hg, In, Sn, Bi, Cd and Tl materials. Metals such as, Ti, Nb, Ta, Mo, Mn and Al heavily favour hydrogen evolution. Cu-Cu oxide electrodes are highly efficient for electro-chemical reduction of CO_2 yielding hydrocarbons like methane, ethane, ethylene besides hydrogen. Reduction activity and product selectivity are governed by a variety of factors like, pH, CO_2 concentration, nature of the supporting electrolyte, electrode material and catalyst [37, 38]. For instance, changing the supporting electrolyte from $NaHCO_3$ to Na_2CO_3 or $NaHCO_3$ + Na_2CO_3 significantly alters the selectivity towards methanol/ethanol [38].

4.1.5. Role of water as reductant, alkaline medium and reaction pathways

While Teramura et al [11] observed that photo catalytic reduction of CO_2 on neat $NaTaO_3$ with H_2 as reductant under UV radiation proceeds up to CO (~ 0.45 µmoles/g) with no hydrocarbon being formed, in the present investigation on neat $NaTaO_3$, methanol and ethanol along with small amount of methane (Table. 4.2) are observed when water is used as reductant. It is to be noted that Teramura et al [11] studied the process in gas phase within a closed circulating system (with 150 µmoles of CO_2 and 50 µmoles of hydrogen), while in the present case, the reaction was conducted in aqueous alkaline medium and in batch mode, with very high proportion of water (as source for active hydrogen) and relatively limited quantity of CO_2 in dissolved state. Such a situation implies availability of relatively large quantity of active hydrogen by splitting of water, which is conducive for reduction of CO_2 beyond CO in the present case. When external hydrogen is used as reductant, CO_2 photo reduction on $NaTaO_3$ may follow a mechanism similar to the one proposed for oxides like ZrO_2, TiO_2, Ga_2O_3 and MgO [12, 39-41].

In the present case, it is observed that the reaction medium (0.2 mol L^{-1} NaOH at pH-13 initially) on saturation with CO_2 attains pH-8.0. Under these conditions, CO_2 in solution exists as bicarbonate (HCO_3^-) species [42], which on irradiation, undergoes further reduction to hydrocarbons through several intermediate species. Formation of surface formate from adsorbed bicarbonate [41, 43] and directly from adsorbed CO_2

[44] are known to occur on irradiation of titania dispersed in aqueous or alkaline solutions and also in presence of water vapour [45]. Ability of $NaTaO_3$ to adsorb and activate CO_2 is expected to facilitate such surface transformations in the present case. Subsequently, the formate species are converted to methyl and methoxy radicals [44, 45] by the active hydrogen atoms formed by water splitting and ultimately result in the formation of methane and methanol respectively. Ethanol is formed by dimerization of surface C1 species [27]. Formation of traces of ethane also supports this as one of the possible reaction pathways. According to Dimitrijevic et al [44] in the course of these transformations, water plays dual role, acting as both proton donor as well as an electron acceptor. H_2O:CO_2 ratio influences the efficiency of photo catalytic reduction of CO_2, increasing with the increase in ratio and the optimum ratio for methane formation is found to be 5 [46]. Hence water as reductant plays multiple roles during photo catalytic reduction of CO_2.

OH^- ions in the medium act as hole scavengers, form $OH^\cdot$ radicals, and reduce the electron-hole recombination rate. Increase in lifetime of photo electrons would facilitate the reduction of CO_2 [47]. Besides, alkaline medium increases the solubility of CO_2. Kato & Kudo [18] observed the deactivation of NiO/$Na_{(1-x)}La_xTaO_{(3+x)}$ for photo catalytic splitting of water due to solubilisation of NiO and the consequent deactivation of the catalyst [22]. In the present case, alkaline solution prevents the solubilisation of NiO and catalyst deactivation is arrested. This aspect is confirmed by the qualitative EDXA spectral data presented in Fig. 4.14.

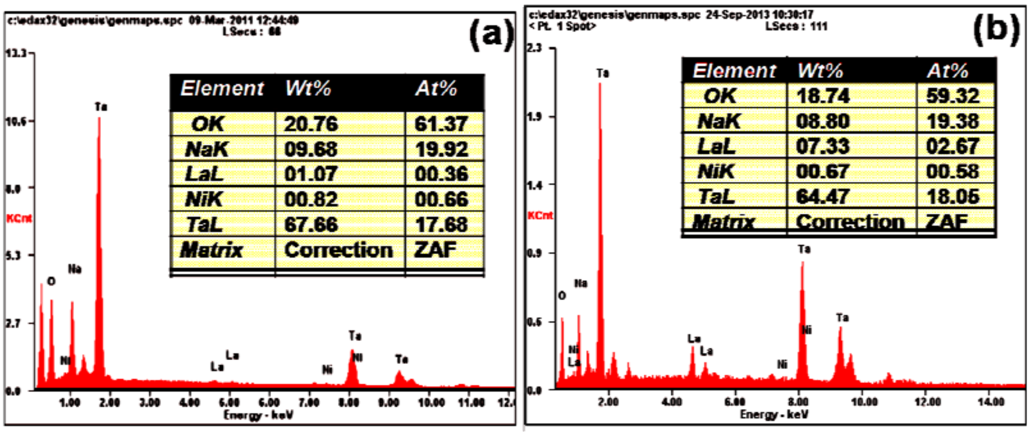

(a)

Element	Wt%	At%
OK	20.76	61.37
NaK	09.68	19.92
LaL	01.07	00.36
NiK	00.82	00.66
TaL	67.66	17.68
Matrix	Correction	ZAF

(b)

Element	Wt%	At%
OK	18.74	59.32
NaK	08.80	19.38
LaL	07.33	02.67
NiK	00.67	00.58
TaL	64.47	18.05
Matrix	Correction	ZAF

Fig. 4.14 EDXA data for 0.2 wt%NiO/$Na_{(1-x)}$ $La_xTaO_{(3+x)}$ (a) Fresh catalyst (b) Used catalyst.

Like water, alkali also plays multiple roles, as hole scavenger, increasing solubility of CO_2 and arresting the solubilization of NiO. XRD, SEM data (Fig. 4.15) for $NiO/Na_{(1-x)}La_xTaO_{(3+x)}$ used for 20 hrs reveal that the perovskite structure, cubic morphology and amount of NiO present on the surface (Fig. 4.14 a & b) has been retained, indicating the stability of the catalyst. SEM for used catalyst indicates slight surface attrition due to continuous agitation.

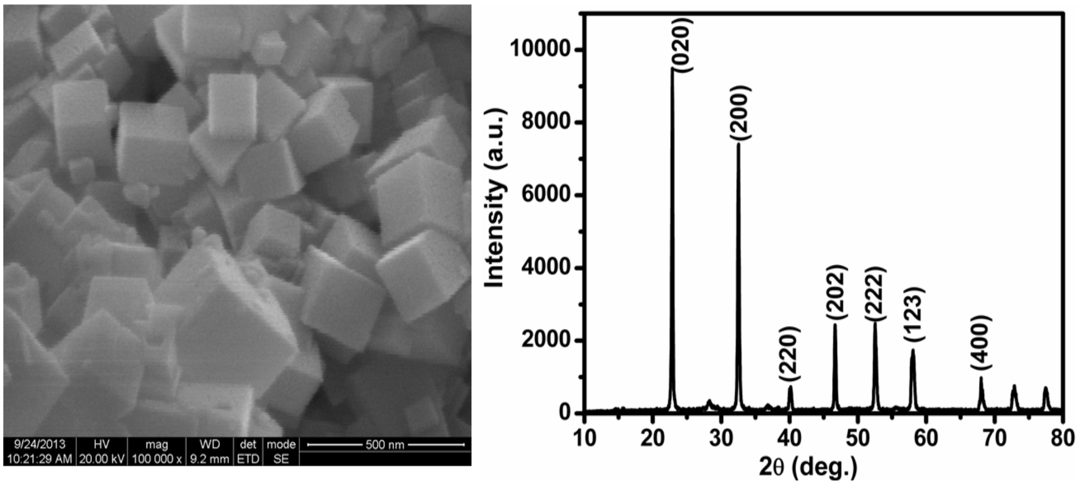

Fig. 4.15 SEM and XRD data for used 0.2 wt% $NiO/Na_{(1-x)}La_xTaO_{(3+x)}$ after 20 hrs of reaction

A recent report by Li et al [21] on CO_2 photo reduction on $KTaO_3$ nano flakes surface using pure water as reductant, with UV light irradiation indicates formation of CO and H_2 as major products with traces of methane. This is in contrast to our studies wherein aqueous alkaline solution at pH-8.0 as the medium and UV-visible range radiation are employed. Bicarbonate (HCO_3^-), as the active species, undergoes facile photo reduction beyond CO to yield different hydrocarbon products as observed in the present case, while CO is the major product observed by Li et al. As shown in Fig. 4.12, matching/coupling of the conduction band energy levels of $NaTaO_3$ with those of co-catalysts, NiO and CuO (for facile transfer of photo electrons and hence increase in activity) observed in the present case, which is not feasible with $KTaO_3$ since the corresponding energy levels are not suitable for transfer of photo electrons [48]. Yields are higher with $KTaO_3$ since high energy UV radiation is used. We do observe an increase in activity with Ag as co-catalyst for $Na_{(1-x)}La_xTaO_{(3+x)}$.

Unique matching/coupling of energy levels in the conduction bands of $NaTaO_3$ is not observed with other tantalates (Li & K) or with co-catalysts other than NiO and CuO. Thus, two distinct mechanisms, coupling of semi-conductors and trapping of photo electrons, both leading to efficient light absorption in visible region and increase the lifetime of excitons because of effective charge separation, are operative in the promoting action of co-catalysts with $Na_{(1-x)}La_xTaO_{(3+x)}$. Adsorption and activation of CO_2 by $NaTaO_3$ is a common additional factor for all the formulations, which contributes towards observed increase in activity for photo catalytic reduction of CO_2.

4.1.6 Conclusions

Lanthanum doped $NaTaO_3$ formulations in conjunction with different co-catalysts display significant activity for the photo reduction of CO_2 with water as reductant, leading to the formation of methanol and ethanol as major products. The location of the conduction band of NiO/CuO with respect to that of $Na_{(1-x)}La_xTaO_{(3+x)}$ facilitates easy transfer of photo-generated electrons from $Na_{(1-x)}La_xTaO_{(3+x)}$ to the conduction band of NiO/CuO, wherein these electrons participate in simultaneous hydrogen generation (by water splitting) and CO_2 photo reduction processes. Other co-catalysts, Pt, Ag, Au and RuO_2 display marginal improvements in activity vis-à-vis neat $NaTaO_3$. Bicarbonate species present in the reaction medium get reduced to surface formate species, which undergo further reduction to yield products like methane, methanol and ethanol. Water as reductant is more efficient than external hydrogen, since water splitting generates active hydrogen atoms that facilitate further conversion of surface formate/CO to hydrocarbons. OH^- ions in alkaline reaction medium act as hole scavengers, increase solubility of CO_2 and stability of the catalyst by arresting solubilisation of NiO. Bimetallic co-catalysts, such as Pt-Cu and Pt-Ni display higher selectivity towards hydrocarbons. $NaTaO_3$ based catalysts could become viable alternatives to titania for this crucial application.

4.2. Modifications in $Na_{(1-x)}La_xTaO_{(3+x)}$: Influence of doping with Nitrogen and Iron (Fe^{3+}) on photo catalytic reduction of CO_2

4.2.1 Introduction

CO_2 emissions from the burning of fossil fuels pose serious environmental issues like green-house gas effect. Conversion of CO_2 into fuels/ hydrocarbons by utilizing photo catalytic routes is an effective strategy that can provide solution to the two main issues, such as meeting energy demand and mitigating green house gas effect. Photo catalytic reduction of CO_2 (PCRC) into fuels/hydrocarbons or artificial photosynthesis, using water as the reductant, is a complex, challenging and multi-step process with high application potential. The process involves two major steps, splitting of water to yield hydrogen and oxygen and reduction of CO_2 to hydrocarbons. Several investigations focusing on a wide range of heterogeneous photo catalysts for the artificial photo synthesis have been reported [13-15, 49-51]. Fundamental aspects involved in the activation of carbon dioxide with water by photo catalytic route include:

i) The design of bi-functional photo catalysts that include components active for both functionalities, namely, H_2O splitting and CO_2 reduction steps

ii) The photo catalyst should possess requisite electronic energy levels, specifically

- ✓ Valence band top energy level to be suitable for splitting of H_2O,
- ✓ Conduction band bottom energy level to be more negative with respect to reduction potential of CO_2
- ✓ Band gap energy which is appropriate for maximum absorption of light in the most abundant visible region

iii) Ability to adsorb and activate CO_2.

In addition, longer life time of the photo generated charge carriers, the shorter diffusion path length of excitons to the catalyst surface are the other desirable parameters that maximize the efficiency of the photo catalysts.

It has been recently reported that tantalum based perovskite materials show significant activities towards photo catalytic applications especially water splitting and CO_2 reduction [18, 51-55]. The salient features of the tantalates, responsible for their photo catalytic activity are:

i. the conduction band of a typical tantalate mainly consists of 5d orbitals whose energy level is in more negative position compared to other transition metal oxides and mixed metal oxides and also more negative than redox potentials for the conversion of CO_2 to products like CH_3OH, CH_4, C_2H_5OH
ii. tantalates, being ferroelectric materials, have internal dipoles that facilitate separation of electrons and holes and retard recombination rate, which results in longer life time
iii. the bond angle of Ta-O-Ta is close to 180° and hence easy transport of photo electron hole pairs across the corner-shared octahedral framework is facilitated
iv. alkali metal tantalates are active for chemisorption of CO_2.

Based on the above characteristics, we have chosen $NaTaO_3$ as an active photo catalyst for PCRC. As shown in Figure 4.16, the conduction band bottom energy (CBM) level $NaTaO_3$ is suitable for the subsequent reduction of CO_2 after initial activation to form $CO_2^{\cdot-}$. Even though $NaTaO_3$ is highly efficient (quantum yield-56% with UV light) for water splitting, its application is limited with UV region due to its wide band gap which absorbs only <5% of solar energy (UV region). Several approaches to improve its visible light activity by doping with cations and anions have been explored via band gap engineering [53, 55-71]. Conduction band is mainly made up of Ta 5d orbitals (Fig. 4.16). A downward shift in the conduction band can be achieved by doping metal ion with lower energy orbital (3d, 4d) at Ta site, and also co-doping with metal ion at Na site, which would help to maintain the cationic charge balance. Studies have demonstrated that the modification of $NaTaO_3$ by doping with

Bi [57, 58], Fe [59], Sr [60], Cu [61]. N [62-65] and co-doping with La-Cr [66, 67], La-Co [68], La-Fe [69], La-Ir [70], La-N [71] promote its photo catalytic activity in the visible region. Valence band maximum (VBM) of $NaTaO_3$ is formed mainly by O 2p orbitals (Fig. 4.16), Upward shift of VBM can be achieved by doping higher energy anions [62-65]. Baochange Wang et al [72] have demonstrated the effect of doping with different anions like N, S, C, P and co-doping with N-N, C-S, P-P and N-P pairs on $NaTaO_3$ on the basis of theoretical calculations. Their calculations show that N doped $NaTaO_3$ shifts VBM towards more positive energy level as compared to pristine and other anion doped $NaTaO_3$ and towards more positive level with respect to the reduction potential for O_2 as well, to produce H_2 and O_2.

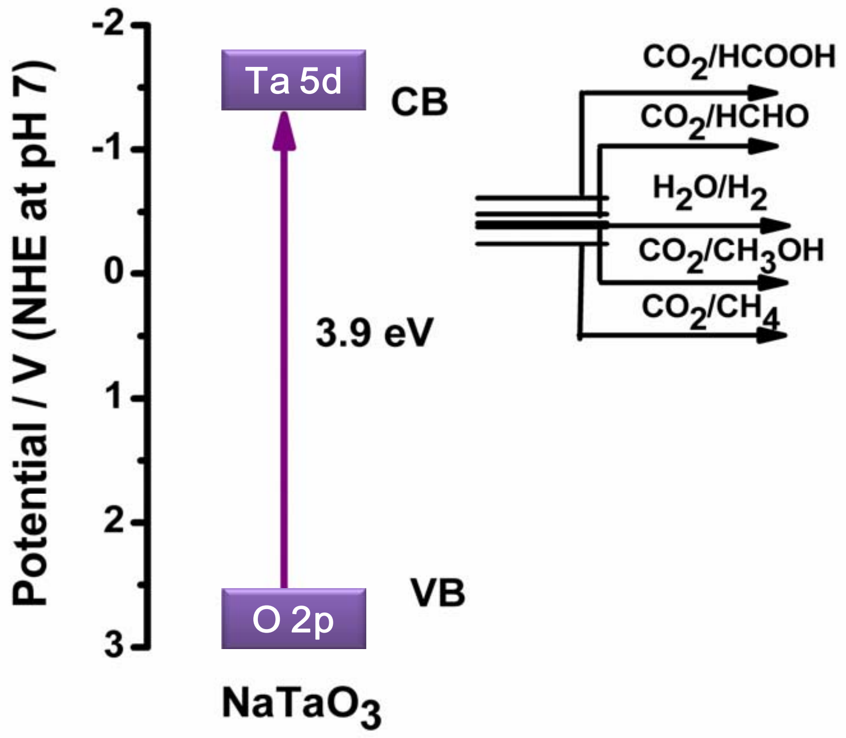

Fig. 4.16 VBM and CBM energy levels of $NaTaO_3$ with respect to the potential for reduction of CO_2 and oxidation of water.

In this context, the effect of doping and co-doping of $Na_{(1-x)}La_xTaO_{(3-x)}$ with Fe and N has been investigated to achieve reduction in the band gap energy so as to increase visible light absorption and increase in the efficiency of the photo catalyst by decreasing recombination rate of charge carriers.

4.2.2 Results and Discussion

4.2.2.1 X-Ray Diffraction Pattern

X- Ray Diffraction (XRD) studies were carried out to investigate the changes in the structure of $NaTaO_3$ due to doping with different elements. XRD patterns for the synthesized materials are shown in Figure 4.17. Peaks at 2Θ values of 22.9(020), 32.5(200), 40.1(022), 46.6(202), 52.4(301), 58.2(123) correspond to orthorhombic crystal structure (JCPDS Card No. 25-0863) of $NaTaO_3$. There is no significant change in XRD patterns with mono and co-doped catalysts and no diffraction peaks related to La_2O_3, Fe_2O_3, Ta_2O_5 were found.

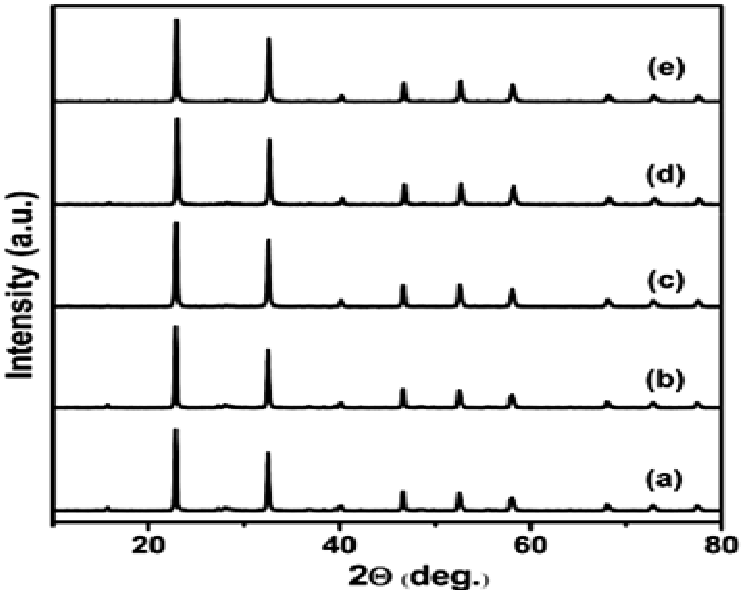

Fig. 4.17 XRD pattern for neat and modified catalyst (a) $NaTaO_3$ (b) $Na_{(1-x)}La_xTaO_{(3+x)}$, (c) N/$Na_{(1-x)}La_xTaO_{(3+x)}$, (d) Fe/$Na_{(1-x)}La_xTaO_{(3+x)}$, (e) Fe-N/ $Na_{(1-x)}La_xTaO_{(3+x)}$.

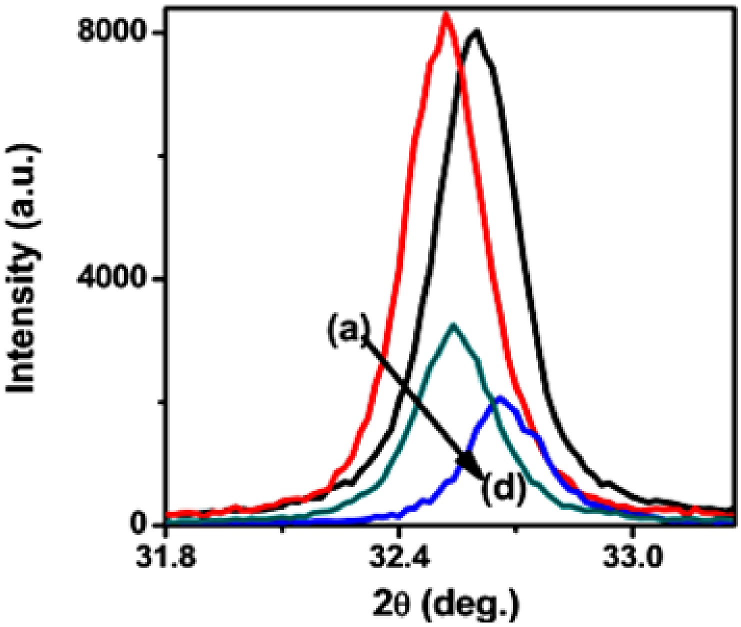

Fig. 4.18 XRD diffraction peak shift with the effect of substitution (a) $Na_{(1-x)}La_xTaO_{(3+x)}$, (b) $NaTaO_3$, (c) Fe/ $Na_{(1-x)}La_xTaO_{(3+x)}$, (d) Fe-N/$Na_{(1-x)}La_xTaO_{(3+x)}$.

This is possibly due to low concentration of dopant elements or at least a part of dopant element has been incorporated into the $NaTaO_3$ lattice, with the ionic radii of the dopants, ie, Fe^{3+} and La^{3+} being closer. As reported in literature [18, 69, 73] substitution of A site cation Na^+ (1.39Å) by La^{3+} (1.36Å in12 coordinated octahedral site) and B site cation Ta^{5+} (0.64 Å) by Fe^{3+} (0.65 Å in 6 fold coordinated site) in the ABO_3 crystal lattice of $NaTaO_3$ resulted in small shift in d-lines as shown in Fig. 4.18. Crystallite sizes of the synthesized photo catalysts were calculated by the Scherrer's formula, shown in Table 4.3. As La-Fe co-doping maintains the cationic charge balance ($Na^+ + Ta^{5+} = La^{3+} + Fe^{3+}$) of the material [69], less crystal defects are expected, compared to mono doped $NaTaO_3$. Calculated lattice parameters are shown in Table 4.3. Surface area of $Na_{(1-x)}La_xTaO_{(3+x)}$ as measured by BET method was 2.9 m^2/g and no significant changes in the texture were observed with the modified photo catalysts.

4.2.2.2 DRS UV-Visible Spectra

UV-Visible DRS spectra of the pristine and modified $NaTaO_3$ catalysts are shown in Fig. 4.19. The onset of absorption edge for the pristine $NaTaO_3$ is at 310 nm, ie absorption only in the Ultra Violet region with a band gap of 4.0 eV [18]. It is apparent that the DR spectra for all the modified $NaTaO_3$ catalysts showed red shift towards visible region.

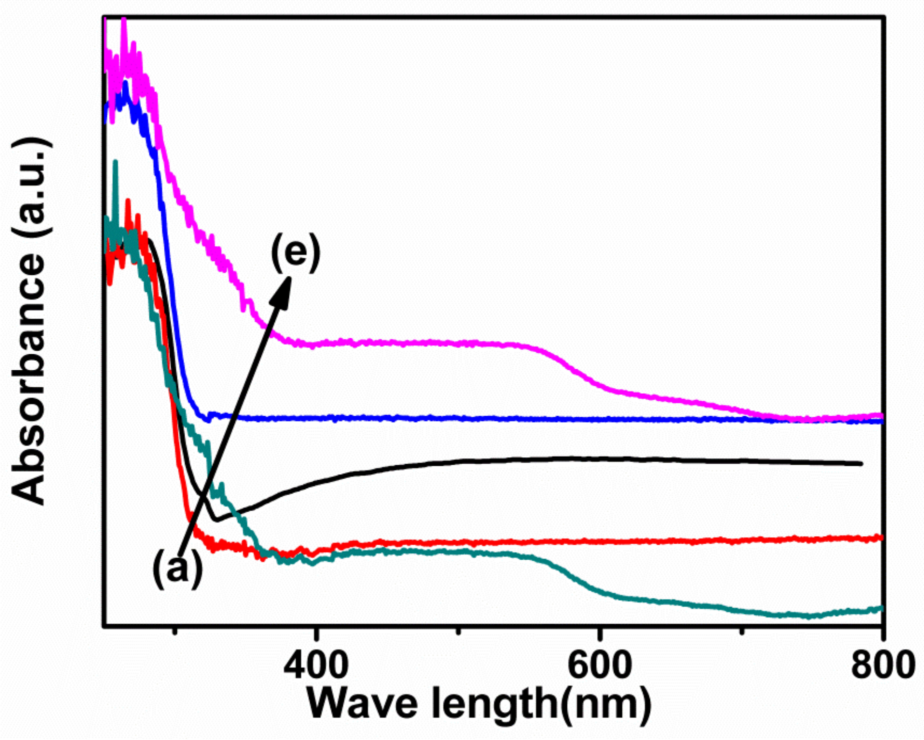

Fig. 4.19 Diffuse reflectance spectra of neat and modified $NaTaO_3$ catalysts

(a) $Na_{(1-x)}La_xTaO_{(3+x)}$, (b) $NaTaO_3$, (c) Fe/$Na_{(1-x)}La_xTaO_{(3+x)}$,

(d) N/ $Na_{(1-x)}La_xTaO_{(3+x)}$, (e) Fe-N/ $Na_{(1-x)}La_xTaO_{(3+x)}$.

As stated earlier, in pristine $NaTaO_3$, VBM is mainly composed of O 2p orbitals, while CBM is mainly composed of Ta 5d orbitals. In the case of N doped $NaTaO_3$, N 2p orbital energy level is higher than that of O 2p (VBM) orbital energy level and hence, the doped N 2p orbitals are situated at the top of the VBM of $NaTaO_3$ as impurity state [62-65]. The observed narrow band gap with N doped photo catalyst

(Fig. 4.19d, Table 4.3) can be ascribed due to the electron transition from impurity states (O 2p + N 2p) to the bottom of the CB of $NaTaO_3$ [63, 71, 72]. A steep increase of the absorption at λ>390 nm with Fe doped catalyst, is ascribed to the electron excitation of 3d e- of Fe^{3+} to CBM of $NaTaO_3$ sample [59, 69] and the prominent peak at 590 nm was also observed with Fe doped $NaTaO_3$. Similar absorption peak in Fe doped $NaTaO_3$ was observed in the earlier reports [59, 69], which could be due to d-d transition $^2T_{2g} \rightarrow {}^2A_{2g}$, $^2T_{1g}$ of Fe^{3+} or charge transfer transition between iron ions ($Fe^{3+} + Fe^{3+} \rightarrow Fe^{4+} + Fe^{2+}$) [74, 75].

Table 4.3 Crystallite size and band gap energy data for neat and modified $NaTaO_3$ Photocatalysts

Photocatalyst	**Lattice Parameter (Å)**			**Cry. Size**	**Band Gap**
	(a)	**(b)**	**(c)**	**(nm)**	**(eV)**
$NaTaO_3$	5.489	7.681	5.497	48.1	3.9
$Na_{(1-x)}La_xTaO_{(3+x)}$	5.506	7.780	5.505	47.2	4.1
$N/Na_{(1-x)}La_xTaO_{(3+x)}$	5.498	7.768	5.487	49.4	3.7
$Fe/Na_{(1-x)}La_xTaO_{(3+x)}$	5.498	7.751	5.491	45.5	3.4
$Fe\text{-}N/Na_{(1-x)}La_xTaO_{(3+x)}$	5.498	7.774	5.479	45.2	3.3

4.2.2.3 Electron Microscopy Analysis

Morphology and elemental composition of the synthesized catalysts has been established by SEM and EDXA studies. Fig. 4.20 and Fig. 4.21 shows SEM images for the neat $NaTaO_3$ and Fe-N modified La doped $NaTaO_3$ catalysts. SEM image clearly reveals that cubic morphology is retained with modified photo catalyst.

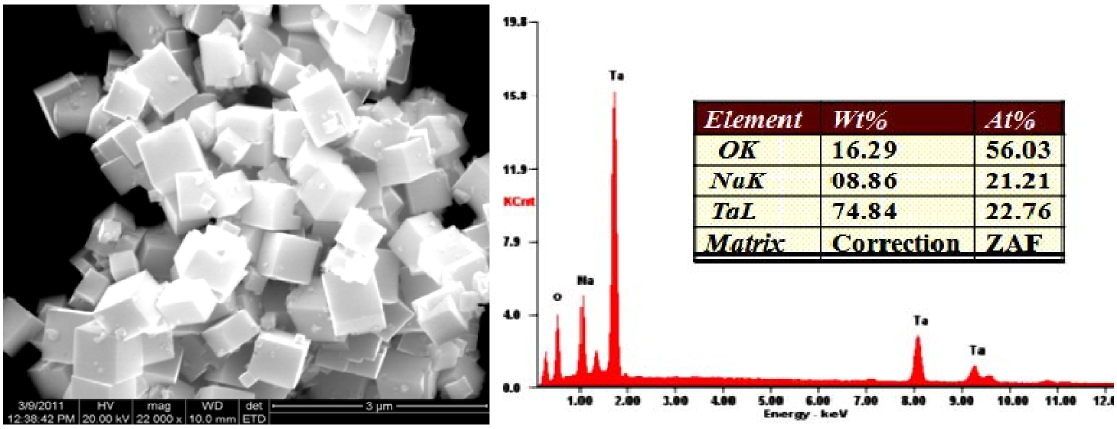

Element	Wt%	At%
OK	16.29	56.03
NaK	08.86	21.21
TaL	74.84	22.76
Matrix	Correction	ZAF

Fig. 4.20 SEM image and EDXA spectrum for $NaTaO_3$ photocatalyst.

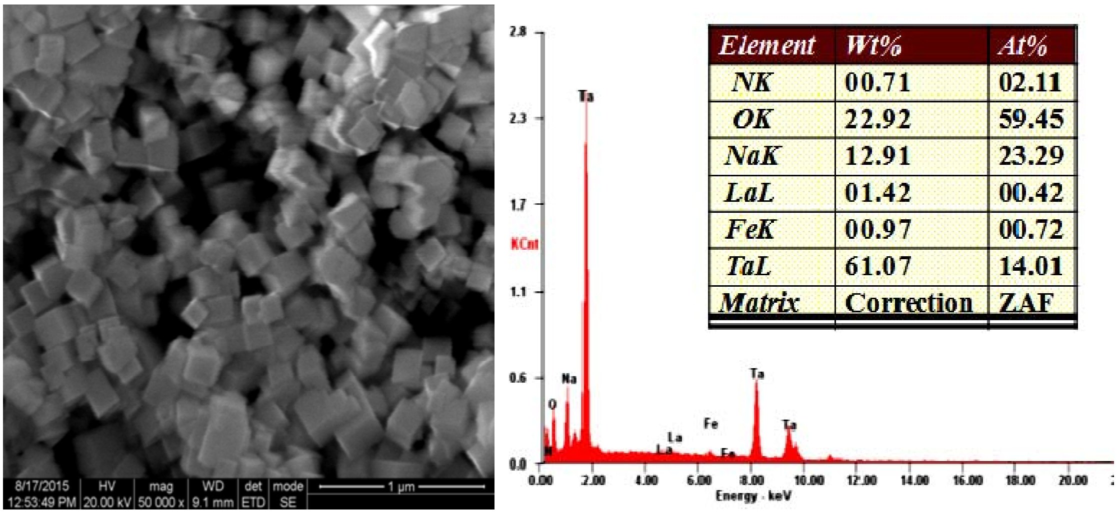

Element	Wt%	At%
NK	00.71	02.11
OK	22.92	59.45
NaK	12.91	23.29
LaL	01.42	00.42
FeK	00.97	00.72
TaL	61.07	14.01
Matrix	Correction	ZAF

Fig. 4.21 SEM image and EDXA spectrum for Fe-N/$Na_{(1-x)}La_xTaO_{(3+x)}$ photo catalyst

TEM (Fig. 4.22a & b) further confirms the cubic architecture of the $Na_{(1-x)}La_xTaO_{(3+x)}$ and Fe-N/$Na_{(1-x)}La_xTaO_{(3+x)}$ respectively. SAED (Fig. 4.22c) shows the highly crystalline nature of $NaTaO_3$ nano cubes, and d-value of 0.389 nm measured from HRTEM (Fig. 4.22d) corresponds to (002) planes of orthorhombic phase of $NaTaO_3$. The presence of added dopants can be confirmed by EDXA measurements. Fig. 4.20 and Fig. 4.21 show EDXA spectra for neat and Fe-N modified $NaTaO_3$ catalysts.

Presence of dopants such as Fe, N, La implies that all the added elements were effectively incorporated into the tantalate matrix during hydrothermal reaction. STEM-EDS elemental mapping of Na(Kα), Ta(Lα), La(Lα), Fe(Kα), O(Kα) and N(Kα) shown in Fig. 4.23 for the Fe-N/$Na_{(1-x)}La_xTaO_{(3+x)}$ photo catalyst, further confirms the uniform distribution of dopants elements in the tantalate matrix.

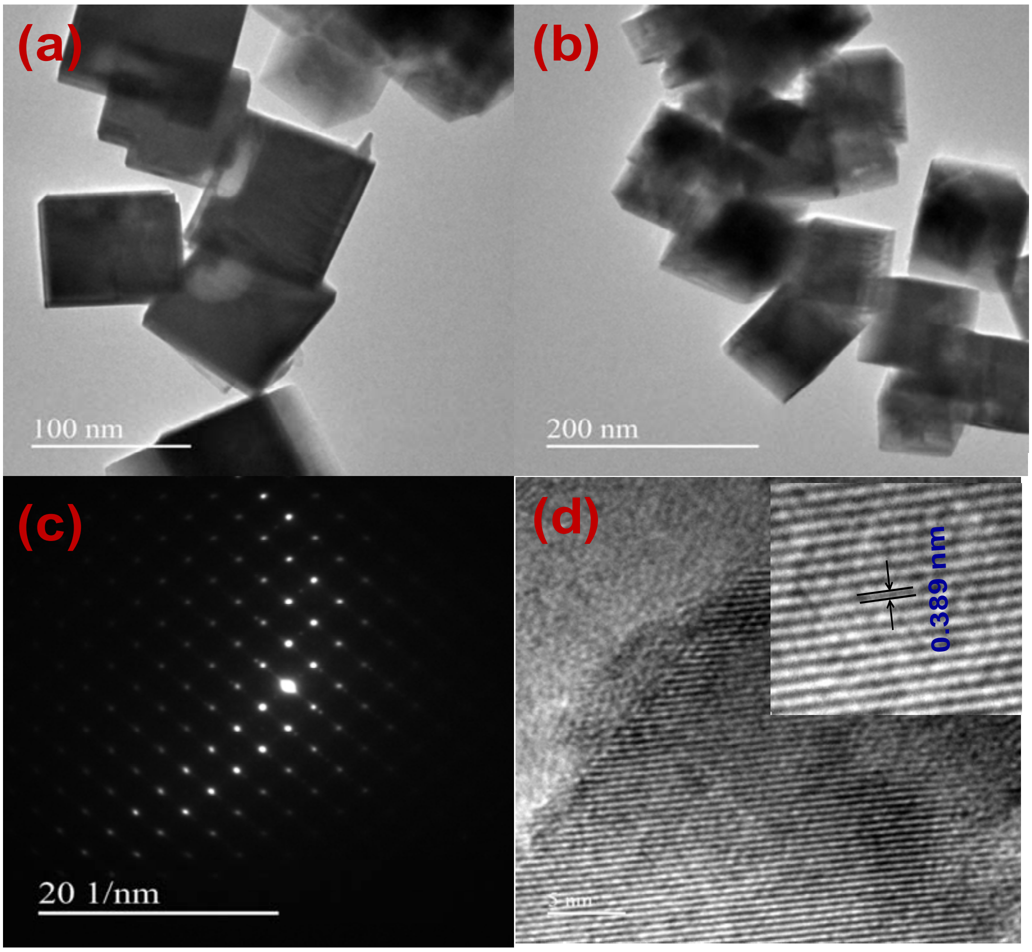

Fig. 4.22 Transmission Electron Microscopic images for (a) $Na_{(1-x)}La_xTaO_{(3+x)}$ (b) Fe-N/$Na_{(1-x)}La_xTaO_{(3+x)}$ (c) SAED for Fe-N/$Na_{(1-x)}La_xTaO_{(3+x)}$ (d) HRTEM for Fe-N/$Na_{(1-x)}La_xTaO_{(3+x)}$.

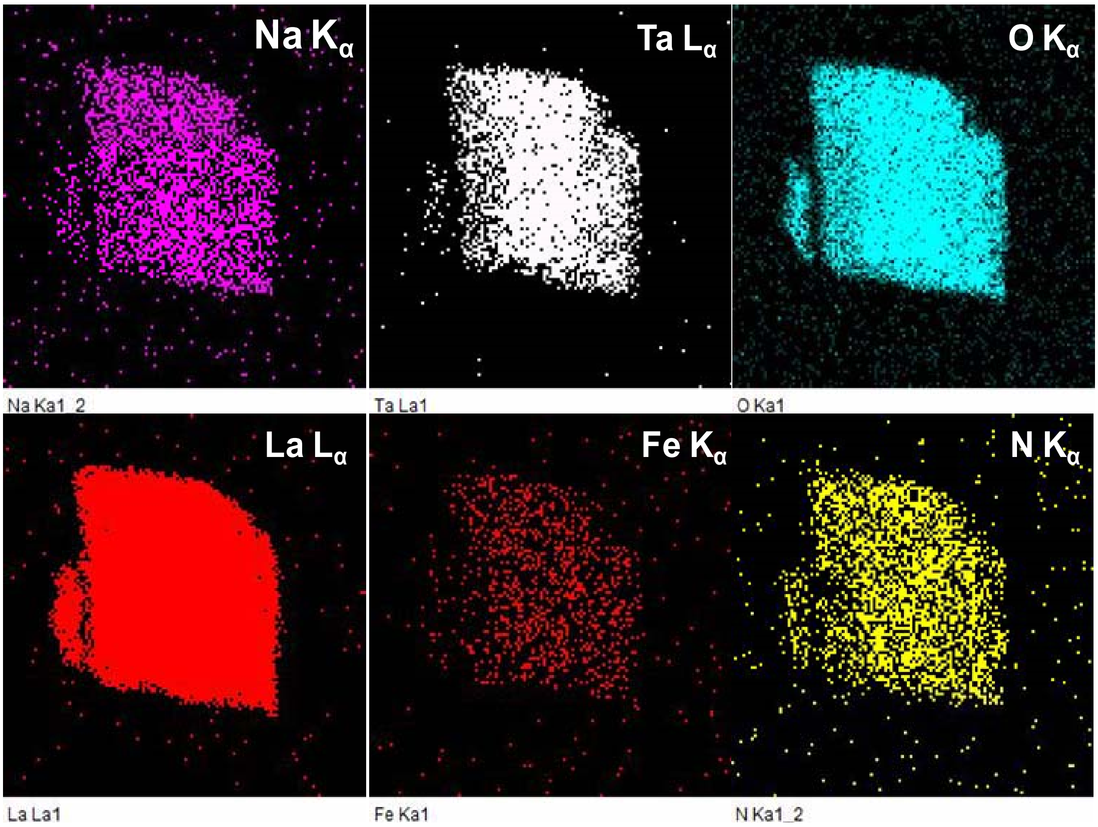

Fig. 4.23 EDS elemental mapping for Fe-N/$Na_{(1-x)}La_xTaO_{(3+x)}$ photo catalyst

4.2.2.4 X-ray Photoelectron Spectra

XPS measurements were carried out to analyse chemical composition and to identify chemical states of the dopant elements present in the synthesized photo catalysts. Typical XPS survey spectra for the synthesized photo catalysts are shown in Fig. 4.24. Binding energy values for the main XPS peaks for possible elements present in the synthesized materials are tabulated in Table 4.4a, and surface chemical composition of the possible elements in Table 4.4b.

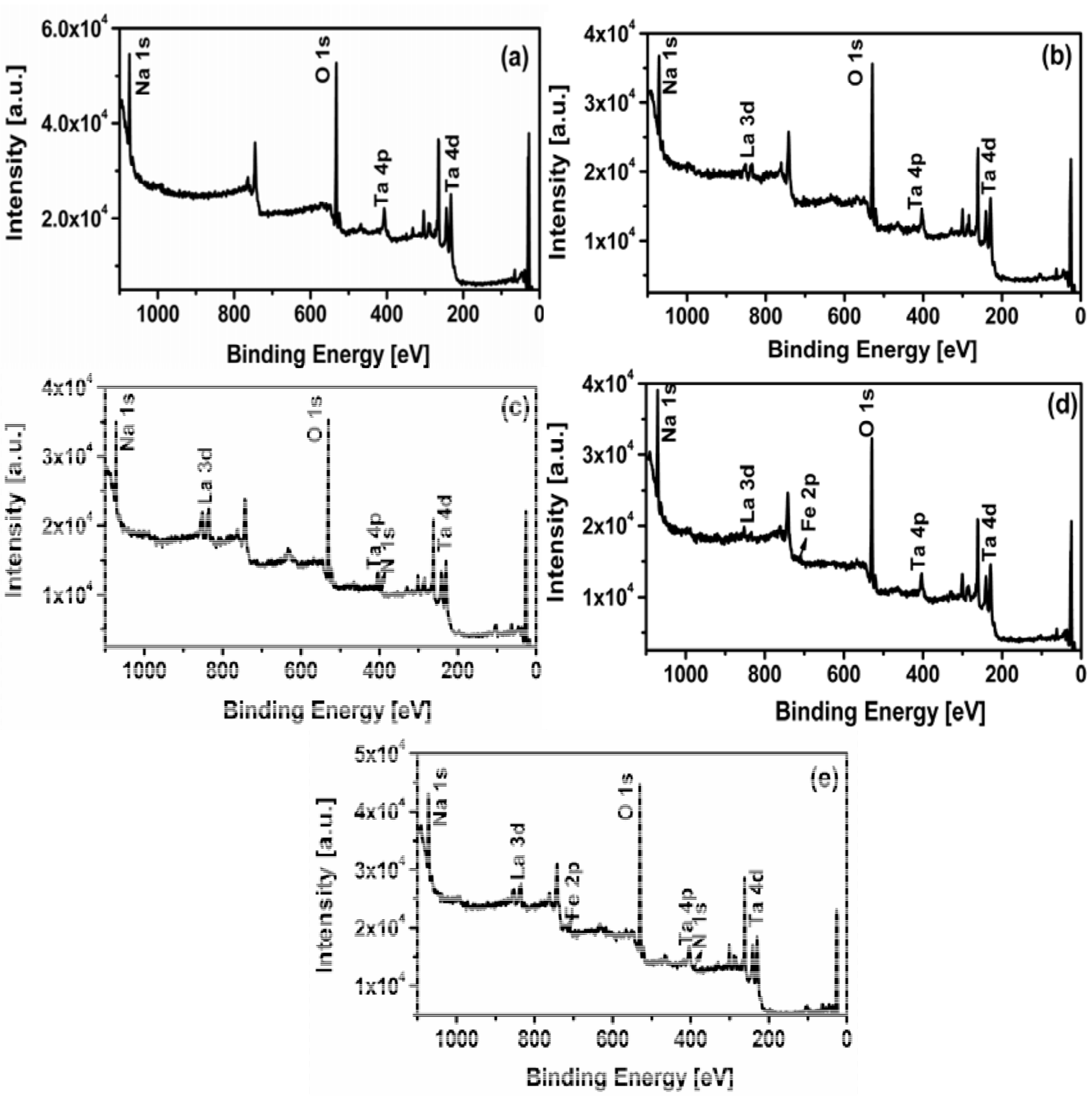

Fig. 4.24 XPS survey spectra of synthesized $NaTaO_3$ photo catalysts

(a) $NaTaO_3$ (b) $Na_{(1-x)}La_xTaO_{(3+x)}$, (c) $N/Na_{(1-x)}La_xTaO_{(3+x)}$,

(d) $Fe/Na_{(1-x)}La_xTaO_{(3+x)}$, (e) $Fe\text{-}N/Na_{(1-x)}La_xTaO_{(3+x)}$.

High resolution spectra of Na 1s, Ta 4d and O 1s present in the neat and modified photo catalysts are shown in Fig. 4.25. Main peaks for Na 1s (1071 eV), Ta 4d (229.6 eV) and O 1s (529.5 eV) were observed in pristine $NaTaO_3$ and similar peaks with small shift in binding energy (BE) were observed for the modified catalysts. The shifts in BE can be ascribed to the slight distortion of the $NaTaO_3$ lattice brought out by added dopant elements. Two types of O 1s peak are observed in all the neat and modified catalysts. The peak centered at 529 eV corresponds to lattice oxygen of Ta-O-Ta in octahedral TaO_6 crystal lattice and the other small area peak centered at 531 eV can be ascribed to surface hydroxyl group or adsorbed oxygen.

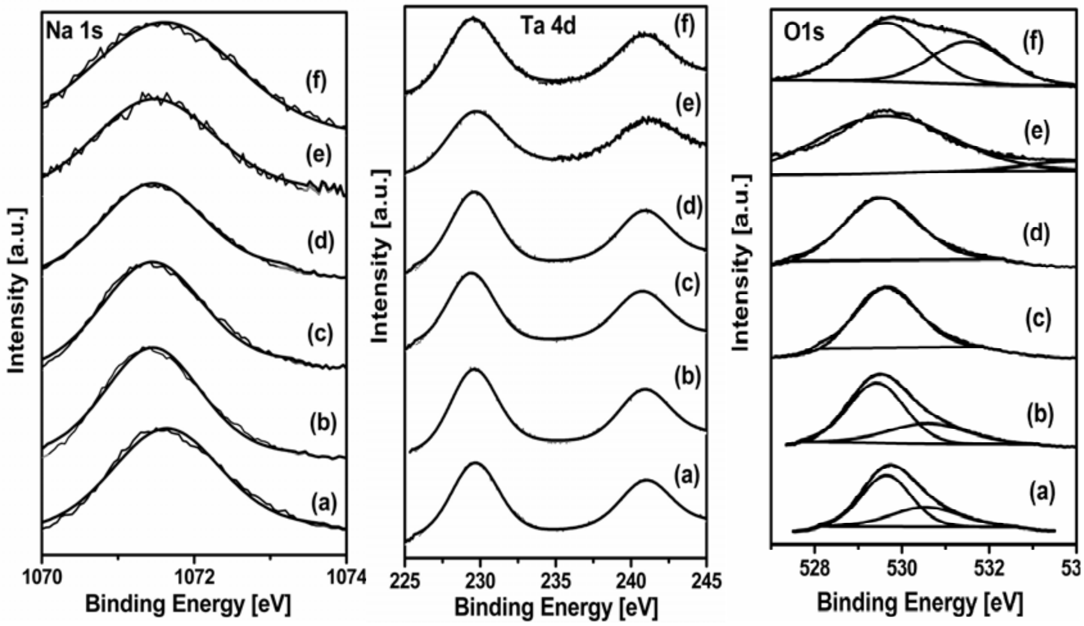

Fig. 4.25 High resolution XP spectra of Na 1s, Ta 4d and O 1s for neat and modified catalyst (a) $NaTaO_3$ (b) $Na_{(1-x)}La_xTaO_{(3+x)}$, (c) N/ $Na_{(1-x)}La_xTaO_{(3+x)}$, (d) Fe/ $Na_{(1-x)}La_xTaO_{(3+x)}$, (e) Fe-N/ $Na_{(1-x)}La_xTaO_{(3+x)}$, (f) 0.5 wt% MgO/ Fe-N/ $Na_{(1-x)}La_xTaO_{(3+x)}$.

Table 4.4a Binding energy data for main XPS peaks for neat and modified $NaTaO_3$

Photo catalysts	Binding Energy (eV)						
	Na 1s	**Ta 4d**	**Ta 4f**	**O 1s**	**La 3d**	**Fe 2p**	**N 1s**
$NaTaO_3$	1071.60	229.60	25.48	529.65 530.68	-	-	-
$Na_{(1-x)}La_xTaO_{(3+x)}$	1071.13	229.56	25.43	529.42 530.63	834.52	-	-
N/ $Na_{(1-x)}La_xTaO_{(3+x)}$	1071.12	229.42	24.89	529.65	834.33	-	399.2
Fe/ $Na_{(1-x)}La_xTaO_{(3+x)}$	1070.87	229.47	25.10	529.0	834.63	711.95	-
Fe-N/$Na_{(1-x)}La_xTaO_{(3+x)}$	1070.82	229.70	25.30	529.55	834.42	711.12	399.8

Fig. 4.26A shows high resolution XP spectra for La 4d, wherein the peak centered at 834.6 eV corresponds to La^{3+} ion, indicating that dopant is incorporated into the

tantalate lattice, since ionic radii of La^{3+} (1.36Å) and Na^{+} (1.39Å) ions being closer [71, 73, 76]. High resolution XP spectra for Fe 2p shown in Fig. 4.27B, displays a peak centered at 711.9 eV due to the dopant Fe present as Fe^{3+} ion. Presence of Ta^{5+} ions around Fe^{3+} ions in the lattice results in a shift in the BE to 711.9 eV, compared to 710.7 eV observed for Fe^{3+} in precursor Fe_2O_3 [77]. The shift in BE is due to the interaction between Fe^{3+} and Ta^{5+} ions in crystal lattice, which clearly shows that some of the doped Fe^{3+} ions have been incorporated into TaO_6 crystal lattice. Since ionic radii of Ta^{5+} and Fe^{3+} ions are closer, Fe^{3+} ions occupy Ta^{5+} ion sites in the lattice.

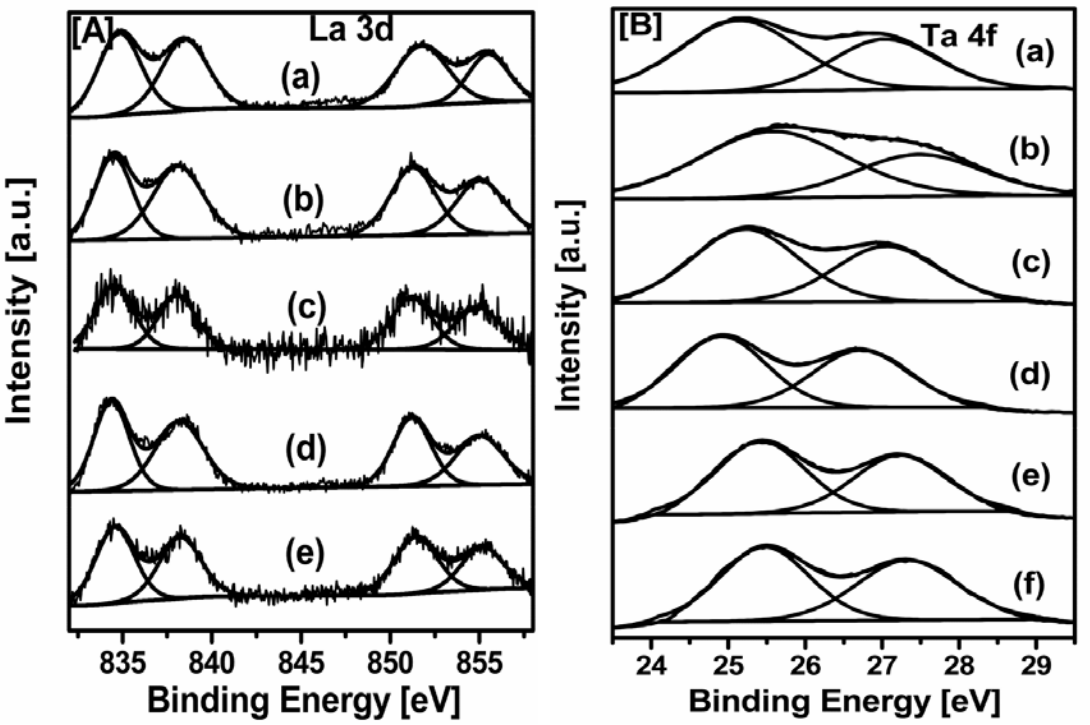

Fig. 4.26 High resolution XP spectra of La 3d [A], Ta 4f [B] for neat and modified catalyst (a) 0.5 wt% $MgO/Fe\text{-}N/Na_{(1-x)}La_xTaO_{(3+x)}$, (b) $Fe\text{-}N/Na_{(1-x)}La_xTaO_{(3+x)}$, (c) $Fe/Na_{(1-x)}La_xTaO_{(3+x)}$, (d) $N/Na_{(1-x)}La_xTaO_{(3+x)}$, (e) $Na_{(1-x)}La_xTaO_{(3+x)}$, (f) $NaTaO_3$.

Table 4.4b Elemental composition from XPS data for modified $NaTaO_3$ based photo catalysts

Photo catalysts	Composition at%					
	Na	**Ta**	**O**	**La**	**Fe**	**N**
$NaTaO_3$	6.79	21.76	71.44	-	-	-
$Na_{(1-x)}La_xTaO_{(3+x)}$	6.65	20.40	71.70	1.290	-	-
N/ $Na_{(1-x)}La_xTaO_{(3+x)}$	6.51	19.02	71.22	1.059	-	3.209
Fe/ $Na_{(1-x)}La_xTaO_{(3+x)}$	6.74	19.50	71.60	0.861	-	-
Fe-N/ $Na_{(1-x)}La_xTaO_{(3+x)}$	6.34	19.49	71.28	0.825	0.407	1.658

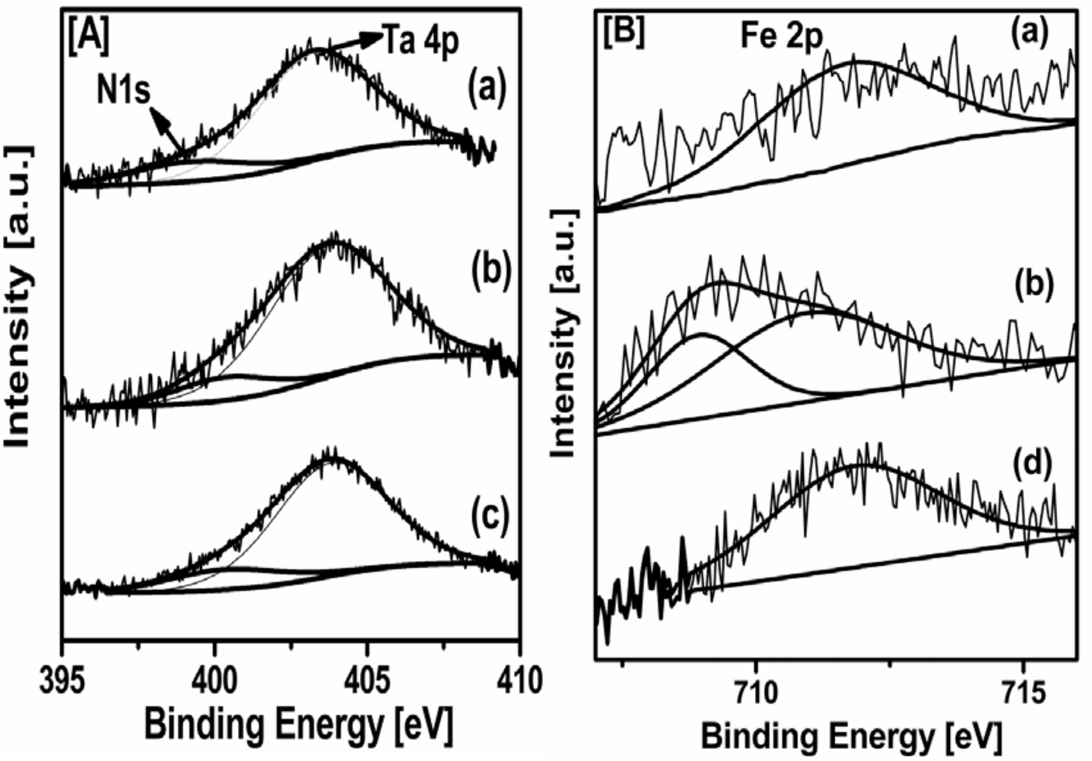

Fig. 4.27 High resolution XPS spectra of N 1s [A] and Fe 2p [B] for neat and modified catalyst (a) 0.5 wt% MgO/Fe-N/ $Na_{(1-x)}La_xTaO_{(3+x)}$, (b) Fe-N/ $Na_{(1-x)}La_xTaO_{(3+x)}$, (c) N/ $Na_{(1-x)}La_xTaO_{(3+x)}$, (d) Fe/$Na_{(1-x)}La_xTaO_{(3+x)}$.

Fig. 4.27A shows N 1s spectra for N doped $NaTaO_3$ samples shows two new peaks, one centered at 399 eV corresponding to substitutional N ie Ta-N bond and another peak centered at 400 eV, corresponding to interstitial nitrogen (Ta-O-N) or adsorption of nitride on the N modified photo catalyst surface. The above results are consistent with the earlier literature reports [63-65, 78, 79]. The observed N 1s spectra implies that some of the oxygen sites are substituted by doped nitrogen atoms and some of the nitrogen is present in the interstitial position in the crystal lattice of $NaTaO_3$. As reported by Zhao et al., synergetic effect of La-N co doping also promotes the incorporation of nitrogen into the lattice [71].

High resolution XP spectra for Ta 4f are shown in Fig. 4.26B. The peaks centered at 25.5 and 27.5 eV correspond to Ta $4f_{7/2}$ and Ta $4f_{5/2}$ respectively. It is seen from the Fig. 4.26B that Ta $4f_{5/2}$ peak is shifted to lower binding energy side when the $NaTaO_3$ was doped with nitrogen, as reported by Michikazu Hara et al [79]. This can be ascribed that formation of Ta-N bond with N doped $NaTaO_3$ photo catalyst. Ta-O bond is less covalent than Ta-N bond. Hence dopant nitrogen increases electron cloud around Ta [63, 80], consequently lowering BE. Binding energy shift on lower side of Ta 4f peaks further confirms the incorporation of doped nitrogen into oxygen sites of $NaTaO_3$ lattice.

4.2.2.5 Photoluminescence Spectra

Photoluminescence spectra for the neat and modified catalysts (Fig. 4.28) give additional features of the doped catalysts. An emission peak, centred at 469 nm is observed for the neat and modified $NaTaO_3$, demonstrating that doping of the photo catalyst does not result in any new PL spectral line, but the intensity of the line is reduced. PL spectra mainly result from the recombination of charge carriers and its intensity is directly proportional to the probability of the recombination of charge carriers. When the pristine catalyst was doped with N, the intensity of the PL spectral line is reduced to some extent. It can be seen that, there is a sharp reduction in the intensity of the PL spectral line, when the pristine catalyst is doped with Fe and co doped with Fe-N. Decrease in the intensity of the PL line implies that dopant (Fe or N) or co-dopants (Fe-N) could inhibit the probability of the charge carriers recombination, leading to an increase the life time of the charge carriers.

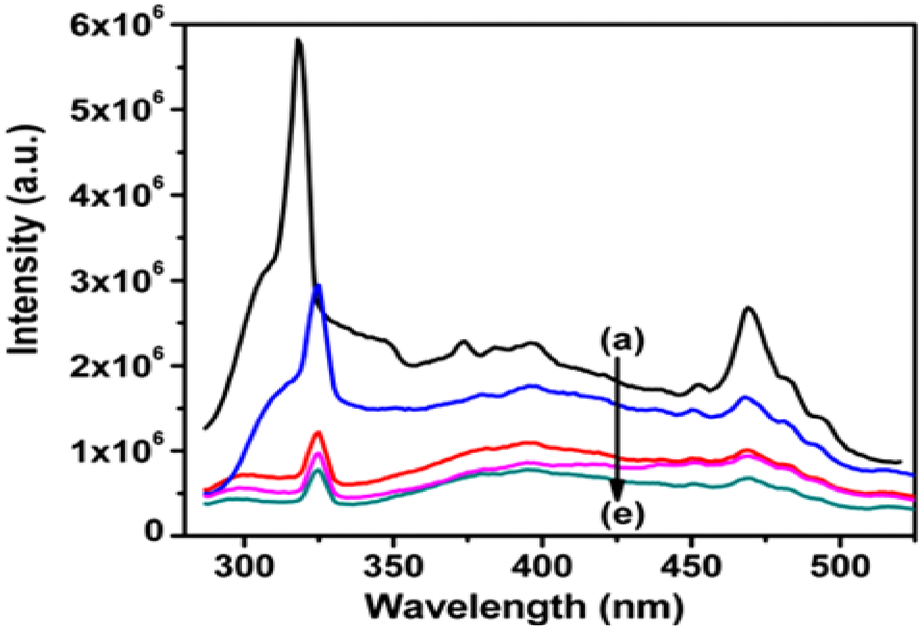

Fig. 4.28 Photo luminescence spectra for neat and modified $NaTaO_3$ catalysts (a) $NaTaO_3$, (b) $Na_{(1-x)}La_xTaO_{(3+x)}$, c) N/ $Na_{(1-x)}La_xTaO_{(3+x)}$, (d) Fe/ $Na_{(1-x)}La_xTaO_{(3+x)}$, (e) Fe-N/ $Na_{(1-x)}La_xTaO_{(3+x)}$.

4.2.3 Photo catalytic reduction of carbon dioxide

All the experiments were carried out up to 20 hrs. Trends in the formation of major products, methanol and ethanol, with respect to time of irradiation up to 20 hrs, are given in Fig. 4.29.

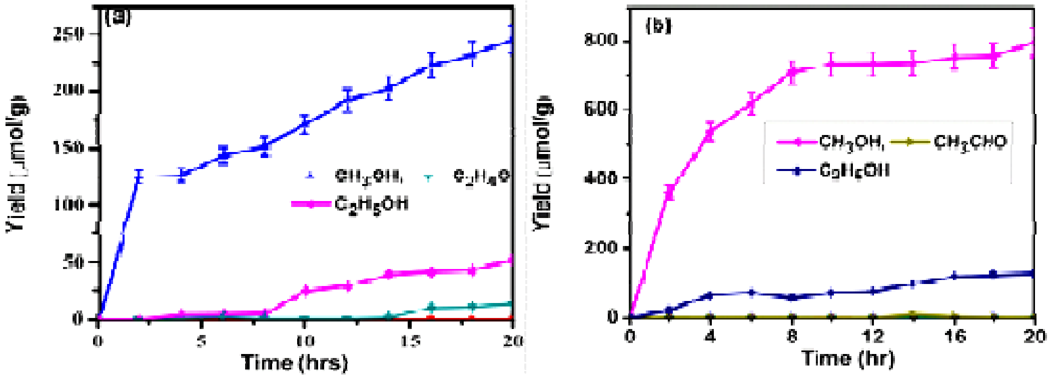

Fig. 4.29 Trends in photo catalytic activity for CO_2 reduction with alkaline medium - Time on stream plots - (a) $NaTaO_3$, (b) Fe-N/$Na_{(1-x)}La_xTaO_{(3+x)}$.

Besides hydrogen and oxygen, methane, ethylene and ethane were formed in very small quantities (~0.1-10 micromoles/g) and hence not considered in the plots. CO and formic acid were detected at trace levels and hence could not be quantified. As shown in Fig. 4.7, large amounts of methanol is formed when the aqueous alkaline solution is saturated with carbon dioxide compared to very small quantities formed after saturation with nitrogen, indicating that the observed methanol/products were obtained from CO_2 photo reduction, not from surface carbon impurities on the catalyst. Rates of formation of products are high during initial 8-10 hrs, beyond which the product formation tends to slow down. Based on the initial rates (μ mol g^{-1} h^{-1}) for the formation of different products, and the number of photo electrons involved in each case, apparent quantum yields (AQY) for all the photo catalysts have been calculated and presented in Table 4.5.

Table 4.5 Products distribution and quantum yield data for neat and modified $NaTaO_3$

Photo catalysts	**Products obtained from CO_2 reduction (μmol g^{-1} h^{-1})**								**AQY (%)**
	CH_4	**C_2H_4**	**C_2H_6**	**CH_3OH**	**C_2H_4O**	**C_2H_5OH**	**C_3H_6**	**H_2**	**x10^{-3}**
$NaTaO_3$	0.01	-	0.01	20.6	0.6	2.5	-	0.13	2.99
NTO*	0.02	-	0.00	16.2	4.01	6.4	0.05	0.02	4.04
N/ NTO	0.07	0.06	0.03	44.4	1.7	10.4	0.04	0.41	7.67
Fe/ NTO	0.03	0.04	0.02	49.1	0.7	10.5	0.03	0.15	7.98
Fe-N/ NTO	0.03	0.05	0.03	62.2	0.05	8.5	0.02	0.04	8.89

* $Na_{(1-x)}La_xTaO_{(3+x)}$.

It is observed from Table 4.5 that lanthanum and Fe-N incorporated in La doped $NaTaO_3$ significantly influence the overall quantum yield as well as selectivity to various products. Doping of lanthanum, nitrogen or iron separately to $NaTaO_3$ results in marginal increase in quantum yield. In case of co-doping ie Fe-N doped photo catalyst, quantum yield increased by three times with respect to neat $NaTaO_3$. Fe-N modified $NaTaO_3$ photo catalyst displays maximum increase in activity and relatively higher selectivity towards alcohols. Comparison of different hydrocarbon formation after 20 hrs of irradiation with various synthesized photo catalysts are shown in Fig. 4.30. Doping with N and Fe separately does promote CO_2 photo reduction but are not as effective as Fe-N co-doped photo catalyst.

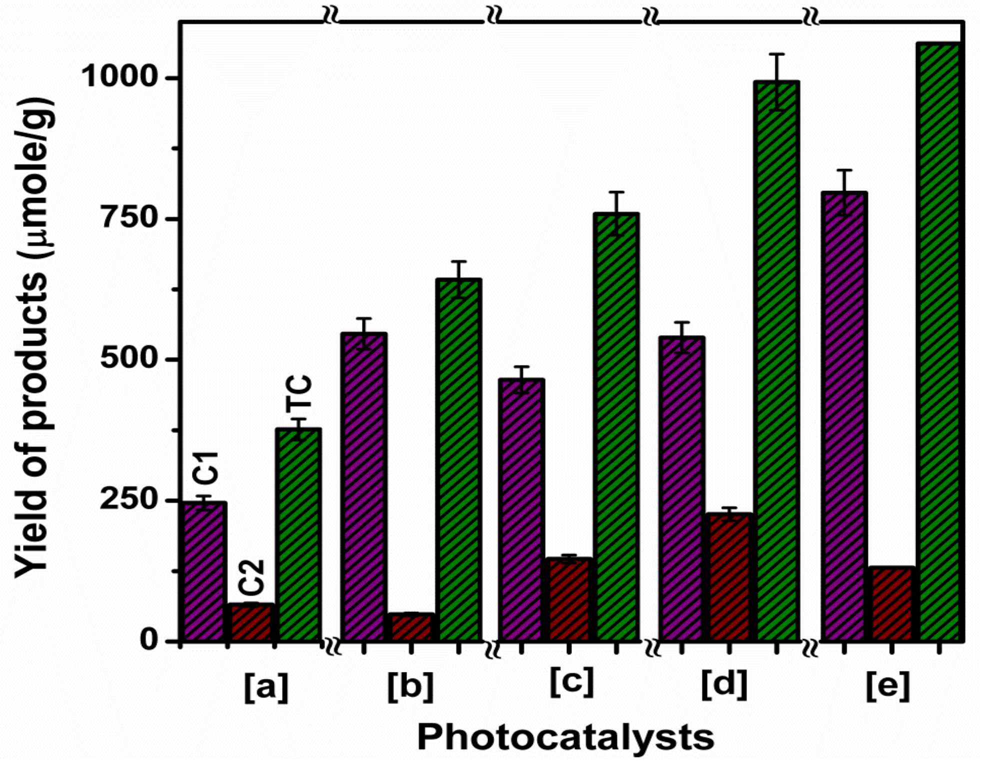

[C1 – C_1 carbon product, C2 – C_2 carbon product, TC- Total Carbon product].

Fig. 4.30 Comparison of photocatalytic activity for neat and modified catalysts after 20 hrs of irradiation: (a) $NaTaO_3$ (b) $Na_{(1-x)}La_xTaO_{(3+x)}$, (c) N/ $Na_{(1-x)}La_xTaO_{(3+x)}$,(d) Fe/ $Na_{(1-x)}La_xTaO_{(3+x)}$,(e) Fe-N/$Na_{(1-x)}La_xTaO_{(3+x)}$.

Since the dopant Fe 3d orbital energy level is smaller than Ta 5d orbital, it will create new energy level below the conduction band resulting in downward shift of CB [59] as shown in Fig. 4.31. As evident from the XRD and XPS data, Fe^{3+} ion occupies Ta^{5+} site in the lattice. Dopant Fe^{3+} ion possesses the ability to trap and de-trap the charge carriers, ie, Fe^{3+} ion can easily trap photo generated electrons from the CB of $NaTaO_3$, since dopant energy level for electron trapping ie Fe^{3+}/Fe^{2+} (0.77 V vs NHE) is below the CBM of $NaTaO_3$ (-1.06 V vs NHE). Also, Fe^{3+} can easily trap photo generated holes from VB $NaTaO_3$ since dopant energy level for hole trapping ie Fe^{4+}/Fe^{3+} (2.2 V vs NHE) is above the VB of $NaTaO_3$ (2.94 V vs NHE). The above characteristic nature of Fe^{3+} would help to enhance the charge carrier life time, as is evident from fluorescence spectra (Fig. 4.28) [81, 82].

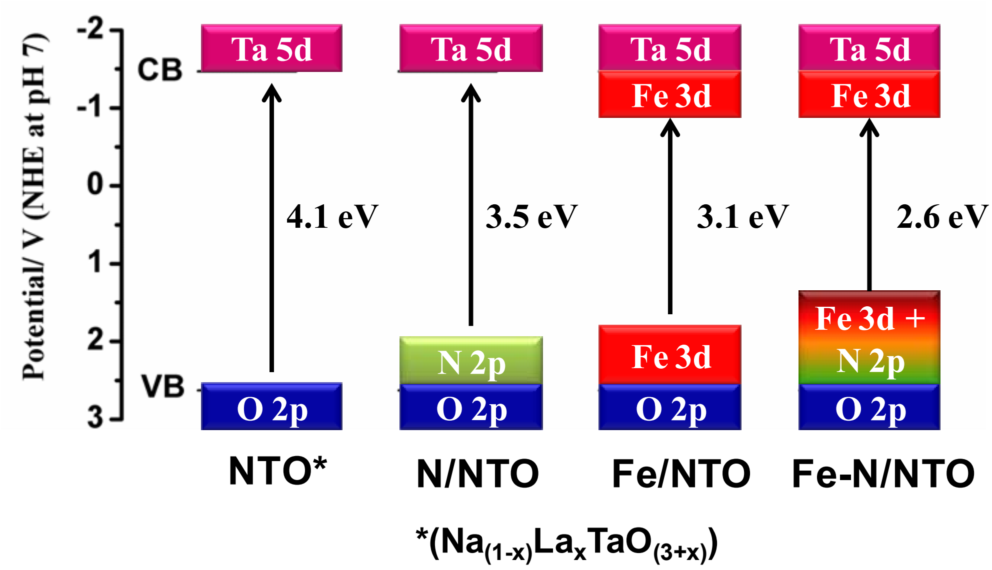

Fig. 4.31 VBM & CBM energy levels of $Na_{(1-x)}La_xTaO_{(3+x)}$ and its Fe-N modified catalysts vis-a-vis potential for reduction of CO_2 and oxidation of water.

De-trapping of exciton (charge carriers) is also important factor as far as photo catalysis concerned, because trapped excitons has to reach surface adsorbed species to get converted into useful products. According to crystal field theory, Fe^{3+} is most stable form of Fe because of its d^5 electronic configuration. Hence, as mentioned above Fe^{4+} and Fe^{2+} ions can have the tendency to release their trapped charges to surface adsorbed species to become most stable Fe^{3+} [81, 74]. As observed from XPS data, doped La as La^{3+} can easily diffuse into perovskite lattice and cationic charge was maintained by Fe^{3+} doping at Ta^{5+} site and La^{3+} at Na^+ site [$Na^+ + Ta^{5+} \rightarrow La^{3+} + Fe^{3+}$], which will reduce defect sites [69]. Synergetic effect of La-N co-doping also reduces the point defects [71], and these defect sites could serve as a charge recombination centre. Thus, increase in photo catalytic activity with Fe-N modified $Na_{(1-x)}La_xTaO_{(3+x)}$ can be ascribed due to increase in absorption towards visible region as well as increase in life time of charge carriers. The changes in the electronic energy levels taking place when doping with N & Fe separately and co-doping with Fe-N are depicted in Fig. 4.31 below. The changes are in line with the experimental values for band gap energy measured by DRS.

4.2.4 Conclusions

Neat and modified $NaTaO_3$ photo catalysts have been synthesized by simple one step hydrothermal method. The effect of doping/co-doping on the photo physical properties of the catalysts has been investigated by applying various experimental techniques. XRD and XPS results reveal that La^{3+} occupies Na^+ ion sites, Fe^{3+} ions Ta^{5+} ions site and N the O^{2-} sites, possibly as N^{3-} in the tantalate matrix. Incorporation of the dopants in the tantalate matrix has been established by SEM-EDXA and STEM-EDS elemental mapping and surface composition analysis by XPS. Synergistic effects of La, Fe and N co-doping in tantalate matrix results in the narrowing of the band gap due to the creation of additional energy levels within the band gap. Band gap narrowing promotes visible light absorption. Presence of dopants in the lattice ensures electro-neutrality. Efficient charge trapping and de-trapping by Fe^{3+} and Fe^{4+} ions reduces the probability of charge carrier recombination. Synergetic effect due to co-doping with La, Fe and N and conduction band edge energy levels suitable for CO_2 reduction with water help to improve the photo catalytic properties of co-doped $NaTaO_3$.

4.3 Modifications in $Na_{(1-x)}La_xTaO_{(3+x)}$: Effect of addition of MgO on photo catalytic reduction of Carbon Dioxide

4.3.1 Introduction

As stated by Liu et al, there are some aspects that affect the efficiency of CO_2 photo reduction, especially with H_2O, the major one being the limited adsorption of CO_2 molecules on catalyst surface, which is in competition with the adsorption of H_2O molecules [83]. Adsorption of CO_2 is hindered by H_2O molecules on photo catalyst surface suspended in aqueous medium, due to higher binding energy of H_2O (-0.64 eV) vis-a-vis that of CO_2 (-0.34 eV) [23, 84]. Teramura et al [11] has demonstrated that the photo catalytic reduction of CO_2 on solid base catalysts such as ZrO_2, MgO and Ga_2O_3 proceed smoothly due to effective adsorption of CO_2, an acidic moiety. Linear CO_2 molecules transform into non-linear or destabilized/active CO_2, upon adsorption on the surface of solid base [85-89]. Hence, addition of a basic oxide could enhance adsorption of CO_2 on band gap engineered photo-catalyst, Fe-N/$Na_{(1-x)}La_xTaO_{(3+x)}$. In this study, we have chosen MgO as solid base material in order to increase adsorption ability of CO_2 on the active catalyst surface in the presence of H_2O.

4.3.2 Results and discussion

4.3.2.1 Characterization of catalysts

Various amounts of MgO, (0.3%, 0.5% and 1%, all w/w) were loaded on the band gap engineered Fe-N/$Na_{(1-x)}La_xTaO_{(3+x)}$ photo-catalyst by impregnation method. MgO loaded catalysts were characterized by a range of experimental techniques, vis-à-vis that of the formulation without added MgO. Fig. 4.32 shows XRD patterns for the synthesized MgO loaded photo catalysts. The diffraction patterns clearly show that addition of MgO to Fe-N/$Na_{(1-x)}La_xTaO_{(3+x)}$ phase has not resulted in any structural changes in the tantalate matrix. Most likely, MgO is present as an amorphous layer on the tantalate surface.

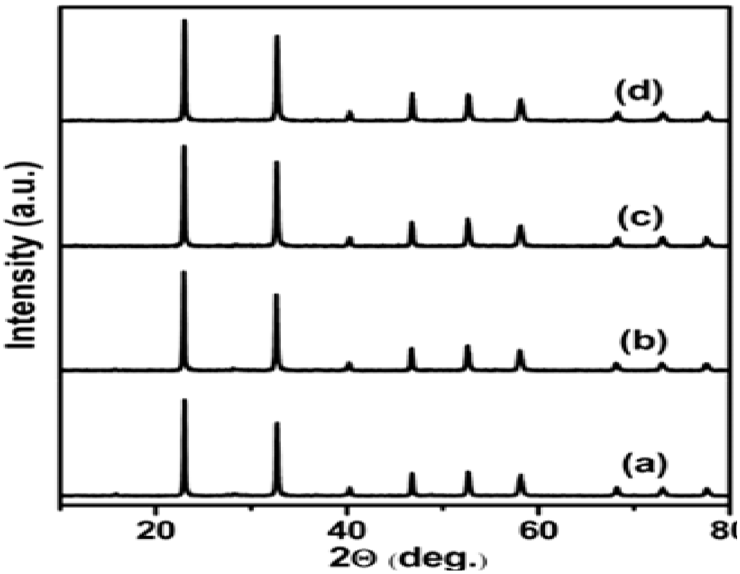

Fig. 4.32 Effect of addition of MgO on the XRD pattern for neat and modified catalyst (a) Fe-N/ $Na_{(1-x)}La_xTaO_{(3+x)}$, (b) 0.3 wt% MgO/Fe-N/ $Na_{(1-x)}La_xTaO_{(3+x)}$, (c) 0.5 wt% MgO/Fe-N/ $Na_{(1-x)}La_xTaO_{(3+x)}$, (d) 1 wt% MgOFe-N/ $Na_{(1-x)}La_xTaO_{(3+x)}$.

UV-Visible diffuse reflectance spectra for the catalysts modified with MgO (Fig. 4.33) do not reveal any change in optical/electronic properties. SEM and TEM images of the MgO loaded samples display cubic morphology of the base photo catalyst. XPS spectra presented in Fig. 4.25f (Na 1s, Ta 4d, O 1s), Fig. 4.26a (La 3d, Ta 4f) and 4.27a (N 1s, Fe 2p) further confirm there are no changes in the structure or oxidation state of components in the MgO doped Fe-N/$Na_{(1-x)}La_xTaO_{(3+x)}$ catalyst. Basicity measurements by CO_2-TPD indicate that the amount of chemisorbed CO_2 on 0.5 wt% MgO loaded photo catalyst is 29.3 µmole g^{-1}, which is higher than chemisorbed CO_2 (27.1 µmole g^{-1}) on Fe-N/ $Na_{(1-x)}La_xTaO_{(3+x)}$ surface. The basic nature of added MgO has increased the overall basicity of MgO modified tantalate. Increased basicity would improve CO_2 adsorption [9].

All the above characteristics confirm that added MgO has not changed the crystal structure, electronic or optical properties of the photo catalyst, but only its basicity has increased. The increase in basicity of the photo catalyst favours CO_2 adsorption, resulting in the availability of more number of adsorbed/active CO_2 molecules for the PCRC with water.

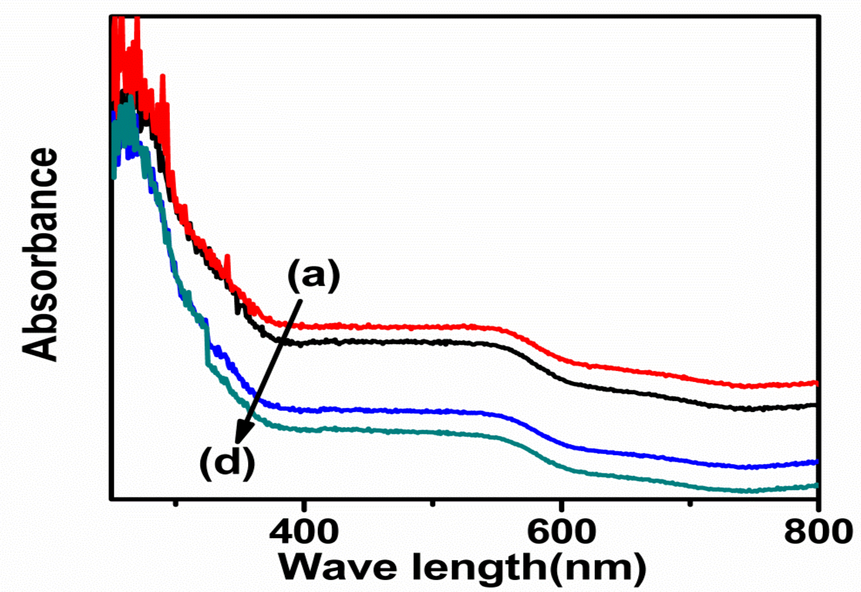

Fig. 4.33 Effect of addition of MgO: Diffuse reflectance spectra of neat and modified $NaTaO_3$ catalysts (a) Fe-N/ $Na_{(1-x)}La_xTaO_{(3+x)}$, (b) 0.3 wt% MgO/Fe-N/ $Na_{(1-x)}La_xTaO_{(3+x)}$, (c) 0.5 wt% MgO/Fe-N/ $Na_{(1-x)}La_xTaO_{(3+x)}$, (d) 1 wt% MgO/Fe-N/ $Na_{(1-x)}La_xTaO_{(3+x)}$.

4.3.2.2 Photo catalytic reduction of CO_2 on MgO modified catalysts

The photo catalytic activity of MgO loaded samples and the observed product distribution have been tabulated in Table 4.6. It is observed that the activity increases with increasing amount of

MgO up to 0.5 wt% and further increase in the amount of MgO retards the photo catalytic activity of Fe-N/$Na_{(1-x)}La_xTaO_{(3+x)}$. Excess amount of MgO perhaps hinders the charge transfer from active surface $NaTaO_3$ to CO_2 molecules to get reduce into products. The optimum loading of MgO on this particular catalyst surface for this critical application is found to be 0.5 wt% which gives higher selectivity towards methanol (Fig. 4. 34).

Table 4.6 Products distribution and quantum yield data for MgO loaded photo catalysts

Photo catalysts	Products obtained from CO_2 reduction (μmol g^{-1} h^{-1})								AQY (%)
	CH_4	C_2H_4	C_2H_6	CH_3OH	C_2H_4O	C_2H_5OH	C_3H_6	H_2	x 10^{-3}
Fe-N/NTO*	0.03	0.05	0.03	62.2	0.05	8.5	0.02	0.04	8.89
0.3 wt%MgO /Fe-N/NTO	0.04	0.07	0.04	76.6	0.8	8.1	0.03	0.04	10.57
0.5 wt%MgO/ Fe-N/NTO	0.11	0.08	0.03	81.4	1.0	7.9	0.03	0.05	11.11
1 wt%MgO/ Fe-N/NTO	0.07	0.04	0.01	20.7	1.7	8.6	0.03	0.1	4.62

*$Na_{(1-x)}La_xTa_{(1-y)}Fe_yO_{(3-z)}N_z$.

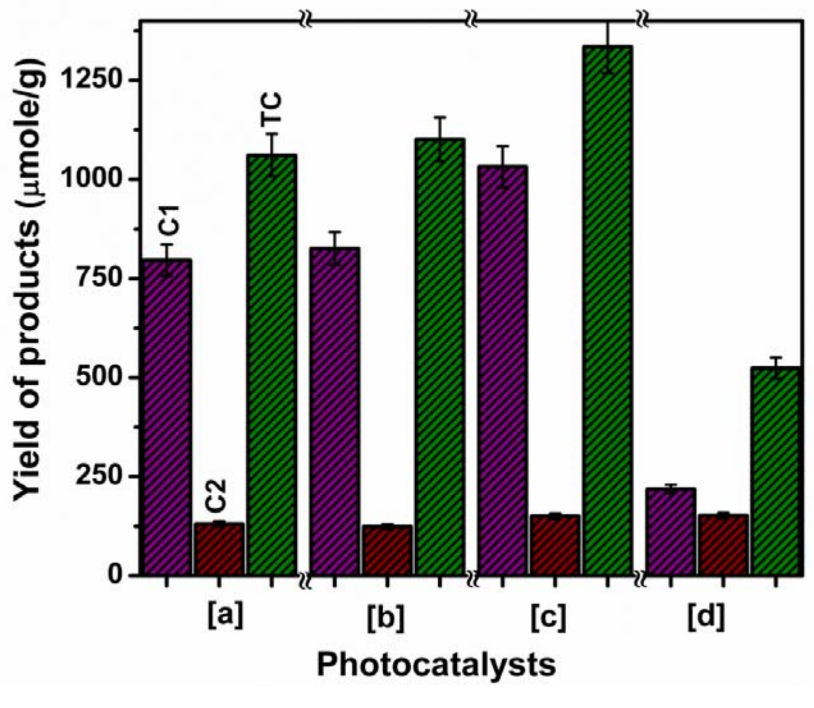

[C1 – C_1 carbon product, C2 – C_2 carbon product, TC- Total Carbon product].

Fig. 4.34 Effect of addition MgO on photo catalytic activity for neat and modified catalysts after 20 hrs of irradiation: (a) Fe-N/ $Na_{(1-x)}La_xTaO_{(3+x)}$, (b) 0.3 wt% MgO/Fe-N/ $Na_{(1-x)}La_xTaO_{(3+x)}$, (c) 0.5wt% MgO/Fe-N/ $Na_{(1-x)}La_xTaO_{(3+x)}$, (d) 1wt% MgOFe-N/ $Na_{(1-x)}La_xTaO_{(3+x)}$.

After 20 hrs of reaction, the used catalyst was centrifuged, dried and pre-treated at 573 K in air for 3 hrs and characterized with XRD (Fig. 4.35), SEM and EDXA (Fig. 4.36). It is observed that the perovskite structure, cubic morphology and amount of dopant elements present in the MgO/Fe-N/ $Na_{(1-x)}La_xTaO_{(3+x)}$ lattice (Fig. 4.36) have been retained, indicating the stability of the catalyst. SEM for used catalyst indicates slight surface attrition due to continuous agitation.

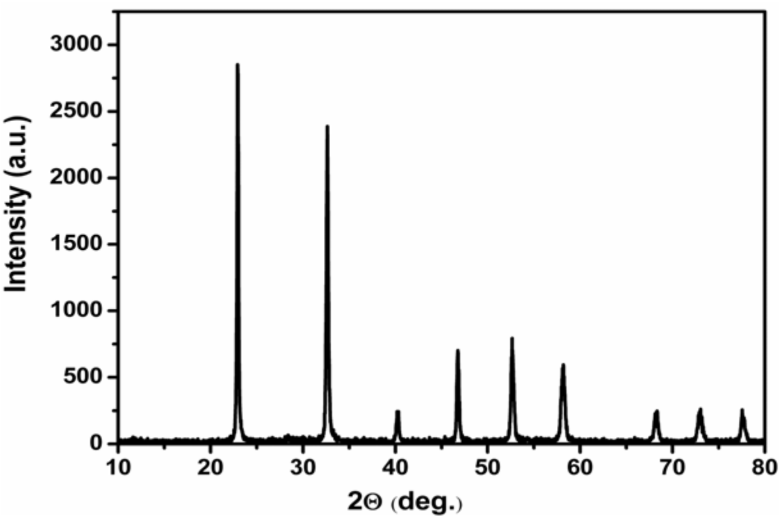

Fig. 4.35 XRD pattern for for 0.5 wt% MgO Fe-N/ $Na_{(1-x)}La_xTaO_{(3+x)}$ after 20 hrs of irradiation.

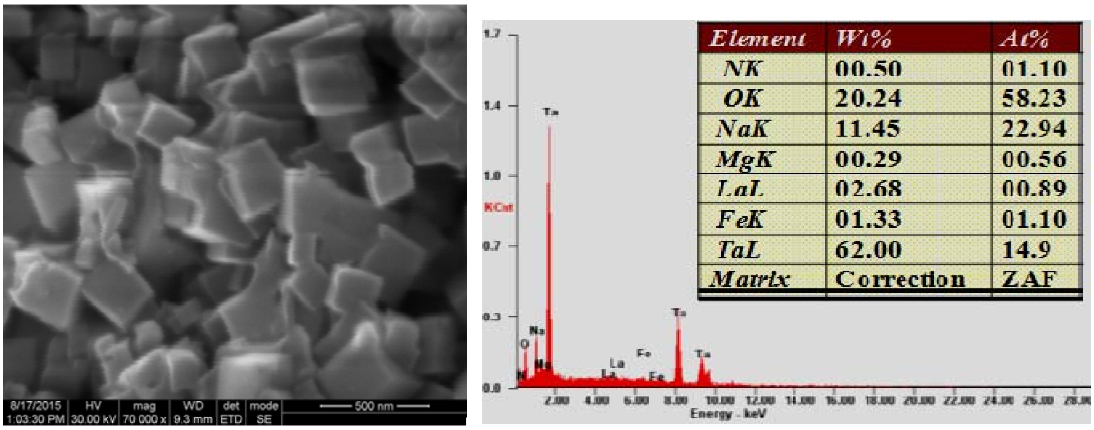

Element	Wt%	At%
NK	00.50	01.10
OK	20.24	58.23
NaK	11.45	22.94
MgK	00.29	00.56
LaL	02.68	00.89
FeK	01.33	01.10
TaL	62.00	14.9
Matrix	Correction	ZAF

Fig. 4.36 SEM and EDXA spectra for 0.5 wt% MgO Fe-N/ $Na_{(1-x)}La_xTaO_{(3+x)}$ after 20 hrs of irradiation.

4.3.3 Conclusions

Co-doping with La, Fe and N in $NaTaO_3$ matrix shows better activity towards CO_2 photo reduction with water, hence Fe-N/ $Na_{(1-x)}La_xTaO_{(3+x)}$ employed as support for MgO loaded photo catalysts. On loading with MgO, the crystal structure and optical properties of the Fe-N/ $Na_{(1-x)}La_xTaO_{(3+x)}$ has not changed, whereas added MgO increases basicity. Since CO_2 is an acidic moiety, its adsorption on basic catalyst is increased, leading to significant improvements in photo efficiency of the material due to increase in the availability of CO_2 molecules compared to bare support. 0.5 wt% MgO loaded on Fe-N/ $Na_{(1-x)}La_xTaO_{(3+x)}$ photo catalyst displays maximum activity for this crucial application under our experimental conditions.

4.4 Modifications in $Na_{(1-x)}La_xTaO_{(3+x)}$: Effect of sensitization with Cobalt Tetra Phenyl Porphyrin on photo catalytic reduction of CO_2

4.4.1 Introduction

Global demand for energy is set to increase up to 50% by the year 2030. It is expected that fossil fuels would continue to be the major source of energy. CO_2 emissions from the fossil fuels pose serious environmental issues like green-house gas effect. Conversion of CO_2 into fuels/ hydrocarbons is an effective strategy to contain the effects of CO_2 emissions. Photo-catalytic reduction of CO_2 into fuels/hydrocarbons or artificial photosynthesis, using water as the reductant, is a complex, challenging and multi-step process with high application potential to mitigate green house gas effect and provide sustainable source of energy. Several investigations focusing on a wide range of heterogeneous photo catalysts for the artificial photo synthesis process have been reported [13-15]. Tantalum based perovskites, in particular, have received considerable attention [51-54] since: (i) the energy of conduction band minimum of tantalum based compounds are more negative compared to other transition metal oxides and also more negative than redox potentials for the conversion of CO_2 to products like CH_3OH, CH_4, C_2H_5OH (ii) tantalates, being ferroelectric materials, have internal dipoles that facilitate separation of electrons and holes, so as to retard recombination rate and increase their life time (iii) bond angle of Ta-O-Ta is close to 180º and hence easy transport of photo electron-hole pairs across the corner-shared octahedral framework is favoured and (iv) alkali metal tantalates are active for chemisorption of CO_2.

Amongst the three alkali metal tantalates, $ATaO_3$ (A=Li, Na & K), $NaTaO_3$ modified with lanthanum and NiO as co-catalyst, displays maximum activity for hydrogen production [18] by splitting of water with a quantum efficiency of 56% under UV radiation (270nm). Teramura et al. [11] have observed that these alkali metal tantalates catalyse photo catalytic reduction of CO_2 using external hydrogen as reductant, forming only CO and no hydrocarbons. However, as reported in our earlier previous chapter, La modified $NaTaO_3$, when loaded with various co-catalysts, like, Pt, Ag, Au, CuO, NiO and RuO_2, display significant activity for photo reduction of CO_2 to yield hydrocarbons like methanol, ethanol and methane using water as reductant.

$NaTaO_3$ being a typical wide band gap semi-conductor, absorbs only <5% of solar energy (UV region). Several approaches to improve its visible light activity by doping with cations and anions have been explored [53, 55-71]. Shunsuke Sato et al. [19, 20] reported CO_2 photo reduction using N-doped Ta_2O_5 linked with Ru complexes, which showed high activity and selectivity towards HCOOH. Coupling with light harvesting moieties is yet another strategy for the utilization of visible light by tantalates. Metallo porphyrins are good candidates for such coupling, due to their ability to absorb visible light and their structural similarity with the natural light harvesting moieties [90]. Choice of metal complexes for sensitizing large band gap semiconductor depends on certain characteristics like:

i. suitable redox potential with respect to the conduction band of the semi-conductor
ii. optical absorption, mainly in the visible solar region,

iii. strongly bound to the semiconductor surface,

iv. photo conductivity and chemical stability.

Phorphyrin derivatives display the requisite characteristics and have unique values for HOMO and LUMO energy levels to sensitize large band gap semiconductors like TiO_2, $NaTaO_3$. Porphyrins possess suitable ground and excited state redox potentials with respect to the semiconductor conduction band and a π- electron conjugate system which facilitates conductivity of the material and light absorption in the solar visible region [91-93]. Besides, sensitization results in multi electron reduction products compared to other modifications, due to high conductivity and high absorption co-efficient of such sensitizers within the solar region.

Considering the such advantages with metallo porphyrins, photo catalytic reduction of carbon dioxide with water by using Cobalt tetra phenyl porphyrin (CoTPP) as sensitizer for wide band gap photo catalyst $Na_{(1-x)}La_xTaO_{(3+x)}$ has been investigated. To the best of our knowledge, this is the first report covering sensitization of $NaTaO_3$ by metallo porpyrins to enable visible light utilization.

4.4.2 Computational Details

All the calculations in the present study were carried out using Gaussian 09 program package [94]. In order to calculate the reduction potential of the CoTPP complex, density functional theory (DFT) was used. The geometry optimization of the complex was performed at Becke's three-parameter exchange Lee, Yang and Parr correlation (B3LYP) hybrid functional with lanl2dz basis set [94]. The vibrational frequency analysis of the optimized geometry confirmed that the optimized geometry corresponded to minimum on the potential energy surface as revealed from the real values for all vibrational frequencies. Time-dependent density functional theory (TDDFT) calculations were carried out to simulate the electronic transitions at the same basis set. The optimized geometry of the CoTPP is shown in Fig. 4. 37.

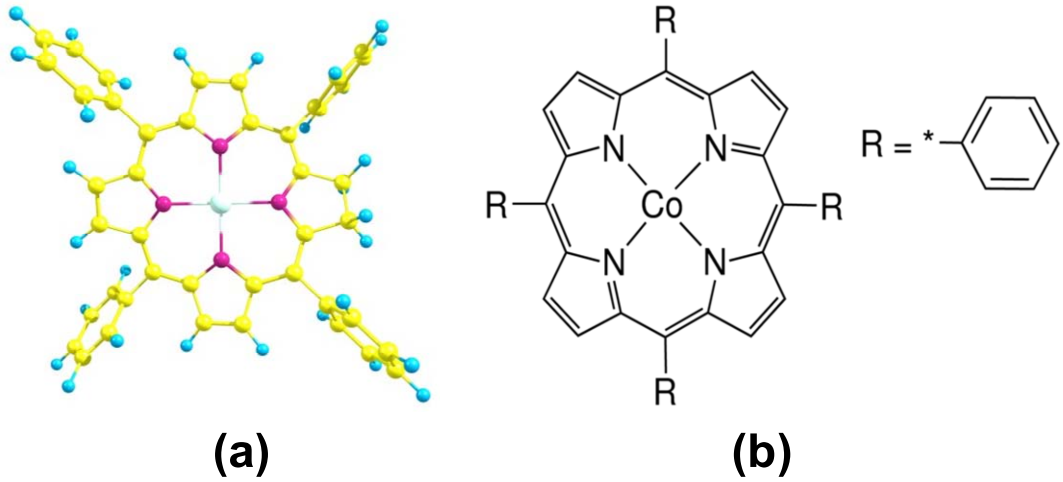

[● - Cobalt, ● - Nitrogen, ● - Carbon, ●- Hydrogen]

Fig. 4.37 meso-Tetra phenyl porphyrin cobalt(II) complex (a) Optimized geometry (b) Chemical structure.

4.4.3 Results and Discussions

4.4.3.1 Redox potential calculation For CoTPP

Theoretical calculations were employed to get exact position of HOMO and LUMO levels for CoTPP and compare with $Na_{(1-x)}La_xTaO_{(3+x)}$ band edges. GaussSum program was used to calculate the frontier molecular orbitals (FMOs). HOMO and LUMO orbitals of CoTPP are given in Fig. 4. 38 and molecular orbital diagram for CoTPP is shown in Fig. 4.39. The calculated molecular orbital energy values are given in Table 4.7 and the calculated redox potentials of ground (S_0) and excited state (singlet (S_1) of CoTPP complex are given in Table 4.8. The above calculation shows that HOMO level for the CoTPP complex is at -4.99 V vs absolute vacuum scale (AVS) and that of LUMO is at -2.37 V (vs AVS). CoTPP is a suitable complex for sensitizing $Na_{(1-x)}La_xTaO_{(3+x)}$, since CoTPP redox potential/conduction band (-2.07V vs NHE) is more negative compared to $Na_{(1-x)}La_xTaO_{(3+x)}$ conduction band potential (-1.47V vs NHE) [22].

Table 4.7 Molecular orbital energy values (Absolute vacuum scale) for CoTPP complex

Energy levels	Energy (eV)
E (LUMO + 2)	-1.18
E (LUMO + 1)	-1.76
E (LUMO)	-2.37
E (HOMO)	-4.99
E (HOMO -1)	-5.26
E (HOMO - 2)	-6.06

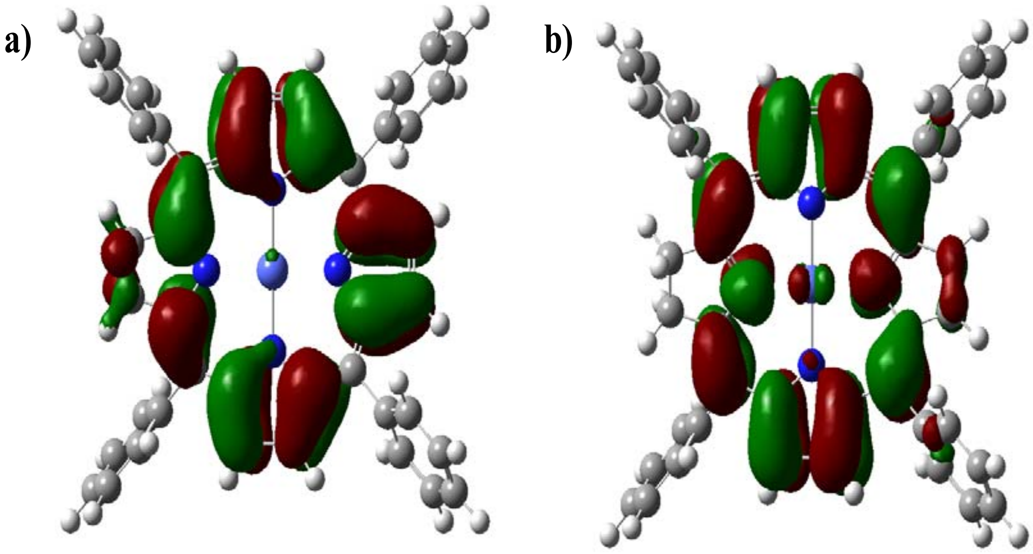

Fig. 4.38 Schematic representation of (a) HOMO and (b) LUMO orbitals of the Cobalt tetra phenyl porphyrin Complex

Table 4.8 The redox potentials of ground (S_0) and excited state (singlet (S_1)) of CoTPP complex in NHE scale.

	Oxidation potential (eV)	Reduction potential (eV)
S_0	+0.55	-2.01
S_1	+0.52	-2.00

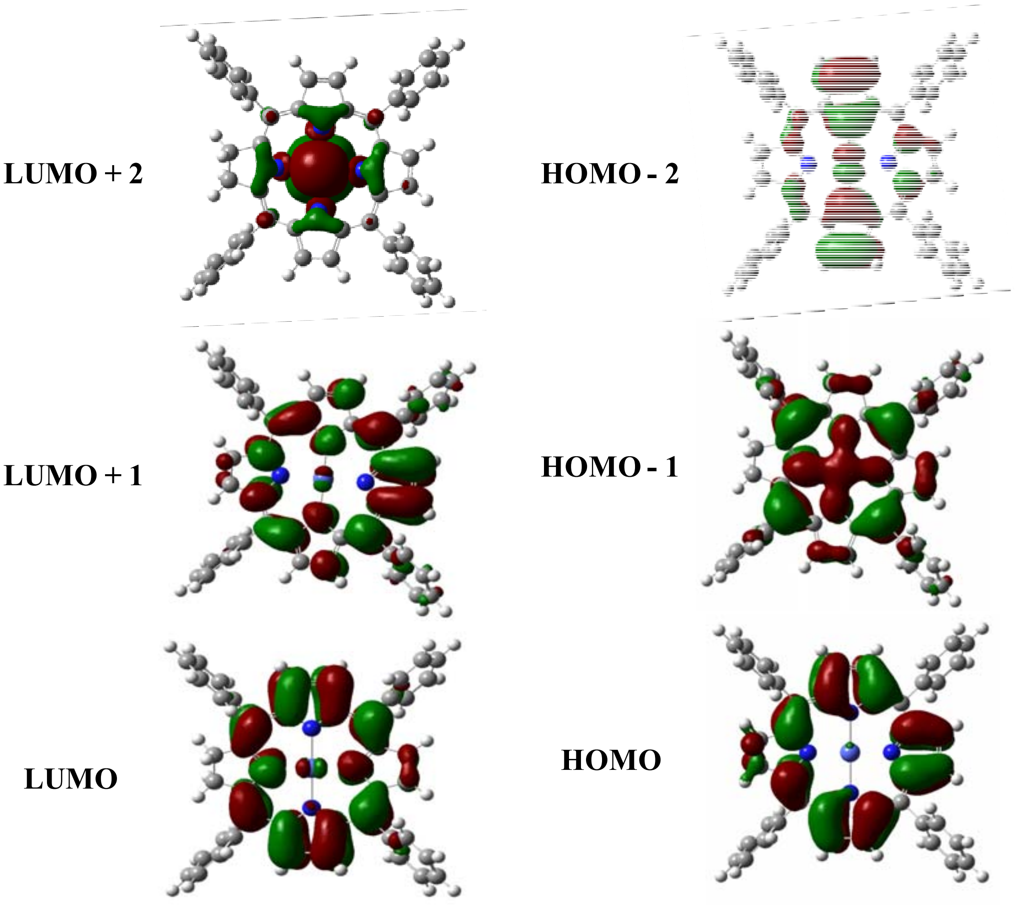

Fig. 4.39 Molecular orbital diagram for CoTPP complex

4.4.3.2 X-ray Diffraction pattern

XRD patterns for the synthesized materials are shown in Fig. 4.40. Peaks at 2θ values of 22.9(020), 32.5(200), 40.1(022), 46.6(202), 52.4(301), 58.2(123) correspond to orthorhombic crystal structure (JCPDS Card No. 25-0863) of $NaTaO_3$. CoTPP sensitized composite shows that, there is no significant change in crystal structure as well as crystalline nature of the catalyst. Crystallite sizes, calculated by adopting Scherrer's formula, are given in Table 4.9.

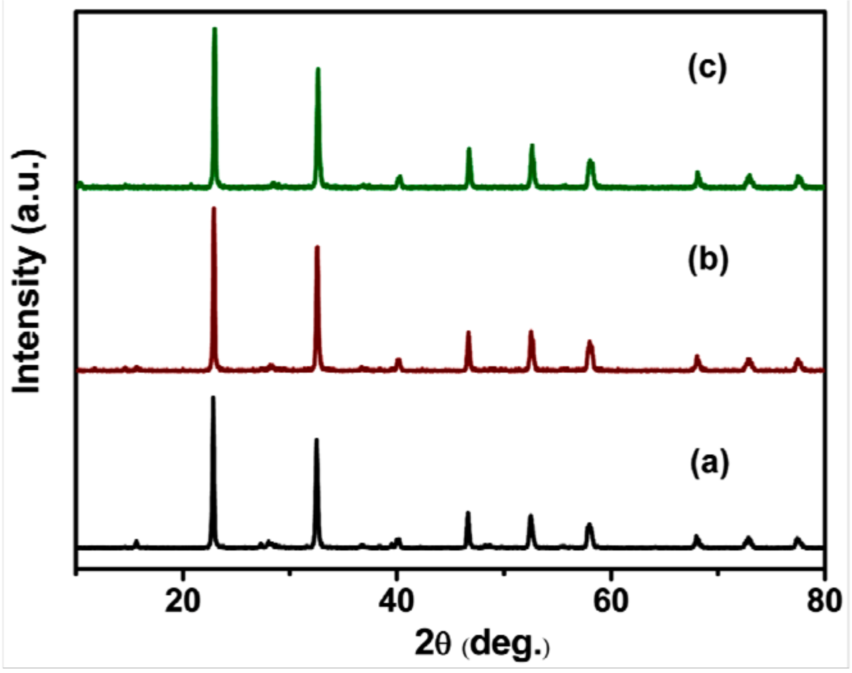

Fig. 4.40 XRD pattern for neat and sensitized catalyst (a) $Na_{(1-x)}La_xTaO_{(3+x)}$ (b) CoTPP/$Na_{(1-x)}La_xTaO_{(3+x)}$ (c) Used CoTPP/$Na_{(1-x)}La_xTaO_{(3+x)}$.

Table 4.9 Crystallite size and band gap energy data for neat and sensitized $Na_{(1-x)}La_xTaO_{(3+x)}$.

Photo catalysts	Lattice Parameters (Å)			Crys.size	Band gap
	a	b	c	(nm)	(eV)
$Na_{(1-x)}$ $La_xTaO_{(3+x)}$	5.51	7.78	5.5	47.2	4.1
CoTPP/$Na_{(1-x)}La_xTaO_{(3+x)}$	5.49	7.75	5.5	48.5	3.76

4.4.3.3 DRS UV-visible spectra

DRS UV-visible spectra (Fig. 4.41) show characteristic absorption peak of $Na_{(1-x)}La_xTaO_{(3+x)}$. There is small shift towards red region with CoTPP sensitized composite which indicates interaction between CoTPP and $Na_{(1-x)}La_xTaO_{(3+x)}$. Characteristic absorption bands for CoTPP observed at around 419 nm, 541 nm, and 656 nm, are close to those reported for CoTPP [95]. The band at 419 nm corresponds to HOMO-3 → LUMO (81% absorption) and band at 541 nm corresponds HOMO →

LUMO transition (83% absorption) of a CoTPP complex, both in the visible region. This observation implies that porphyrin structure has not changed after being loaded on $Na_{(1-x)}La_xTaO_{(3+x)}$ surface. Band gap values, calculated by standard method are given in Table. 4.9.

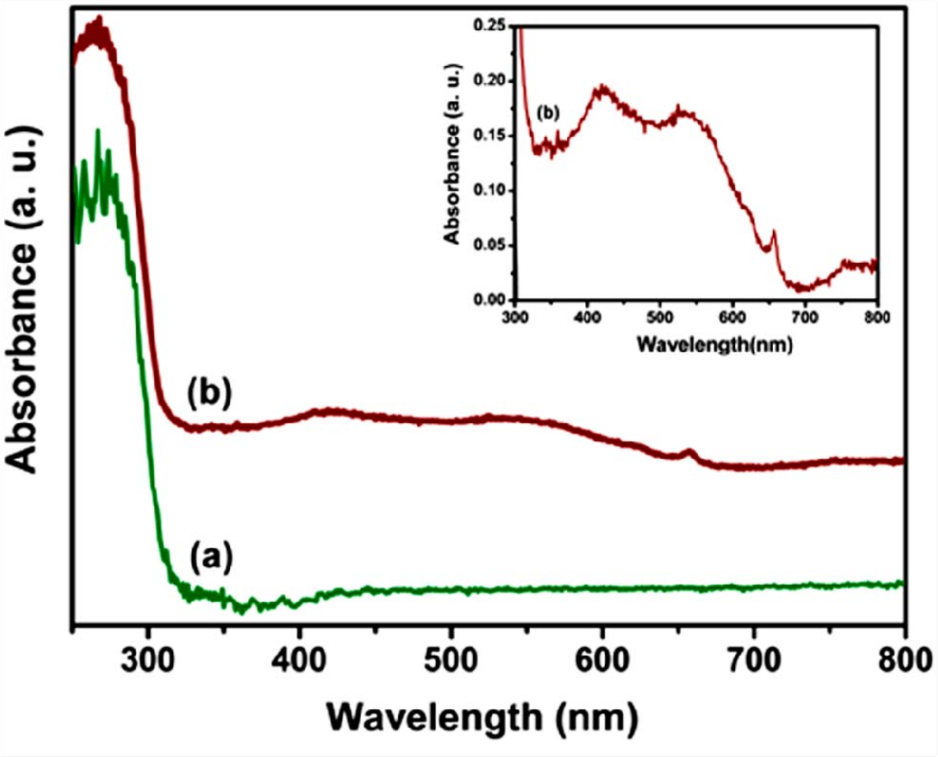

Fig. 4.41 Diffuse Reflectance spectra for neat and sensitized catalyst (a) $Na_{(1-x)}La_xTaO_{(3+x)}$, (b) CoTPP/$Na_{(1-x)}La_xTaO_{(3+x)}$

4.4.3.4 FT-IR Spectra

Presence of CoTPP structure on the surface of sodium tantalate is confirmed by FT-IR spectra shown in Fig. 4.42. Fig. 4.42a and b are IR spectra for neat $Na_{(1-x)}La_xTaO_{(3+x)}$ and $Na_{(1-x)}La_xTa\ O_{(3+x)}$ sensitized with CoTPP respectively. In Fig. 4.42b, the band at 913 cm^{-1} corresponds to metal-ligand (Co-N) vibration. The bands at 1442 cm^{-1}, 1480 cm^{-1} are assigned to the C-C, C-N stretching vibrations respectively. The band at 1590 cm^{-1} is attributed to C=N and pyrrole ring vibration. The band at 1600 cm^{-1} is due to C-C vibration of phenyl substituent. The above mentioned peaks are the characteristic absorption maxima for CoTPP [95-97]. L. Zheng et al observed similar band absorptions for CoTPP complex supported on reduced graphene oxide surface [97]. These observations confirm the presence of CoTPP complex on the sodium tantalate surface. The used sensitized tantalate also has similar bands in IR spectra (Fig. 4.42c) with respect to fresh material, which confirms that no structural changes take place during 20 hrs of photochemical reduction of carbon dioxide.

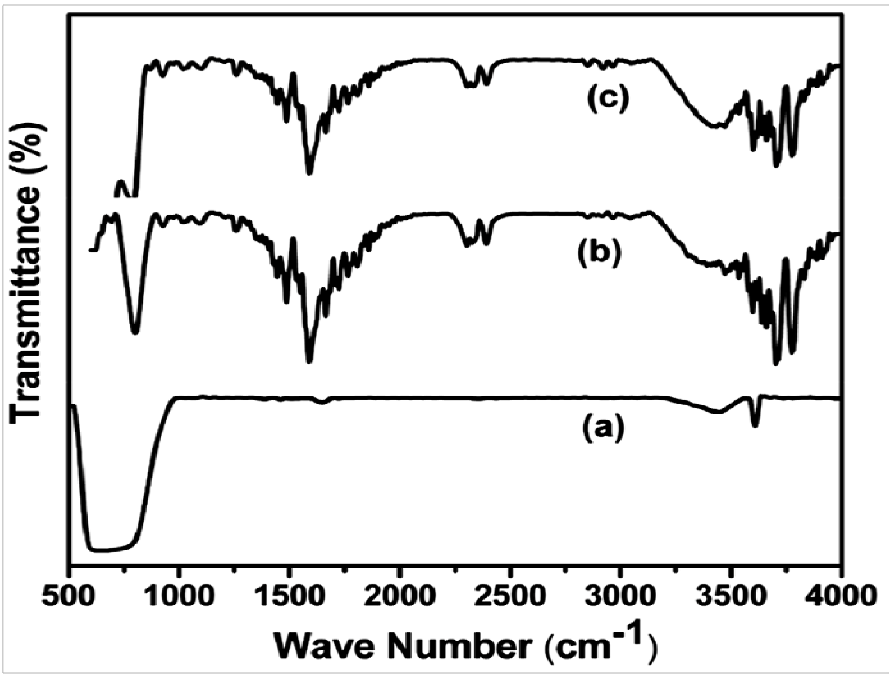

Fig. 4.42 FT IR spectra for neat and sensitized catalyst (a) $Na_{(1-x)}La_xTaO_{(3+x)}$ (b) $CoTPP/Na_{(1-x)}La_xTaO_{(3+x)}$. (c) Used $CoTPP/Na_{(1-x)}La_xTaO_{(3+x)}$.

4.4.3.5 Electron Microscopy Analysis

Fig. 4.43a shows that SEM image of synthesized $Na_{(1-x)}La_xTaO_{(3+x)}$, which is characterized by nano cube morphology. Sensitized tantalate (Fig. 4.43b) did not show any change in morphology, which may be due to very small quantity of CoTPP (1% w/w) present on the surface.

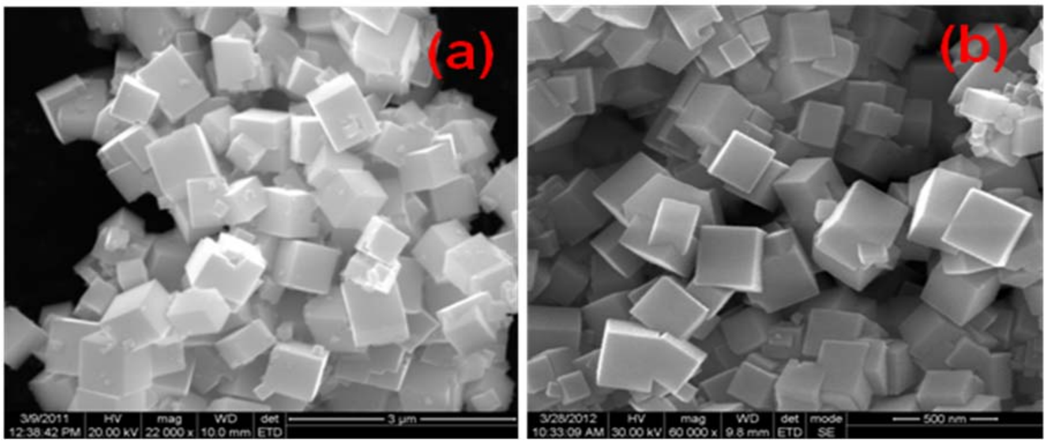

Fig. 4.43 SEM image for (a) Na$_{(1-x)}$La$_x$TaO$_{(3+x)}$ (b) CoTPP/Na$_{(1-x)}$La$_x$TaO$_{(3+x)}$

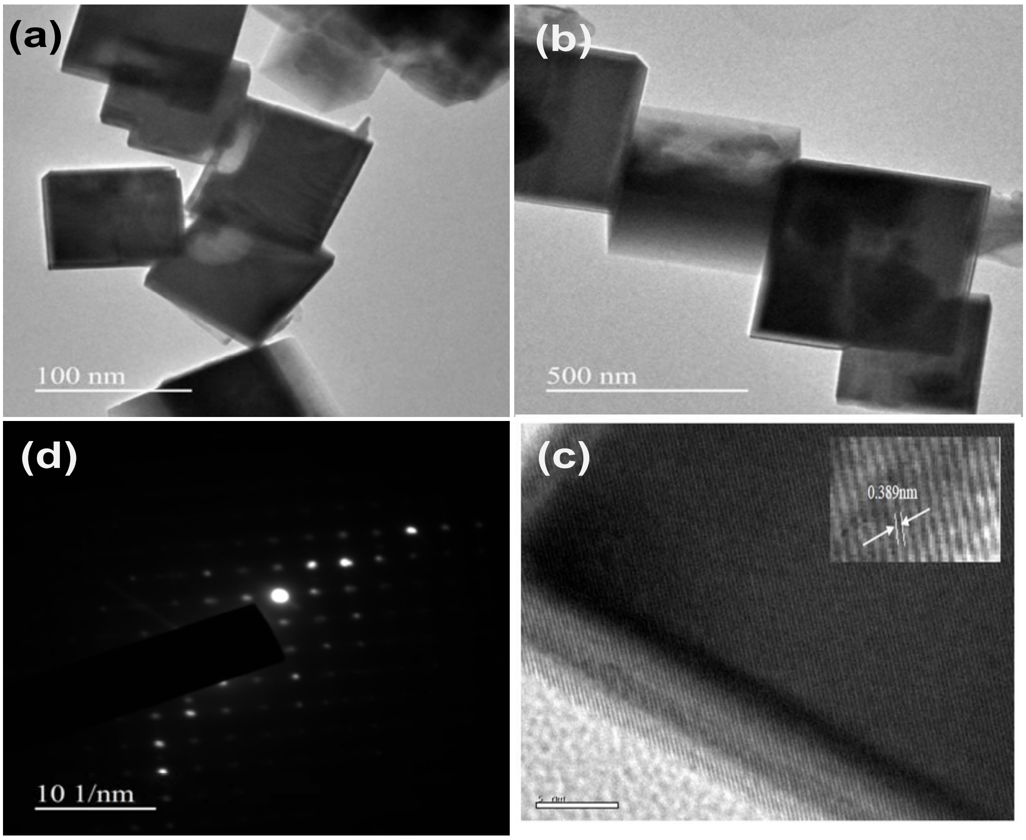

Fig. 4.44 Electron Microscopic images of TEM image for (a) Na$_{(1-x)}$La$_x$TaO$_{(3+x)}$ (b) CoTPP/Na$_{(1-x)}$La$_x$TaO$_{(3+x)}$ (c) SAED for CoTPP/Na$_{(1-x)}$La$_x$TaO$_{(3+x)}$ (d) HRTEM for CoTPP/Na$_{(1-x)}$La$_x$TaO$_{(3+x)}$.

TEM (Fig. 4.44a) further confirms the cubic architecture of the $Na_{(1-x)}La_xTaO_{(3+x)}$ and no changes are observed with sensitized material (Fig. 4.44b). SAED (Fig. 4.44c) shows the highly crystalline nature of CoTPP/$Na_{(1-x)}La_xTaO_{(3+x)}$ nano cubes, and d-value of 0.389 nm measured from HRTEM (Fig. 4.44d) corresponds to (002) planes of orthorhombic phase of $Na_{(1-x)}La_xTaO_{(3+x)}$.

STEM-EDS elemental mapping of Na(Kα), Ta(Lα), La(Lα), Co(Kα), O(Kα), N(Kα) shown in Fig. 4.45 and EDAX data presented in Fig. 4.46 further confirm the presence of CoTPP complex on the $Na_{(1-x)}La_xTaO_{(3+x)}$ matrix.

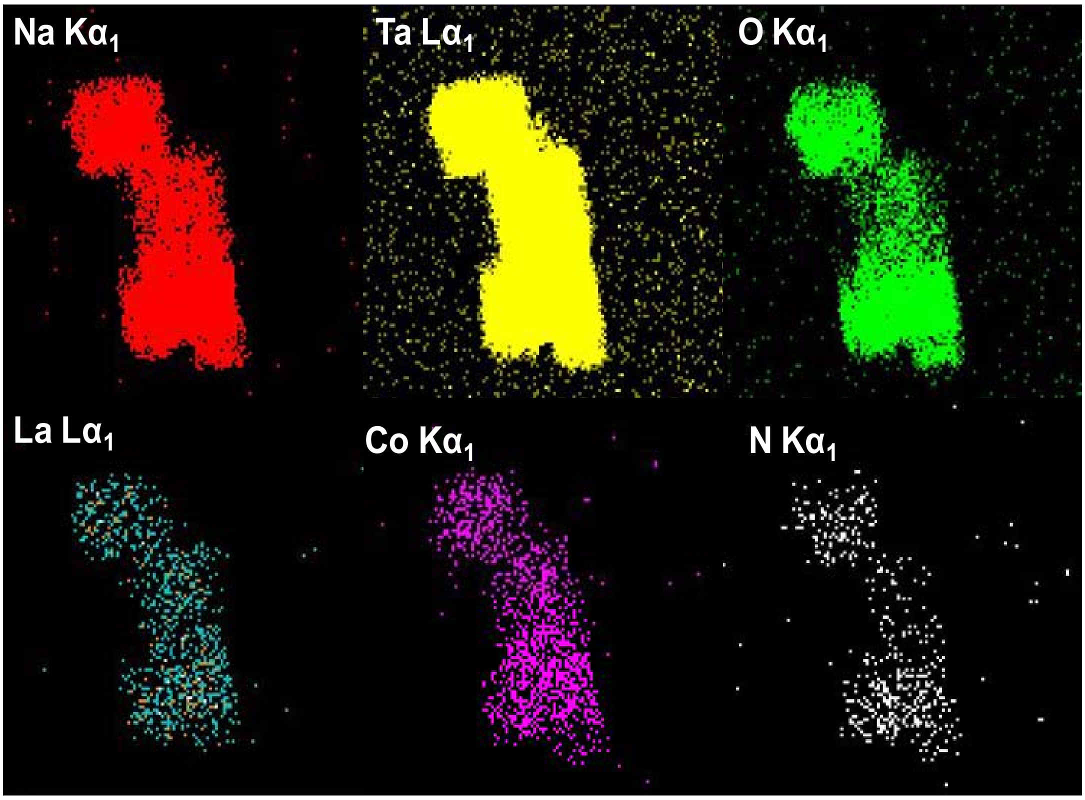

Fig. 4.45 STEM-EDS elemental mapping for CoTPP/$Na_{(1-x)}La_xTaO_{(3+x)}$.

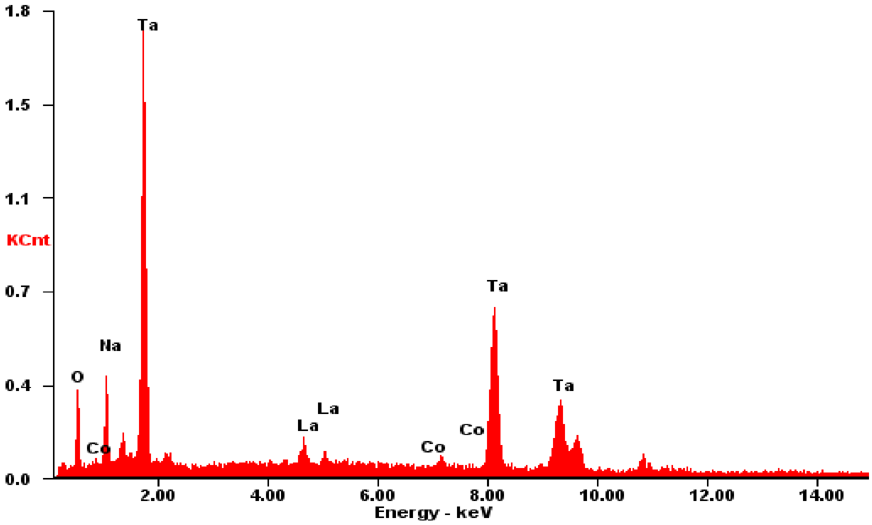

Fig. 4.46 EDS for CoTPP/$Na_{(1-x)}La_xTaO_{(3+x)}$

4.4.3.6 Photoluminescence Spectra

Photoluminescence spectra for the neat and sensitized tantalates are shown in Fig. 4.47. Intensity of the photo luminescence lines for sensitized tantalate are less when compared with those pristine material, indicating an increase in life time of charge carriers.

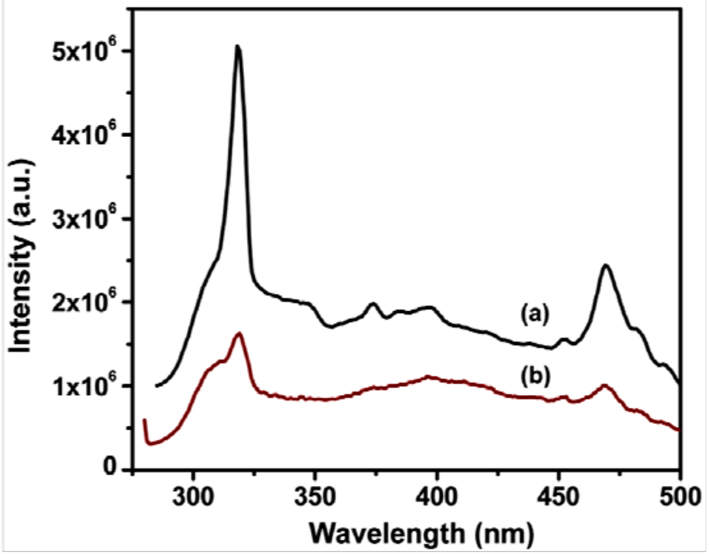

Fig. 4.47 Photoluminescence Spectra (a) $Na_{(1-x)}La_xTaO_{(3+x)}$, (b) CoTPP/$Na_{(1-x)}La_xTaO_{(3+x)}$.

4.4.3.7 Activity and Product Patterns

Photo catalytic reduction of CO_2 on synthesized catalysts was carried out up to 20 hrs of irradiation. The trends in the formation of different products with irradiation time are plotted in Fig. 4.48. Yields of all the products formed from CO_2 photo-reduction increase with irradiation time. As shown in Fig. 4.7 large amounts of methanol is formed when the aqueous alkaline solution is saturated with carbon dioxide, compared to very small quantities formed from the solution saturated with nitrogen, indicating that the observed products are obtained from CO_2 photo reduction and not from carbon impurities on the catalyst surface. We have carried out the reaction with UV cut off filter in order to find out the effectiveness of the sensitized photo catalysts. various products observed in this reaction were identified, quantified and given in Table 4.10. Based on the initial formation of products from 0-10 hr, the rate of formation of products and Apparent Quantum Yield (AQY) for both catalysts are calculated and given in Table 4.10.

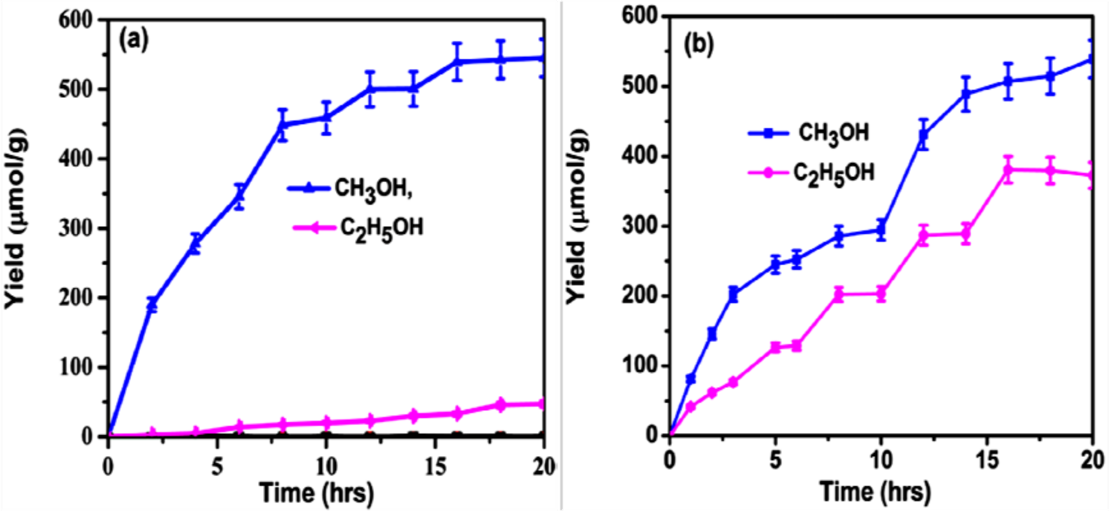

Fig. 4.48 Trends in photo catalytic activity for CO_2 reduction with alkaline water – Time on stream plots – (a) $Na_{(1-x)}La_xTaO_{(3+x)}$, (b) $CoTPP/Na_{(1-x)}La_xTaO_{(3+x)}$.

When the irradiation light is in visible region (ie, 436 nm cut off filter used experiment) the reduced products are less compared to neat $Na_{(1-x)}La_xTaO_{(3+x)}$ as well as sensitized $Na_{(1-x)}La_xTaO_{(3+x)}$ photo catalyst. Since at this wavelength region, the only active molecule is CoTPP, $Na_{(1-x)}La_xTaO_{(3+x)}$ will not be active due to its higher band gap energy. Photo catalytic activity data clearly show that, the CoTPP sensitized composite has higher activity, compared with neat $Na_{(1-x)}La_xTaO_{(3+x)}$ (Fig. 4.49) under similar experimental conditions. After 20 hrs of illumination, yield of methanol is almost same before and after sensitization of $Na_{(1-x)}La_xTaO_{(3+x)}$, by CoTPP. The rate of formation of 12 e- reduction product, ethanol yield increases in the case of sensitized material. After 20 hrs of illumination the ethanol yield was found to be 350 μmol g^{-1}, where as it was only 48 μmol g^{-1} in the case of pristine $Na_{(1-x)}La_xTaO_{(3+x)}$.

Table 4.10 Products distribution and quantum yield data for neat and CoTPP modified $Na_{(1-x)}La_xTaO_{(3+x)}$ catalysts.

Photo catalysts	**Products obtained from CO_2 reduction (μmol$g^{-1}h^{-1}$)**								**AQY**
	CH_4	**C_2H_4**	**C_2H_6**	**CH_3OH**	**C_2H_4O**	**C_2H_5OH**	**C_3H_6**	**H_2**	**x10^{-3} (%)**
NTO*	0.02	-	-	35.0	4.01	3.1	0.05	0.4	4.0
CoTPP/NTO	0.64	0.14	0.07	36.2	3.3	21.4	0.1	0.1	11.5
CoTPP/NTO (Cut off filter 436 nm)	0.04	-	0.02	16.9	0.8	2.9	-	0.05	2.69

* $Na_{(1-x)}La_xTaO_{(3+x)}$.

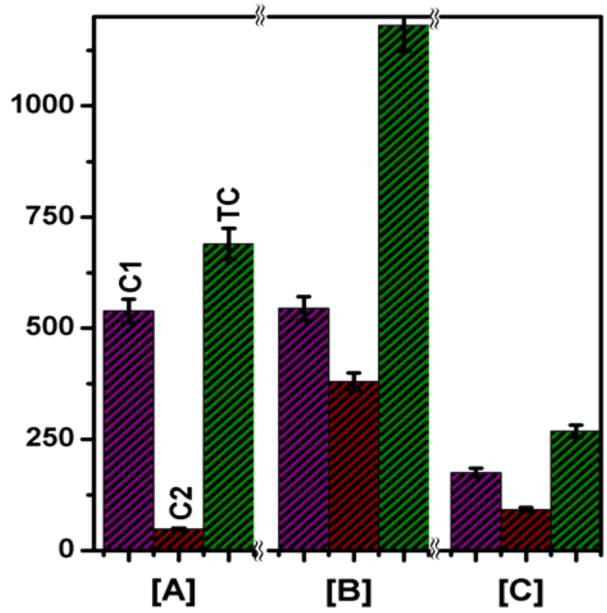

[C1 – Methanol, C2 – Ethanol, TC- Total Carbon product].

Fig. 4.49 Comparison of photocatalytic activity for neat and sensitized catalysts: $Na_{(1-x)}La_xTaO_{(3+x)}$, (B) CoTPP/$Na_{(1-x)}La_xTaO_{(3+x)}$, (C) CoTPP/$Na_{(1-x)}La_xTaO_{(3+x)}$ (Cut-off filter 436 nm).

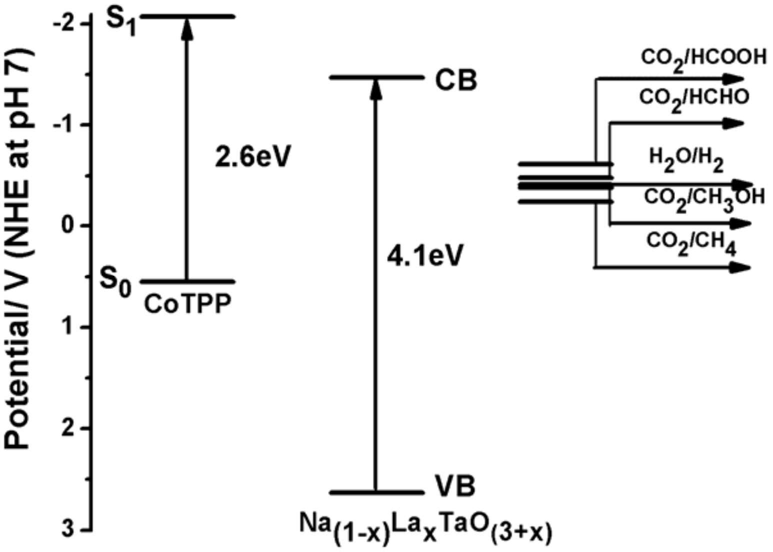

Fig. 4.50 VB & CB energy levels of CoTPP with respect to the $Na_{(1-x)}La_xTaO_{(3+x)}$ vis-a-vis potential for reduction of CO_2 and oxidation of water.

CoTPP reduction potential for S_0 (HOMO) and S_1 (LUMO) states are +0.55, -2.00 V vs NHE respectively. As shown in Fig. 4.50, the excited energy (S_1) of CoTPP is more negative compared to conduction band level of $Na_{(1-x)}La_xTaO_{(3+x)}$. On irradiation of the sensitized catalyst, both CoTPP and $Na_{(1-x)}La_xTaO_{(3+x)}$ absorb light as shown in Scheme 4.4.1 below:

$$\mathbf{CoTPP + h\upsilon_{(visible)} \longrightarrow CoTPP^{*}}$$

$$\mathbf{CoTPP^{*} \longrightarrow CoTPP + e^{-}_{CB/\,(NTO)}}$$

$$\mathbf{NaTaO_3 + h\upsilon_{(UV)} \longrightarrow h^{+}_{\ VB/(NTO)} + e^{-}_{\ CB/\,(NTO)}{}^{\ddagger}}$$

$$\mathbf{CO_2 + 6e^{-}_{CB/\,(NTO)} + 6H^{+} \longrightarrow CH_3OH + H_2O}$$

$$\mathbf{2CO_2 + 12e^{-}_{CB\,/(NTO)} + 12H^{+} \longrightarrow C_2H_5OH + 3H_2O}$$

Scheme 4.4.1 Photo chemical reactions on CoTPP/$Na_{(1-x)}La_x\,TaO_{(3+x)}$ surface.

‡ (NTO - $Na_{(1-x)}La_xTaO_{(3+x)}$)

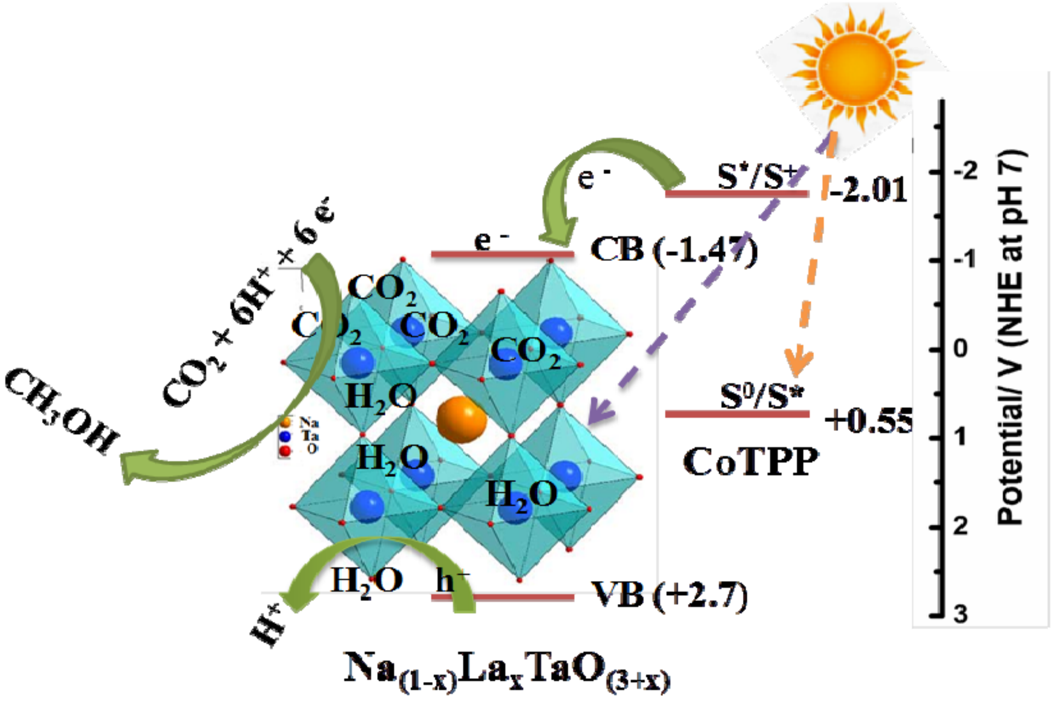

Scheme 4.4.2 Plausible mechanism for CoTPP sensitized on $Na_{(1-x)}La_xTaO_{(3+x)}$ for CO_2 photo reduction with water.

In presence of both UV and visible light, $Na_{(1-x)}$ $La_xTaO_{(3+x)}$ VB electrons are excited into CB due to absorption of UV light, simultaneously, CoTPP molecules gets excited and S_0 to S_1 transition occurs due to visible light absorption as shown in scheme 4.4.2. Excited electrons from CoTPP (S_1) are then injected into the CB of sodium tantalate due to thermodynamically favorable position. Thus, on sensitization, more excited electrons are available on the CB of active $Na_{(1-x)}La_xTaO_{(3+x)}$ surface, where the adsorbed CO_2 molecules get reduced, forming multi-electron reduction products. Thermodynamically redox potential for the formation of ethanol (-0.33V Vs NHE pH 7) is favorable compared to that of methanol (redox potential -0.38 V vs NHE pH 7). Increase in the multi-electron reduction product with sensitized material mainly due to the appropriate band edge position and less band gap energy of sensitizer CoTPP, which results absorption in most abundant visible region and increase in life time of charge carrier. Such a phenomenon explains the increase in rate of formation of ethanol with sensitized material compared to pure $Na_{(1-x)}La_xTaO_{(3+x)}$. XRD (Fig. 4.40c) and FT-IR spectroscopic data (Fig. 4.42c) for the used sensitized catalyst indicate structural and compositional stability during the reaction.

4.4.4 Conclusions

Lanthanum modified sodium tantalate, $Na_{(1-x)}La_xTaO_{(3+x)}$, in conjunction with cobalt tetra phenyl porphyrin (CoTPP) as sensitizer, displays significant activity for the photo catalytic reduction of CO_2 with water. Methanol and ethanol are the major products, besides trace levels of methane, ethane and ethylene. HOMO and LUMO energy level characteristics and redox potentials show that sensitization of $Na_{(1-x)}La_xTaO_{(3+x)}$, with visible light is favoured. Sensitized tantalate simultaneously absorbs both visible and UV radiation, resulting in the direct transfer of photo generated electrons to its conduction band. Sensitization also retards charge carrier recombination rates, as indicated by the photo luminescence spectral data for the pristine and sensitized $Na_{(1-x)}La_xTaO_{(3+x)}$. These factors contribute towards enhancement of photo catalytic activity that results in an increase in the formation of ethanol, via multi-electron reduction process. Sensitized catalyst exhibits chemical and structural stability after 20 hrs of irradiation.

4.5 References

1. T. Inoue, A. Fujishima, S. Konishi, K. Honda, Nature, 1979, 277, 637.
2. A.X. Fujishima, D. Zhang, Donald, A. Tryk, Int. J. Hydrogen Energy 2007, 32, 2664.
3. M.A. Scibioh, B. Viswanathan, Proc. Indian National Sci. Academy, 2004, 70A, 407.
4. S.C. Roy, O. K. Varghese, M. Paulose, C. A. Grimes, ACS Nano, 2010, 4, 1259.
5. V.P. Indrakanti, J.D. Kubicki, H.H. Schobert, Energy Environ. Sci., 2009, 2, 745.
6. Z. Jiang, T. Xiao, V. L. Kuznetsov, P. P. Edwards, Phil. Trans. R. Soc. A 2010, 368, 3343.
7. K. Koci, L. Obalova, Z. Lancy, Chemical Papers, 2008, 62, 1.
8. A. Fujishima, X. Zhang, D.A. Tryk, Surf. Sci. Reports, 2008, 63, 515.
9. G. Palmisano, E. Garcı´a-Lo´ pez, G. Marcı´, V.Loddo, S. Yurdakal, V. Augugliaro, L. Palmisano, Chem. Comm., 2010, 46, 7074.
10. K. Li, D. Martin, J. Tang, Chinese J. Catal., 2011, 32, 879
11. K. Teramura, S. Okuokab, H. Tsuneoka, T. Shishido, T. Tanaka, Appl. Catal. B, 2010, 96, 565.
12. C.C. Lo, C-H-Hung, C.S. Yuan, J.F. Wu, Solar Energy Materials & Solar Cells, 2007, 91, 1765.
13. Y. Izumi, Coord. Chem. Review, 2013, 257, 171.
14. V. Jeyalakshmi, K. Rajalakshmi, R. Mahalakshmy, K. R. Krishnamurthy, B. Viswanathan, Res. Chem. Intermed. 2013, 39, 2565.
15. V. Jeyalakshmi, R. Mahalakshmy, K. R. Krishnamurthy, B. Viswanathan, Materials Science Forum, 2013, 734, 1.
16. K. Iizuka, T. Wato, Y. Miseki, K. Saito, A. Kudo, J. Amer. Chem. Soc. 2011, 133, 20863.

17. H. Zhou, J. Guo, P. Li, T. Fan, D. Zhang, J. Ye, Scientific Reports, 2013, 3, 1667.
18. H. Kato, K. Asakura, A. Kudo, J. Amer. Chem. Soc., 2003, 125, 3082.
19. Shunsuke Sato, Takeshi Morikawa, Shu Saeki, Tsutomu Kajino, Tomoyoshi Motohiro, Angew. Chem. Int. Ed. 2010, 49, 5101.
20. Ken-ichi Yamanaka, Shunsuke Sato, Masayo Iwaki, Tsutomu Kajino, and Takeshi Morikawa, J. Phys. Chem. C, 2011, 115, 18348.
21. K. Li, A. D. Handoko, M. Khraisheh, J. Tang, Nanoscale, 2014, 6, 9767.
22. H. Kato, A. Kudo, J. Phys. Chem. B, 2001, 105, 4285.
23. L. Liu, Y. Li, Aerosol and Air Quality Research, 2014, 14, 453.
24. T. Mizuno, K. Adachi, K..Ohta, A. Saji, J. Photochem. & Photobiol. A: Chem. 1996, 98, 87.
25. A.H. Yahaya, M.A. Gondal, A. Hameed, Chemical Physics Letters 2004, 400, 206.
26. M.A. Asi, C. He, M. Su, D. Xia, L. Lin, H. Deng, Y. Xiong, R. Qiu, X-Z Li Catal. Today 2011, 175, 256.
27. Y. Liu, B. Huang, Y. Dai, X. Zhang, X. Qin, M. Jiang, M-H. Whangbo Catal. Comm. 2009, 11, 210.
28. S. Basumallick, J. Adv. Chem. Sci. 2015, 1, 53.
29. Y. Ku, W-H Lee, W-Y Wang, J. Mol. Cat. A: Chem. 2004, 212, 191.
30. P-W Pan, Y-W Chen, Catal. Comm. 2007, 8, 1546.
31. M.R. Hoffmann, J.A. Moss, M.M. Baum, Dalton Trans., 2011, 40, 5151
32. D. Uner, M.M. Oymak, Catal. Today, 2012, 181, 82.
33. W-N. Wang, W-J. An, B. Ramalingam, S. Mukherjee, D.M. Niedzwiedzki, S. Gangopadhyay, P. Biswas, J. Am. Chem. Soc. 2012, 134, 11276.
34. Li, Y.; Wang, W. N.; Zhan, Z. L.; Woo, M. H.; Wu, C. Y.; Biswas, P. Appl. Catal., B 2010, 100, 386.

35. S. Link, M. A. El-Sayed, J. Phys. Chem. B 1999, 103, 4212; P. K. Jain, K.S. Lee, I.H. El-Sayed, M.A. El-Sayed, J. Phys. Chem. B 2006, 110, 7238.
36. C. Costentin, M. Robert, J-M Save´ant, Chem. Soc. Rev., 2013, 42, 2423.
37. Y. Hori, A. Murata, R. Takahashi, J. Chem. Soc. Faraday Trans. 1, 1989, 85, 2309.
38. J.F. de Brito, A.A. da Silva, A.J. Cavalheiro, M.V.B. Zanoni, Int. J. Electrochem. Sci., 2014, 9, 5961.
39. Y. Kohno, H. Hayashi, T. Takenaka, T. Tanaka, T. Funabiki, S. Yoshida, J. Photochem. Photobiol. A 1999, 126, 117.
40. K. Teramura, H. Tsuneoka, T. Shishido, T. Tanaka, Chemical Physics Letters, 2008, 467, 191.
41. K. Teramura, T. Tanaka, H. Ishikawa, Y. Kohno, T. Funabiki, J. Phys. Chem. B 2004, 108, 346.
42. X. Yang, T. Xiao P. P. Edwards, Int. J. Hydrogen Energy, 2011, 36, 6546.
43. Z. Goren, I. Willner, A. J. Nelson, A. J. Frank, J. Phys. Chem., 1990, 94, 3784.
44. N.M. Dimitrijevic, B. K. Vijayan, O.G. Poluektov, T. Raijh, K.A. Gray, H .He, P. Zapol, J. Amer. Chem. Soc., 2011, 133, 3964.
45. J. C. S. Wu, Catal. Surv. Asia, 2009, 13, 30.
46. M. Anpo, H. Yamashita, Y. Ichihashi, S. Ehara, J. Electro anal. Chem. 1995, 396, 21.
47. I-H Tseng, W-C. Chang, J. C. S. Wu, Appl. Catal. B 2002, 37, 37.
48. H. Kato, A. Kudo, Catal. Today, 2003, 78, 561.
49. TJ Meyer, JM Papanikolas, Heyer CM Catal. Lett, 2011, 141, 1.
50. SN Habisreutinger, L Schmidt- Mende, JK Stolarczyk, Angew. Chem. Int. Ed 2013, 52, 7372.
51. S Das, WMA Wan Daud, RSC Adv, 2014, 4, 20856.
52. P Zhang, J Zhang, J Gong, Chem. Soc. Rev 2014, 43, 4395.

53. P. Kanhere, Z Chen, Molecules 2014, 19, 19995-20022.
54. CC Hu, H Teng, Appl. Catal. A: General, 2007, 331, 44.
55. M. Li, Peng Li, Kun Chang, Tao Wang, Lequan Liu, Qing Kang, Shuxin Ouyang, Jinhua, Chem. Comm. 2015, 51, 7645
56. P. Kanhere, P. Shenai, S. Chakraborty, R. Ahuja, J. Zhenge, Z. Chen Phys. Chem. Chem. Phys., 2014, 16, 16085.
57. P.D. Kanhere, J. Zheng, Z. Chen, J. Phys. Chem. C, 2011, 115, 11846.
58. P. Kanhere, J. Zheng, Z. Chen, Int. J. Hydrog. Energy, 2012, 37, 4889.
59. Xin Zhou, Jingying Shi, Can Li, J. Phys. Chem. C, 2011, 115, 8305–8311
60. L. An, H. Onishi, ACS Catal. 2015, 5, 3196
61. Y. Liu, Y. Su, H. Han, X. Wang, J. Nanosci. & Nanotech., 2013, 13, 853.
62. P. Han, X. Wang, Y.H. Zhao, C. Tang, Adv. Mater. Res. 2009, 79–82,1245.
63. L. Qi X. Li, J Sol-Gel Sci Technol, 2014, 69, 625.
64. H. Fu, S. Zhang, L. Zhang, Y. Zhu, Materials Research Bulletin 2008, 43, 864–872.
65. D-R. Liu, C-D. Wei, B. Xue, X-G. Zhang, Y-S. Jiang, J. Hazardous Mater., 2010, 182, 50–54.
66. Z.G. Yi, J.H. Ye, J. App. Phys. 2009, 106, 074910.
67. M. Yang, X. Huang, S. Yan, Z. Li, T. Yu, Z. Zou, Mater. Chem. Phys., 2010, 121, 506.
68. Z.G. Yi, Ye, Phys. Lett. 2007, 91, 254108.
69. P. Kanhere, J. Nisar, Y. Tang, B. Pathak, R. Ahuja, J. Zheng, Z. Chen, J. Phys. Chem. C 2012, 116, 22767.
70. A. Iwase, K. Saito, Kudo, Bull. Chem. Soc. Jpn. 2009, 82, 514.
71. Z. Zhao, R. Li, Z. Li, Z. Zou, J. Phys. D Appl. Phys. 2011, 44, 165401.
72. B. Wang, P. D. Kanhere, Z. Chen, J. Nisar, B. Pathak, Rajeev Ahuja, JPCC 2013, 117, 22518.
73. X. Li, J. Zang Cat. Comm., 2011, 12, 1380–1383

74. J. Zhu, W. Zheng, B. He, J. Zhang, M. Anpo, J. Mol. Cat. A: Chemical 2004, 216, 35.
75. J. Zhu, F. Chen, J. Zhang, H. Chen, M. Anpo, J. Photochem. & Photobio. A: Chem 2006, 180, 196–204
76. J. Liqiang, S. Xiaojun, X. Baifu, W. Baiqi, C. Weimin, F. Honggang, J. Solid State Chem., 2004, 177, 3375–3382,
77. Y. Yang, C. Tian, Res Chem Intermed, 2010, 36, 889.
78. J.W. Nah, W.S. Choi, S.K. Hwang, C.M. Lee, Surf. & Coatings Tech., 2000, 123, 1.
79. M. Hara, E. Chiba, A. Ishikawa, T. Takata, J. N. Kondo, K. Domen, J. Phys. Chem. B 2003, 107, 13441
80. J-L. Ruan, J-L Huang, H-H Lu, J.S. Chen, D-F Lii, Thin Solid Films, 2011, 519, 4987.
81. W. Choi, A. Termin, M. R. Hoffmann, J. Phys. Chem. 1994, 98, 13669.
82. Y. Yang, H. Zhong, C. Tian, Z. Jiang, Surf. Sci., 2011, 605, 1281.
83. L. Liu, C. Zhao, H. Zhao, D. Pitts, Y. Li, Chem. Commun., 2013, 49, 3664.
84. H. He, P. Zapol, L. A. Curtiss J. Phys. Chem. C 2010, 114, 21474.
85. K. Teramura, S. Iguchi, Y. Mizuno, T. Shishido, T. Tanaka, Angew. Chem. Int. Ed. 2012, 51, 8008.
86. W. Tu, Y. Zhou, Z. Zou, Adv. Mater. 2014, 26, 4607.
87. F. Sastre, A. Corma, H. García, J. Am. Chem. Soc. 2012, 134, 14137.
88. D. Cornu, H. Guesmi, J-M Krafft, H. Lauron-Pernot, J. Phys. Chem. C 2012, 116, 6645.
89. S. Xie, Y. Wang, Q. Zhang, W. Deng, Y. Wang, ACS Catal. 2014, 4, 3644.
90. D. Christopher, M.V. Windle, A.K. Campian, D. Klair, A. Elizabeth, R.N. Robin, J. Schneider, Chem. Commun., 2012, 48, 8189.
91. L. Giribabu, R. Kanaparthi, Current Science, 2013, 104, 7.
92. G. Yao, J. Li, Y. Luo, W. Sun, J. Mol. Cat. A: chemical, 2012, 361, 29.

93. W.M. Campbell, A.K. Burrell, D.L. Officer, K.W. Jolley, Coord. Chem. Rev. 2004, 248, 1363.
94. M.J. Frisch, Gaussian 09, Revision B.01; Gaussian, Inc.: Wallingford, CT, 2010. R. Kumar, M. Sankar, Inorg. Chem 2014, 53, 12706.
95. G. Yao, J. Li, Y. Luo, W. Sun, J. Mol. Catalysis A chemical, 2012, 361, 29.
96. Q. Wang, W.M. Campbell, E.E. Bonfantani, K.W. Jolley, D.L. Officer, P.J. Walsh, K. Gordon, R. Humphry-Baker, M.K. Nazeeruddin, M. Gra1tzel, J. Phys. Chem. B 2005, 109, 15397.
97. L. Zheng, D. Ye, L. Xiong, J. Xu, K. Tao, Z. Zou, D. Huang, X. Kang, S. Yang, J. Xia, Analytica Chimica Acta, 2013, 768, 69.

CHAPTER 5

STUDIES ON STRONTIUM TITANATE BASED CATALYSTS FOR PHOTO CATALYTIC REDUCTION OF CO_2

5.1 Modifications in $Sr_3Ti_2O_7$ catalyst to enable visible light absorption

5.1.1 Introduction

Photo Catalytic Reduction of CO_2 (PCRC) with water to yield hydrocarbons or artificial photo synthesis is a topic that is being extensively investigated due to its scientific as well as technological importance [1]. The process is considered as one of the options for mitigation of global warming originated due to the rising levels of atmospheric CO_2 and the possible use of CO_2 as an alternative source for energy [2]. A wide range of binary/ternary and multi component semi-conducting oxides [3] have been explored for PCRC. The most essential characteristics of a viable catalyst for this application are [4]

a) The valence band top energy level has to be more positive with respect to the oxidation potential for water
b) The conduction band bottom energy level has to be more negative with respect to the reduction potential for CO_2.

TiO_2, ZnO, CdS, GaP, SiC, $SrTiO_3$ are some of the oxides that satisfy the above criteria. While majority studies on PCRC are concerned with titania and its modified versions [5] as catalysts, several mixed metal oxide semi-conductors like, $NaTaO_3$ [6], $ZnGa_2O_4$ [7] and Zn_2GeO_4 [8] along with a range of promoters/co-catalysts have been explored. Mixed metal oxides that belong to the family of perovskites ABO_3, like $SrTiO_3$ [9] and $NaTaO_3$ [10] with various co-catalysts Pt, Ag, Au, CuO, NiO and RuO_2 display significant and stable activity for photo reduction of CO_2. In addition, perovskites with layered structure like, $ALa_4Ti_4O_{15}$ (A= Ca, Sr, Ba) with Ag as co-catalyst [11] exhibit better performance, since the layered structure facilitates faster transport of charge carriers and the interlayer space could be used as oxidation/reduction reaction sites, leading to the separation of charge carriers [12].

In this chapter, results on PCRC on another layered perovskite type oxide, $Sr_3Ti_2O_7$, which, in combination with NiO as co-catalyst, is known to be an efficient catalyst for photo catalytic splitting of water, are presented [13]. Though the parent perovskite $SrTiO_3$, has been explored for PCRC [9], to the best of our knowledge, there are no such reports on $Sr_3Ti_2O_7$. As shown in Fig. 5.1, the conduction band bottom energy level is suitable for the subsequent reduction of CO_2 after the initial activation to form $CO_2^{-\cdot}$ and hence $Sr_3Ti_2O_7$ is an ideal candidate for investigation, but for the wider band gap, incorporation of suitable dopants could render $Sr_3Ti_2O_7$ active in the visible region. Increasing the life time of the photo generated charge carriers is another important factor responsible for improving the efficiency of the photo catalytic reduction. In the present chapter, the effect of doping/co-doping $Sr_3Ti_2O_7$ with N, S and Fe (band gap engineering) has been explored in order to achieve reduction in the band gap energy and minimize the charge carrier recombination.

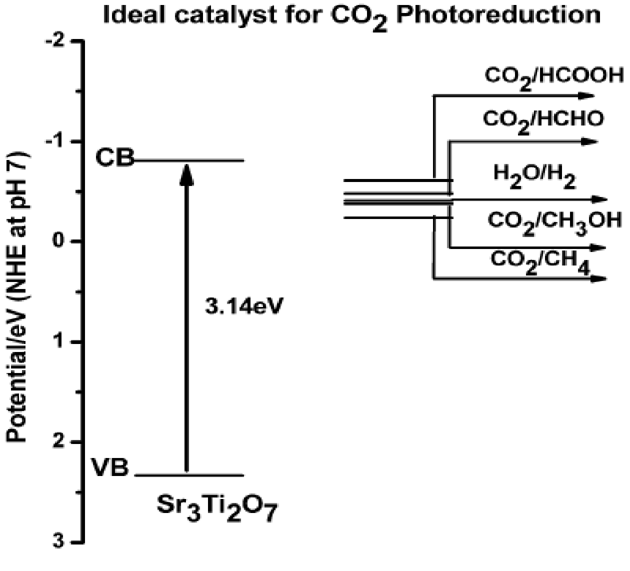

Fig. 5.1 VB and CB energy levels of $Sr_3Ti_2O_7$ with respect to the potential for reduction of CO_2 and oxidation of water.

5.1.2 Results and Discussions

5.1.2.1 X-ray Diffraction Study

X-ray diffraction patterns of the prepared layered strontium titanate photo catalysts in pristine and differently doped formulations are presented in Fig. 5.2. All the characteristic d-lines for $Sr_3Ti_2O_7$ phase [13] are observed in the XRD patterns for neat and doped samples. The amount of dopants being small, no major changes in the XRD patterns for the doped samples are observed, except for a small shift in d-lines for Fe doped samples, as shown in Fig. 5.3. This shift in d-line could be due to the location of doped Fe^{3+} ions with ionic radius of 0.64 Å in Ti^{4+} ion (0.61 Å) sites in the titanate lattice.

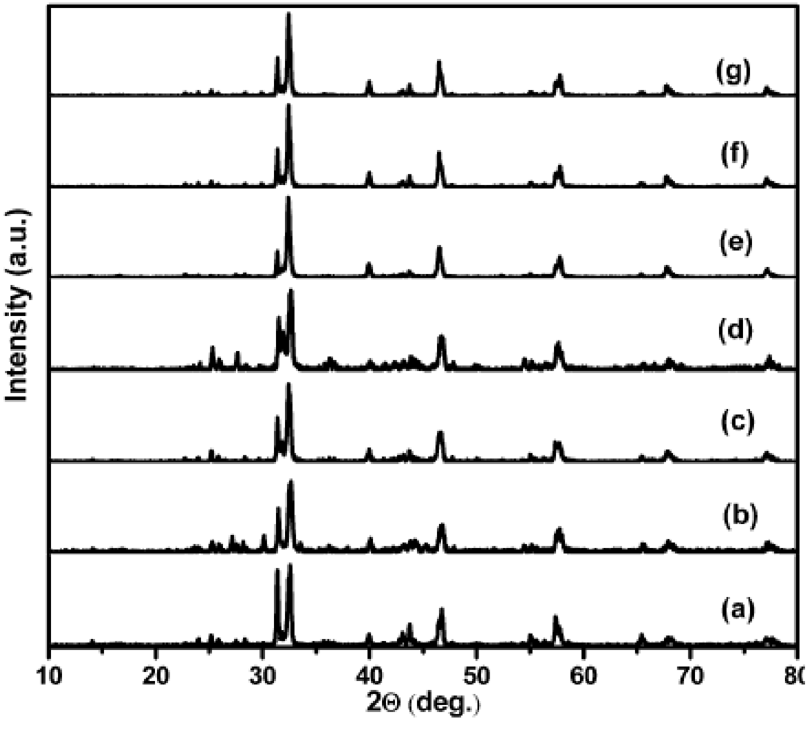

Fig. 5.2 XRD patterns for neat and doped $Sr_3Ti_2O_7$: (a) $Sr_3Ti_2O_7$, (b) $Sr_3Ti_2O_{(7-x)}N_x$, (c) $Sr_3Ti_{(2-x)}S_xO_{(7-y)}N_y$, (d) $Sr_3Ti_{(2-x)}Fe_xO_7$, (e) $Sr_3Ti_{(2-x)}Fe_xO_{(7-y)}N_y$, (f) $Sr_3Ti_{(2-x-y)}Fe_xS_yO_{(7-z)}N_z$, (g) $Sr_3Ti_{(2-x-y)}Fe_xS_yO_{(7-z)}N_z$-Used.

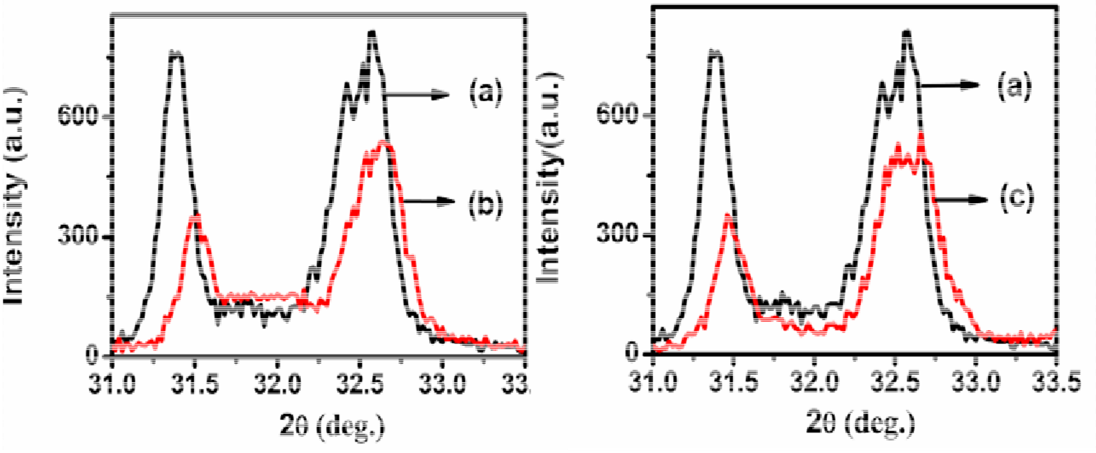

Fig. 5.3 Shift in d-lines for doped $Sr_3Ti_2O_7$ for (a) $Sr_3Ti_2O_7$, (b) $Sr_3Ti_{(2-x)}Fe_xO_7$, (c) $Sr_3Ti_{(2-x-y)}Fe_xS_yO_{(7-z)}N_z$.

The crystallite size of the synthesized materials, calculated by using Scherer's formula shown in Table 5.1.

Table 5.1 Crystallite size and band gap values for neat and doped $Sr_3Ti_2O_7$ catalysts.

Photo catalysts	**Lattice parameter**		**Crys. size**	**Band gap**
	a(Å)	**c(Å)**	**(nm)**	**(eV)**
$Sr_3Ti_2O_7$	3.90	20.4	46.3	3.14
$Sr_3Ti_2O_{(7-x)}N_x$	3.90	20.5	37.2	2.99
$Sr_3Ti_{(2-x)}S_xO_{(7-y)}N_y$	3.89	20.6	34.3	2.85
$Sr_3Ti_{(2-x)}Fe_xO_7$	3.87	20.3	33.5	2.73
$Sr_3Ti_{(2-x)}Fe_xO_{(7-y)}N_y$	3.89	20.4	24.9	2.57
$Sr_3Ti_{(2-x-y)}Fe_xS_yO_{(7-z)}N_z$	3.90	20.5	21.9	2.39

5.1.2.2 Surface area Analysis

Preparation by polymer complex method has resulted in moderate BET surface area of 25 m^2/g for the pristine $Sr_3Ti_2O_7$ sample and no significant changes were observed with modified $Sr_3Ti_2O_7$ photo catalysts.

5.1.2.3 Scanning Electron Microscopic Analysis

SE micrograph for the neat $Sr_3Ti_2O_7$ as shown in Fig. 5.4 reveals a distinct plate like morphology. Doping with N, S and Fe brings out perceptible changes in the morphology. A gradual decrease in crystallite size, as measured by X-ray line broadening analysis of doped $Sr_3Ti_2O_7$ catalysts, is observed (Table. 5.1).

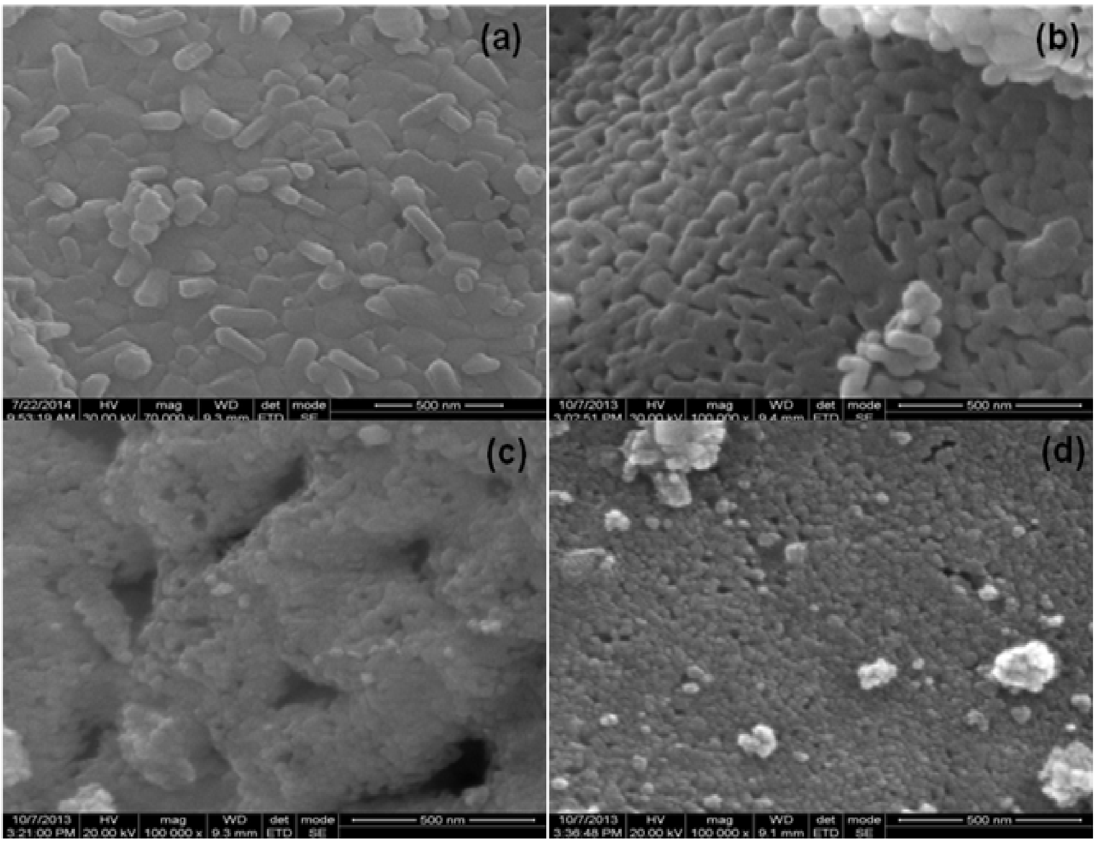

Fig. 5.4 Changes in the morphology of doped $Sr_3Ti_2O_7$ catalysts-SE micrographs.
(a) $Sr_3Ti_2O_7$, (b) $Sr_3Ti_2O_{(7-x)}N_x$, (c) $Sr_3Ti_{(2-x)}S_xO_{(7-y)}N_y$,
(d) $Sr_3Ti_{(2-x-y)}Fe_xS_yO_{(7-z)}N_z$.

5.1.2.4 EDXA spectra

Addition of the dopants prior to polyester/gel formation has ensured effective incorporation of the dopant elements N, S and Fe into the titanate matrix. This aspect is confirmed by the qualitative EDXA spectral data presented in Fig. 5.5.

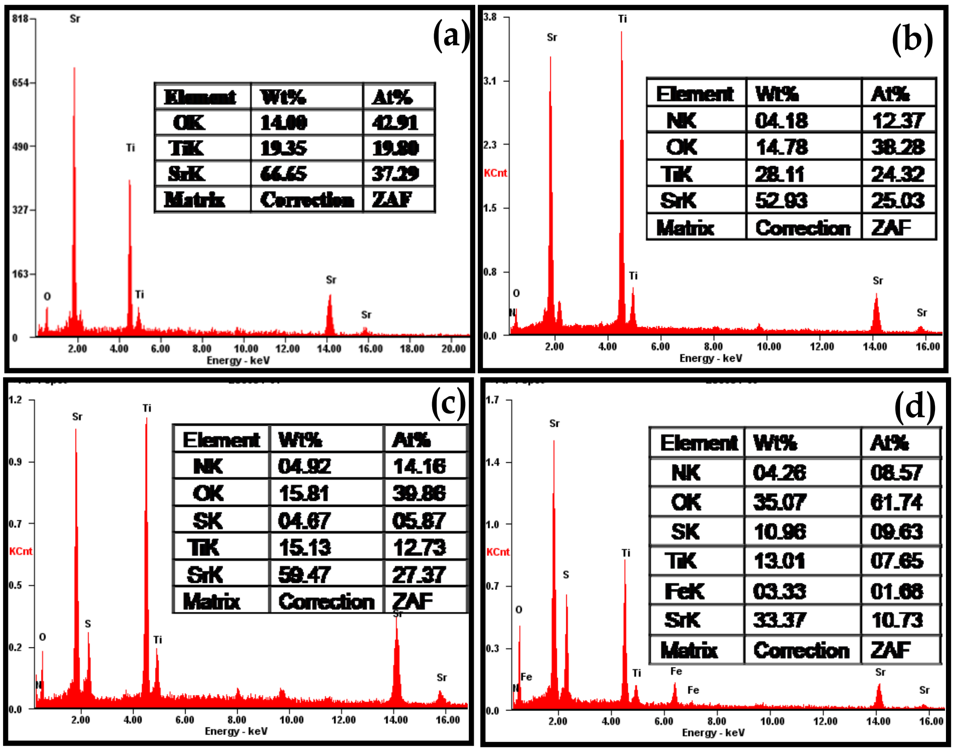

(a)

Element	Wt%	At%
OK	14.00	42.91
TiK	19.35	19.80
SrK	66.65	37.29
Matrix	Correction	ZAF

(b)

Element	Wt%	At%
NK	04.18	12.37
OK	14.78	38.28
TiK	28.11	24.32
SrK	52.93	25.03
Matrix	Correction	ZAF

(c)

Element	Wt%	At%
NK	04.92	14.16
OK	15.81	39.86
SK	04.67	05.87
TiK	15.13	12.73
SrK	59.47	27.37
Matrix	Correction	ZAF

(d)

Element	Wt%	At%
NK	04.26	08.57
OK	35.07	61.74
SK	10.96	09.63
TiK	13.01	07.65
FeK	03.33	01.68
SrK	33.37	10.73
Matrix	Correction	ZAF

Fig. 5.5 EDXA spectra & elemental composition for neat and modified $Sr_3Ti_2O_7$ catalysts. (a) $Sr_3Ti_2O_7$, (b) $Sr_3Ti_2O_{(7-x)}N_x$, (c) $Sr_3Ti_{(2-x)}S_xO_{(7-y)}N_y$, (d) $Sr_3Ti_{(2-x-y)}Fe_xS_yO_{(7-z)}N_z$.

5.1.2.5 DRS UV visible Spectra

DRS profiles for neat and doped/co-doped (separately with N, N-S, Fe-N, Fe-N-S and Fe) $Sr_3Ti_2O_7$ catalysts are shown in Fig. 5.6. Band gap energy of 3.14 eV observed for neat $Sr_3Ti_2O_7$ in the present case is close to the value of 3.2 eV reported earlier [13]. When doped with N or co-doped with N and S (profiles b & c in Fig. 5.6) a distinct shift in light absorption edge, tending towards visible region, is evident. With Fe, either alone or by co-doping with N or N-S, the adsorption edge turns into a near continuum, extending deeper into the visible region indicating excitations from two different energy levels within the band gap. Band gap energy values, observed for the doped/co-doped catalysts, (Table 5.1) decrease gradually, from 3.14 to 2.39 eV.

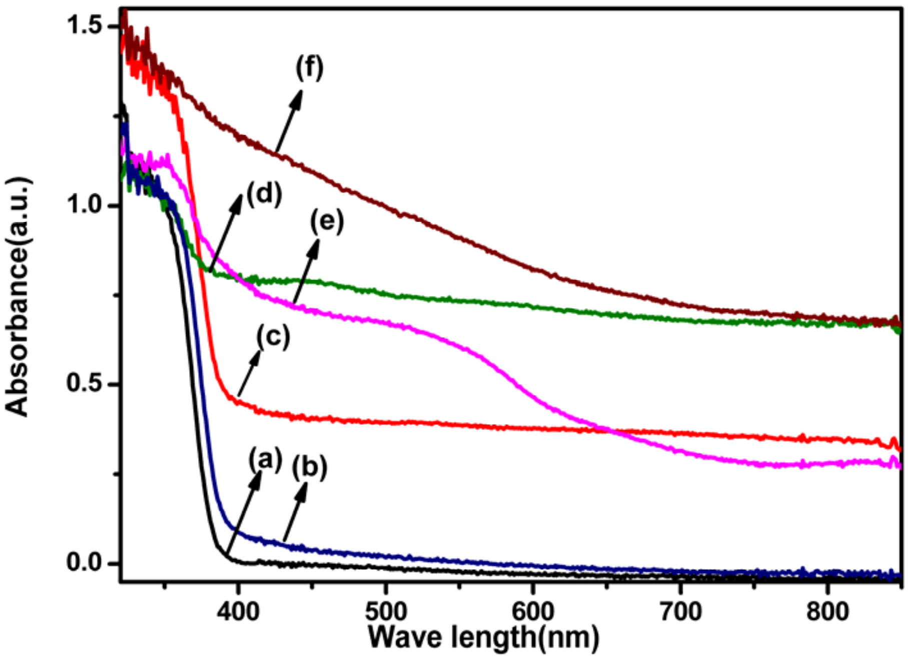

Fig. 5.6 Diffuse Reflectance spectra for neat and doped $Sr_3Ti_2O_7$ catalysts. (a) $Sr_3Ti_2O_7$, (b) $Sr_3Ti_2O_{(7-x)}N_x$, (c) $Sr_3Ti_{(2-x)}S_xO_{(7-y)}N_y$, (d) $Sr_3Ti_{(2-x)}Fe_xO_7$, (e) $Sr_3Ti_{(2-x)}Fe_xO_{(7-y)}N_y$, (f) $Sr_3Ti_{(2-x-y)}Fe_xS_yO_{(7-z)}N_z$.

5.1.2.6 Photoluminescence studies

Photo luminescence spectra of the catalysts (Fig. 5.7) bring out additional features of doped catalysts. Undoped $Sr_3Ti_2O_7$ shows two photo luminescence (PL) emission lines at 470 nm and 482 nm with significant intensity, arising due to the recombination of charge carriers. With N doping and co-doping of N and S, the intensity of the PL lines is reduced to some extent. However, on doping with Fe and co-doping of Fe with N and N-S, sharp reduction in intensity of the PL lines is observed. Decrease in the intensity of PL lines indicates that the recombination of charge carriers is retarded in presence of the dopants. Such an effect would lead to an increase in the life time of the photo generated electrons and holes and hence, an increase in PCRC activity. These modifications brought out by the dopants in the electronic structure of $Sr_3Ti_2O_7$ have profound influence on the PCRC activity.

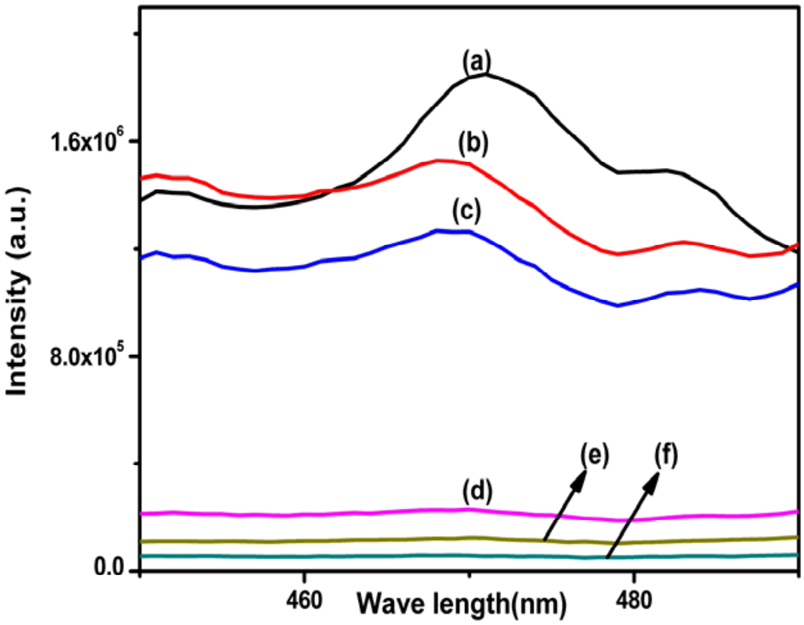

Fig. 5.7 Photo luminescence spectra for neat and doped $Sr_3Ti_2O_7$ catalysts. (a) $Sr_3Ti_2O_7$, (b) $Sr_3Ti_2O_{(7-x)}N_x$, (c) $Sr_3Ti_{(2-x)}S_xO_{(7-y)}N_y$, (d) $Sr_3Ti_{(2-x)}Fe_xO_{(7-y)}N_y$, (e) $Sr_3Ti_{(2-x-y)}Fe_xS_yO_{(7-z)}N_z$, (f) $Sr_3Ti_{(2-x)}Fe_xO_7$.

5.1.2.7 X-ray photoelectron Spectra

XPS measurements were carried out to analyse chemical composition and to identify chemical states of the dopant elements present in the synthesized photo catalysts. High resolution XPS spectra of Sr 3d (Fig. 5.8 [A]), Ti 2p (Fig. 5.8 [B]) and O 1s (Fig. 5.8 [C]) present in the neat and modified photo catalysts are shown in Fig. 5.8. The main peaks for Sr 3d (133 eV), Ti 2p (458 eV) and O 1s (529.5 eV) observed in $Sr_3Ti_2O_7$ and similar peaks with small shift in binding energy was observed with modified catalysts, which can be ascribed to the slight distortion of the $Sr_3Ti_2O_7$ crystal structure, brought about by the dopants.

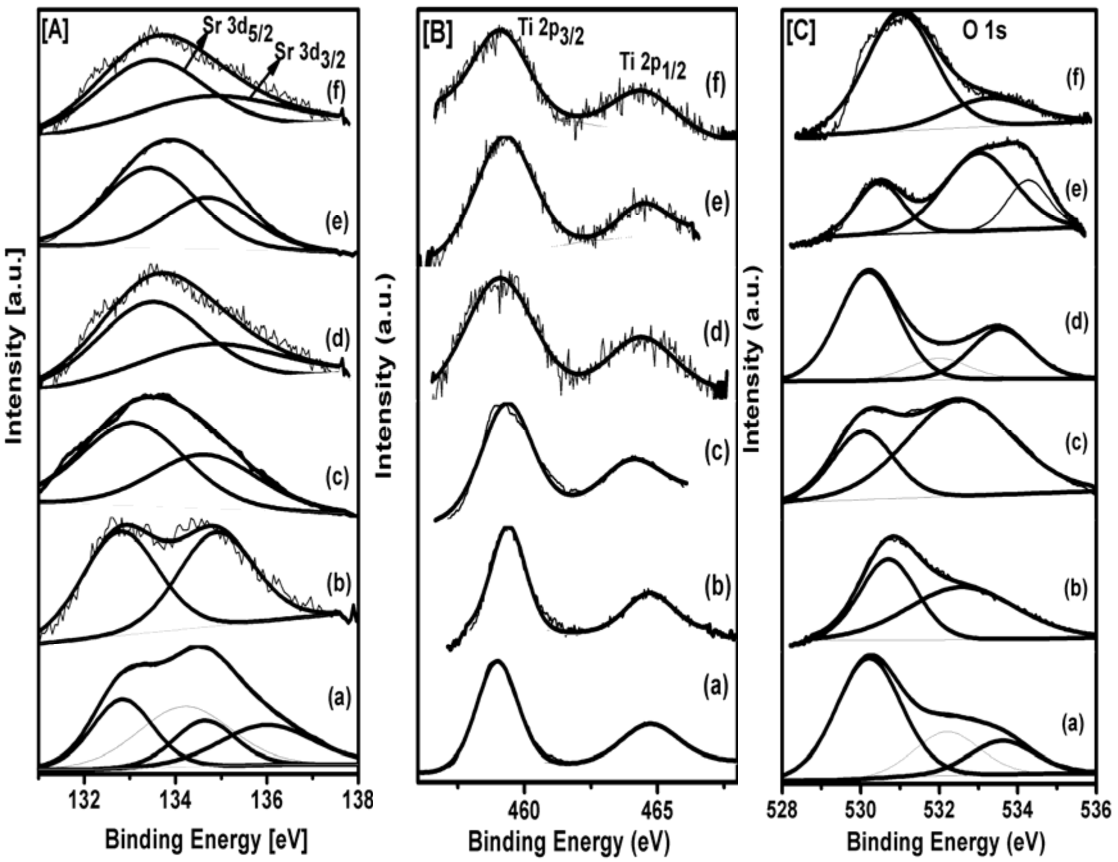

Fig. 5.8 High resolution XPS spectra of Sr 3d [A], Ti 2p [B] and O 1s [C] for neat and modified Catalysts (a) $Sr_3Ti_2O_7$, (b) $Sr_3Ti_2O_{(7-x)}N_x$, (c) $Sr_3Ti_{(2-x)}S_xO_{(7-y)}N_y$, (d) $Sr_3Ti_{(2-x)}Fe_xO_7$, (e) $Sr_3Ti_{(2-x)}Fe_xO_{(7-y)}N_y$, (f) $Sr_3Ti_{(2-x-y)}Fe_xS_yO_{(7-z)}N_z$.

Two types of O 1s peak observed in the neat and all modified catalysts (Fig. 5.8 [C]). The peak centered at 529 eV corresponds to lattice oxygen of Ti-O-Ti in octahedral TiO_6 crystal lattice and another small area peak centered at 531 eV could be ascribed to surface hydroxyl group or adsorbed oxygen. N 1s core level for N doped sample is observed at 398.4 eV (Fig. 5.9 [A]). N and S co-doped sample presents a broad profile, which could be resolved into a main peak at 398.5 eV and another of low intensity at 400.6 eV. For Fe, N and S co-doped sample, N 1s core level is observed at 400.1 eV. N and S co-doped and Fe, N and S co-doped samples show S $2p_{1/2}$ lines at 168.9 and 168.4 eV respectively, due to S^{6+} species (Fig. 5.9 [C]). Fe $2p_{3/2}$ lines at 709.4 and 714.0 eV are attributed to Fe^{3+} species (Fig. 5.9 [B]).

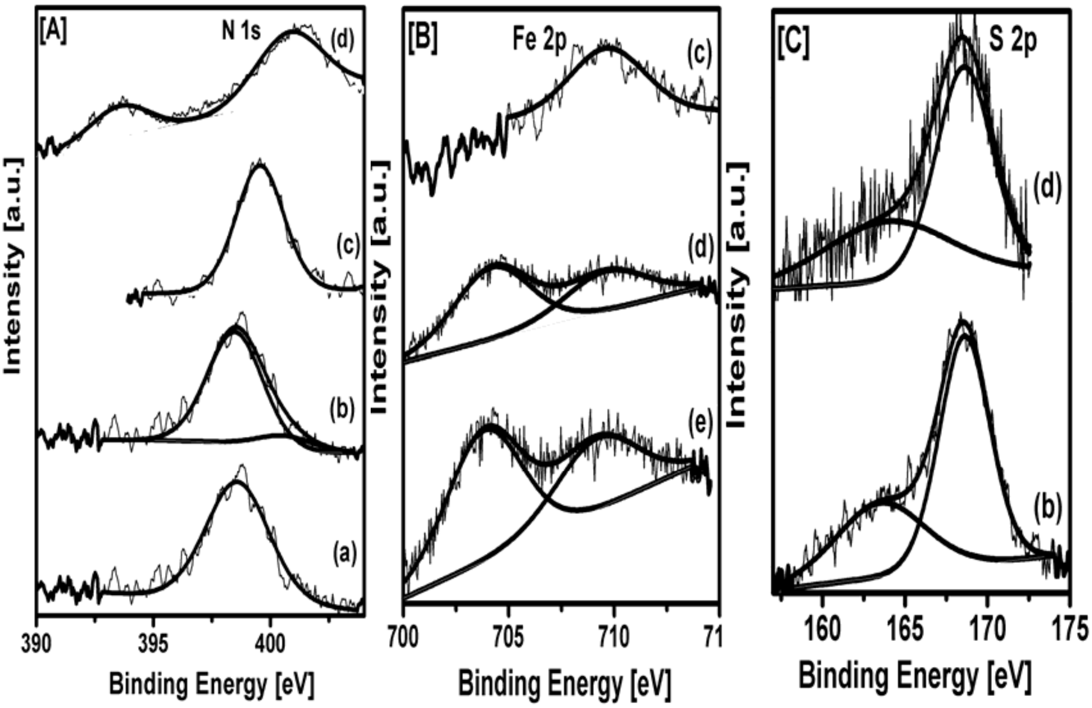

Fig. 5.9 High resolution XPS spectra of N 1s [A], Fe 2p [B], S 2p [C] for neat and modified catalyst. (a) $Sr_3Ti_2O_{(7-x)}N_x$, (b) $Sr_3Ti_{(2-x)}S_xO_{(7-y)}N_y$, (c) $Sr_3Ti_{(2-x)}Fe_xO_{(7-y)}N_y$, (d) $Sr_3Ti_{(2-x-y)}Fe_xS_yO_{(7-z)}N_z$, (e) $Sr_3Ti_{(2-x)}Fe_xO_7$.

5.1.2.8 Photo catalytic reduction of CO_2 on neat and doped $Sr_3Ti_2O_7$

Typical trends in product distribution on the neat $Sr_3Ti_2O_7$ and Fe, N and S co-doped $Sr_3Ti_2O_7$, for PCRC during 20 hrs on stream period are presented in Fig. 5.10a and b. Similar trends are observed on other doped catalysts as well, with variations in the rate and the quantities of products formed. Methanol is the major product, followed by ethanol and acetaldehyde. Methane, ethane and ethylene are formed in trace quantities. Hydrogen and oxygen were also detected in the gas phase. All the catalysts exhibit activity up to 20 hrs. Rates of formation of products are high during initial 6-8 hrs, beyond which the rate of product formation tends to slow down. Based on the initial rates (up to 10 hrs in micro moles/g/hr) for the formation of different products, and the number of photo electrons involved in each case, apparent quantum yields (AQY) for all the catalysts have been calculated and presented in Table. 5.2.

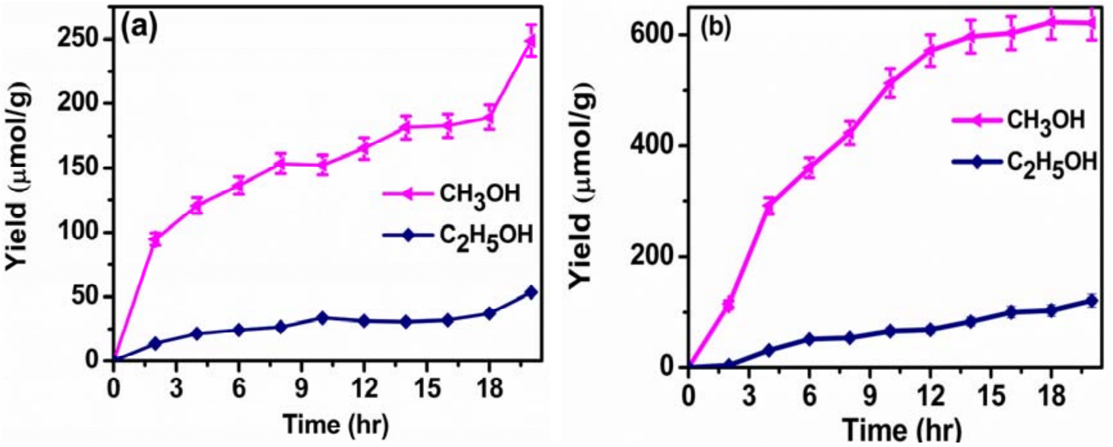

Fig. 5.10 Trends in products distribution during CO_2 photo reduction (a) $Sr_3Ti_2O_7$ and (b) $Sr_3Ti_{(2-x-y)}Fe_xS_yO_{(7-z)}N_z$ catalysts.

Table 5.2 Products distribution and quantum yield data for neat and doped $Sr_3Ti_2O_7$ catalysts.

Photo catalysts	**Products obtained from CO_2 reduction (μmol g^{-1} h^{-1})**									**AQY**
	CH_4	**C_2H_4**	**C_2H_6**	**CH_3OH**	**C_2H_4O**	**C_2H_5OH**	**C_3H_6O**	**C_3H_6**	**H_2**	**$x10^{-3}$ (%)**
$Sr_3Ti_2O_7$	0.16	0.08	0.03	19.9	1.5	1.9	-	0.04	1.7	3.17
$Sr_3Ti_2O_{(7-x)}N_x$	0.07	0.01	0.02	21.2	3.1	2.1	-	0.08	1.0	5.01
$Sr_3Ti_{(2-x)}S_xO_{(7-y)}N_y$	0.01	0.04	0.14	41.3	0.1	3.4	0.8	0.01	0.6	5.85
$Sr_3Ti_{(2-x)}Fe_xO_7$	0.23	0.55	0.12	29.9	0.7	6.1	2.7	0.01	0.3	5.76
$Sr_3Ti_{(2-x)}Fe_xO_{(7-y)}N_y$	0.22	0.23	0.19	48.9	0.35	7.8	3.1	0.08	0.5	8.92
$Sr_3Ti_{(2-x-y)}Fe_xS_yO_{(7-z)}N_z$	0.13	1.1	0.3	60.1	3.99	9.9	3.5	0.04	0.7	10.7

Main carbon products obtained from PCRC under our experimental conditions with 20 hrs of photo illumination are shown in Fig. 5.11. It is observed that $Sr_3Ti_2O_7$ co-doped with Fe-N-S photo catalysts display better PCRC activity compared to bare and mono doped layered strontium titantate. It is clear that doping/co-doping of $Sr_3Ti_2O_7$

with Fe, N and S has brought out significant improvements in PCRC, as indicated by the increase in AQY values. XRD patterns for the fresh Fe, N and S doped $Sr_3Ti_2O_7$ (Fig. 5. 2f) and for the same catalyst after 20 hrs of use (Fig. 5.2g), do not reveal any significant changes, indicating structural stability of the catalyst.

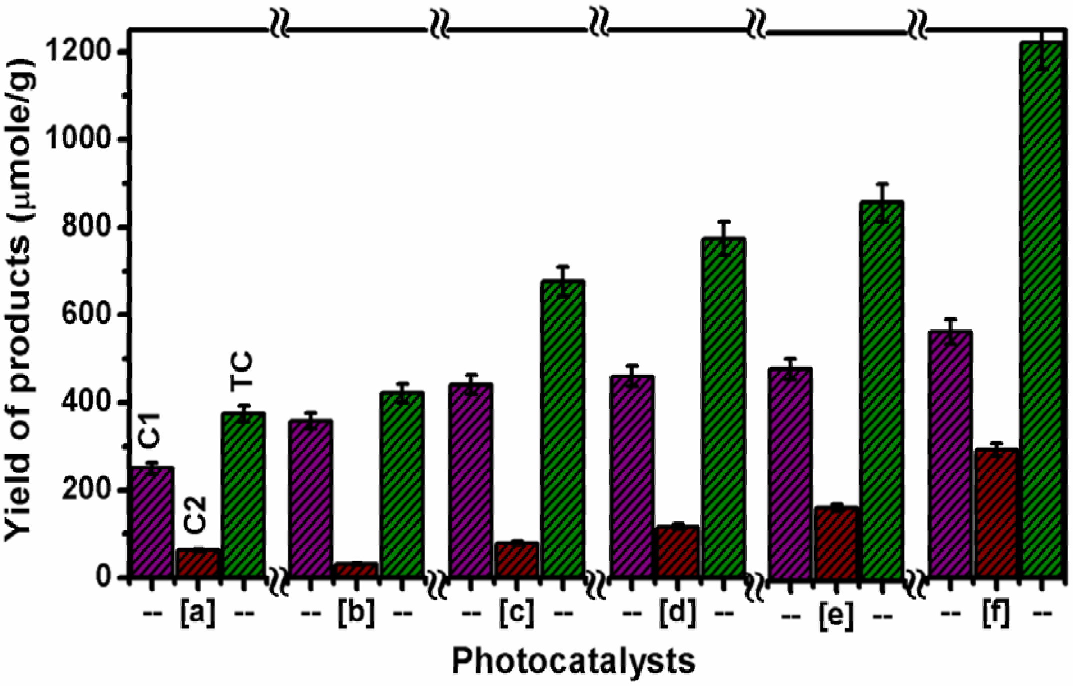

[C1 – C_1 carbon product, C2 – C_2 carbon product, TC- Total Carbon product].

Fig. 5.11 Comparison of photocatalytic activity for neat and modified catalysts after 20hrs of irradiation: (a) $Sr_3Ti_2O_7$, (b) $Sr_3Ti_2O_{(7-x)}N_x$, (c) $Sr_3Ti_{(2-x)}S_xO_{(7-y)}N_y$, (d) $Sr_3Ti_{(2-x)}Fe_xO_7$, (e) $Sr_3Ti_{(2-x)}Fe_xO_{(7-y)}N_y$, (f) $Sr_3Ti_{(2-x-y)}Fe_xS_yO_{(7-z)}N_z$.

5.1.2.9 Photo physical characteristics and activity

While the effect of doping $SrTiO_3$ (with cubic perovskite structure) with anions like, N, S and metal oxides (of Fe, Co, Ni and Mn) has been studied in detail [14-17], to the best of our knowledge, similar investigations on doped $Sr_3Ti_2O_7$ phases have not been reported so far. Structurally, $Sr_3Ti_2O_7$ is closely related to $SrTiO_3$ and is one of the intergrowth phases (known as Ruddlesden Popper-RP phases) formed from $SrTiO_3$ with a general formula SrO $(SrTiO_3)_n$ with n=2. The structural models of the possible RP phases are given in Fig. 5.12. In $Sr_3Ti_2O_7$ every two cubic perovskite ($SrTiO_3$) layer is separated by a single SrO layer. The band gap energy values for both $SrTiO_3$ and $Sr_3Ti_2O_7$ are nearly the same (~3.2 eV). While doping $Sr_3Ti_2O_7$ with N reduces the band gap from 3.14 to 2.99 eV (Table. 5.1), co-doping with N and S leads to further reduction to 2.85 eV. This is due to the synergistic effect of co-doping, wherein, the 2p-states of both N and S overlap with that of O 2p, leading to narrowing of the band gap. Such effects due to co-doping with N and S have been observed in $SrTiO_3$ and TiO_2 [15, 19, 20].

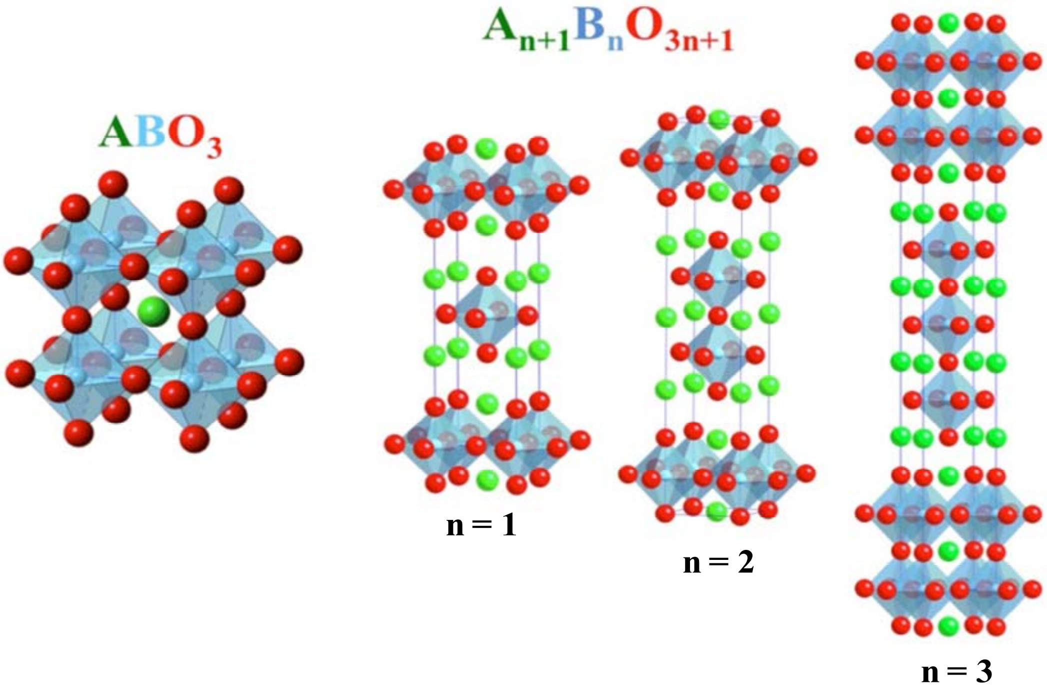

Fig. 5.12 Structural models of Ruddlesden Popper phases.

N 1s core level binding energy value of 398.4 eV observed for N doped $Sr_3Ti_2O_7$, is close to the value of 398.5 eV reported [21] for nitrogen doped $SrTiO_3$, indicating the presence of anionic nitrogen in substitutional locations of oxygen. Co-doping with N and S shows a main peak at 398.5 eV, besides a small intensity peak at 400.6 eV, while with Fe, N and S co-doping, a broad major peak at 400.1 eV is observed, due to nitrogen species in the interstitial locations involving N in different environments like, N-O-Ti-O or O-N-Ti-O [22, 23]. These observations are in line with the literature reports [24-26] on nitrogen doping in TiO_2, wherein two energy levels corresponding to substitutional and interstitial nitrogen within the band gap is proposed.

S $2p_{1/2}$ lines observed for N, S and Fe, N-S doped $Sr_3Ti_2O_7$ samples at 168.9 and 168.4 eV (Fig. 5.9 [C]) respectively shows that S is present as S^{6+} species in the lattice. Presence of S^{2-} species is ruled out, as its ionic size is too large (0.184 nm) to be located in the place of O^{2-} (0.14 nm).

Studies on the effect of doping of $SrTiO_3$ with Fe [19, 20] have revealed that additional energy levels, identified with Fe^{3+} and Fe^{2+} states, are created within the band gap. Excitation of electrons from these levels to the conduction band of $SrTiO_3$ corresponds to light absorption in the visible region. Recently, Zhou et al [16], based on DFT calculations on the electronic level characteristics Fe doped $SrTiO_3$, have shown that Fe^{3+} ions could take up substitutional sites of Ti^{4+} ions and some Fe 3d states are located just above the top of the O 2p valence band. Such a configuration results in narrowing of the band gap. Similar changes occurring in Fe doped $Sr_3Ti_2O_7$ could explain the reduction in band gap values. Shift in the XRD d-lines observed for Fe, N and S co-doped $Sr_3Ti_2O_7$ is indicative of the location of doped Fe^{3+} ions in the titania matrix (Fig. 5.3). Incorporation of Fe^{3+} in $Sr_3Ti_2O_7$ [27] and TiO_2 [28] lattice networks have been reported earlier.

Apart from enabling the visible light absorption, Fe doping plays a prominent role amongst the dopants, in increasing the life time of charge carriers. Amongst several metal ions explored as electron traps for titania, Fe^{3+} is considered to be the most effective one [29-31] as it can easily transform from stable Fe^{3+} (d^5) configuration to relatively unstable Fe^{2+} (d^6), which, can again transfer electron to form Fe^{3+}. In this manner, Fe could effectively trap electrons and release it to enable charge migration and interfacial charge transfer. This aspect is very well reflected in the photoluminescence spectra of Fe doped samples (Fig. 5.7). All the elementary steps in a typical photo chemical reaction like, charge pair generation, charge trapping, charge release/de-trapping, migration and interfacial charge transfer [32, 33] could be facilitated by doping with Fe. As suggested by Cong et al. for TiO_2 [34], N doping could help in quenching photo luminescence by trapping of electrons in oxygen vacancies and holes by the doped anionic nitrogen species in the following steps:

$O_V^0 + e^-_{CB} \rightarrow O_v$ ----------- (5.1)

$N^- + h_{VB}^+ \rightarrow N^0$ ----------- (5.2)

It is reported that sulfation of titania surface increases the number and strength of the acid sites, which in turn, retard recombination of charge carriers [35, 36]. Such an effect due to sulfur doping would be applicable to sulfated $Sr_3Ti_2O_7$ as well, resulting in the minimization of recombination. In this manner, all the three dopants play dual roles, of reducing the band gap and minimizing the recombination of charge carriers.

The extension of light absorption edge into visible region and increased life time of charge carriers are the two major factors responsible for the observed increase in PCRC activity (Table 5.2). Besides, decrease in the crystallite size observed for doped samples, is the other contributing factor, since smaller size could shorten the path length for the diffusion of charge carriers from the bulk to the surface and hence reduce the probability for recombination [37]. Additionally, the layered structure of $Sr_3Ti_2O_7$ facilitates easy transport of charge carriers and separation of oxidation/reduction reaction centers within the interlayer space [12]. The formulation, with co-doping of N, S and Fe together, wherein the influence of these factors is maximum, displays maximum activity (Table 5.2). When modified suitably, $Sr_3Ti_2O_7$ could be a better alternative for PCRC application.

5.1.3 Conclusions

Neat and doped $Sr_3Ti_2O_7$ samples have been prepared by modified polymer complex method. The influence of doping has been investigated by detailed characterization of the catalysts with XRD, EDXA, SEM, DRS, Photo luminescence and X-ray photo electron spectroscopic techniques. Doping/co-doping with anions N, S and metals like Fe, results in the creation of additional energy levels within the band gap, leading to the absorption of visible light and also minimization of the recombination of charge carriers. Fe^{3+} ions in the lattice function effectively trapping/de-trapping centres. Formation of smaller crystallites also reduces the probability for recombination. Layered structure of $Sr_3Ti_2O_7$ facilitates easy transport of charge carriers and separation of oxidation/reduction reaction centers. These factors contribute towards the significant improvement in activity for CO_2 photo reduction on $Sr_3Ti_2O_7$ co-doped with N, S and Fe together, wherein the influence of dopants is maximum.

5.2 Layered perovskite titanates ($SrTiO_3$, $Sr_3Ti_2O_7$ and $Sr_4Ti_3O_{10}$) as catalysts for photo reduction of CO_2

5.2.1 Introduction

In heterogeneous photo catalysis, ABO_3 type perovskite family materials play significant role due to their chemical composition, crystal structure and band edge positions. Especially, perovskites with layered structure, like, $ALa_4Ti_4O_{15}$ (A= Ca, Sr, Ba) with Ag as co-catalyst [11] exhibit better performance for PCRC, since the layered structure facilitates faster transport of charge carriers and the interlayer space could be used as oxidation/reduction reaction sites, leading to the separation of charge carriers [12]. Application of layered perovskites as photo catalysts is well-known [38, 39]. Several layered perovskites have been reported as efficient photo catalysts for water splitting, such as, $K_2Nb_6O_{17}$ [40], $K_2La_2Ti_3O_{10}$ [41], $RbNdTa_2O_7$ [42], $RbLnTa_2O_7$ [43], $Sr_2(Ta_{1-x}Nb_x)_2O_7$ [44], $MCa_2Ta_3O_{10}$ [45], $A_5Nb_4O_{15}$ (A = Sr and Ba) [46], $HCa_2Nb_3O_{10}$, $HSr_2Nb_3O_{10}$ & $HLaNb_2O_7$ [47], $HCa_2Nb_3O_{10}$ [48] and $MLa_2Ti_3O_{10}$ [49].

$SrTiO_3$, with cubic perovskite structure, is one of the earliest catalysts [3] to be explored for PCRC. Layered perovskites like, $Sr_3Ti_2O_7$ and $Sr_4Ti_3O_{10}$ are structurally closely related to $SrTiO_3$ and are actually the intergrowth phases (known as Ruddlesden Popper-RP phases) formed from $SrTiO_3$ with a general formula SrO $(SrTiO_3)_n$ with n=2 & 3. The structural models of the possible RP phases are given in Fig. 5.12. In $Sr_3Ti_2O_7$, every two cubic perovskite ($SrTiO_3$) layer is separated by a single SrO layer, while in $Sr_4Ti_3O_{10}$, every three cubic $SrTiO_3$ layer is separated by a single SrO layer and has a neutral interlayer with electron density [50].

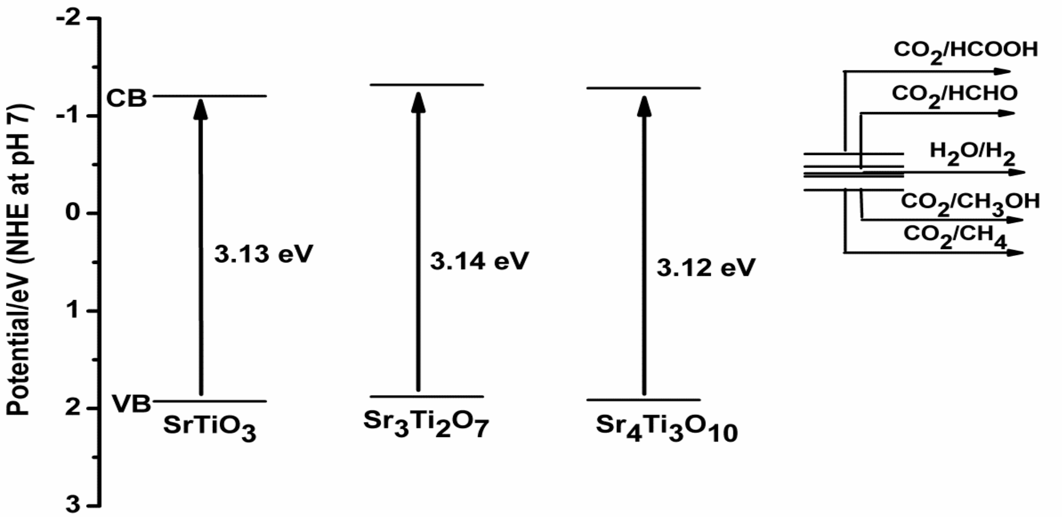

Fig. 5.13 VBM and CBM energy levels of Strontium titanate based photo catalysts with respect to the potential for reduction for CO_2 and oxidation of water.

Though all three titanates are active for photo catalytic splitting of water under UV radiation, both $Sr_3Ti_2O_7$ and $Sr_4Ti_3O_{10}$ are 5-6 times more active for hydrogen evolution under identical conditions [12], compared to $SrTiO_3$, which shows the significant role played by layered structures. Beside, the conduction band energy level of $Sr_4Ti_3O_{10}$, like that of $Sr_3Ti_2O_7$, is suitable for PCRC, but has not been explored so far. It would be an interesting study and compare the characteristics and performance of the two layered strontium titanates, $Sr_3Ti_2O_7$ and $Sr_4Ti_3O_{10}$, along with that of a simple perovskite, $SrTiO_3$, for PCRC. CBM energy levels of all three titanates are suitable for PCRC with water as shown in Fig. 5.13. Since the three titanates are typical wide band semi-conductors, active only in UV region, they have to be modified, by co-doping with N,S and Fe in order to enable visible light absorption.

$Sr_4Ti_3O_{10}$, $SrTiO_3$ and their modified versions [N-S-Fe] have been synthesized by the same method adopted for $Sr_3Ti_2O_7$ by varying stoichiometric amount of precursors. The prepared materials were characterized by various techniques to identify crystal structure and optical properties.

5.2.2 Results and Discussion

5.2.2.1 X-ray Diffraction pattern

X-ray diffraction patterns for $SrTiO_3$ based materials are shown in Fig. 5.14 [A]. All the diffraction peaks correspond to $SrTiO_3$ cubic crystal structure (JCPDS: 35-0734) with lattice constant a = 3.89 Å. This is consistent with literature reports [51]. Fig. 5.14 [B] shows the diffraction patterns corresponding to $Sr_4Ti_3O_{10}$, which is similar with previously reported pattern [50].

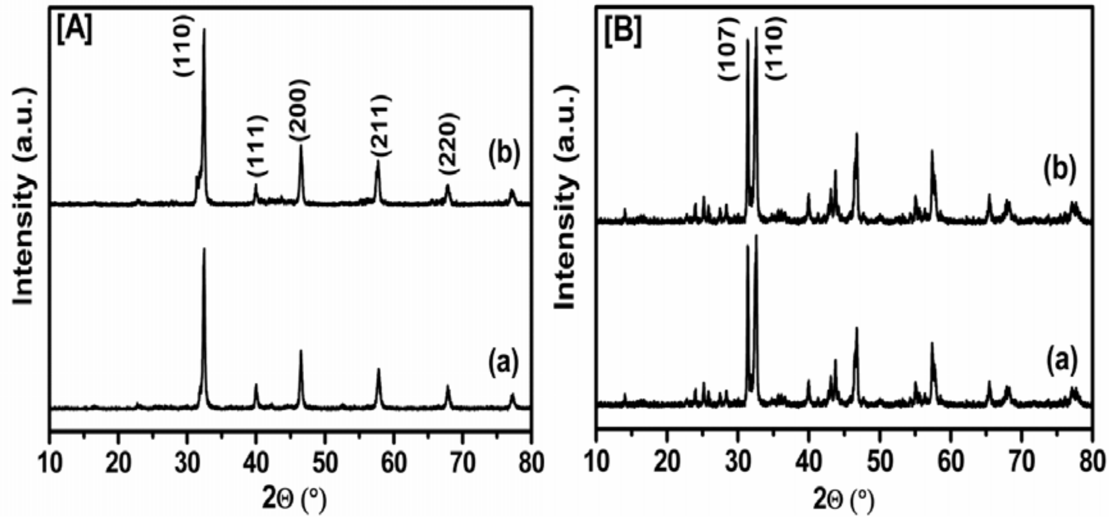

Fig. 5.14 XRD pattern for neat and modified strontium based catalysts [A] $SrTiO_3$ [B] $Sr_4Ti_3O_{10}$; (a) pristine (b) Fe-N,S modified photo catalysts.

As already observed in Chapter 5.1 for $Sr_3Ti_2O_7$, the amounts of dopants added being small, no peaks corresponding to Fe_2O_3 could be observed for $SrTiO_3$ and layered

$Sr_4Ti_3O_{10}$. Instead, a small shift in d-line, similar to that for $Sr_3Ti_2O_7$ (Fig. 5.3) could be observed in Fig. 5.15. The shift is due to the location of doped Fe^{3+} ions (ionic radius - 0.64 Å) at Ti^{4+} ion (ionic radius- 0.61 Å) sites as ionic radii values are closer. The crystallite size values calculated from Scherrer's formula are listed in Table 5.3.

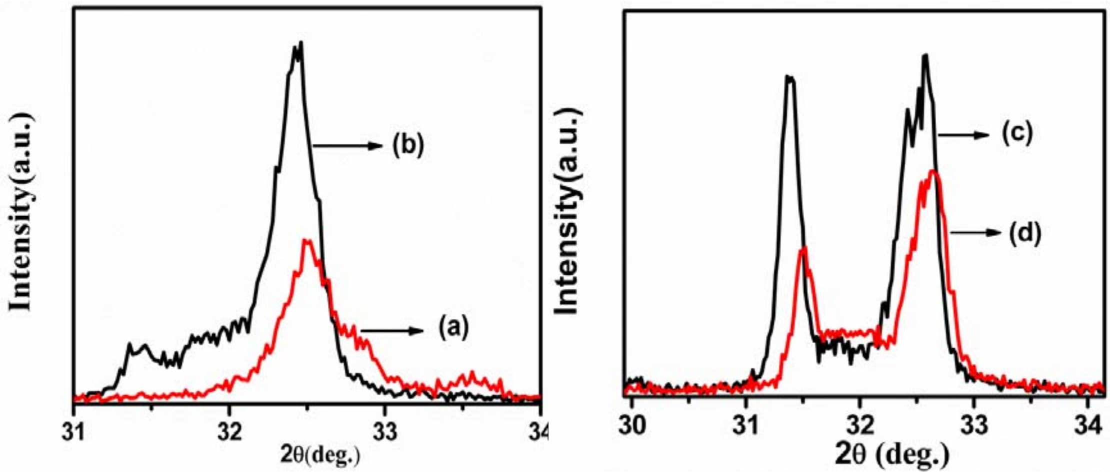

Fig. 5.15 Shift in XRD diffraction peak due to substitution (a) $SrTiO_3$, (b) $SrTi_{(1-x-y)}Fe_xS_yO_{(3-z)}N_z$, (c) $Sr_4Ti_3O_{10}$, (d) $Sr_4Ti_{(3-x-y)}Fe_xS_yO_{(10-z)}N_z$..

5.2.2.2 DRS UV-Visible Spectra

Fig. 5.16 shows the DRS UV-Visible spectra for $SrTiO_3$ and layered $Sr_4Ti_3O_{10}$ along with their Fe-N-S modified catalysts. It is seen that both titanates display their intrinsic absorption peak near around 395 nm, and on modification with Fe-N-S, the catalysts extend their absorption towards visible region. The calculated band gap values are listed in Table 5.3. The observed band gap energy values are in line with literature reports [50, 51]. Generally, the band gap energy of the layered perovskite materials are affected by certain factors, like, M-O-M bond angle, thickness of perovskite layer, electronegativity and ionic radii of elements in octahedral and 12-fold co-ordinate sites [46]. It is also reported that, Ruddlesden Popper phase compounds have similar band gap energy provided the M-O bond distance and bond angles are similar [39]. In the present case, measured band gap values are similar.

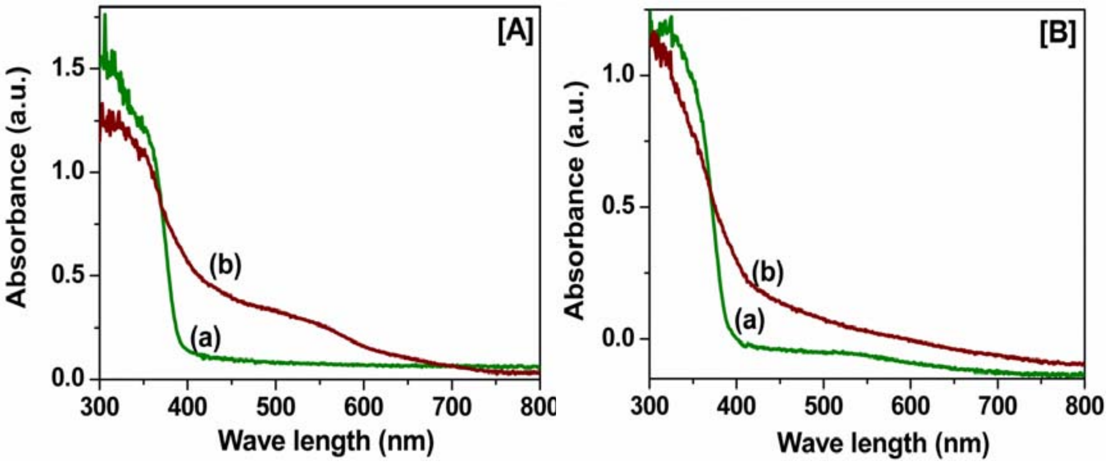

Fig. 5.16 DRS UV-Visible spectra for neat and modified strontium based catalysts [A] $SrTiO_3$ [B] $Sr_4Ti_3O_{10}$; (a) pristine (b) Fe-N,S modified photo catalysts.

This can be ascribed to the fact that, for the three titanates, CBM is mainly composed of Ti 3d and VBM mainly constitute of O 2p, and they differ structurally in terms of number of inter layers of $SrTiO_3$ and SrO. However, the contribution of interlayer cations/anions to the band gap being negligible similar band gap energy values, typical of $SrTiO_3$ unit is observed [45]. In all the three Fe-N-S modified titanates, Fe doping creates impurity level below the conduction band, whereas anions (N,S) creates impurity level above the valence band, resulting in narrowing the of the band gap as shown in Table 5.3. However, the band gap narrowing for Fe-N-S modified $Sr_3Ti_2O_7$ is more (3.14 to 2.40 eV) compared to the narrowing in the other two perovskite.

5.2.2.3 Surface Area Analysis

Synthesized pristine $SrTiO_3$ and $Sr_4Ti_3O_{10}$ have moderate BET surface area of 12 and 15 m^2/g respectively, and no significant changes are observed on modification with Fe-N-S dopants.

5.2.2.4 Scanning Electron Microscopic Analysis

Scanning electron micrographs for neat and modified $SrTiO_3$ and $Sr_4Ti_3O_{10}$ photo catalysts indicate plate like morphology (Fig. 5.17). However, changes in crystallite sizes are observed, which is supported by X-ray line broadening analysis of doped materials (Table 5.3).

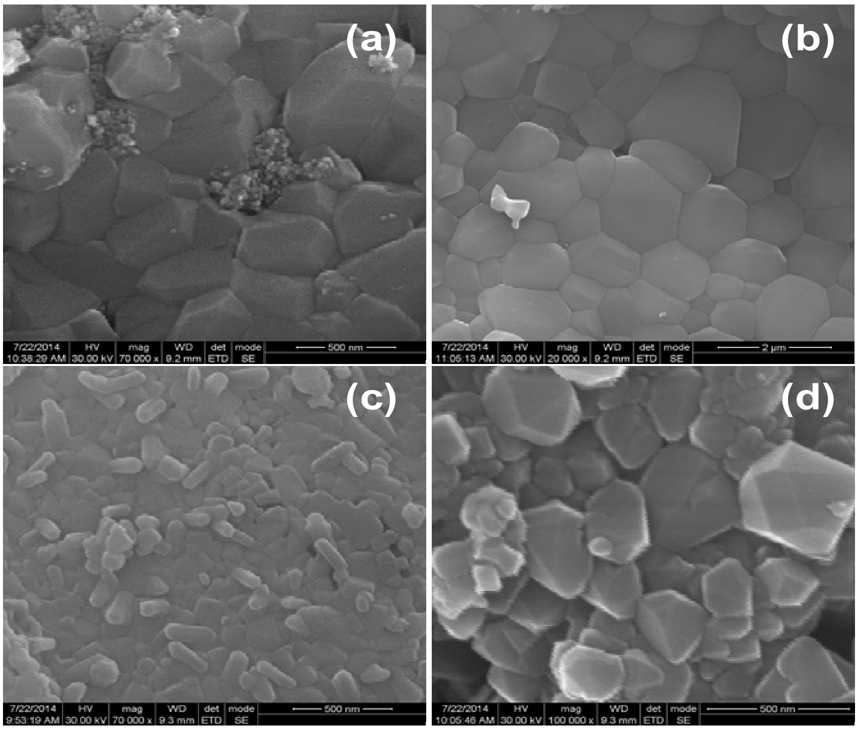

Fig. 5.17 SEM images of strontium titanate based photocatalysts (a) $SrTiO_3$, (b) $SrTi_{(1-x-y)}Fe_xS_yO_{(3-z)}N_z$, (c) $Sr_4Ti_3O_{10}$, (d) $Sr_4Ti_{(3-x-y)}Fe_xS_yO_{(10-z)}N_z$.

5.2.2.5 EDXA Spectra

As described in the previous section, the presence of doped species in the layered titanates has been confirmed by the EDXA spectra, which display characteristic X-ray lines due to Fe, N and S in addition to Sr, Ti and O lines, as shown in Fig. 5.18. Thus the presence of dopants in titania matrix is confirmed.

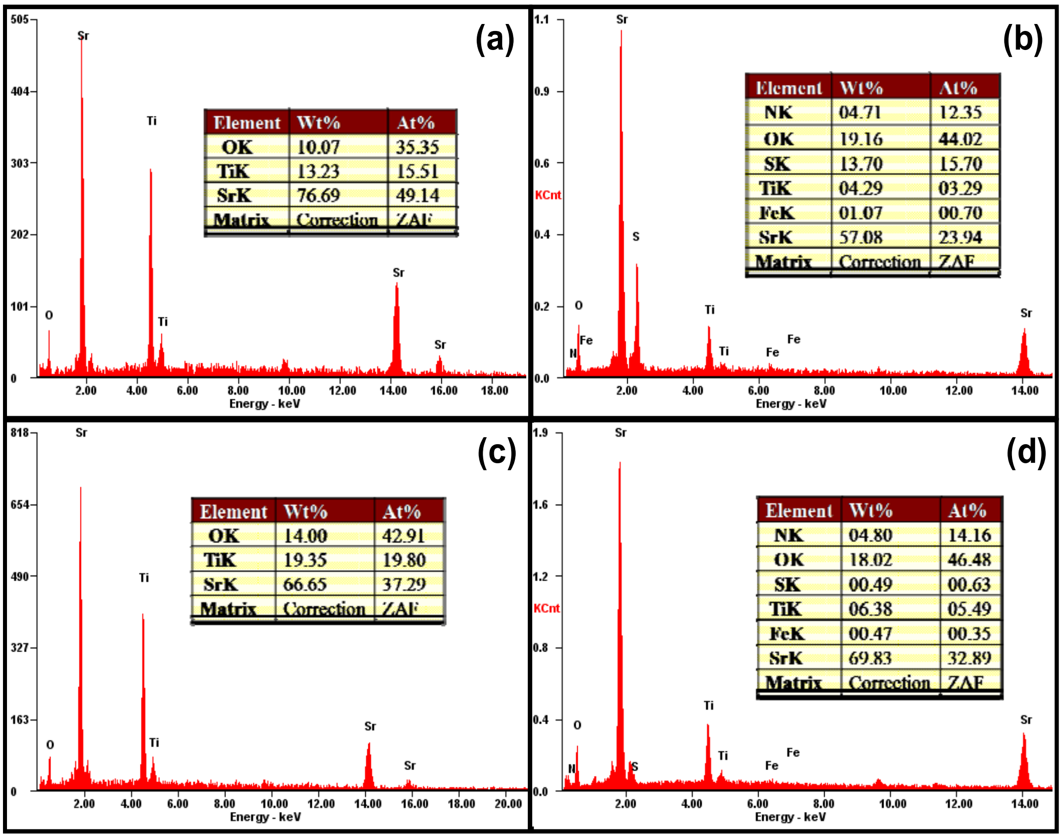

(a)

Element	Wt%	At%
OK	10.07	35.35
TiK	13.23	15.51
SrK	76.69	49.14
Matrix	Correction	ZAF

(b)

Element	Wt%	At%
NK	04.71	12.35
OK	19.16	44.02
SK	13.70	15.70
TiK	04.29	03.29
FeK	01.07	00.70
SrK	57.08	23.94
Matrix	Correction	ZAF

(c)

Element	Wt%	At%
OK	14.00	42.91
TiK	19.35	19.80
SrK	66.65	37.29
Matrix	Correction	ZAF

(d)

Element	Wt%	At%
NK	04.80	14.16
OK	18.02	46.48
SK	00.49	00.63
TiK	06.38	05.49
FeK	00.47	00.35
SrK	69.83	32.89
Matrix	Correction	ZAF

Fig. 5.18 EDXA Spectra for strontium titanate based photocatalysts (a) $SrTiO_3$, (b) $SrTi_{(1-x-y)}Fe_xS_yO_{(3-z)}N_{z,}$ (c) $Sr_4Ti_3O_{10,}$ (d) $Sr_4Ti_{(3-x-y)}Fe_xS_yO_{(10-z)}N_{z.}$

Table 5.3 Crystalline size and band gap energy data for neat and modified Strontium titanate based photo catalysts

Photo Catalyst	Crystallite size (nm)	Band gap (eV)
$SrTiO_3$	28.9	3.13
$SrTi_{(1-x-y)}Fe_xS_yO_{(3-z)}N_z$	33	2.75
$Sr_3Ti_2O_7$	46	3.14
$Sr_3Ti_{(2-x-y)}Fe_xS_yO_{(7-z)}N_z$	21.9	2.4
$Sr_4Ti_3O_{10}$	52.7	3.12
$Sr_4Ti_{(3-x-y)}Fe_xS_yO_{(10-z)}N_z$	46.7	2.71

5.2.2.6 X-ray photoelectron Spectra

XPS measurements were carried out to analyse chemical composition and to identify chemical states of the dopant elements present in neat and modified $SrTiO_3$ and $Sr_4Ti_3O_{10}$ catalysts. XP spectra for pristine perovskites display lines due to Sr 3d at 133 eV, Ti 2p at 458 eV and O 1s at 529.5 eV. High resolution XPS spectra for Fe 2p, N 1s and S 2p are shown in Fig. 5.19. Modified perovskites display XPS lines due to Fe 2p at 709.1 eV, N 1s at 399.8 eV and S 2p at 168.9 eV, in addition to the lines due to pristine phases, indicating the incorporation of dopant elements in the perovskites structure. The observed results are similar to those obtained for double layered perovskite, $Sr_3Ti_2O_7$ (Figs. 5.8 & 5.9). The results indicate that doped Fe as Fe^{3+} is substituted in Ti^{4+} site [19, 20], doped S is present as cationic S^{6+} substituting for Ti^{4+} [19, 20], and doped N is present as substitutional (O-Ti-N) as well as interstitial (Ti-N-O) type of nitrogen [21-26].

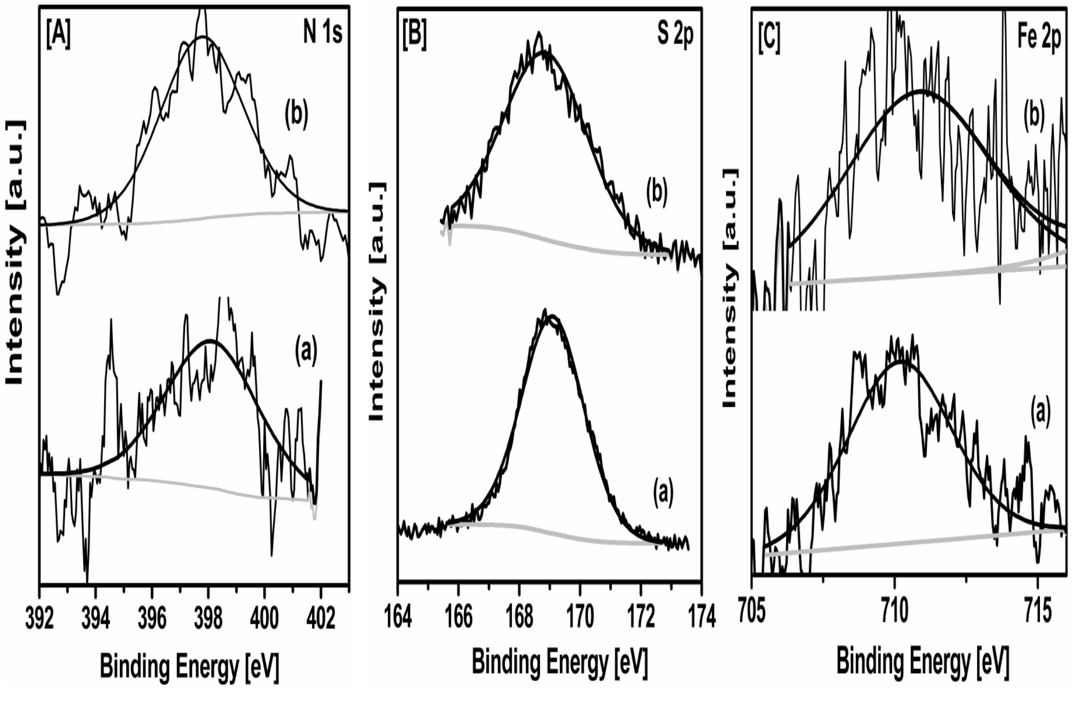

Fig. 5.19 High resolution XP spectra of N 1s [A], S 2p [B] and Fe 2p [C] for modified strontium titanate based photo catalysts; (a) $SrTiO_3$, (b) $Sr_4Ti_3O_{10}$.

5.2.2.7 Photoluminescence Spectra

Intensity of the photoluminescence spectra indicates the recombination rate of excited charge carriers. Photoluminescence spectra for both $SrTiO_3$ and $Sr_4Ti_3O_{10}$ in neat and modified versions are shown in Fig. 5.20. The recombination rate of photo generated charge carriers has been reduced significantly on modification with Fe-N-S. In this aspect all the three titanates on modification retard recombination (Figs. 5.7 & 5.20).

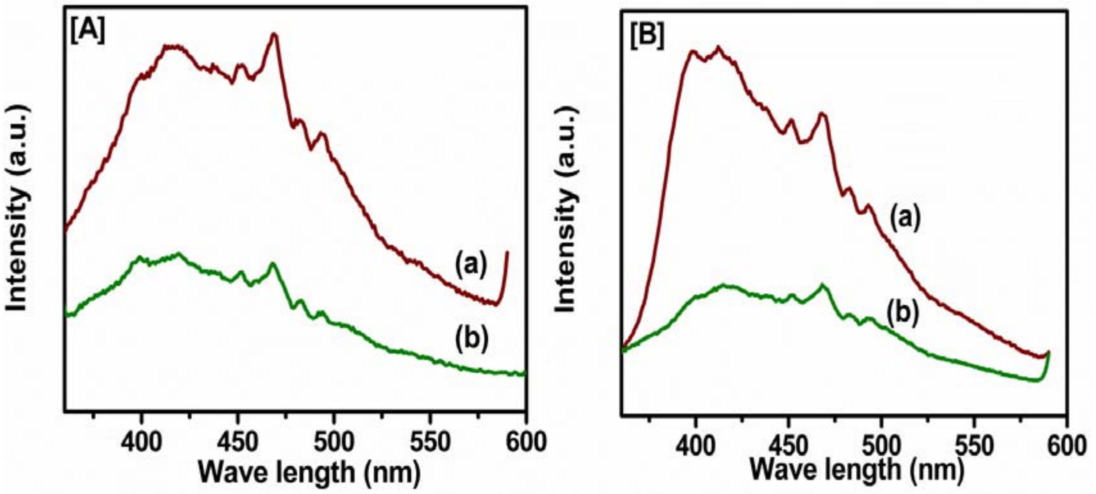

Fig. 5.20 Photoluminescence spectra for neat and modified strontium based catalysts [A] $SrTiO_3$ [B] $Sr_4Ti_3O_{10}$; (b) pristine (a) Fe-N,S modified photo catalysts.

5.2.3 Photo catalytic reduction of carbon dioxide with water

Pristine and modified titanates were evaluated for the application of CO_2 photo reduction with water. All the reactions were carried out under the same experimental conditions adopted for double layered perovskite ($Sr_3Ti_2O_7$). The major product obtained from the perovskite materials are methanol, ethanol and also trace quantities of other hydrocarbons like methane, ethylene and propylene as listed in Table 5.4. All the catalysts show activity up to 20 hrs. Based on the initial rate of formation of products, apparent quantum yield has been calculated and tabulated in Table 5.4.

Table 5.4 Product distribution and quantum yield data for neat and modified Strontium titanate based photo catalysts

Photo catalysts	Products obtained from CO_2 reduction ($\mu mol\ g^{-1}\ h^{-1}$)									AQY
	CH_4	C_2H_4	C_2H_6	CH_3OH	C_2H_4O	C_2H_5OH	C_3H_6O	C_3H_6	H_2	x10^3 (%)
$SrTiO_3$	0.02	-	0.03	9.10	0.01	5.10	0.01	-	0.2	2.18
Fe-N,S/$SrTiO_3$	0.02	-	0.00	27.3	0.05	6.60	0.30	-	0.8	4.54
$Sr_3Ti_2O_7$	0.16	0.08	0.03	19.9	1.50	1.90	-	0.04	1.7	3.17
Fe-N,S/$Sr_3Ti_2O_7$	0.13	1.10	0.30	60.1	3.99	9.90	3.50	0.04	0.7	10.7
$Sr_4Ti_3O_{10}$	0.04	0.31	0.00	11.1	0.02	9.10	0.05	1.20	2.2	3.33
Fe-N,S/$Sr_4Ti_3O_{10}$	0.01	0.01	0.04	24.9	0.23	8.85	0.10	-	1.8	4.82

It is clearly seen that, layered perovskites material exhibit reasonable activity for hydrocarbon production, which varies with time. The observed results are consistent with the idea that CBM edge potentials is more negative compared to CO_2 reduction products as shown in Fig. 5.13. Compared to cubic ABO_3 perovskite, $SrTiO_3$, perovskites with layered structure, such as $Sr_3Ti_2O_7$ and $Sr_4Ti_3O_{10}$, give better photo catalytic activity, implying that interlayer space is acting as photoactive centre in addition to crystalline surface [45]. Besides, SrO-terminated surface shows natural basicity owning to the accumulation of excess negative charge from the layer structure perovskites [38]. Basic surface is beneficial for CO_2 adsorption due to its acidic nature. These results in an increase in the availability of CO_2 molecules in layered perovskites compared to neat $SrTiO_3$, which explains the enhanced photo catalytic activity displayed by the two layerd perovskites (Table 5.4).

Compared to pristine perovskite photo catalysts such as $SrTiO_3$, $Sr_3Ti_2O_7$ and $Sr_4Ti_3O_{10}$ their respective Fe-N-S modified perovskites shows significant increase in activity as shown in Fig. 5.21 and Table 5.4. As described Chapter 5.1, Fe-N-S tri-doping increases the life time of charge carriers (PL spectra, Fig. 5.20) and enhanced absorption in visible region as (DR spectra, Fig. 5.16).

Furthermore, in a perfect cubic perovskite the negative charge centre and positive charge centre are in the same site forming highly symmetric structure and the crystal is non-polarized. Whereas, the introduction of dopant elements induces asymmetrical/distorted structure, which results in intra-crystal polarization in a perfect cubic crystal. The newly generated polarization within crystal is beneficial for photo catalytic reactions which facilitates the separation of photo excited electrons and holes [38] and may be helpful in the activation of CO_2.

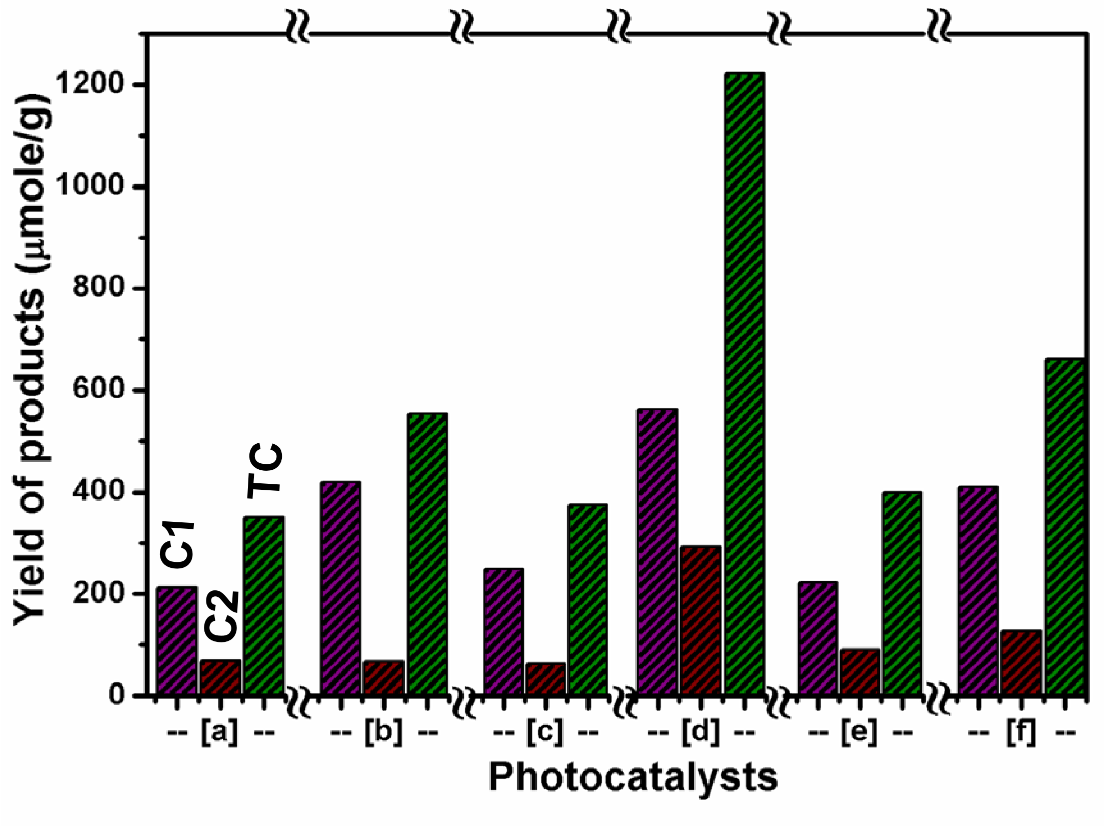

[C1 – C_1 carbon product, C2 – C_2 carbon product, TC- Total Carbon product.]

Fig. 5. 21 Comparison of photocatalytic activity for neat and modified catalysts after 20 hrs of irradiation: (a) $SrTiO_3$, (b) $SrTi_{(1-x-y)}Fe_xS_yO_{(3-z)}N_z$, (c) $Sr_3Ti_2O_7$, (d) $Sr_3Ti_{(2-x-y)}Fe_xS_yO_{(7-z)}N_z$, (e) $Sr_4Ti_3O_{10}$, (f) $Sr_4Ti_{(3-x-y)}Fe_xS_yO_{(10-z)}N_z$.

In the case of Fe-N-S modified layered perovskites, double layered perovskite ($Sr_3Ti_2O_7$) shows higher activity compared to triple layered perovskite ($Sr_4Ti_3O_{10}$). Even though both layered structures absorb visible light, the activity varies tremendously, implying matching band gap with visible region is not the only the criteria for the efficiency of a photo catalyst. Modifications for improving visible light absorption might, in some cases, lower the CBM level, which may, to some extent, adversely affect PCRC activity [38]. CBM edge potential vs the CO_2 reduction potential for a semiconductor is one of the important parameters which affects the overall efficiency for PCRC process. In the present case, CBM of double layered perovskite $Sr_3Ti_2O_7$ (-1.319 V vs NHE at pH 7) is more negative compared to triple layered perovskite $Sr_4Ti_3O_{10}$ (-1.285 V vs NHE at pH 7). Higher the negative potential, higher will be the reducing capacity. Consequently, the probability of CO_2 reduction with double layered $Sr_3Ti_2O_7$ is higher when compared to triple layered $Sr_4Ti_3O_{10}$ and this has been observed experimentally (Fig. 5.21 and Table. 5.4).

When the n value increases to 3, 4 and so on, the intergrowth of Ruddlesden-Popper phases are more frequent than n=2 ($Sr_3Ti_2O_7$). Such a frequent occurrence of stacking faults with increasing n values leads to a disordered layered stacking sequence [52]. In order to evaluate the difference between two layered and three layered perovskite structure, Machida et al. [42, 43, 45] attempted computational study on those type of perovskite materials. Their study reveals that the oxidation capability of VB hole in layer structure depends on the number of perovskite layers and in three layered perovskites, terminal oxygen site facing the interlayer space contribute largely to the top of the VBM [45]. This is due to the fact that when the n value increases, there is a corresponding increase in the variety of oxygen (bridging and terminal) and titanium environments, which does not occur in two layer perovskite materials. Hence three layered perovskites make a strong contribution to VBM which is favorable for water splitting. Besides, the degree of hydration is high in the interlayer galleries with increasing n value [47]. These characteristics indicate that $Sr_4Ti_3O_{10}$ is highly favorable for water splitting due to its specific characteristics, whereas in $Sr_3Ti_2O_7$ photo catalyst is more suitable for simultaneous reduction of CO_2 and H_2O oxidation due to its more negative conduction band edge and favorable perovskite layer gallery.

Thus $Sr_3Ti_2O_7$ stands out as the most active phase amongst the three perovskites, $SrTiO_3$, $Sr_3Ti_2O_7$ and $Sr_4Ti_3O_{10}$.

5.2.4 Conclusions

Among the three layered perovskites materials $SrTiO_3$, $Sr_3Ti_2O_7$, $Sr_4Ti_3O_{10}$ and its Fe-N-S modified photo catalysts, Fe-N-S modified $Sr_3Ti_2O_7$ photo catalysts shows significant photo catalytic activity for PCRC. Conduction band edge plays significant role in photo catalytic activity since among the three perovskites, $Sr_3Ti_2O_7$ has more negative potential. Doping induces dipole moment along the perovskite layers which retards the recombination rate of charge carriers and also modified material absorbs in visible region. Appropriate interlayer spacing with double layered perovskite, prolonged the life time of charge carriers and absorption in visible region are the important factors responsible for increase in photo catalytic activity of Fe-N-S modified $Sr_3Ti_2O_7$ for this crucial application.

5.3 References

1. Y. Izumi, Coord. Chem. Reviews, 2013, 257, 171;V. Jeyalakshmi, K. Rajalakshmi, R. Mahalakshmy, K. R. Krishnamurthy, B. Viswanathan, Res. Chem. Intermed. 2013, 39, 2565; V. Jeyalakshmi, R. Mahalakshmy, K. R. Krishnamurthy, B. Viswanathan, Matl. Sci.Form. 2013, 734, 1-62, Trans Tech. Pub. Switzerland; T.J. Meyer, J.M. Papanikolas, C.M.Heyer, Catal. Lett., 2011, 141, 1
2. S.C. Roy, O. K .Varghese, M. Paulose , C. A. Grimes , ACS Nano letters 2010, 4, 1259; Z. Jiang , T. Xiao , V.L. Kuznetsov, P.P. Edwards , Phil. Trans. R. Soc. A 2010, 368, 3343; J.C.S. Wu, Catal. Surv. Asia, 2009, 13, 30; M.A. Scibioh and B. Viswanathan, Proc. Indian .Natl. Sci. Acad. 2004, 70A, 407
3. M. Halmann, Nature, 1978, 275, 115; B. A-Blajeni, M. Halmann, J. Manassen, , Solar Energy, 1980, 25, 165; M. Halmann, M. Ulman, B. A. Blajeni, Sol. Energy, 1983, 31, 429; V. Jeyalakshmi, R. Mahalakshmy, K.R.

Krishnamurthy, B. Viswanathan, Indian. J. Chem. 2012, 51A, 1263; K. Li, D. Martin, J. Tang, Chinese J. Catal., 2011, 32, 879.

4. T. Inoue, A. Fujishima, S. Konishi and K. Honda, Nature, 1979, 277, 637.
5. V.P. Indrakanti, J.D. Kubicki, H.H. Schobert, Energy Environ. Sci. 2009, 2, 745; K. Mori, H.Yamashita, and M.Anpo, RSC Advances, 2012, 2, 3165.
6. K. Teramura, H. S-I. Okuoka, H. Tsuneoka, T. Shishido, T. Tanaka, Appl. Catal. B: Environ., 2010, 96, 565.
7. S. C. Yan, S. X. Ouyang, J. Gao, M. Yang, J. Y. Feng, X. X. Fan, L. J. Wan, Z. S. Li, J.H. Ye, Y. Zhou, and Z. G. Zou, Angew. Chem. Int. Ed. 2010, 49, 6400.
8. N. Zhang, S. X. Ouyang, P. Li, Y. J. Zhang, G. C. Xi, T. Kako, & J. H. Ye, Chem. Commun. 2011, 47, 2041.
9. M. Halmann, M. Ulman, B. A. Blajeni, Sol. Energy, 1983, 31, 429:B. A-Blajeni, M. Halmann, J. Manassen, Solar Energy, 1980, 25, 165; H. Zhou, J. Guo, P. Li, T. Fan, D. Zhang and J. Ye, SCIENTIFIC REPORTS,| 3 : 1667 | DOI: 10.1038/srep01667 (2013)
10. V. Jeyalakshmi, R. Mahalakshmy, K.R. Krishnamurthy, B. Viswanathan, - 6th Asia Pacific Congress on Catalysis-APCAT-6, Oct 13-17, 2013, Taipei,Tai
11. K. Iizuka, T. Wato, Y. Miseki, K. Saito, and A. Kudo, J. Am. Chem. Soc., 2011, 133, 20863.
12. A. Kudo, Miseki. Chem. Soc. Rev., 2009, 38, 253.
13. H. Jeong, T. Kim, D. Kim, K. Kim. Intern. J. Hydrogen Energy, 2006, 31, 1142
14. U.Sulaeman, S.Yin, T.Sato, J. Nanomaterials, doi:10/1155/2010/629727
15. J.Wang, H.Li, H.Li,S.Yin, T.Sato, Solid State Sci., 2009, 11, 182.
16. X. Zhou, J.Shi, C. Li, J. Phys. Chem. C 2011, 115, 8305.
17. T. Ohno, T. Tsubota, Y. Nakamura, K.Sayama, Applied Catalysis A: General, 2005, 288, 74.

18. D.C. Meyer, A.A. Levin, T. Leisegang, E. Gutmann, P.Paufler, M. Reibold, W. Pompe , Appl. Phys.A, 2006, 84, 31
19. T-H. Xie, X. Sun, J.Lin, J. Phys. Chem. C, 2008, 112, 9753.
20. F. J. Morin, J. R. Oliver, Phys. ReV. B
21. J. Wang, Y. Shu, T. Sato, J. Photochem. Photobiol. A: Chem. 2007, 187, 72.
22. C. S. Gopinath, J. Phys. Chem B, 2006, 110, 7079.
23. M. Satish, B. Viswanathan, R. P. Viswanath, C.S. Gopinath, Chem Mater, 2005, 17, 6349.
24. M. Anpo, M. Takeuchi, J Catal, 2003, 216, 505.
25. C. D. Valentin, G. Pacchioni, A. Selloni, S. Livraghi, Giamello, J Phys. Chem B, 2005, 109, 11414.
26. D.Valentin, E. Finazzi, G. Pacchioni, A. Selloni, S. Livraghi, M.C. Paganini, E. Giamello, Chem. Phys, 2007, 339, 44.
27. Carlos J Navas Perez "Synthesis, electrical conductivity and non-stoichiometry of doped layered perovskites" Ph.D Thesis, Massachsetts Institute of Technology, USA (1999)
28. Y.Yang, C. Tian, Res. Chem. Intermed. 2010, 36, 889
29. M.R. Hoffman, S.T.Martin, W. Choi, D.W. Bahnemann, Chem. Rev. 1995, 95, 69;
30. S. T. Martin, H. Herrmann, W. Choi, M.R. Hoffmann, Trans. Faraday Soc., 1994, 90, 3315; Y.H. Zhang, A. Reller, Mater. Sci. Eng C, 2002, 19, 323
31. Y. H. Zhang, A. Reller, Mater. Sci. Eng C, 2002, 19, 323.
32. W. Choi, A. Termin, and M R. Hoffmann, J. Phys. Chem. 1994, 98, 13669;
33. P. Goswami, J.N. Ganguli, Mat. Res. Bull. 2012, 47, 2077
34. Y. Cong, J. Zhang, F. Chen, M. Anpo, J. Phys. Chem. C, 2007, 111, 6976
35. Y. Liu, J. Liu, Y. Lin, Y. Zhang, Y. Wei, Ceram. Int. 2009, 35, 3061.
36. K.J. Antony Raj, B. Viswanathan, ACS Appl. Mater. Interfaces 2009, 1, 2462
37. A.L. Linsebigler, G. Lu, J.T. Yates, Chem. Rev. 1995, 95, 735.

38. X. Liu, K. Sohlberg, Complex Metals, 2014, 1:1, 103.
39. H. W. Eng, P. W. Barnes, B. M. Auer, P. M. Woodwar, J. Solid State Chem., 2003, 175, 94–109.
40. A. Kudo, A. Tanaka, K. Domen, K. Maruya, K. Aika, T. Ohnishi, J. Catal. 1988, 111, 67.
41. T. Takata, K. Shinohara, A. Tanaka, M. Hara, J. N. Kondo, K. Domen, J. Photochem. Photobiol. 1997, 106, 45.
42. M. Machida, J. Yabunaka, T. Kijima, Chem. Commun., 1999, 1939.
43. M. Machida, J. Yabunaka, T. Kijima, Chem. Mater. 2000, 12, 812.
44. H. Kato, A. Kudo, Journal of Photochem. & Photobiol. A: Chem., 2001, 145, 129.
45. M. Machida, T. Mitsuyama, K. Ikeue, S. Matsushima, M. Arai, J. Phys. Chem. B 2005, 109, 7801-7806.
46. Y. Miseki, H. Kato, A. Kudo, Energy Environ. Sci., 2009, 2, 306–314
47. K. Maeda, T. E. Mallouk, J. Mater. Chem., 2009, 19, 4813–4818
48. T. I. Draskovic, T. H. Wang, C. N. Henderson, T. E. Mallouk, Inter. J. Hydrogen Energy 2014, 39, 4576.
49. Y. Wang, X. Lai, X. Lü, Y. Li, Q. Liu, J. Lin, F. Huang, Cryst. Eng. Comm, 2015, 17, 8703
50. Y-G. Ko, W. Y. Lee, Catal. lett., 2002, 83, 157
51. L.F. da Silva, L.J.Q. Maia, M.I.B. Bernardi, J.A. Andres, V.R. Mastelaro, Mater. Chem. & Phys., 2011, 125, 168.
52. T. Hungria, I. MacLaren, H. Fuess, J. Galy, A. Castro, Mater. Lett., 2008, 62, 3095.

CHAPTER 6

SUMMARY AND CONCLUSIONS

The primary objective of the present investigation is to design novel catalysts for photo catalytic reduction of CO_2 (PCRC). Detailed literature survey on different types of catalysts investigated so far has revealed that two perovskite type catalysts, $NaTaO_3$ and $Sr_3Ti_2O_7$, which display significant activity for splitting of water and possess conduction and valance band energy levels suitable for PCRC, have not been exploited so far. Both oxides, being wide band gap semi-conductors, are to be suitably modified to enable visible light absorption. Attempts have been made to modify these oxides and explore their activity for PCRC. Besides, meso-porous character of the photo-catalysts is known to improve the photo catalytic activity as shown in Table 1.11. In order to explore this aspect, a comparative study of standard titania P-25 and a lab-made mesoporous titania in pristine and doped (N,S & Fe) forms have been investigated. Accordingly, investigations covering the preparation, characterization, evaluation of the performance of the catalysts for PCRC and understanding the performance in terms of the photo physical properties have been carried out around these three main catalyst systems, namely TiO_2, $NaTaO_3$ and $Sr_3Ti_2O_7$.

6.1 Studies on titania based catalysts

Two different types of TiO_2, standard TiO_2-P-25 and meso porous TiO_2 (TiO_2-MP) synthesized in the laboratory, have been studied. Considering the fact that TiO_2 is not active in the visible region, both pristine TiO_2 catalysts have been modified with anions, N & S. TiO_2-MP in pristine and N, S co-doped forms, containing only anatase phase, was prepared by hydrothermal method. The presence of Type IV isotherm and Type A hysteresis curves for N_2 adsorption-desorption at 77K confirm the meso porous structure of TiO_2-MP. Anion (N&S) doping results in the red shift in the absorption of UV-visible radiation by doped TiO_2. XPS spectra confirm that the doped N is incorporated into the lattice of TiO_2 at O^{2-} sites, with some of them located in the interstitial position with strong interaction with nearby oxygen of TiO_2. Doped

S is located in the Ti^{4+} site as S^{6+}, representing cationic substitution. Photo luminescence (PL) spectra of the doped Vs pristine TiO_2 show that the recombination of charge carriers is retarded, due to modification of TiO_2 by anions, N & S. Doping/ co-doping of P-25 TiO_2 also lead to similar changes in photo physical properties. These changes observed in both meso-porous and P-25 TiO_2 samples result in improved activity for PCRC vis-à-vis the respective pristine samples. The increase in activity with anion modified photo catalysts is mainly due to the availability of more number of surface active sites, increased adsorption ability of reactants, favorable crystalline size, efficient absorption in visible region and longer the life of charge carriers. Compared to commercial P-25 TiO_2 nano-particles, synthesized meso-porous TiO_2 (TiO_2-MP) displays better activity, expressed as Apparent Quantum Yield (AQY). Meso-porous structure enhances the diffusion of charge carriers to the surface active sites where the adsorbed reactants get reduced into products.

TiO_2-MP is further modified by tri- doping with Fe, N & S (TiO_2- FNST) and supported on sepiolite with clay structure and basic characteristics. TiO_2- FNST has been characterized by XRD, Raman spectroscopy, EDAX and XPS studies, which reveal that the dopants have been incorporated into meso-porous titania matrix. DRS spectra reveal that, tri doping causes band gap narrowing, due to the creation impurity energy levels below the CBM and above the VBM of pristine TiO_2. A significant decrease in the intensity of PL spectra for tri-doped FNST indicates retardation of charge carrier recombination rate. Further retardation of recombination is brought about by the clay structured sepiolite support. Notable enhancement of photo catalytic efficiency with sepiolite composite compared to pristine TiO_2 and FNST was observed. The synergistic effect of FNST and clay structure increases adsorption of reactant molecules, prolongs life time of charge carriers and facilitates desorption of reduced product from active catalyst surface. These factors resulted in increase in PCRC activity. 50% FNST loaded on sepiolite is the optimum FNST loading on sepiolite which gives higher photo-catalytic activity compared to less/high concentration of FNST. Hence sepiolite is identified as an ideal support for PCRC.

6.2 Studies on sodium tantalate based catalysts

Studies on lanthanum modified sodium tantalate based catalysts has been divided into four parts, namely,

i. Effect of addition of various co-catalysts
ii. Effect of doping/co-doping with N & Fe
iii. Influence of the addition of basic component, MgO
iv. Sensitization with Cobalt tetra phenyl porphyrins

In first part, La doped $NaTaO_3$ ($Na_{(1-x)}La_xTaO_{(3+x)}$) was prepared by hydrothermal method and characterised by various analytical techniques. Co-catalysts, Ag, Au, Pt, Pd, NiO, CuO and RuO_2 were introduced separately by incipient wetness method and activated suitably. The co-catalysts extend the light absorption edge of the tantalate into the visible region and also retard the recombination of charge carriers. Catalyst formulations in conjunction with different co-catalysts display significant activity for PCRC with water as reductant, leading to the formation of methanol and ethanol as major products. The location of the conduction band of NiO/CuO with respect to that of $Na_{(1-x)}La_xTaO_{(3+x)}$ facilitates easy transfer of photo-generated electrons from $Na_{(1-x)}La_xTaO_{(3+x)}$ to the conduction band of NiO/CuO, wherein these electrons participate in simultaneous hydrogen generation (by water splitting) and CO_2 photo-reduction processes. Hence $Na_{(1-x)}La_xTaO_{(3+x)}$ modified with co-catalysts NiO & CuO display maximum activity. Other co-catalysts, Pt, Ag, Au and RuO_2 display marginal improvements in activity vis-à-vis neat $NaTaO_3$. Bimetallic co-catalysts, Pt-Cu & Pt-Ni also display improved CO_2 conversions and higher selectivity towards hydrocarbons. OH^- ions in alkaline reaction medium act as hole scavengers, increase solubility of CO_2 and stability of the catalyst by arresting solubilisation of NiO. $NaTaO_3$ based catalysts could become viable alternatives to titania for this crucial application.

In the second part, the effect of doping/co-doping with N & Fe on the photo physical properties of the $Na_{(1-x)}La_xTaO_{(3+x)}$ has been studied. XRD & XPS results reveal that doped La^{3+}, Fe^{3+} and N (possibly as N^{3-}) ions occupy Na^+, Ta^{5+} and O^{2-} ion sites respectively, in the tantalate matrix. Incorporation of the dopants in the tantalate matrix has been established by SEM-EDXA, STEM-EDS elemental mapping, and surface composition analysis by XPS. Synergistic effects of La, Fe & N co-doping in tantalate matrix results in the narrowing of the band gap due to the creation of additional energy levels within the band gap. Band gap narrowing promotes visible light absorption. Presence of suitable dopants in the lattice ensures electro-neutrality. Efficient charge trapping and de-trapping by Fe^{3+} and Fe^{4+} reduces the probability of charge carrier recombination. Synergetic effects due to co-doping with La, Fe and N and suitable conduction band edge energy levels for CO_2 reduction with water help to improve the photo catalytic properties of co-doped $NaTaO_3$. Compared to neat $NaTaO_3$, AQY for La-N-Fe co-doped $NaTaO_3$ is nearly three times higher.

In the third part, the effect of addition of basic component, MgO, on Fe-N/$Na_{(1-x)}La_xTaO_{(3+x)}$ surface, has been explored. MgO is expected to increase basicity, and facilitate adsorption and activation of CO_2, leading to significant improvements in photo efficiency of the material due to increase in the availability of CO_2 molecules, compared to unmodified tantalate. 0.5 % w/w MgO loaded tantalate displays high photo catalytic activity (AQY-11.1x 10^{-3} %). Thus MgO modified La-N-Fe-$NaTaO_3$ could be an efficient visible light active photo catalyst for CO_2 reduction with water.

In the fourth part, the sensitization of $Na_{(1-x)}La_xTaO_{(3+x)}$ surface by Cobalt tetra phenyl porphyrin (CoTPP) on has been studied. $Na_{(1-x)}La_xTaO_{(3+x)}$, in conjunction with cobalt tetra phenyl porphyrin (CoTPP) as sensitizer, displays significant improvement in activity for PCRC with water. Methanol and ethanol are the major products, besides trace levels of methane, ethane and ethylene. HOMO and LUMO energy level characteristics and redox potentials show that sensitization of $Na_{(1-x)}La_xTaO_{(3+x)}$, with visible light is favoured. Sensitized tantalate simultaneously absorbs both visible and

UV radiation, resulting in the direct transfer of photo generated electrons to its conduction band. Sensitization also retards charge carrier recombination rates, as evidenced from photo luminescence spectral data for the pristine and sensitized $Na_{(1-x)}La_xTaO_{(3+x)}$. These factors contribute towards enhancement of photo-catalytic activity that results in an increase in the formation of ethanol, via multi-electron reduction process. Sensitized catalyst exhibits chemical and structural stability after 20 hrs of irradiation.

6.3 Studies on strontium titanate based catalysts

Investigations on this topic are covered in two parts, namely,

i. Effect of doping with Fe, N & S

ii. Comparative evaluation of layerd titanate phases, $SrTiO_3$, $Sr_3Ti_2O_7$, $Sr_4Ti_3O_{10}$.

Neat and doped $SrTiO_3$, $Sr_3Ti_2O_7$, $Sr_4Ti_3O_{10}$ samples have been prepared by modified polymer complex method and characterized by various techniques. All the three titanate phases display significant activity for PCRC. Doping/co-coping improves the activity further. Doping/ co-doping with anions N, S and cation like Fe, results in the creation of additional energy levels within the band gap, leading to the absorption of visible light and also minimization of the recombination of charge carriers. Formation of smaller crystallites also reduces the probability for recombination. Layered structure of $Sr_3Ti_2O_7$, $Sr_4Ti_3O_{10}$ facilitates easy transport of charge carriers and separation of oxidation/reduction reaction centers. These factors contribute towards the significant improvement in activity for CO_2 photo-reduction on $Sr_3Ti_2O_7$ co-doped with N, S and Fe together, wherein the influence of dopants is maximum.

Neat and tri-doped $SrTiO_3$, $Sr_3Ti_2O_7$, $Sr_4Ti_3O_{10}$ samples have been prepared by modified polymer complex method and characterized by various techniques. While all the three titanate phases, on modifications with Fe,N & S, display significant activity for PCRC, $Sr_3Ti_2O_7$ shows maximum activity, due to higher conduction band edge potential compared to other two titanate phases.

6.4 Salient features of the present investigation

- Choice of preparation methods play a crucial role in achieving desired characteristics of photo catalysts, like, crystal structure, particle size, crystalline nature, porous structure, surface area and morphology which are the major factors that influence the PCRC with water.
- Bicarbonate species present in the reaction medium (pH-8.0) get reduced to surface formate species, which undergo further reduction to yield products like methane, methanol and ethanol. Water as reductant is more efficient than external hydrogen, since water splitting generates active hydrogen atoms that facilitate further conversion of surface formate/CO to hydrocarbons.
- N & S co-doped mesoporous TiO_2 show enhanced photo catalytic activity compared to commercial P-25 TiO_2. Synergetic effect of N,S co-doping enhances visible light absorption and meso porous structure enhances diffusion rate resulting in improved photo catalytic activity.
- Fe-N-S tri doped TiO_2 (FNST) supported on sepiolite composite is found to be suitable photo catalyst composite, which enhances the adsorption of reactants on the active surface and retards the recombination of charge carriers and hence displays increase in photo catalytic activity.
- Co-catalysts (Ag, Au, Pt, NiO, CuO and RuO_2) loaded on La doped $NaTaO_3$ show better photo catalytic activity. In particular, NiO and CuO as co-catalysts show higher activity, since the location of the conduction band of NiO/CuO with respect to that of $Na_{(1-x)}La_xTaO_{(3+x)}$ facilitates easy transfer of photo-generated electrons from $Na_{(1-x)}La_xTaO_{(3+x)}$ to the CBM of NiO/CuO, wherein these electrons participate in simultaneous hydrogen generation (by water splitting) and CO_2 photo reduction processes.
- Metal-Non metal (Fe-N) doping on $Na_{(1-x)}La_xTaO_{(3+x)}$ significantly enhances the activity due to narrowing of band gap and prolonged the lifetime of photo generated charge carriers.

- MgO as basic component increases adsorption of reactant molecules on active surface and consequently increase in activity is observed.
- Sensitization of $Na_{(1-x)}La_xTaO_{(3+x)}$ by Cobalt tetra phenyl porphyrin (CoTPP) results in better activity in solar region, since the band edge positions of CoTPP and $Na_{(1-x)}La_xTaO_{(3+x)}$ are suitable for easy transfer of photo generated electrons to the surface reactant molecules.
- Layered structure of $Sr_3Ti_2O_7$, $Sr_4Ti_3O_{10}$ and its Fe-NS tri-doped photo catalysts show better activity compared to $SrTiO_3$ and their pristine photo catalysts. Layered structure and doping with elements enhances the lifetime of charge carriers and visible light absorption, resulting improved photo catalytic activity.
- $NaTaO_3$ and $Sr_3Ti_2O_7$, with suitable modifications as described in the work, have been identified as highly efficient catalysts for photo catalytic reduction of CO_2 with water.
- Understanding the performance of the catalysts on the basis of their respective photo-physical properties would be helpful in the design of better catalysts.

It is hoped that the results of this research contributes a new insight for the designing of visible light driven photo catalysts for the reduction of carbon dioxide with water.

LIST OF PUBLICATIONS

Publications in Journals

1. Photo catalytic reduction of CO_2 by Water on Titania - Role of Photo physical and Structural Properties.

   K. Rajalakshmi, **V. Jeyalakshmi**, K. R. Krishnamurthy and B. Viswanathan, **Indian Journal of Chemistry**, Vol. 51A, March 2012, pp. 411-419.
2. Titania based catalysts for photo reduction of carbon dioxide: Role of modifiers

   V. Jeyalakshmi, R. Mahalakshmy, K. R. Krishnamurthy and B. Viswanathan, **Indian Journal of Chemistry** Vol. 51A, Sept-Oct 2012, pp. 1263-1283.
3. Application of Photo catalysis for the mitigation of Carbon dioxide

   V. Jeyalakshmi, K. Rajalakshmi, R. Mahalakshmy, K. R. Krishnamurthy and B. Viswanathan, **Res Chem Intermed,** DOI 10.1007/s11164-012-0783-7.
4. Visible light driven reduction of carbon dioxide with water on modified $Sr_3Ti_2O_7$ catalysts

   V. Jeyalakshmi, R. Mahalakshmy, K. Ramesh, P. V. C. Rao, N. V. Choudary, G..S. Ganesh, K. Thirunavukkarasu, K. R. Krishnamurthy and B. Viswanathan, **RSC Advances**, 5, 2015, 5958.
5. Photo catalytic reduction of carbon dioxide in alkaline medium on La modified Sodium tantalate with different co-catalysts under UV-Visible radiation

   V. Jeyalakshmi, R. Mahalakshmy, K. R. Krishnamurthy and B. Viswanathan, **Catalysis Today**- ID- CATTOD9782.

Book Chapter

1. Photocatalytic reduction of Carbon dioxide by water: A step towards sustainable fuels and chemicals

   V. Jeyalakshmi, R. Mahalakshmy, K. R. Krishnamurthy and B. Viswanathan, **Materials Science Forum** Vol. 734 (2013) pp 1-62 © (2013) Trans Tech Publications, Switzerland doi:10.4028/www.scientific.net/MSF.734.1., Photocatalytic Materials & surfaces for Environmental Cleanup-II, Editor: Rajesh J. Tayade.

Presentations in International Conferences

1. Photo catalytic reduction of carbon dioxide by water on La modified sodium tantalate with different co-catalysts under UV-Visible radiation
   V. Jeyalakshmi, R. Mahalakshmy, K.R. Krishnamurthy and B. Viswanathan, **6th Asia Pacific Congress on Catalysis-** APCAT- 6 held at Taiwan, Oct 13-17, 2013.
2. Visible light driven reduction of CO_2 on modified $Sr_3Ti_2O_7$.
   V. Jeyalakshmi, R. Mahalakshmy, K Ramesh, P V C Rao, N V Choudary, G Sriganesh, K.R Krishnamurthy and B. Viswanathan, **248th National Meeting of ACS Division of Energy & Fuels,** San Francisco, Aug.10-14, 2014.

Presentations in National Conferences

1. Sodium tantalate based catalysts for photo catalytic reduction of Carbon dioxide, **V. Jeyalakshmi**, K. Rajalakshmi, K. R. Krishnamurthy and B. Viswanathan, **15th National Workshop on The Role of New materials in Catalysis**, IIT Madras, December 11-13, 2011.
2. Photo catalytic reduction of Carbon dioxide with water on CuO-TiO_2 – Influence of the characteristics of titania supports, **V. Jeyalakshmi**, R. Mahalakshmy, K. R. Krishnamurthy and B. Viswanathan, **15th National Workshop on The Role of New materials in Catalysis**, IIT Madras, December 11-13, 2011.
3. Hetero structured CuO-TiO_2 catalyst for Photocatalytic reduction of Carbon dioxide with water, **V. Jeyalakshmi**, R. Mahalakshmy, K. R. Krishnamurthy and B. Viswanathan, **21stNational Symposium on catalysis**, IICT Hyderabad, Feb. 10-13, 2013.
4. Visible light reduction of CO_2 with water on mesoporous Titania Catalysts.
   V. Jeyalakshmi, R. Mahalakshmy, K. R. Krishnamurthy and B. Viswanathan, **16th National Workshop on Catalysis for Sustainable Development,** CSIR-NEERI, Nehru Marg, Nagpur, Feb 4-5, 2014.

5. Carbon neutral processes for fuels and chemicals

   V. Jeyalakshmi, K. Ramesh, P.V.C. Rao, N. V. Choudary, G. Sri Ganesh, K. R. Krishnamurthy and B. Viswanathan.

   International Conference on "Emerging Environmental and Advanced Oxidation Technologies for Energy, Environment and Sustainability" **Anna University - Chennai**, Sep 29th-30th 2014.

6. Visible light driven reduction of CO_2 on modified $Sr_3Ti_2O_7$

   V. Jeyalakshmi, R. Mahalakshmy, K Ramesh, P V C Rao, N V Choudary, G Sriganesh, K.R Krishnamurthy and B. Viswanathan.

   22nd National Symposium on Catalysis, CSIR-CSMCRI, Bhavnagar, Gujarat, Jan 7-9, 2015.

7. Influence of basicity on photo catalytic reduction of carbon dioxide by modified $Na_{(1-x)}La_xTaO_{(3+x)}$ surface.

   V. Jeyalakshmi, R. Mahalakshmy, K. R. Krishnamurthy and B. Viswanathan.

   10th Mid-Year CRSI Symposium in Chemistry, NIT, Trichy, Tamil Nadu, July 23-25, 2015.

Patents

1. Catalyst composition for photo catalytic reduction of carbon dioxide

   V. Jeyalakshmi, K. R. Krishnamurthy, B. Viswanathan, K. Ramesh, P.V.C. Rao, N.V. Choudary and G. Sriganesh,

   Indian Patent Appl. No: 2039/MUM/2013 filed on 17th June, 2013.

2. Catalyst composition for photo catalytic reduction of carbon dioxide

   V. Jeyalakshmi, K. R. Krishnamurthy, B. Viswanathan, K. Ramesh, P.V.C. Rao, N.V. Choudary and G. Sriganesh.

   PCT/IN2013/000521 27th August, 2013

3. Layered oxide catalyst composite for photo catalytic reduction of carbon dioxide

   V. Jeyalakshmi, K. R. Krishnamurthy, B. Viswanathan, K. Ramesh, P.V.C. Rao, N.V. Choudary and G. Sriganesh,

   Indian Patent Appl- Provisional- 100/MUM/2014, 10th January, 2014.